Crystallographic and quantum chemical studies of electron density distribution and topological analysis of interactions in molecular crystals

Krystalograficzne i kwantowochemiczne badania rozkładu gęstości elektronowej oraz analiza topologiczna oddziaływań w kryształach molekularnych

Mikołaj Pyziak

Supervisor: prof. dr hab. Maciej Kubicki

Department of Chemistry

Adam Mickiewicz University

This dissertation is submitted for the degree of

Doctor of Philosophy
October 2024

I dedicate this work to my wife

You are the light of my life

Acknowledgements

It is with immense gratitude and respect that I express my thanks to my research supervisor, **Prof. Maciej Kubicki**, for enabling me to undertake my PhD studies under his guidance. His contagious scientific enthusiasm and unwavering support throughout this period have been invaluable. I also appreciate deeply the exceptionally positive cooperation we have shared over the years.

I wish to thank **Prof. Marcin Hoffmann** for his ongoing scientific and organisational support in the field of quantum chemical studies, and all the mentorship I had pleasure of experiencing in the process.

I am very thankful to **Prof. Benoit Guillot** and **Prof. Christian Jelsch** from CRM^2 laboratory in Nancy for their support in using the MoPro software suite, as well as the inspiring discussions on charge density research.

There are not enough words in any language that would fully allow to express my gratitude to **Dr Jadwiga Pyziak**, my beloved wife. It is she who first introduced me to the intricate world of quantum chemical studies. Darling, without your inexhaustible love and everyday support this work would not have been possible.

I would like to thank **Dr Bartosz Musznicki** for his subtle yet significant acts of motivation and all the practical tips he kindly shared with me.

I wish to express my deep gratitute to aunt **Elżbieta Woźniak** and my father, **Grzegorz Pyziak**. Their selfless offers of financial support were crucial to continuing my studies in the trying years before obtaining professional stability.

I sincerely thank **Mgr Grzegorz Dutkiewicz** for his contributions in obtaining high-resolution measurements of several compounds studied in this work. I am also grateful for all his practical advice, which has significantly improved my daily work as a crystallographer.

I would like to express my gratitude towards **Prof. Andrzej Gzella** for generously sharing his measurement of 2-[(2,4-Dimethoxyphenyl)amino]-1,3-thiazolidin-4-one with our team. I deeply appreciate his willingness to support our work.

I would like to extend my gratitude to **Prof. Maria Korabik** for her generosity in lending the crystal of Copper(II) 3,5-dichlorobenzoate trihydrate to our team.

I gratefully acknowledge Polish high-performance computing infrastructure PLGrid (HPC Centers: CI TASK, ACK Cyfronet AGH, WCSS) for providing computer facilities and support within computational grant no. PLG/2024/017342.

Abstract

Noncovalent interatomic interactions are of prime interest for chemists, chemical physicists and pharmacologists ever since we understood the role which fine aspects of electron distribution play in branches of science like supramolecular chemistry or drug design. For the majority of branches of chemistry, recognizing causes and effects of variations in charge density distribution became indispensable.

In solids, it is possible to derive charge density distribution from X-ray beam scattering if the irradiated substance is organised periodically. For sufficiently high quality data, the fine features of charge density distribution relevant for intermolecular interactions properties can be measured. In this work, high resolution X-ray diffraction data was used as basis for solving and refining molecular models that incorporated the variations in charge density in physically and chemically meaningful manner. Hansen-Coppens multipolar model was used in high-resolution refinement, obtaining a molecule representation that was further studied using topological analysis in conjunction with Bader's atoms-in-molecules theory.

A set of compounds that contain scientifically valuable cases of intermolecular interactions was chosen. These compounds contain research-worthy cases of strong hydrogen bonds, atypical halogen bonds, and chalcogen bonds. In order to further deepen the understanding of these interactions, high-order X-ray data refinement was supplemented with a series of quantum chemical studies of these systems, widening the possible scientific insight on chosen intermolecular interactions.

Many of chosen compounds contained at least one sulphur atom, a chemical element notorious for challenging when present in system undergoing high-order refinement. The challenge has been successfully overcome, allowing for detailed insight into charge density topology of interactions containing sulphur. Reciprocal S$\cdots$S bond was found and analysed, proving that such σ-hole involving contact can be indeed binding. Similarly, an interaction of chlorine atoms depending on fine variations in charge density was identified, analysed and finally modelled in silico.

Topological analysis of charge density distribution was based on both diffraction data as well as on quantum chemical studies, with two approaches supporting and complementary to each other. Data collected using these methods was used to build a better understanding of studied noncovalent interactions nature, as well as to cross verify the obtained results. During this work, mutual support and testability of crystallographic and quantum chemical approaches to charge density modelling was confirmed as a viable and valuable approach.

Most of studied systems were modelled basing on less-than-perfect data sets that, whilst allowing for obtaining credible results, required careful and creative problem solving. In this process, a novel multistep procedure basing on synergy between diffraction and quantum chemical based charge density appproximation was applied. The developed procedure has the potential of enabling charge density studies for a plethora of molecular crystals that were previously considered insufficient for detailed diffraction data based analysis.

Streszczenie pracy

Niekowalencyjne oddziaływania międzycząsteczkowe są przedmiotem szczególnego zainteresowania chemików, fizyków chemicznych i farmakologów odkąd tylko zrozumiano rolę, jaką pełnią drobne niuanse rozkładu elektronów w dziedzinach nauki takich, jak chemia supramolekularna lub projektowanie leków. Dla większości dziedzin chemii, rozpoznawanie przyczyn i skutków wariacji w rozkładzie elektronów stało się nieodzowne.

Dla ciał stałych możliwym jest obliczenie rozkładu gęstości elektronowej na podstawie sposobu rozpraszania promieniowania rentgenowskiego, jeśli tylko substancja naświetlana zorganizowana jest w sposób periodyczny. Przy dostatecznie dobrej jakości danych, zmierzone zostać mogą szczegółowe osobliwości rozkładu gęstości ładunku istotne dla własności tworzonych oddziaływań międzycząsteczkowych. W przedstawianej pracy użyte zostały wysokorozdzielcze dane rentgenograficzne, na podstawie których rozwiązane i udokładnione zostały modele cząsteczkowe uwzględniające szczegółową zmienność gęstości ładunku nadając im sens chemiczny i fizyczny. W udokładnianiu wysokorozdzielczym zastosowano multipolowy model Hansena-Coppensa, otrzymując w ten sposób reprezentację molekuły będącą bazą do topologicznej analizy rozkładu gęstości elektronowej przy pomocy teorii atomów w cząsteczkach R.Badera.

Za podstawę pracy został wybrany zestaw cząstek zawierających naukowo cenne oddziaływania międzycząsteczkowe. Związki te zawierają w swoich kryształach molekularnych interesujące przypadki silnych wiązań wodorowych, nietypowych wiązań halogenowych oraz chalkogenowych. W celu dalszego pogłębienia wiedzy i zrozumienia tych oddziaływań, wysokorozdzielcze badania rentgenograficzne wsparte zostały szeregiem kwantowochemicznych badań tychże systemów, rozszerzając możliwy wgląd w wybrane oddziaływania międzycząsteczkowe.

Wiele z badanych związków posiadało w swej strukturze co najmniej jeden atom siarki, pierwiastek znany ze sprawiania trudności podczas wysokorozdzielczego udokładniania. Trudności te zostały z sukcesem pokonane, pozwalając na szczegółowy wgląd w topologię rozkładu gęstości oddziaływań obejmujących atom siarki. Zidentyfikowano i zbadano wzajemne wiązanie S$\cdots$S, dowodząc że taki angażujący dziurę σ kontakt może w rzeczy samej być wiązaniem międzycząsteczkowym. Podobnie, interakcja atomów chloru zależąca od drobnych zmienności w ich gęstości elektronowej została zidentyfikowana, zanalizowana i modelowana in silico.

Analiza topologiczna rozkładu gęstości elektronowej prowadzona była zarówno w oparciu o dane dyfrakcyjne, jak i kwantowochemiczne. Oba podejścia wspierały i uzupełniały się wzajemnie. Dane zebrane przy pomocy tych metod stanowiły podstawę do zbudowania lepszego zrozumienia charakteru badanych oddziaływań niekowalencyjnych, jak również pozwalały na krzyżową weryfikację otrzymywanych wyników. W ramach tej pracy naukowej potwierdzono wzajemne wspieranie się oraz wzajemną weryfikację krystalograficznych i kwantowochemicznych modeli rozkładu gęstości elektronowej jako prawidłową i cenną strategię badawczą.

Większość z badanych systemów była modelowana na podstawie danych rentgenograficznych odbiegających od idealnych, jednak pozwalających na otrzymanie wiarygodnych wyników pod wymogiem ostrożnego, rozsądnego udokładniania i kreatywnego podejścia do napotykanych problemów. Owocem tego procesu jest nowa, wieloetapowa procedura oparta o synergię metod obliczania rozkładu gęstości w oparciu o dane rentgenograficzne oraz obliczenia kwantowochemiczne. Opracowana procedura ma w sobie potencjał umożliwienia badań gęstościowych dla szerokiej grupy kryształów molekularnych dotychczas uważanych za niedostatecznie dobrej jakości na potrzeby wysokorozdzielczych badań dyfraktometrycznych.

Table of contents

List of figures

List of tables

Nomenclature

Symbols

ε	Bond ellipticity
$\lambda_{1...3}$	Hessian matrix eigenvalues
$\nabla^2(\mathbf{r})$	Laplacian of electron density
$\rho(\mathbf{r})$	Electron density

Acronyms / Abbreviations

arb.u.	Arbitrary unit
BCP	Bond critical point
BSSE	Basis set superposition error
CCD	Charge coupled device
CD	Charge density
compl.	completeness
CP	Critical point
CSD	Cambridge Structural Database
DF	Density functional
DFT	Density functional theory
ED	Electron density

GGA	Generalized gradient approximation
GTO	Gaussian-type orbital
HAR	Hirshfeld atom refinement
IAM	Independent atom model
inf.	infinity
Lapl.	Laplacian
MM	Multipolar model
MO	Molecular orbital
rdy.	redundancy
STO	Slater-type orbital

Names

aug-cc-pVQZ	Dunning's correlation consistent basis set with quadruple ζ, augmented with diffuse functions
aug-cc-pVQZ/C	Auxillary basis set with core correlation functions for aug-cc-pVQZ
B3LYP	Becke three-parameter hybrid exchange functional combined with the Lee, Yang and Parr correlation functional
B97M-V	Head-Gordon's DF B97M-V with VV10 nonlocal correlation
def2-TZVPD	Ahlrich's ("Karlsruhe") def2 basis set with triple zeta
6-31++G(d,p)	Pople's 6-31G basis set wit one set of first polarization functions and diffuse functions on all atoms
6-311++G(d,p)	Pople's 6-311G basis set wit one set of first polarization functions and diffuse functions on all atoms
6-31G(d,p)	Pople's 6-31G basis set wit one set of first polarization functions on all atoms

M06-2X	The Minnesota M06-2X meta-GGA DF with 54% HF exchange
PWPB95	Goerigk and Grimme's mixture of modified PW91, modified B95, and SOS-MP2
vdW-DF	Van der Waals' density functional
ωB97M-V-D3BJ	Modified ωB97M-V with D3BJ correction by Najibi and Goerigk
ωB97M-V	Head-Gordon's range-separated DF ωB97M-V with VV10 nonlocal correlation

Chapter 1

Introduction

1.1 Basic theoretical background

Electrons are primary source of X-ray scattering and consequently, if the irradiated substance is organised periodically, of the resulting diffraction pattern. Thus, it is a valid assumption that the pattern measured is nearly exclusively a result of electron distribution in the solid. Under that basic premise, it is possible to determine the electron distribution within investigated sample; that is, if the given sample is internally ordered enough to yield a discrete X-ray diffraction of sufficient quality - be it peaks in powder diffraction or reflections in single crystal diffraction experiment.

Scattering by electrons

The scattering of an X-ray beam by a solid is a result of ray's electric component interacting with the electrons. In the classical theory of scattering, those are considered as dipole oscillators undergoing harmonic vibrations, and emitting rays with the same (elastic scattering, the one of experimental value) or lower frequency (inelastic scattering, incoherent to incident beam and contributing to background noise only). At large distances, the scattered wave is spherical. Protons (and, in consequence, nuclei) can indeed interact in the same manner, but this effect can be safely neglected as amplitude and intensity of scattered wave are inversely proportional to particle's mass.

When regarding more than one free point electron, interference between radiation scattered by different centres has to be taken into account. According to classical

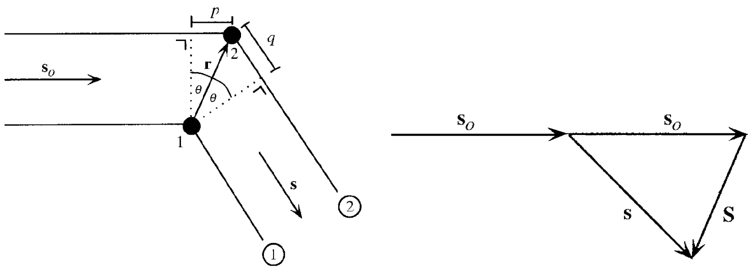

(a) two electron scattering (b) scattering vectors

Fig. 1.1 Geometry of scattering

treatment, for a simple case of system comprising from two free electrons, one at its origin and second at position **r**, the incident beam will be scattered in a following manner: if direction of the incident beam is given by vector $\mathbf{s}_0$ and direction of the scattered beam by vector **s** (both having unit length for convenience), the path difference equals $p+q=\lambda[\mathbf{r}\cdot(\mathbf{s}_0-\mathbf{s})]$.

The phase angle difference resulting from different path lengths covered by the beams passing through first and second electron can be then expressed as:

$$-2\pi\lambda[\mathbf{r}\cdot(\mathbf{s}_0-\mathbf{s})]/\lambda = 2\pi\mathbf{r}\cdot\mathbf{S}, \tag{1.1}$$

where $\mathbf{S}=\mathbf{s}-\mathbf{s}_0$. The length of scattering vector **S** is then given by $|\mathbf{S}| = 2sin\theta/\lambda$. For the scattering by two point electrons at distance **r**, using the rules for addition of coherent waves, the per unit incident amplitude E_0 will be given as:

$$A = \left(1+e^{2\pi i\mathbf{S}\cdot\mathbf{r}}\right)\frac{e^2}{mc^2} \tag{1.2}$$

For a continuous electron distribution $\rho(\mathbf{r})$, the summation over waves of different phase will be replaced by an integration leading to a diffraction amplitude:

$$A(\mathbf{S}) = \int \rho(\mathbf{r})e^{2\pi i\mathbf{S}\cdot\mathbf{r}}d\mathbf{r} \tag{1.3}$$

Thus, the amplitude of scattering is the Fourier transform of electron density.

Scattering by atoms

Even though electrons in atoms are not free, it is usually a good approximation to treat them as such; this will remain valid as long as frequency of incident radiation is sufficiently different from atom's natural absorption frequencies. Under those conditions, the scattering amplitude of an atom is called the atomic scattering factor f and its value decreases significantly with θ angle increasing. This is due to interference occurring between waves scattered by electrons within the electron cloud; the spatial resolution of scattering sources results in phase difference between rays and their destructive interference. At $\theta = 0$, all electrons scatter in phase and atomic scattering factor takes the value of number of electrons in an atom. For wavelengths nearing atomic absorption and for heavy atoms in general (heavy meaning here all elements outside first three rows of the periodic table), corrections for anomalous scattering need to be regarded. The atomic scattering factor is then altered to $f_{anom.} = f + f' + if''$, with f' being the real part and f'' imaginary part of the correction to be applied It is important to note that f'' is $\pi/2$ in phase ahead of f. This scattering is anomalous only de nomo; the process is well understood and makes an invaluable tool for resolving structures of macromolecular crystals. Atomic scattering factors' values are a direct result of scattered waves interference, and thus their exact value can be calculated through Fourier transform of atomic electron density $\rho(\mathbf{r})$.

The nature of the phenomenon results in $sin(\theta)/\lambda$ related scattering amplitude drop getting dramatically stronger pronounced when atomic electron density is more diffuse (Fig. 1.2).

In consequence, less diffuse core shell electrons scatter significantly further (to higher $sin(\theta)/\lambda$) than valence shell electrons. It is therefore beneficiary to obtain high angle data not only due to the improved model quality granted by measuring extra reflections; information they carry is especially valuable for localizing atoms. This fact underlies high-order refinement; using the method, only reflections collected at high angles are utilized during initial steps of modelling, omitting the problem of secondary features obscuring correct solution. Nonetheless, only measurements of exceptionally high resolution and quality are suitable for analysing molecule's secondary features - it is of utter importance to precisely determine core shell electrons contribution to unit cell's total electron density beforehand.

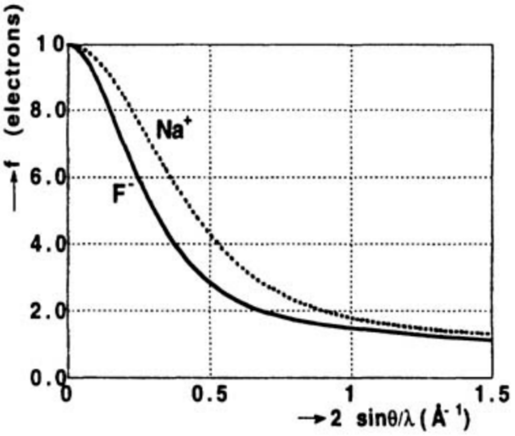

. Being isoelectronic, the factor drop rate difference is related only to orbital contraction.

Fig. 1.2 Spherical atom scattering factors for two isoelectronic ions

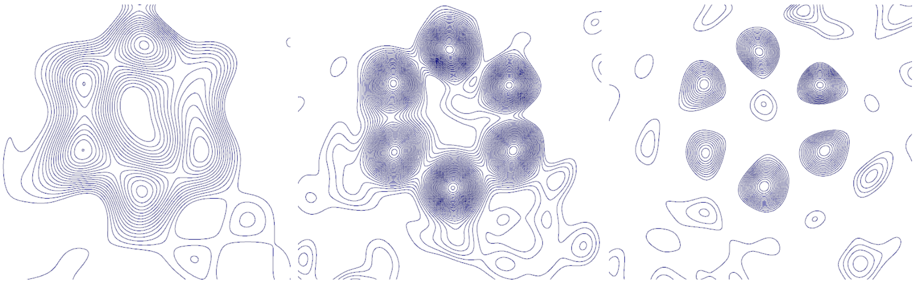

(a) 0.0-0.4 $\AA^{-1}$ low resolution

(b) 0.0-0.8 $\AA^{-1}$ high resolution

(c) 0.4-0.8 $\AA^{-1}$ high-order subset

. Negative values of electron density omitted for clarity.

Fig. 1.3 Fourier images of a phenyl group calculated applying different cutoffs

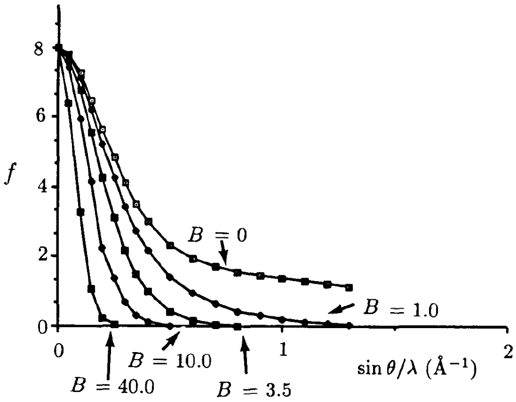

plotted for several chosen values of B-factor (its units discussed elsewhere)

Fig. 1.4 Atomic factor in relation to $sin\theta/\lambda$

Atomic factor drop rate is also affected by apparent smearing of electron density caused by thermal vibrations. This motion can never be frozen out, because of the persistence of zero-point motion, yet performing the experiment with the crystal cooled down well below room temperature - usually done by cloaking it in a jet of nitrogen only few Kelvins above its boiling temperature - improves the situation significantly. Since electrons move incomparably faster than atomic nuclei (and the process of X-ray scattering is about five orders of magnitude faster than the period of lattice vibration), it is safe to assume their instantaneous adjustment to any changes in nuclear spatial configuration. The assumption underlies Born-Oppenheimer approximation, which allows treating nuclear and electronic energies and movement separately.

This makes taking thermal motion into account relatively straightforward, performed by replacing static electron density $\rho(\mathbf{r})$ with time-averaged electron density $\langle\rho(\mathbf{r})\rangle$. Assuming further that electrons can be assigned to specific nuclei and follow them perfectly, the time-averaged electron density is a product of static $\rho(\mathbf{r})$ and nuclear probability distribution P(u) convolution: $\langle\rho_{dynamic}(\mathbf{r})\rangle = \rho_{static}(\mathbf{r}) * P(\mathbf{u})$. According to Fourier convolution theorem, the Fourier transform of the convolution of functions is the product of Fourier transforms of individual functions; hence, it is possible to treat time-averaged atom diffraction as a convolution of its atomic factor and temperature factor $T(\mathbf{S}) : \langle f(\mathbf{S})\rangle = f(\mathbf{S})T(\mathbf{S})$.

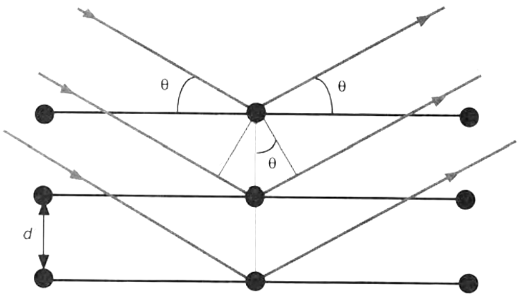

Fig. 1.5 Graphical representation of Bragg diffraction

Bragg's diffraction law

Atoms in a crystal are organised in a lattice, and sets of parallel planes passing through lattice points - the lattice planes - can be treated as mirror planes for X-ray beam. The planes are perpendicular to relevant scattering vectors and constitute basis for geometrical conditions under which a diffracted beam can be observed. Those are stated in Bragg's law, which is expressed as:

$$2d_{hkl}sin\theta_{hkl} = n\lambda \tag{1.4}$$

where θ stands for the angle between lattice planes and incident/reflected beam, the X-ray wavelength is denoted as λ, and d is the plane spacing. The multiplicity n is customarily left with the value of 1, as all other can be replaced by choosing appropriate lattice planes. Since crystal lattice is three-dimensional, reflections observed will take the form of sharp peaks. While the phenomenon is strictly based on constructive/destructive diffraction of scattered X-rays, their reflection is in this context mathematically equivalent. It is worth noting that Bragg's law, apart from a simple and astoundingly precise method of determining cell size and reflections' indexes, underlies the most common expression of resolution: while resolution is determined by maximum θ found in a set of reflexes, it will be written as minimum value of d calculated employing Bragg's Law. Alternatively, resolution is often denoted referring to the scattering vector, as maximum value of $sin(\theta)/\lambda$ found within the experimental set.

Structure factor

The intensities of measured Bragg reflections are affected by a number of factors, including experiment setup related (incident X-ray beam wavelength and intensity or single frame ω scan speed), or sample's intrinsic qualities (sample size, unit cell volume, absorption of scattered rays, their polarizability, fraction of total frame time spent at diffracting position). Paramount for structural studies is the one directly related to diffraction by crystal's unit cell: the structure factor, $F(\mathbf{S})$. The structure factor is a mathematical quantity describing the Bragg reflection with indices *hkl* produced by a whole unit cell (as indices *hkl* are, in a crystal lattice, a term interchangeable with the scattering vector **S**, the structure factor will be denoted as F_{hkl} for lattice scattering from now on). There is a direct proportionality between the reflected beam intensity and squared value of relevant structure factor:

$$I_{hkl} \propto |F_{hkl}|^2 \tag{1.5}$$

The conversion of experimentally measured intensities to final $|F_{hkl}|$ involves taking all corrections mentioned above into account, leaving data ready for structure solving and refinement. The process is termed data reduction, and will usually be followed by data merging - averaging all equivalent reflections into a single occurrence.

Electron density in a crystal

The electron density in a crystal is periodic, and therefore can be represented as a Fourier series.

Temperature factor

The necessity to describe X-ray scattering attenuation caused by thermal motion atom movements is solved by introducing the temperature factor $T(\mathbf{S})$ defined as the Fourier transform of atomic probability distribution. For harmonic isotropic oscillator, the temperature factor equals:

$$I_{hkl} \propto |F_{hkl}|^2 \tag{1.6}$$

where $B = 8\pi^2\langle\rangle$, named Debye-Waller factor. For a trivariat harmonic anisotropic oscillator, isotropic mean square displacement $\langle u^2\rangle$ is replaced with $< u^j u^k >$, where $jk = 1,2,3$ are the displacement coordinates. T(S) equals then:

$$T(\mathbf{S}) = e^{-\frac{1}{4}(h^2B_{11}(a^*)^2+k^2B_{22}(b^*)^2+l^2B_{33}(c^*)^2+2hkB_{12}(a^*)(b^*)+2hlB_{13}(a^*)(c^*)+2klB_{23}(b^*)(c^*))} \tag{1.7}$$

There are currently three commonly used parameters to choose from when describing thermal displacement: tensoral β, Debye-Waller factors B described above, and atomic displacement parameters U. Each has its place in the solid state science, this dissertation will however use Debye-Waller factors due to their arguably most intuitive range of values taken.

Anharmonic Motion

If the deviations from harmonic potential energy function are significant, idealised rectilinear motion assumed for $P(\mathbf{u})$ so far needs to be replaced by a substantially more complicated model. Anharmonicity or curvilinear motion of atoms is approximated by a Taylor-series-like statistical expansions, typically a three-dimensional Gram-Charlier expansion:

$$P(\mathbf{u}) = (1 - c^j D_j + \frac{c^{jk}}{2!} D_j D_k - \frac{c^{jkl}}{3!} D_j D_k D_l + \cdots + (-1)^r \frac{c^{\alpha 1 \ldots \alpha_r}}{r!} D_{\alpha_1} \ldots D_{\alpha_r}) P_0(\mathbf{u}) \tag{1.8}$$

Where $P_0(\mathbf{u})$ is harmonic probability distribution, $D_{\alpha_1} \ldots D_{\alpha_r}$ r-th partial covariant derivative operator $\delta^r/(\delta u^{\alpha_1} \ldots \delta u^{\alpha_r})$ and $c^{\alpha_1 \ldots \alpha_r}$ a contravariant component of the coefficient tensor. Since $P_0(\mathbf{u})$ is a Gaussian distribution, the series may be rewritten using Hermite polynomials:

$$H_{\alpha_{1\ldots r}}(\mathbf{u}) = e^{\frac{1}{2}\sigma_{jk}^{-1} u^j u^k} \times (-1)^r D_{\alpha_1} D_{\alpha_2} \ldots D_{\alpha_r} e^{\frac{1}{2}\sigma_{jk}^{-1} u^j u^k} \tag{1.9}$$

for $w_j = \sigma^{-1}_{jk} u^k$, $\sigma^{-1}_{jk} = \sigma^{-1}_{kj}$, and $w_j w_k = w_k w_j$, first relevant Hermite polynomials are expressed as:

$$\begin{aligned} H_{jkl}(\mathbf{u}) = w_j w_k w_l - w_j \sigma^{-1}_{kl} - w_k \sigma^{-1}_{lj} - w_l \sigma^{-1}_{jk} &= w_j w_k w_l - 3 w_{(j\sigma^{-1}_{kl})} \\ H_{jklm}(\mathbf{u}) &= w_j w_k w_l w_m - 6 w_{(j w_k \sigma^{-1}_{lm})} + 3\sigma^{-1}_{j(k\sigma^{-1}_{lm})} \\ H_{jklmn}(\mathbf{u}) &= w_j w_k w_l w_m w_n - 10 w_{(l w_m w_n \sigma^{-1}_{jk})} + 15 w_{(n\sigma^{-1}_{jk}\sigma^{-1}_{lm})} \end{aligned} \tag{1.10}$$

where brackets indicate averaging over all permutations of the bracketed indices which produce distinct terms. $H(\mathbf{u})$, $H_j(\mathbf{u})$ and $H_{jk}(\mathbf{u})$ are omitted, as they do not modify anharmonic distribution. The Gram-Charlier series then equals:

$$P(\mathbf{u}) = (1 + \frac{1}{3!} c^{jkl} H_{jkl}(\mathbf{u}) + \frac{1}{4!} c^{jklm} H_{jklm}(\mathbf{u}) + \frac{1}{5!} c^{jklmn} H_{jklmn}(\mathbf{u}) + \ldots) \tag{1.11}$$

The anharmonic temperature factor is the Fourier transform of this probability distribution, giving:

$$T(\mathbf{S}) = (1 + \frac{i^3}{3!} c^{jkl} S_j S_k S_l + \frac{i^4}{4!} c^{jklm} S_j S_k S_l S_m + \frac{i^5}{5!} c^{jklmn} S_j S_k S_l S_m S_n + \ldots) T_0(\mathbf{S}) \tag{1.12}$$

Truncating at the cubic term is usually sufficient, and the necessity to incorporate higher terms is significantly less common. It may be beneficial to truncate at quintic term only in exceptional cases. Adding anharmonicity to structure model should be in any case, however, performed with utmost caution. Anisotropic parameters are generally susceptible to data set errors and it is relatively easy to introduce those into the model; even more so when regarding relatively minute corrections applied with Gram-Charlier expansion.

1.2 Modelling and Refinement

Like most natural sciences, crystallography describes studied objects of interest through their idealised representations. The description is done using structure models of varying precision. Inevitably, a disparity between the idealised representation of studied objects and gathered experimental data will occur. The disparity is addressed by:

1. increasing model accuracy through refinement,
2. choosing a more detailed model if justified,
3. describing the remaining disparity.

Independent atom model

The independent atom model (IAM) is the staple of molecular modelling in crystals. It relies on assumption that the electron density is sufficiently well described by a set of spherically averaged density of isolated atoms. The simple, yet sound IAM is described by equation:

$$\rho_{IAM}(\mathbf{r}) = \sum_k \rho_k^0(r - R_k) \tag{1.13}$$

Where R_k is the position of atom k. In this model, the negative charge is localized around the nuclei. Each molecule is a superposition from individual, spherical, non-interacting atoms. Due to this characteristics, the resulting structures are formally named promolecules.

IAM is commonly used in standard resolution crystallography, with structures resolved and published yearly at the order of magnitude of tens of thousands. It is especially fitting for use with heavier atoms, as model accuracy increases with falling ratio of valence to total electrons. Simplifications come at a cost to accuracy: IAM omits intra- and intermolecular charge shifts, enforces electroneutrality and spherical atom form, artificially shortens X-H distances due to hydrogen lacking any non-valent electrons.

Kappa model

Kappa model[1], also known as κ-formalism, is an improvement allowing for charge transfer between atoms. The atoms are still modeled as spherical. The total density of an atom is defined by the sum of core and valence electron density:

$$\rho_{atom}(\mathbf{r}) = \rho_{core}(\mathbf{r}) + P_{valence}\kappa^3\rho_{valence}(\kappa\mathbf{r}) \tag{1.14}$$

Where ρ_{core} and $\rho_{valence}$ are spherical core and spherical valence densities, respectively. It is assumed that core electrons are not perturbed. Parameter κ scales the radial coordinate r: when $\kappa > 1$, same density is obtained at lower r, the valence shell is contracted. For $\kappa < 1$, the valence shell is expanded. Hence, the parameter is named expansion/contraction coefficient. Application of the κ model yields net charges in agreement with expected on basis of electronegativity, and the molecular dipole moment is approximating values obtained through other experimental methods. The model is a significant improvement over IAM, however it still neglects non-spherical charge distribution: interatomic bonds and lone pairs are not modelled, X-H distances are still artificially shortened, atoms remain spherical.

Hansen-Coppens model

Atomic orbitals are, apart from the simplest cases, not spherical. Advanced X-ray scattering models must also contain nonspherical components. In the Hansen-Coppens multipolar model[2] the total atomic electron density is expressed as:

$$\rho_{atom}(\mathbf{r}) = \rho_{core}(\mathbf{r}) + P_{valence}\kappa^3\rho_{valence}(\kappa\mathbf{r}) + \sum_{l=0}^{l_{max}} \kappa_l'^3 R_{nl}(\kappa'\mathbf{r}) \sum_{m=0}^{l} P_{lm\pm} y_{lm\pm}(\theta,\phi) \tag{1.15}$$

Where ρ_{core} and $\rho_{valence}$ are spherical core and nonspherical valence densities, respectively. The third term represents the sum of angular functions $y_{lm\pm}(\theta,\phi)$, accounting for aspherical deformations. Angular functions are defined in local axis context, that is with each atom possessing its own coordinate system, independent of crystal unit. The coefficients $P_{valence}$ and $P_{lm\pm}$ correspond to multipole populations for spherical and nonspherical valence populations, respectively. Parameters κ and κ' serve same purpose like in the kappa model, with κ' used for nonspherical part. The model allows for modelling of anisotropic effects on atomic charge distribution.

In order for the model to be meaningful high quality, high resolution diffraction data should be employed. Furthermore, refinement should be done with careful consideration; parameters may display correlation effects, leading to incorrect shifts in parameter values. With high resolution diffraction data resulting in a big data set, and several times more parameters per atom as compared to simpler models, refining Hansen-Coppens model is somewhat computationally heavy. Still, it is at least an order of magnitude less resource-intensive than Hirshfeld atom refinement.

It is important to remember that, despite apparent similarities, multipoles do not describe actual molecular orbitals. The model describes a molecule not as a set of atoms with populated molecular orbitals, but as one comprising of pseudoatoms with non-spherical charge distribution. Furthermore, multipolar atom-centered models do not explicitly account for two-center orbitals. In this sense, pseudoatoms are also isolated - though their nonspherical components can and do significantly overlap. While we can infer fine details of molecular charges, bond strengths and intramolecular interactions from an obtained model, generally a set of multipoles centered around a given atomic position should not be studied in isolation from neighbours. Analysis of obtained charge densities is done employing topological analysis.

There do exist alternative multipolar models, e.g. Stewart's model[3]: a deformation density formalism with a single crystal-coordinate system. In this work, the term multipolar model (MM) will be used as a synonym to Hansen-Coppens model.

Least squares refinement

During the refinement the least-squares method was used to minimize the following function:

$$E = \sum_{\mathbf{H}} W_{\mathbf{H}} (I_{obs} - I_{calc})^2 \tag{1.16}$$

The summation over reflections **H** is classically performed over the structure-factor moduli difference $|F|_{obs} - |F|_{calc}$. In this work, refinements were performed over the reflection intensity difference $I_{obs} - I_{calc}$ unless stated otherwise. The reflection weighting scheme follows the equation $W_{\mathbf{H}} = 1/\sigma_I^2$, where σ_I is the reflection measurement uncertainty. Reflections are measured on relative rather than absolute scale, necessitating the use of a refineable scale factor k.

$$\Delta I = \frac{1}{k} I_{obs} - I_{calc} \tag{1.17}$$

Scale factor k is classically a scalar value. Valence and core scattering vary in influence at different resolutions, which may lead to artifacts in refined electron density. This can be partly corrected by using a non-scalar scale factor. In this work, a scale factor that is a polynomial function of reciprocal resolution $s = 1/2d$ was used for some structures:

$$k = k_0 + k_1 s + k_2 s^2 + \ldots + k_n s^n \tag{1.18}$$

Restraints

Even though at first glance refinement is a well-known mathematical process of finding a function minimum, in reality the process is nonlinear, requiring constant supervision and corrections from the researcher. Crystallographers need to influence the process, else the resulting model may not be physically and chemically reliable. Many of refined values are correlated, and must be refined, especially at the initial stages, separately. Even high quality data routinely need additional input, realized as an additional parameters to the minimized function:

$$E = \sum_{\mathbf{H}} W_{\mathbf{H}} (I_{obs} - I_{calc})^2 + \sum_{restraints} W_R (R_{target} - R_{calc})^2 \tag{1.19}$$

Where W_R is restraint weight, R_{target} the target value for a given system property, R_{calc} the actual value calculated from model. Restraint weight W_R is defined as $W_R = 1/\sigma^2_{R_{target}}$, where $\sigma_{R_{target}}$ is allowed standard deviation from target value.

Constraints

In many cases a restraint is still too permissive if data quality does not justify refining a parameter, or system's properties make refining a given value unjustified (or even wrong). The common case are hydrogen atom bond lengths, especially in biomolecules. One could regard constraints a special case of restraints, where restraint weight approaches infinity; of course, it is simpler and computationally more effective to exclude a constrained parameter from least squares refinement altogether.

Hirshfeld atom refinement

HAR opiszemy później, albo wyrzucimy - było użyte przy S3, S4 i mako jako sposób uzyskania lepszych koordynatów

Model quality assessment

R factor

Weighted R factor

Goodness of fit

Residual density

Deformation density

[4]

The deformation density is defined as the difference between the total

1.3 Quantum chemical studies

Since at atomic scale wave-particle duality is prominent, the motion of a particle will obey the de Broglie relation in an observable manner. It follows that the electron, a charged atomic particle, will assume behaviour which can be expressed as a time-dependent wave function $\Psi(\mathbf{r},t)$. The wavefunction takes the generalized form of time-dependent Schrödinger equation:

$$i\hbar\frac{\partial}{\partial t}\Psi(\mathbf{r},t) = \left\{-\frac{\hbar^2}{2m}\nabla^2 + V(\mathbf{r})\right\}\Psi(\mathbf{r},t) \tag{1.20}$$

where ∇^2 is the Laplace operator (Laplacian), a second-order differential operator in the three-dimensional orthogonal space. For constant energy systems, the time-dependent factor can be separated out through $\Psi(\mathbf{r},t) = \psi(\mathbf{r})e^{-iEt/\hbar}$. The time-independent Schrödinger equation, on which the vast majority of quantum mechanics applications to chemistry base, is expressed as:

$$\left\{-\frac{\hbar^2}{2m}\nabla^2 + V(\mathbf{r})\right\}\psi(\mathbf{r}) = E\psi(\mathbf{r}) \tag{1.21}$$

An atomic particle moving under the influence of varying external field is bound to assume one of quantized energy levels. This energy may be expressed as a function of particle's position and momentum, described by the quantum-mechanical Hamiltonian operator:

$$\hat{H} = -\frac{\hbar^2}{2m}\nabla^2 + V(\mathbf{r}) \tag{1.22}$$

thus, the time-independent Schrödinger equation may be further reduced to $\hat{H}\psi = E\psi$.

Basis sets

The probability distribution of a single electron present in an atom can be solved exactly. It is, however, the common scientific consensus that — except for a handful of fringe cases — chemistry as a science deals with systems comprising at least two electrons. Applying quantum mechanics to chemistry is therefore inherently involving approximations. The Born-Oppenheimer approximation described in Section 1.1 finds itself commonly applied in quantum chemical modelling, with the assumption that the nuclei positions are not only independent of electron movement, but also positionally fixed. As such, they bring no kinetic energy contributions into the modelled system, removing electron influence on nuclear positions from the Schrödinger equation. The standard strategy is to assume that each spinorbital is sufficiently well described through the LCAO approximation: as a linear combination of single electron atomic orbitals

$$\psi_i \approx \sum_{\nu}^{K} c_{\nu_i}\phi_\nu \tag{1.23}$$

High-level molecular computations relevant to this work start with the Hartree-Fock approximation method, which assumes that the N-body wavefunction is successfully

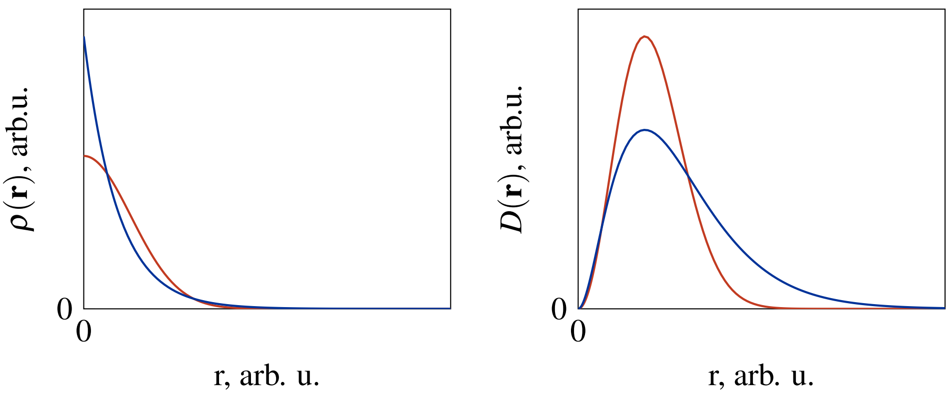

Fig. 1.6 Density $\rho(\mathbf{r})$ and radial distribution $D(\mathbf{r})$ functions calculated for exemplary Slater Type orbital (blue) and Gaussian equivalent (red).

approximated by the simplest form of a wavefunction that satisfies the antisymmetry principle, a Slater determinant

$$\Psi(1,2,\ldots,N) = \frac{1}{\sqrt{N!}} \begin{vmatrix} \phi_a(1) & \phi_a(2) & \cdots & \phi_n(1) \\ \phi_b(1) & \phi_b(2) & \cdots & \phi_n(2) \\ \vdots & \vdots & \ddots & \vdots \\ \phi_N(1) & \phi_N(2) & \cdots & \phi_N(N) \end{vmatrix} \tag{1.24}$$

Solving Hartree-Fock equations directly is not a practical approach for multiatomic molecules. In order to reduce computational complexity, each fo the molecular orbitals is expressed as a linear combination of n basis functions f_i

$$\phi_a = \sum_i^n c_{a_i} f_i \tag{1.25}$$

Where coefficients c_{a_i} are computed using the Roothaan – Hall self consistent field procedure. A set of basis functions comprises, with only a handful of exceptions, of Gaussian-type orbitals. This is consequence of the complexity barrier posed by Slater-type orbitals. A Gaussian function has the major advantages of lower inherent computational complexity, as well as the product of two Gaussian functions also being a Gaussian function. In consequence, a product of two gaussians around two different centers can be reduced to a single gaussian around a new center. Such characteristics move the barrier of calculated molecule's size exponentially. The advantages of a simple Gaussian approximation are countered by its unacceptable inaccuracy (Fig. 1.6).

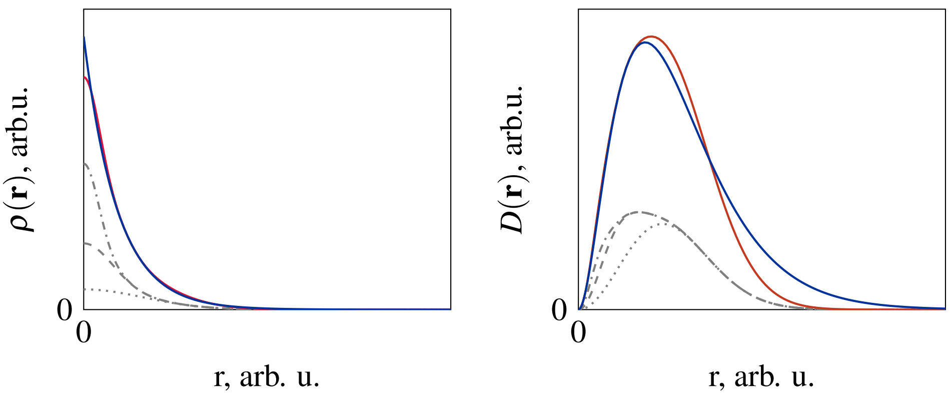

Fig. 1.7 Density $\rho(\mathbf{r})$ and radial distribution $D(\mathbf{r})$ functions calculated for exemplary Slater Type orbital (blue) and its Gaussian type equivalent (red). Chosen expansion terms visible on graph (1st GTO: dotted gray, 2nd: dashed, 3rd: dash-dotted).

The limited accuracy problem can be largely resolved if an atomic orbital is represented by a fixed linear combination of multiple primitive Gaussian functions

$$\phi_\mu = \sum_i^L d_{i_\mu} \phi_i(\alpha_{i_\mu}) \tag{1.26}$$

where d_{i_μ} is the primitive Gaussian function coefficient, and α_{i_μ} is this function's exponent. The coefficients and exponents are found by least–squares fitting, maximizing the overlap (Fig. 1.7) between the Slater-type orbital and the linear combination of primitives. Nevertheless, even higher expansions typically suffer from too low amplitudes away from nuclear centres that have to be corrected with more complex orbitals definitions especially when studying weak intermolecular interactions. Basis set functions are usually enhanced with polarization functions, allowing for modelling charge perturbation in response to present electrostatic potential. Additionally, a basis set may – and in the case of this work, should – be enhanced with highly diffuse functions in order to remedy the aforementioned inherent deficiency in charge distribution at larger distances from atomic nucleus.

Density functional theory

An alternative to calculating the full N-electron wavefunction is to calculate only the total electronic energy and density distribution. The key idea behind this simplification is that there exists a relationship between the two values such, that defining the electron density suffices to uniquely determine the ground-state energy of a system [5]. In other words, the electronic energy is a functional of the density: $E = E[\rho]$. The energy functional can be divided into four contributions, as described by Kohn-Sham formalism:

$$\begin{aligned} E[\rho(\mathbf{r})] = \sum_{i}^{N} \int \psi_i(\mathbf{r}) \left(-\frac{\nabla^2}{2}\right) \psi_i(\mathbf{r}) d(\mathbf{r}) + \frac{1}{2} \iint \frac{\rho(\mathbf{r}_1)\rho(\mathbf{r}_2)}{|r_1 - r_2|} d(\mathbf{r}_1) d(\mathbf{r}_2) \\ + E_{XC}[\rho(\mathbf{r})] - \sum_{A}^{M} \int \frac{Z_A}{|\mathbf{r} - \mathbf{R}_A|} \rho(\mathbf{r}) d\mathbf{r} + \sum_{A<B} \frac{Z_A Z_B}{R_{AB}} \end{aligned} \tag{1.27}$$

or, in short,

$$E[\rho(\mathbf{r})] = E^K[\rho(\mathbf{r})] + E^J[\rho(\mathbf{r})] + E^{XC}[\rho(\mathbf{r})] + E^V[\rho(\mathbf{r})] \tag{1.28}$$

where $E^K[\rho(\mathbf{r})]$ is the functional of non-interacting electrons with same density as the real system, $E^J[\rho(\mathbf{r})]$ is the electron-electron potential energy, $E^{XC}[\rho(\mathbf{r})]$ the exchange-correlation functional, and $E^V[\rho(\mathbf{r})]$ the potential energy of nuclear-electronic and internuclear interactions. The form of $E^{XC}[\rho(\mathbf{r})]$ is not provided above, as it is not known and needs to be approximated. By expressing the density $\rho(\mathbf{r})$ as $\rho(\mathbf{r}) = \sum |\psi_i(\mathbf{r})|^2$ and applying the appropriate variational condition, a generalization of one-electron Hartree-Fock equations is obtained

$$\left\{ -\frac{\nabla^2}{2} - \sum_{A}^{M} \frac{Z_A}{|\mathbf{r} - \mathbf{R}_A|} + \int \frac{\rho(\mathbf{r}_2)}{r_{12}} d\mathbf{r}_2 + V^{XC}[\mathbf{r}_1] \right\} \psi_i(\mathbf{r}_1) = \varepsilon_i \psi_i(\mathbf{r}_1) \tag{1.29}$$

where $V^{XC}[\mathbf{r}_1]$ is known as the exchange-correlation functional, related to the exchange-correlation energy through:

$$V^{XC}[\mathbf{r}_1] = \left(\frac{\delta E_{XC}[\rho(\mathbf{r})]}{\delta \rho(\mathbf{r})} \right) \tag{1.30}$$

the $E[\rho(\mathbf{r})]$ is then calculated from Eq. (1.27). Solving the Kohn-Sham equations requires a self-consistent approach.

Clearly, a correct exchange-correlation functional approximation is crucial to the success, or failure, of density functional approach. Thankfully, even relatively simple expressions can yield useful results for simple enough systems. Over the decades, the number of available exchange-correlation functionals has reached triple digits. While many of those are specialized and really only applicable to a narrow selection of tasks and chemical elements, a wide selection is available for general purpose calculations. Throughout the rest of this work, the term "functional" will be used as a synonym for exchange-correlation functional.

Dispersion correction

Dispersion forces are weak, long-range attractive forces acting between molecules also in case when the molecules, or molecular moieties, are electrostatically neutral. Taken at average charge density granularity level, the electron clouds of neutral molecules should repel each other if no favourable dipole moments are present. At electronic level, however, momentary perturbations in electron density induce a dipole moment in atoms of neighbouring molecules. The created London forces decay with the inverse of sixth power of the intermolecular distance and, being weak to start with, can be omitted for most cases of quantum chemical studies.

Studies of intermolecular contacts are not one of those cases. Neither Hartree-Fock model nor Kohn-Sham equations provide means for modelling London forces, since these formalisms consider only local molecular charge density. In order to describe and model dispersion forces, a nonlocal component is necessary. The most widely used form that achieves that is by introducing a nonlocal term to exchange-correlation energy, accounting for weak forces:

$$E^{XC} = E^{X}_{LDA/GGA} + E^{C}_{LDA/GGA} + E^{C}_{NL} \tag{1.31}$$

where standard components of local (LDA) or semilocal (GGA) density approximation are used, and E^{C}_{NL} represents the nonlocal term describing vdW-DF energy. In primitive implementations, E^{C}_{NL} is computed in a non self-consistent manner. Refined expressions of NL functional are, unfortunately, almost as computationally expensive as the first two terms of Eq. (1.31) combined.

Chapter 2

Aim of studies

2.1 Charge density distribution studies

There are, in principle, two complementary ways of gathering information about a certain interaction. One can rely on the enormous source of structural information which is provided by the Cambridge Crystallographic Data Center – the CSD. Comparing thousands of structures may (and often does) lead to the identification, on the basis of statistics, of certain interactions and to the determination of their principal – although mainly geometrical – features. This approach has been widely used throughout the structural science community, and a number of reports describing such analyses is enormous. The weak point of this approach is the necessity of assuming the arbitrary criteria for classifying the contacts as interactions, typically on basis of relation between distances of two atoms and the sum of their van der Waals radii, and the potential non representability of a sample under consideration. The second approach is connected with detailed analysis of electron density distribution in the crystals, finding the interaction paths, and connecting them with the certain interactions by the topological, energetic, and other quantitative characteristics. This work focuses on the second approach, both on basis of data collected through both high-resolution charge density refinement, as well as on basis of *in silico* structure modelling.

2.2 Multipolar charge density refinement

Since charge density refinement requires exceptionally high quality of collected diffraction data, only a small percentage of all crystals is fit for appropriate high resolution diffraction data collection procedure. Even when studying a monocrystal relatively large and free of imperfections, the process of collecting reflections for high resolution multipolar refinement remains non trivial and time consuming. In consequence, the majority of the aforementioned small percentage is never even considered as candidates for charge density studies. A selection of sub perfect measurements was used as basis for multipolar refinement, using several methods: applying conventionally applied for macromolecules multipole database transfer, carefully balancing restraints and constraints against R_{free} values, and/or applying a novel combination of refinement steps including Hirshfeld atom refinement. These methods shift the charge density studies quality barrier, making the studies approachable and applicable to a significantly larger set of crystallised compounds. This work applies a novel sequence of refinement procedures, and contrasts the obtained results against those obtained *in silico*.

2.3 Analysis of interactions in molecular crystals

Intermolecular noncovalent interactions constitute one of the principal factors in the determination of a molecular crystal architecture, as well as supramolecular interactions outside the solid phase. The ultimately materialized crystal structure is a consequence of fine interplay between a number of factors, including space-group requirements, tendency toward close packing, and so forth. Predicting the crystal structure of a given chemical compound remains a challenging task, prone to failure despite significant progress that has been achieved over last two decades. For the purpose of crystal engineering, moderately polarized contacts such as chalcogen bonds, chalcogen bonds, and noncovalent bonds employing delocalized aryl rings are most useful. Also in drug design, the challenges of understanding how all the minute effects contribute to molecule's affinity to specific nooks and crannies of a given biomolecule can only be addressed with proper knowledge about the underlying supramolecular phenomena.

This work extends the knowledge base in the subject of weak intermolecular interactions, including chalcogen$\cdots$chalcogen bonds which are particularly useful in electroactive crystal engineering, as well as analysing in detail the intermolecular interactions formed in crystals of substances from groups with well documented biological activity.

Chapter 3

4-[[4-(Methoxy)-3-quinolinyl]thio]-3-thiomethylquinoline

3.1 Introduction

Quinolines are a class of heterocyclic aromatic compounds with important biological and pharmaceutical applications [6–9]. They exhibit a broad range of activity, including antibacterial [10–15], antiviral [16–18], antimalarial [19–22], anticancer [23–29], and anti-inflammatory properties [20, 30–32]. Quinolines are crucial in drug discovery, serving as scaffolds for developing new therapeutic agents. Recently, quinolines have shown promise in treating neurodegenerative diseases, further expanding their therapeutic potential. Their versatility extends to industrial applications, where they are used in the synthesis of dyes and agrochemicals [33–35].

4-[[4-(Methoxy)-3-quinolinyl]thio]-3-thiomethylquinoline (**1**) is a derivative containing two different quinoline moieties, bound by a sulphur atom. It is this sulphur atom that is particularly interesting: it forms a strong chalcogen bond, a very unique one: a reciprocal homoatomic contact. This chapter provides an in-depth analysis of the aforementioned bond. The molecule serves also as a vessel for comparing three modelling approaches: the independent atom model (IAM), the multipolar model (MM), as well as IAM + DFT, with a selection of popular functionals and bases used.

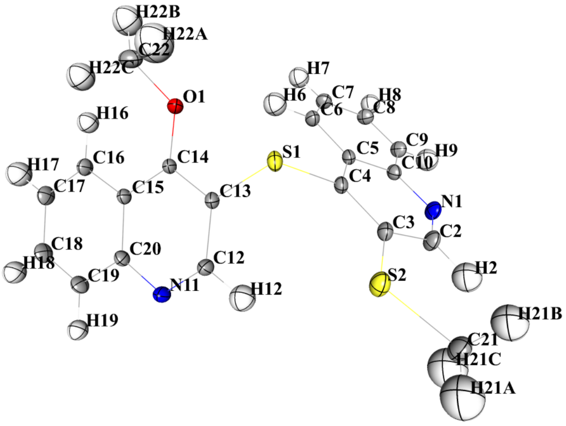

Fig. 3.1 Anisotropic ellipsoid representation of **1** with labeling scheme. Ellipsoids are drawn at 50% probability level

3.2 Structure and interactions

Compound **1** has a biplanar geometry, enforced by S1 atom connecting two quinoline derivatives. The C4–S1–C13 angle measures at 102.9°, which is somewhat outside of typical sp^3 angle range for sulphur. This is caused by aromatic rings packing geometry, which themselves are also slightly deformed near the S1 atom: the C–C–C–S1 torsion angles measure approximately 173°, which is significantly less than 180° expected for sp^2 carbon atoms. The structure of this compound measured at standard resolution has been reported and described in detail previously [36].

The molecule **1** has a total of 16 symmetry equivalents in their immediate vicinity, as presented on Section 3.2. Of these, 12 are symmetry independent. Out of this number, a total of 5 symmetry mates participate in the particularly interesting interactions, described in more detail below. They are depicted in and described in detail later on.

The analysis of normalized contact distances mapped on the Hirshfeld surface (**??**) brings attention to the S1 sulfur atom area, where there is a minimum of -0.15. Similarly, relatively short $OCH_3 \cdots N$ contacts breach van der Waals radii, giving normalized contact distances of -0.10 and -0.09. It is worth noting that, despite its steric hindrance, the O1 atom stays in close contact with its symmetry generated counterpart, but not with the contacting hydrogen atoms.

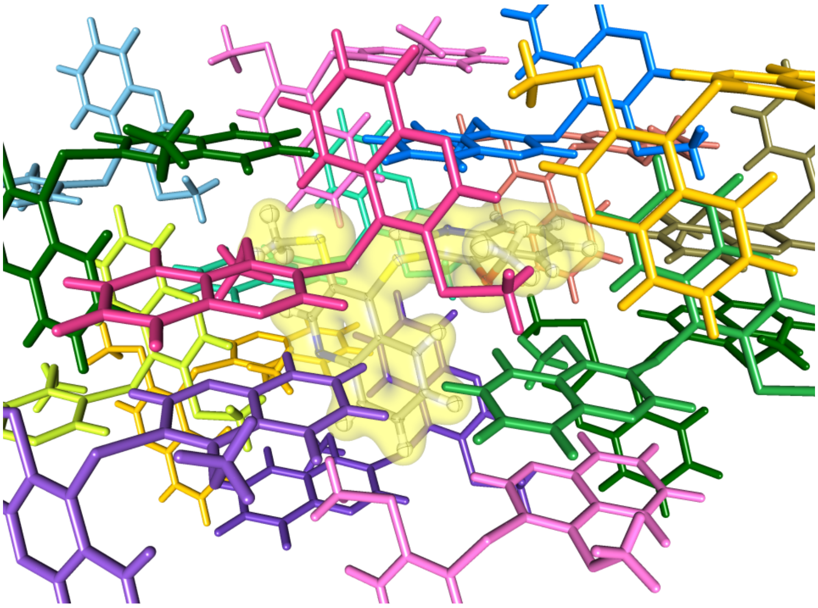

Fig. 3.2 Symmetry equivalents surrounding **1**. A unique colour is used for each unique symmetry equivalent.

Fig. 3.3 Hirshfeld surface of **1**. Surface colouring: d_{norm}. Red: negative, minimum at -0.15; blue: positive, maximum at 1.2

Homoatomic interactions

There are four homoatomic, binding intermolecular contacts. Two of these deserve special attention: $S1 \cdots S1^i$ (^{i} denotes symmetry operation $-x, -y, -z + (1,1,1)$) depicted on Section 3.2, and $O1 \cdots O1^{ii}$ (^{ii} for $-x, -y, -z + (1,2,1)$). For both contacts, the (3, -1) critical points between the atoms have been found along with the appropriate interaction paths, which indicates the probable presence of intermolecular bonding. In previous studies of this system, it has been signaled that the $S1 \cdots S1^i$ distance is significantly smaller than the sum of the van der Waals radii. Static total electron density at this location has value of 0.081 eÅ^{-3}, which is the highest of all intermolecular (3, -1) critical points within this lattice. Laplacian (0.75 eÅ^{-5}) and λ_1 (1.01 eÅ^{-5}) values are smaller only than the corresponding values for the C-H$\cdots$N bond. Detailed analysis based on both crystallographic data and DFT calculations shows the bonding mediated via sulfur free electron pairs and σ–holes. The C4—$S1 \cdots S1^i$ angle of 158.7° lies within the typical range for chalcogen bonds reported earlier. Bond strength has been calculated in the range -3.0 to -12.3 kcal/mol, depending on the functional and calculations base applied. The $S1 \cdots S1^i$ distance of 3.3300(11) Å, as measured in the

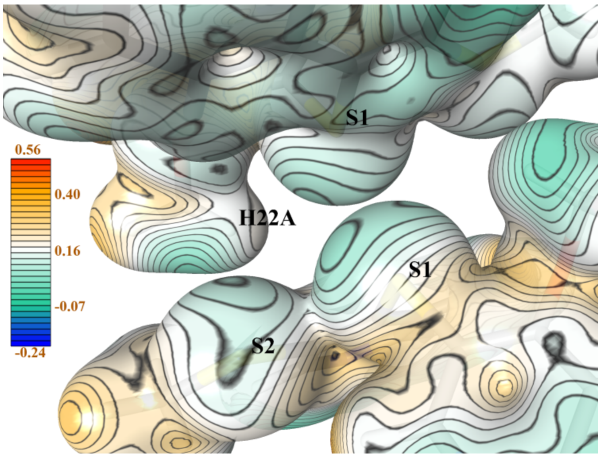

Fig. 3.4 Multipolar model based sulfur electron pairs$\cdots\sigma$-holes bonding region. Electrostatic potential (eÅ^{-1}) mapped over the electron density isosurface of eÅ^{-3}.

crystal is, according to *in silico* studies, optimal. The calculated minimum energy distance is 3.33–3.34 Å depending on the functional base applied. Section 3.2 shows the energy change with intermolecular distance, calculated for different functional bases. Minimum energy values are gathered in Table 3.1.

The strength and privileged location of the S1$\cdots$S1^{i} interaction clearly indicates that it can play an important role in the crystal structure architecture determination and solid state stability. It is a very rare case of a symmetry-generated reciprocal S...S σ–bond between two sulfur atoms. The O1$\cdots$O1^{ii} interactions are relatively weak, with the static electron density of 0.028 eÅ^{-3} at the (3, -1) saddle point, but its relatively high second derivative parameters ($\nabla^2\rho(\mathbf{r}) = 0.49$ and $\lambda_1 = 0.57$) suggest that this is a genuine interaction and not a modelling artifact. This critical point is also, similarly to sulfur$\cdots$sulfur (3, -1) critical point, placed at the inversion center at 1/2 0 1/2 (S$\cdots$S^{i} at 1/2 1/2 1/2). However, it is a peculiar contact, and its share of only 0.1% of Hirshfeld surface strengthens the first impression of an accidental van der Waals radii sum breach; however, the deformation map (Fig. 3.6a) confirms the possibility of the neighboring molecules, related by the center of inversion, attracting (or at least interacting with) each other. Shared lowest unoccupied orbital (LUMO) also indicates that these two oxygen atoms develop a weak bonding interaction.

There are two other homoatomic intermolecular interactions (or – strictly speaking – the contacts for which (3, -1) critical points and bonding paths could be found), namely, H17$\cdots$H17^{iii} (^{iii} : -x, -y, -z + (0,3,1)) and H6$\cdots$H16^{ii},both positioned at the different

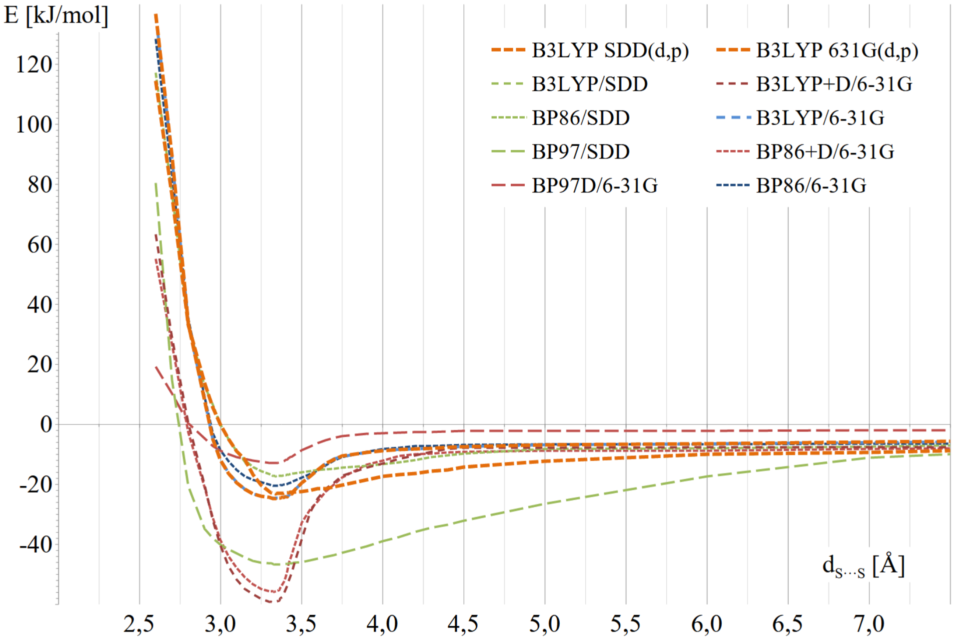

Fig. 3.5 Energy changes upon variation of S1···S1 distance $d_{S \cdots S}$ between two bound molecules.

Source	E_{bond}, kJ/mol
B3LYP 6-31G	-24.6
B3LYP+D 6-31G	-59.2
BP86 6-31G	-20.5
BP86+D 6-31G	-55.7
BP97D 6-31G	-54.0
B3LYP SDD	-23.1
BP86 SDD	-17.2
BP97 SDD	-46.7
B3LYP 6-31G(d,p)	-24.7
B3LYP SDD(d,p)	-23.1
VMoPro (MM)	-30.1
VMoPro (IAM)	-26.3

Table 3.1 Energy Values for S1···S1 at minima for various functionals and basis sets. Electrostatic interaction energy calculated by VMoPro added for comparison.

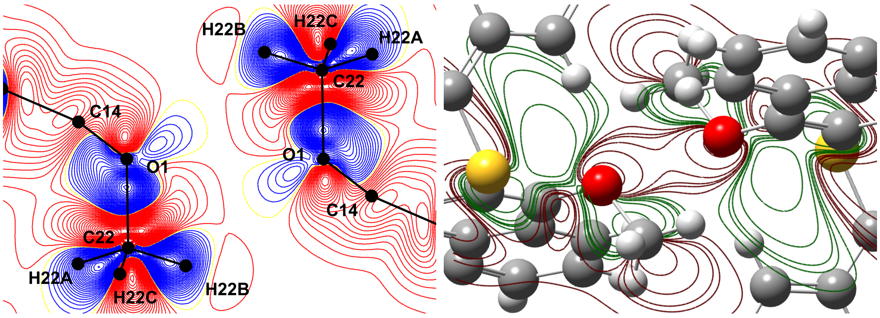

(a) (b)

Fig. 3.6 Homoatomic O1-O1 interaction illustration. Fig. 3.6a: Static deformation map of the O1$\cdots$O1 contact area. Isovalues every 0.01 eÅ^{-3}; blue, negative; red, positive. Fig. 3.6b: LUMO calculated for symmetry mates around O1$\cdots$O1 symmetry center

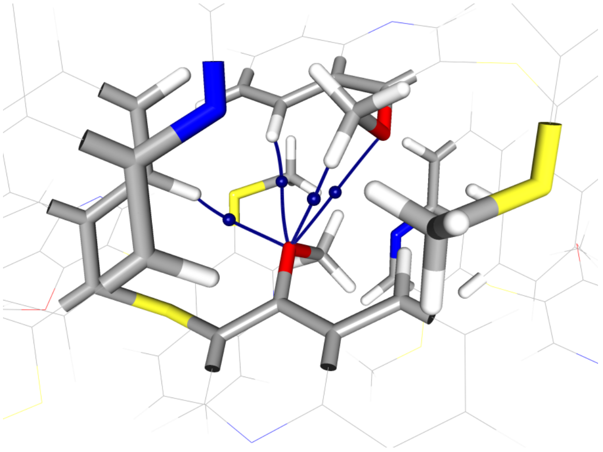

Fig. 3.7 Oxygen O1 atom with its nearest neighbors. Long range interactions marked by blue lines, with positions of critical points marked as blue dots.

inversion centers. While the latter is characterized with parameters rather typical of H$\cdots$H interactions, the H17$\cdots$H17^{iii} bond critical point characterizes with the electron density value of 0.044 eÅ^{-3} and $\lambda 1$ value of 0.86. They, together with other numerical descriptors, are very similar to the C16—H16$\cdots$O1^{ii} contact (hydrogen bond) usually regarded as much stronger. Moreover, the H17$\cdots$H17^{iii} and H6$\cdots$H16 ii distances are nearly identical (2.20 and 2.21 Å, respectively), but the latter has – in contrast – one of the most electron-scarce (3, -1) saddle points of all contacts formed by the molecule, while the H17$\cdots$H17^{iii} (3, -1) critical point is connected with the highest electron density of all hydrogen$\cdots$hydrogen interactions found. This might be used as an argument for the necessity of a deeper analysis of interactions, not based solely on their geometrical features.

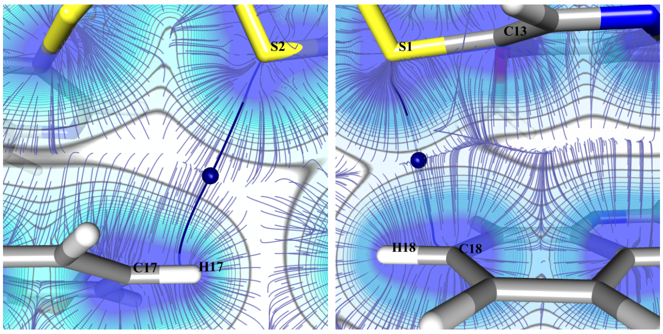

(a) S2···H17—C17 (b) S1···H18—C18

Fig. 3.8 Static total electron density and gradient trajectory plots for S···H—C contacts. Blue dots represent saddle points; black contours mark electron density isovalues, plotted every 0.03 eÅ^{-3}.

Heteroatomic interactions

As the studied molecule lacks strong hydrogen bond donors, only the C—H···X weak hydrogen bonds can be formed. Each sulfur, oxygen, and nitrogen atom accepts at least one such bond, with the nitrogen atoms being undoubtedly dominant. The N1 and N11 atoms interact with both methoxy and thiomethyl hydrogen atoms, forming relatively strong intermolecular bonds with total electron density at the saddle (3, -1) critical points ranging from 0.052 to 0.062 eÅ^{-3}. Laplacian values place themselves among the highest in this system, and – as one might expect – critical points are determined with a relatively high positional certainty. The contribution of the oxygen atom is small, as it is involved only in the C—H···O intermolecular bonds with electron density around 0.035 eÅ^{-3}. The main reason for such weak bonding can be related to the position of the oxygen atom in the lattice: its neighbors sterically hinder (Section 3.2) the access of for hydrogen atoms, necessary to form a stronger bond. The S2 sulfur atom takes part in C—H···S bonding with the methoxy moiety, with saddle point parameters between those of C—H···N and C—H···O interactions. Electron density at the critical point, of 0.30 eÅ^{-3}, is slightly higher than the value 0.25 eÅ^{-3} calculated for the O1···H22B^{ii} contact. However, both the S2···H22A i and O1···H22B^{ii} distances are about 0.2 longer than the sums of appropriate van der Waals radii (however, one should bear in mind the fuzziness of the very concept of van der Waals radius). The contacts S···H—C^{v} (^{v} : -x, -y, -z + (0,2,1)) contacts are less clear to interpretation, since the C—H bond is oriented perpendicular to

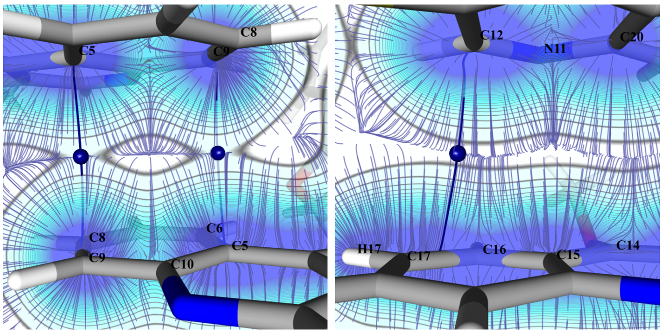

(a) C5···C9 (b) C16···C12

Fig. 3.9 Static total electron density and gradient trajectory plots for ring stacking. Blue dots represent saddle points; black contours mark electron density isovalues, plotted every 0.03 eÅ^{-3}.

the S···H line, and the bond path trajectory tends to fall in between carbon and hydrogen atoms (Fig. 3.8) Nevertheless, these contacts are treated here as C—H···S or σ C—H···S bonds, as the sulfur atom has little access to the carbon scaffold and one could expect reasonably strong electrostatic interactions. The area between the C5 and C8^{iv} (^{iv}: $-x,-y,-z+(1,2,0)$) atoms is characterized with electron density (approximately 0.35 eÅ^{-3}), consistent with the values found for stacking interactions within the lattice. In general, the interactions of this type are characterized as weak, with total static electron density at 0.025–0.035 eÅ^{-3} level, and low Laplacian values at critical points (Fig. 3.9). Even though superficially it seems weaker than the other groups of intermolecular contacts, π—π stacking is not localized in a small area. The low electron density spread over a relatively large space conceals the contribution of stacking in intermolecular interactions when the analysis is based solely on the values at the saddle points. C—H···H—C interactions are numerous and, similarly to surprisingly scarce C—H···π ones, moderately weak, having electron density at a saddle point ranging between 0.030 and 0.045 eÅ^{-3}. Laplacian values vary from 0.25 eÅ^{-5} up to 0.65 eÅ^{-5}. Even though the crucial numerical values describing saddle point properties are similar to those of $\pi\cdots\pi$ stacking, their positional uncertainty is only a fraction of that of the latter. This is intuitively understandable, if only one takes into account the shape differences between π orbital and H atom (Fig. 3.10).

The average measured length of three sulfur sp^2 carbon atom bonds is 1.77(1) Å, with bond saddle points placed halfway for S1 and at off-center positions for S2 sulfur atom. Bond critical points for S2 atom are shifted, in the case of S2—C3 bond closer

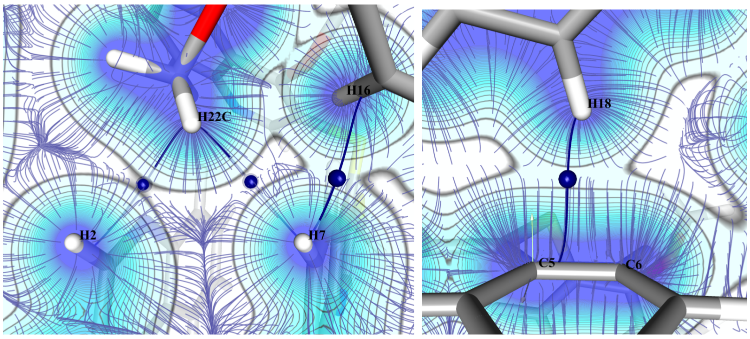

(a) C2$\cdots$H22C$\cdots$H7$\cdots$H16 (b) H8$\cdots\pi$(C5—C6)

Fig. 3.10 Static total electron density and gradient trajectory plots for H$\cdots$H and H$\cdots\pi$(C—C) contacts. Blue dots represent saddle points; black contours mark electron density isovalues, plotted every 0.03 e$\mathring{A}^{-3}$.

to the sulfur atom and in the case of S2—C21 closer to the methyl carbon atom. These four bonds have the lowest total electron density at the saddle point from all covalent bonds within the molecule, with the densities averaging 1.26(1) e$\mathring{A}^{-3}$ (S2—C3 differs from the other bonds with its electron density of 1.30 e$\mathring{A}^{-3}$). The oxygen atom O1 displays similar properties and topology with the total electron density at the saddle point O1—C22 still relatively low: 1.59 e$\mathring{A}^{-3}$. However, its link to the sp^2 C14 carbon is about as populous as the average of the C—C phenyl bond within the molecule. Both nitrogen atoms show interesting and nearly identical topological features. The total electron densities at the (3, -1) saddle points of N1—C2 and N11—C12 bonds take the highest values from among all covalent bonds, with the mean value of 2.52(1) e$\mathring{A}^{-3}$. This is by about 0.3 e$\mathring{A}^{-3}$ higher than the values found for N1—C10 and N11—C20 bonds, yet all four bonds differ in length by not more than 0.05 Å. The critical points are positioned unsymmetrically, shifted toward the nitrogen near the sulfur atoms and toward the carbon near the phenyl ring. Basic characteristics of the covalent bond critical points are gathered in Table 3.4 (Section 3.6). In general, the carbon—carbon bonds within the quinoline system retain the expected bond lengths of 1.42 and 1.38 . Shorter bonds are positioned between the external α and β positions. All (3, -1) bond critical points are positioned halfway between the atoms concerned and lie directly on the bond axes. The average static electron density at the critical points takes the values of 2.05(2) e^{-3} and 2.20(2) for longer and shorter bonds, respectively. The bond between C6 and C7 displays unusual positioning of the critical point, which is placed unsymmetrically: 0.78 from C6 and 0.60 from C7. Detailed analysis revealed an

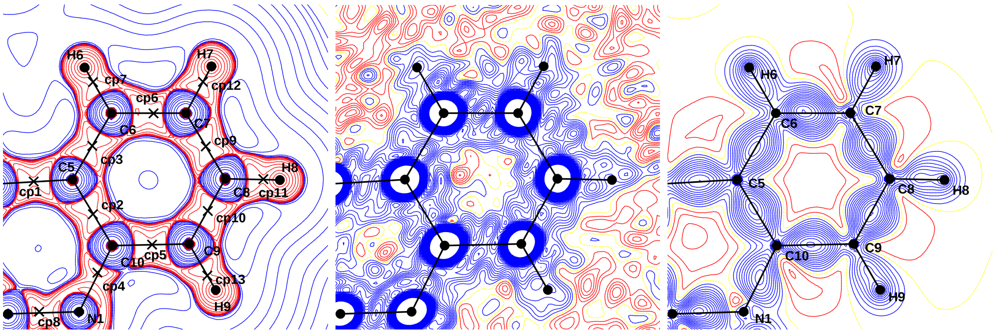

(a) (b) (c)

Fig. 3.11 Charge distribution maps around C6—C7 bond.
Fig. 3.11a: Laplacian map (logarithmic) with cp6 shifted toward C7 atom;
Fig. 3.11b: $1.25F_{obs} - 1.00F_{calc}$ map, no cutoff applied;
Fig. 3.11c: deformation map of the area, isovalues every 0.1 $e\text{Å}^{-3}$.

unexpected electron density peak near C7 (Fig. 3.11), which however disappeared after using s < 1.25 Å –1 or $I/\sigma > 4.0$ cutoff. Therefore, the peak should be interpreted as an effect of random noise mistakenly taken into account by the program and not spotted until topological analysis. However, different noise cutoff levels did not change the deformation density map and the shifts of the critical point position were less than 0.02 . This permits a claim that such an unexpected deviation of electron density results from the stacking interactions with nearby N1 nitrogen atom. The chemically identical C16—C17 bond, which lacks neighbors with strong electronegativity, has its (3, -1) critical point positioned symmetrically. This speaks in favor of weak intermolecular interactions being responsible for the saddle point positional shift.

3.3 Comparison of IAM and MM based charge density analysis

In comparison to standard IAM methods, multipolar refinement is demanding in terms of time consumption. High quality, high resolution, and redundant data required for a reliable multipolar model analysis usually take several days to collect. Noting differences between approaches and marking the line where extra work becomes sustainable is therefore important. The Independent Atom Model gives, by definition, no information on atomic charges and valence electron variations but can be reliably

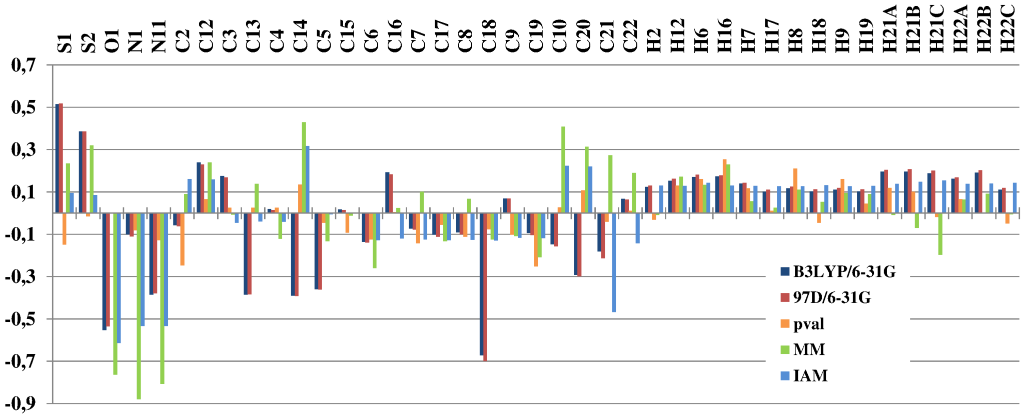

Fig. 3.12 Calculated atomic charge comparison. DFT charges calculated using Mulliken approach, IAM and MM model based calculations rely on atomic basins integration. MM based P_{val} depicts the difference between nucleus charge and electron population.

used as a template for DFT calculations. In contrast, the multipolar model takes valence shell population and shapes into account, but its usefulness as a template remains unchanged. However, incorporating detailed information obtained by charge density studies gives new insight into valence-dependent quantities such as local electron densities, potentials, or intermolecular bond trajectories. Comparison of the atomic charges (Fig. 3.13) shows that MM stays closer to DFT results than IAM does. It is worth noting that the hydrogen atoms taking part in intermolecular interactions with heteroatoms possess slightly negative charges or stay approximately neutral in atomic basin integration approaches, but stay positive in DFT studies where modelling of the molecule together with all neighbors yields a system too big to be effectively modeled using a classical approach. Critical points analysis reveals crucial differences between the IAM and MM approaches. As a natural consequence of the use of the independent atoms model, all covalent bond critical points are positioned at covalent radii. On the contrary, the multipolar model allows differences in atomic charge and additional charge distribution parameters to be taken into account. Thus, heteroatom binding carbon atoms usually have their bond critical points shifted from the covalent radii contact point toward the carbon atom. Moreover, the C6—C7 bond saddle point in the system studied is positioned at the bond center in IAM model, concealing the influence of a strong neighboring nitrogen atom. Intermolecular bonding description also differs significantly: While the multipolar model yields 144

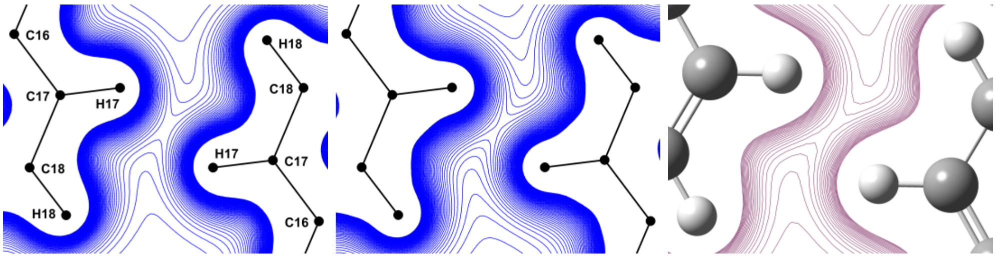

(a) H17···H17, MM (b) H17···H17, IAM (c) H17···H17, DFT

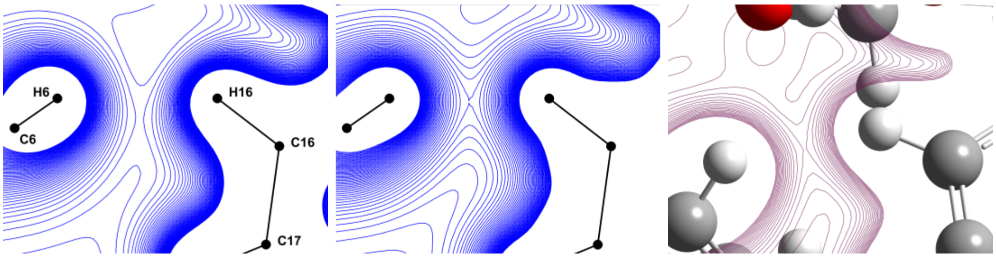

(d) H6···H16, MM (e) H6···H16, IAM (f) H6···H16, DFT

Fig. 3.13 Charge density comparison for MM, IAM and DFT (B3LYP-6-31G(d,p)). Electron density isovalues every 0.01 e^{-3}

model	interaction	$\rho(\mathbf{r})$, eÅ^{-3}	$\nabla^2\rho(\mathbf{r})$, eÅ^{-5}	λ_1	λ_2	λ_3
MM	H17···H17	0.0447	0.59	0.86	-0.13	-0.15
IAM	H17···H17	0.0787	0.63	1.09	-0.22	-0.24
MM	H6···H16	0.0305	0.55	0.73	-0.08	-0.09
IAM	H6···H16	0.0805	0.66	1.08	-0.18	-0.24

Table 3.2 Comparison of CP characteristics for selected H···H interactions

intermolecular saddle points, the same analysis in the independent atoms model yields only 130 points. It is important that differences occur at the crucial positions: the O1···O1 interaction described above is virtually nonexistent in the IAM approach. A weak bond obtained in the MM approach is replaced by an even weaker, less localized (3, -1) intermolecular bond saddle point at the very edge ($\lambda_2 = -0.002$) of converting to the (3, +1) ring center point. Close hydrogen···hydrogen contacts, specifically H17···H17 and H6···H16, differ significantly between the models as shown in Table 3.2 and depicted in Fig. 3.13. These differences reveal the inaccuracy of the standard model, rendering it less trustworthy for the detailed system analyses. Another difference between the models compared concerns the electrostatic potentials: in general, volume enclosed by isosurfaces compared rises when using the multipolar model approach. It is especially noticeable near intermolecular contacts, which

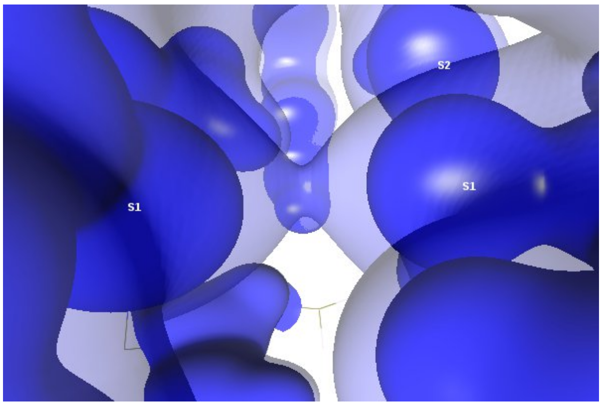

Fig. 3.14 Comparison of the same electrostatic potential isosurfaces around S1$\cdots$S1. Inner surface for IAM, outer (semitransparent) for MM.

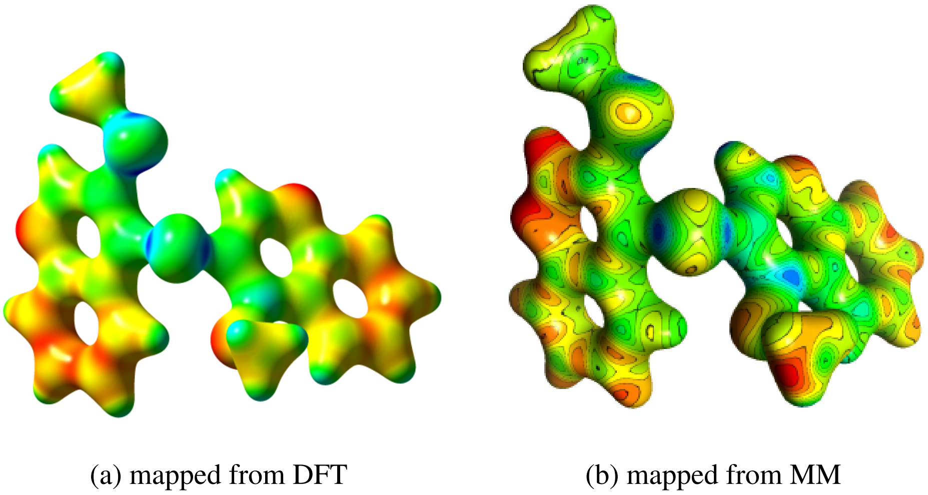

(a) mapped from DFT (b) mapped from MM

Fig. 3.15 Electrostatic potential mapped over isosurfaces of same electron density value. Red colour for most negative potential, blue for most positive.

again raises the issue of IAM being less appropriate for the detailed interaction studies. illustrates the effect on contact interpretation. It is not surprising, as without incorporating the charge density distribution variations, electrostatic potential values depend solely on the element type. The variations in IAM can be introduced using DFT calculations, giving an electrostatic potential map in satisfactory agreement with that obtained from the MM (Fig. 3.15). The most important features, σ-holes and lone electron pairs, as well as nitrogen atoms and other features, stay in good agreement. The main differences, such as phenyl ring hydrogen atoms charge, most probably stem from the theoretical studies conducted for a free molecule. Theoretical and experimental models seem to be in very good agreement. Slight differences are

Model	Diffraction		DFT		
	IAM	MM	6-31G	LANL2DZ	STO-3G
S1···S1	0.084	0.081	0.057	0.061	0.044
O1···O1	0.035	0.029	0.021	0.033	0.011
O1···H22B	0.04 0	0.035	0.034	0.024	0.018
H17···H17	0.079	0.045	0.304	0.028	0.036
H6···H16	0.081	0.030	0.026	0.022	0.039

Table 3.3 Comparison of CP characteristics for selected H···H interactions

present, but their distribution can be assigned to orbital functional characteristics: Slater-type and Gaussian- type functions produce different distribution far from the nuclei centers. Since the conducted analysis focuses on intermolecular contacts, the calculated electron density is prone to stress out approach differences. The use of various basis sets for DFT approach yields changes in the contact electron density comparable in value to the DFT – MM differences or bigger.

3.4 Summary

Various intermolecular contacts were analyzed and described, most notably a unique reciprocal chalcogen bond between two S1 atoms. In given conditions of no strong hydrogen bond donors, this chalcogen homoatomic bond proves to be the strongest within the system studied. Several different approaches were used and the results compared. The use of MM allows obtaining a model with lower discrepancy index than that of IAM, but – what is most important – a model giving reliable information about intermolecular contacts. The results are comparable to those obtained via *in silico* studies. Some differences, e.g. in molecule's atomic charges and electrostatic potential map, are most probably a result of not considering symmetry mates during the process. While it might be perceived as a method defect, a typical *in silico* study does not apply any surrounding molecule if not necessary. Thus, this study compares and finds good agreement between the multipolar model and the generic theoretical study. Meanwhile, even the best obtainable IAM model occurs to be unreliable until applying further, more advanced approximations.

3.5 Experimental section

Data collection

A colorless crystal with dimensions 0.4 × 0.4 × 0.1 mm was used for data collection at 110 K on an Oxford Diffraction XCalibur EOS four circle κ-cradle diffractometer, equipped with the Sapphire CCD detector and the graphite-monochromated MoKα radiation (λ = 0.71073 Å). Temperature was controlled using an Oxford Instruments Cryosystem cooling device. Images were collected in 31 runs, with the exposure times depending on the θ angle. More details on data quality can be found in **??**. Integration of the reflection intensities and data reduction were carried out with CrysAlisRed. Data sorting and merging was performed with WinGX suite (v 1.80.05) sortmerge tool [37].

Crystal data: $C_{20}H_{16}N_2OS_2$, M_r = 364.47, triclinic $P\bar{1}$, a = 9.2605(8)Å, b = 10.5797(12)Å, c = 10.7704(15)Å, α = 60.921(10)°, β = 85.569(12)°, γ = 65.892(9)°, V = 831.98(18)$Å^3$, Z = 2, F(000) = 380, d_x = 1.46 g/cm, (MoKα) = 0.33 mm^{-1}. A total of 82911 reflections collected up to $2\theta = 135°$ ($\sin(\theta/\lambda) = 1.31Å^{-1}$), of which 28749 were symmetry-independent (R_{int} = 2.30%), 18907 with $I > 2\sigma(I)$. Overall completeness 93.8%, mean redundancy 2.9. Density functional theory (DFT) calculations were carried out using several functionals: two common functionals, pure Becke-Perdew 86 (BP86), the Becke three-parameter hybrid exchange functional combined with the Lee, Young, and Parr (LYP) functional denoted as B3LYP used in connection with 6-31G and SDD basis [38–42]. They were also augmented with the original Grimme's B97-D hybrid functional and empirical Grimme corrections (denoted as BP86+D and B3LYP+D). All computations were carried out with Gaussian09 [43]. The S1$\cdots$S1 bond interaction energy graph was calculated on the basis of a series of two symmetry-dependent molecules, with S1$\cdots$S1 distance varying from 2.6 to 12.0 Å. To ensure that changes in free lone pairs overlapping would not distort the calculated bonding values, the molecules were shifted along the C18$\cdots$C18 direction. Hirshfeld surface presented in **??** were calculated using CrystalExplorer v.21.5 [44].

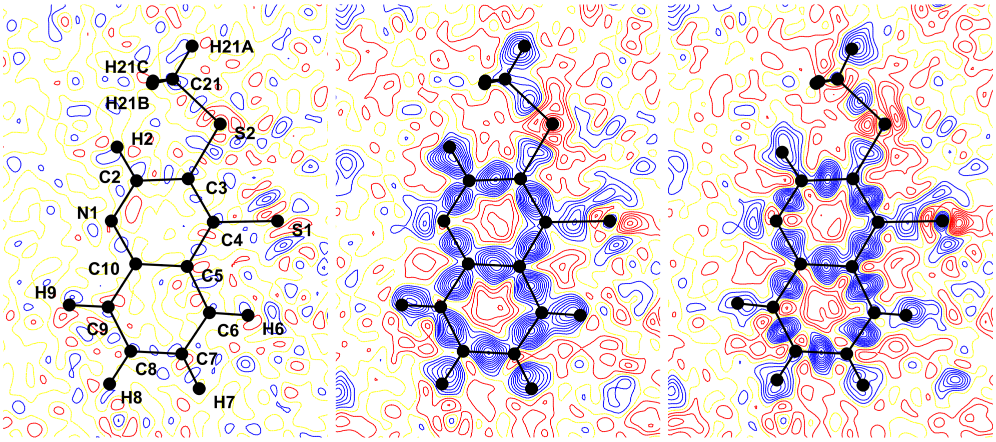

(a) the final model (b) final MM converted to IAM (c) model from SHELX

Fig. 3.16 Comparison of residual electron density maps. Cut-off I/σ(I) > 3; contours 0.05 eÅ^{-3}; blue, negative, and red, positive; s < 0.9 Å^{-1}

Refinement

The crystal structure was solved using SHELXS and standard Independent Atom Model (IAM) refinement was performed using SHELXL [45]. Non-H atoms were refined anisotropically; H atoms positions were found in the difference Fourier maps and isotropically refined. Atom positions are in satisfying agreement with previously reported values [36]. Final residuals for IAM: for all reflections R = 7.05%, wR2 = 12.93%, for I > 2σ(I) R = 4.04%, wR2 = 11.05%, S = 1.02. Max/min $\Delta\rho$ values in the final ΔF map 0.66/-0.53 eÅ^{-3}, located on the covalent bonds. The electron density was subsequently refined against the structure-factor amplitudes with the MoPro software [46, 47] using the multipole Hansen-Coppens model (Eq. (1.15)) for pseudoatom electron density. Before introducing the multipolar model, hydrogen atoms were moved to the positions determined by neutron diffraction, and a few cycles of high-order refinement ($\sin(\theta/\lambda) = 0.7\text{Å}^{-1}$) were performed in order to achieve better deconvolution between the thermal motion and deformation effects. The atomic displacement parameters of H atoms were constrained to the values obtained from the SHADE server generated constraint file **??**. Molecule then underwent following routine: a set of positional / thermal movement corrections followed by valence populations, multipoles and kappa variables separately. This routine was repeated several times. After unrestraining multipoles symmetry and kappa similarities, same routine was applied with an extra final step of refining all charge density parameters at once. Heteroatoms were refined up to hexadecapolar (l = 4) level, carbon atoms up to octupolar (l = 3), and hydrogen atoms up to dipolar (l = 1) level. The positional and displacement parameters of hydrogen atoms were restrained until the end of refinement; their κ and κ' parameters were also restrained at the values of 1.16(1) and 1.18(1), respectively. During final steps hydrogen atoms underwent refining routine separately from the rest of the molecule. Anharmonic refinement brought no apparent improvement in residual noise levels, but the values of some Gram-Charlier parameters were non-negligible (above 3σ level) and were thus incorporated into the model. For the sake of comparison of the models, as well as for the estimation of significance of charge density studies, the final model was used as a basis of the IAM-type model. Coordinates and thermal motion parameters of the final model were retained, but valence populations, multipoles, and κ and κ' parameters were reset to the initial state. Differences in residual density maps between two IAM models and the multipolar model are depicted in Fig. 3.16. Final residuals after multipolar refinement: R(I) = 2.33%, wR2(I) = 2.47%, R(F) = 3.25%, wR(F) = 1.29%, S = 1.62, max/min $\Delta\rho$ values in the final ΔF map 0.36/-0.23 eÅ^{-3}, residual density randomly distributed throughout the cell.

3.6 Supporting information

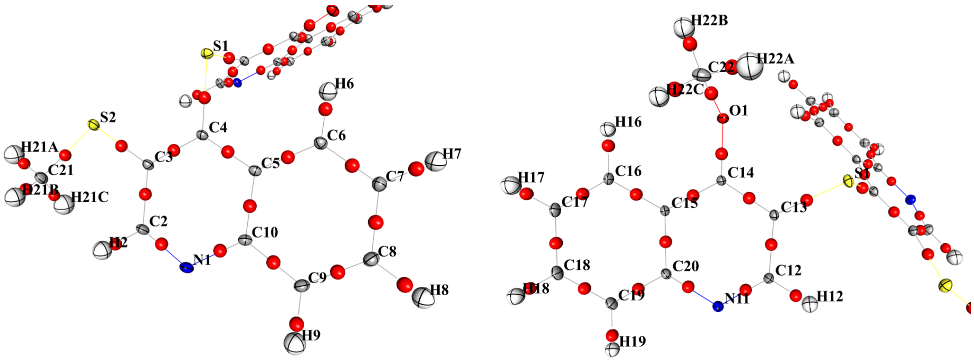

Fig. 3.17 Bond critical points of **1** (MM). Thermal ellipsoids drawn at 25% probability level for clarity.

Table 3.4 List of (3,-1) intramolecular critical points in **1**

Atom1	Atom2	distance, Å	$\rho(\mathbf{r})$, eÅ^{-3}	$\nabla^2\rho(\mathbf{r})$, eÅ^{-5}	λ_1	λ_2	λ_3	Gcp	Vcp	ε
S2	C3	1.758	1.393	-7.08	-8.63	-6.90	8.44	0.158	-0.390	0.25
S1	C4	1.782	1.337	-5.81	-7.69	-7.11	8.99	0.153	-0.367	0.08
S1	C13	1.770	1.328	-5.76	-7.87	-6.99	9.11	0.151	-0.362	0.13
S2	C21	1.808	1.281	-4.29	-7.31	-7.04	10.05	0.150	-0.345	0.04
O1	C14	1.359	2.128	-17.27	-17.33	-16.85	16.92	0.300	-0.779	0.03
O1	C22	1.438	1.589	-10.66	-10.38	-10.31	10.03	0.184	-0.479	0.01
N1	C2	1.317	2.526	-29.56	-21.41	-18.29	10.14	0.354	-1.014	0.17
N11	C12	1.317	2.516	-25.64	-21.74	-18.04	14.14	0.377	-1.020	0.21
N1	C10	1.367	2.193	-20.76	-16.61	-14.79	10.64	0.297	-0.810	0.12
N11	C20	1.374	2.131	-20.08	-16.90	-14.31	11.12	0.282	-0.771	0.18
C7	C6	1.376	2.227	-23.93	-16.51	-13.69	6.27	0.287	-0.822	0.21
C18	C19	1.379	2.223	-22.25	-16.87	-13.69	8.31	0.297	-0.825	0.23
C17	C16	1.375	2.204	-22.17	-17.47	-13.97	9.27	0.291	-0.813	0.25
C8	C9	1.378	2.183	-21.61	-15.95	-13.00	7.34	0.288	-0.801	0.23
C14	C13	1.383	2.162	-21.30	-16.53	-13.01	8.25	0.283	-0.788	0.27
C4	C3	1.390	2.118	-19.31	-15.32	-12.15	8.15	0.283	-0.766	0.26
C7	C8	1.416	2.072	-19.88	-14.60	-12.49	7.20	0.264	-0.734	0.17
C9	C10	1.417	2.061	-19.60	-15.63	-12.94	8.97	0.262	-0.728	0.21

continued on next page

continued from previous page

Atom1	Atom2	distance, Å	$\rho(\mathbf{r})$, eÅ^{-3}	$\nabla^2\rho(\mathbf{r})$, eÅ^{-5}	λ_1 ,eÅ^{-5}	λ_2 ,eÅ^{-5}	λ_3 ,eÅ^{-5}	Gcp	Vcp	ε
C19	C20	1.417	2.057	-19.33	-15.86	-13.04	9.57	0.263	-0.726	0.22
C17	C18	1.415	2.047	-19.17	-15.48	-12.80	9.10	0.261	-0.720	0.21
C15	C20	1.422	2.040	-18.09	-15.52	-12.82	10.25	0.266	-0.719	0.21
C5	C10	1.425	2.032	-18.02	-14.73	-12.82	9.53	0.264	-0.714	0.15
C16	C15	1.416	2.025	-18.44	-15.36	-12.86	9.78	0.259	-0.709	0.20
C15	C14	1.426	2.005	-17.54	-15.57	-12.07	10.10	0.259	-0.699	0.29
C6	C5	1.421	2.004	-17.25	-14.66	-12.46	9.86	0.260	-0.699	0.18
C2	C3	1.428	1.993	-17.50	-14.24	-12.10	8.84	0.255	-0.692	0.18
C13	C12	1.424	1.968	-17.23	-14.69	-11.82	9.28	0.249	-0.677	0.24
C4	C5	1.425	1.962	-16.47	-14.20	-11.70	9.43	0.252	-0.676	0.21
C2	H2	1.081	1.872	-18.17	-18.15	-16.44	16.41	0.213	-0.615	0.10
C6	H6	1.071	1.848	-17.71	-17.15	-16.16	15.60	0.209	-0.602	0.06
C7	H7	1.078	1.758	-17.70	-15.96	-14.49	12.74	0.183	-0.549	0.10
C9	H9	1.078	1.751	-15.53	-16.56	-15.57	16.60	0.196	-0.552	0.06
C8	H8	1.080	1.722	-16.27	-15.61	-14.82	14.16	0.182	-0.533	0.05
C21	H21C	0.992	1.846	-14.84	-15.82	-14.54	15.52	0.228	-0.611	0.09
C21	H21B	0.990	1.839	-14.83	-15.64	-13.76	14.57	0.226	-0.606	0.14
C12	H12	1.083	1.823	-18.48	-18.05	-16.37	15.95	0.196	-0.584	0.10
C17	H17	1.082	1.806	-18.30	-16.99	-15.55	14.23	0.193	-0.575	0.09

continued on next page

continued from previous page

Atom1	Atom2	distance, Å	$\rho(\mathbf{r})$, eÅ^{-3}	$\nabla^2\rho(\mathbf{r})$, eÅ^{-5}	λ_1 ,eÅ^{-5}	λ_2 ,eÅ^{-5}	λ_3 ,eÅ^{-5}	Gcp	Vcp	ε
C18	H18	1.079	1.795	-18.59	-16.16	-15.08	12.65	0.187	-0.567	0.07
C22	H22A	1.049	1.789	-14.89	-16.50	-14.82	16.43	0.211	-0.577	0.11
C16	H16	1.082	1.746	-15.63	-17.00	-15.96	17.33	0.194	-0.549	0.07
C22	H22C	1.050	1.726	-15.37	-15.60	-13.16	13.39	0.190	-0.539	0.19
C21	H21A	1.064	1.725	-12.50	-14.62	-13.73	15.85	0.209	-0.548	0.06
C19	H19	1.077	1.701	-16.00	-16.05	-14.77	14.81	0.178	-0.522	0.09
C22	H22B	1.062	1.691	-15.04	-15.28	-12.75	13.00	0.182	-0.520	0.20

Table 3.5 List of (3,-1) intermolecular critical points in **1** for MM

Atom1	Atom2	symmetry mate	$\rho(\mathbf{r})$, eÅ^{-3}	$\nabla^2\rho(\mathbf{r})$, eÅ^{-5}	λ_1	λ_2	λ_3	ε
N11	C21	-x, -y+2, -z	0.100	0.697	1.149	-0.219	-0.233	0.070
S1	S1	-x+1, -y+1, -z+1	0.072	0.739	0.958	-0.060	-0.159	1.670
C17	C17	-x, -y+3, -z+1	0.071	0.449	0.762	-0.154	-0.159	0.030
N11	C22	-x, -y+2, -z+1	0.067	0.593	0.923	-0.162	-0.168	0.040
N1	C21	-x+1, -y+1, -z	0.063	0.742	1.241	-0.223	-0.277	0.250
C8	C12	-x+1, -y+2, -z	0.057	0.440	0.624	-0.083	-0.101	0.210
S2	C17	x, y-1, z	0.057	0.598	0.795	-0.093	-0.103	0.110
S1	C18	-x, -y+2, -z+1	0.056	0.496	0.684	-0.088	-0.100	0.140
C5	C18	x+1, y-1, z	0.054	0.616	0.823	-0.063	-0.144	1.280
C7	C16	-x+1, -y+2, -z+1	0.053	0.533	0.730	-0.076	-0.122	0.610
N1	C22	x, y, z+1	0.051	0.640	0.923	-0.116	-0.167	0.440
C19	C22	-x, -y+2, -z+1	0.051	0.507	0.679	-0.056	-0.117	1.100
C19	C21	x, y+1, z	0.049	0.607	0.818	-0.078	-0.133	0.700
N11	C9	-x+1, -y+2, -z	0.043	0.348	0.402	-0.017	-0.038	1.160
C8	H21C	x+1, y, z	0.043	0.260	0.351	-0.030	-0.060	0.990
C12	C7	x-1, y, z	0.042	0.342	0.502	-0.074	-0.086	0.170
C7	C12	x+1, y, z	0.041	0.342	0.502	-0.073	-0.086	0.170
C9	C14	-x+1, -y+2, -z	0.040	0.377	0.431	-0.009	-0.045	3.950

continued on next page

continued from previous page

Atom1	Atom2	symmetry mate	$\rho(\mathbf{r})$, eÅ^{-3}	$\nabla^2\rho(\mathbf{r})$, eÅ^{-5}	λ_1 ,eÅ^{-5}	λ_2 ,eÅ^{-5}	λ_3 ,eÅ^{-5}	ε
S2	C8	x-1, y, z	0.036	0.333	0.400	-0.018	-0.049	1.650
C22	H2	x, y, z+1	0.036	0.341	0.439	-0.037	-0.061	0.650
C4	C9	-x+1, -y+2, -z	0.035	0.362	0.432	-0.018	-0.052	1.880
N11	C17	-x, -y+2, -z+1	0.033	0.259	0.292	-0.002	-0.031	15.210
C2	C2	-x+1, -y+1, -z	0.033	0.407	0.538	-0.036	-0.095	1.650
C16	H6	-x+1, -y+2, -z+1	0.033	0.608	0.841	-0.107	-0.126	0.180
C15	C12	-x, -y+2, -z+1	0.033	0.268	0.299	-0.003	-0.028	8.620
C7	H22C	-x+1, -y+2, -z+1	0.032	0.258	0.364	-0.052	-0.054	0.030
S2	C22	-x+1, -y+1, -z+1	0.030	0.432	0.554	-0.038	-0.083	1.170
O1	C16	-x+1, -y+2, -z+1	0.030	0.706	0.971	-0.131	-0.135	0.030
C16	C22	-x+1, -y+2, -z+1	0.028	0.422	0.567	-0.060	-0.086	0.440
N1	C7	-x+1, -y+2, -z	0.027	0.310	0.371	-0.014	-0.047	2.330
O1	H22B	-x+1, -y+2, -z+1	0.026	0.474	0.651	-0.081	-0.096	0.180
C10	H19	x+1, y-1, z	0.021	0.256	0.298	-0.006	-0.036	4.720
C21	H22B	-x+1, -y+1, -z+1	0.019	0.362	0.446	-0.024	-0.060	1.510
O1	O1	-x+1, -y+2, -z+1	0.016	0.515	0.598	-0.015	-0.069	3.590

Table 3.7 List of (3,-1) intermolecular critical points in **1** for IAM

Atom1	Atom2	symmetry mate	$\rho(\mathbf{r})$, eÅ^{-3}	$\nabla^2\rho(\mathbf{r})$, eÅ^{-5}	λ_1	λ_2	λ_3	ε
S1	S1	-x+1, -y+1, -z+1	0.084	0.79	1.15	-0.17	-0.18	0.05
N11	C21	-x, -y+2, -z	0.068	0.74	1.11	-0.17	-0.20	0.16
C16	H6	-x+1, -y+2, -z+1	0.067	0.59	0.89	-0.12	-0.18	0.53
C5	C18	x+1, y-1, z	0.067	0.64	0.85	-0.05	-0.15	1.81
C7	C16	-x+1, -y+2, -z+1	0.063	0.59	0.78	-0.06	-0.12	0.91
C19	C21	x, y+1, z	0.063	0.61	0.82	-0.07	-0.14	0.87
S2	C17	x, y-1, z	0.063	0.63	0.83	-0.07	-0.13	0.68
C6	C16	-x+1, -y+2, -z+1	0.060	0.58	0.63	0.07	-0.12	7.97
N1	C21	-x+1, -y+1, -z	0.060	0.67	1.00	-0.16	-0.17	0.03
C17	C17	-x, -y+3, -z+1	0.059	0.51	0.81	-0.14	-0.16	0.20
O1	C16	-x+1, -y+2, -z+1	0.058	0.70	0.97	-0.11	-0.16	0.50
S2	C18	x, y-1, z	0.054	0.56	0.57	0.07	-0.09	6.89
N11	C22	-x, -y+2, -z+1	0.054	0.61	0.87	-0.12	-0.15	0.19
S1	C18	-x, -y+2, -z+1	0.051	0.52	0.67	-0.06	-0.09	0.43
C8	C12	-x+1, -y+2, -z	0.050	0.50	0.69	-0.09	-0.11	0.24
N1	C22	x, y, z-1	0.050	0.60	0.77	-0.05	-0.12	1.15
C19	C22	-x, -y+2, -z+1	0.049	0.47	0.63	-0.05	-0.11	1.03
C7	C12	x+1, y, z	0.047	0.42	0.64	-0.10	-0.13	0.31

continued on next page

continued from previous page

Atom1	Atom2	symmetry mate	$\rho(\mathbf{r})$, eÅ^{-3}	$\nabla^2\rho(\mathbf{r})$, eÅ^{-5}	λ_1 ,eÅ^{-5}	λ_2 ,eÅ^{-5}	λ_3 ,eÅ^{-5}	ε
S2	C22	-x+1, -y+1, -z+1	0.044	0.42	0.55	-0.05	-0.08	0.74
C8	C21	x+1, y, z	0.042	0.44	0.51	-0.03	-0.04	0.15
O1	C22	-x+1, -y+2, -z+1	0.042	0.53	0.67	-0.06	-0.08	0.42
C20	C22	-x, -y+2, -z+1	0.041	0.44	0.44	0.07	-0.07	5.22
C9	C14	-x+1, -y+2, -z	0.040	0.41	0.47	-0.01	-0.04	3.00
C2	C2	-x+1, -y+1, -z	0.038	0.38	0.49	-0.02	-0.08	2.36
C8	C13	-x+1, -y+2, -z	0.037	0.41	0.41	0.04	-0.05	9.38
C14	H22B	-x+1, -y+2, -z+1	0.037	0.43	0.37	0.09	-0.03	3.07
C4	C9	-x+1, -y+2, -z	0.036	0.40	0.45	-0.01	-0.04	7.48
O1	O1	-x+1, -y+2, -z+1	0.036	0.55	0.59	0.01	-0.05	98.91
N1	C6	-x+1, -y+2, -z	0.035	0.40	0.45	-0.03	-0.03	0.16
C5	C7	-x+1, -y+2, -z	0.033	0.38	0.40	0.02	-0.04	20.73
C5	C10	-x+1, -y+2, -z	0.033	0.37	0.39	0.02	-0.04	21.10
C7	H22C	-x+1, -y+2, -z+1	0.029	0.28	0.35	-0.02	-0.05	1.77
H2	C19	-x, -y+2, -z	0.029	0.27	0.35	-0.03	-0.06	1.07
N1	C2	-x+1, -y+1, -z	0.028	0.31	0.28	0.08	-0.05	2.36
N11	C17	-x, -y+2, -z+1	0.028	0.31	0.34	-0.01	-0.03	3.62
O1	C19	-x, -y+2, -z+1	0.027	0.31	0.27	0.05	-0.01	4.44
S1	C17	-x, -y+2, -z+1	0.027	0.30	0.31	0.02	-0.02	16.98

continued on next page

continued from previous page

Atom1	Atom2	symmetry mate	$\rho(\mathbf{r})$, eÅ^{-3}	$\nabla^2\rho(\mathbf{r})$, eÅ^{-5}	λ_1 ,eÅ^{-5}	λ_2 ,eÅ^{-5}	λ_3 ,eÅ^{-5}	ε
C15	N11	-x, -y+2, -z+1	0.026	0.32	0.35	0.00	-0.02	5.61
C20	C16	-x, -y+2, -z+1	0.026	0.32	0.35	0.00	-0.02	5.60
C14	C20	-x, -y+2, -z+1	0.026	0.31	0.33	0.00	-0.02	43.64
N11	C16	-x, -y+2, -z+1	0.026	0.32	0.33	0.00	-0.02	74.44
C5	C5	-x+1, -y+2, -z	0.025	0.28	0.24	0.03	0.02	-0.93
C15	C15	-x, -y+2, -z+1	0.024	0.28	0.27	0.01	-0.01	17.38
N11	H8	-x+1, -y+2, -z	0.023	0.26	0.17	0.12	-0.03	0.46
C14	C15	-x, -y+2, -z+1	0.023	0.27	0.23	0.02	0.01	-0.94
C4	H8	-x+1, -y+2, -z	0.021	0.24	0.18	0.06	-0.01	1.86
S2	C7	x-1, y, z	0.021	0.22	0.15	0.09	-0.02	0.69
C16	H12	-x, -y+2, -z+1	0.021	0.23	0.17	0.07	-0.02	1.37
C17	C18	-x, -y+3, -z+1	0.020	0.20	0.15	0.08	-0.03	0.86
N11	C7	x-1, y, z	0.017	0.19	0.13	0.08	-0.02	0.57
C8	C18	x+1, y-1, z	0.017	0.18	0.13	0.07	-0.01	0.80
H19	H21B	-x, -y+2, -z	0.017	0.19	0.13	0.08	-0.02	0.74
S1	C5	-x+1, -y+1, -z+1	0.016	0.17	0.10	0.09	-0.02	0.08
C4	H18	x+1, y-1, z	0.016	0.17	0.10	0.09	-0.02	0.08
C4	C19	x+1, y-1, z	0.016	0.17	0.13	0.06	-0.02	1.30
S2	C16	x, y-1, z	0.016	0.17	0.10	0.08	0.00	0.23

continued on next page

continued from previous page

Atom1	Atom2	symmetry mate	$\rho(\mathbf{r})$, eÅ^{-3}	$\nabla^2\rho(\mathbf{r})$, eÅ^{-5}	λ_1 ,eÅ^{-5}	λ_2 ,eÅ^{-5}	λ_3 ,eÅ^{-5}	ε
C16	S2	x, y+1, z	0.016	0.17	0.10	0.08	0.00	0.23
C2	H7	-x+1, -y+2, -z	0.015	0.18	0.12	0.07	-0.01	0.58
C2	C22	-x+1, -y+1, -z+1	0.015	0.16	0.10	0.07	-0.01	0.40
S1	C3	-x+1, -y+1, -z+1	0.014	0.15	0.09	0.07	-0.01	0.22
C4	H22A	-x+1, -y+1, -z+1	0.014	0.15	0.09	0.07	-0.01	0.22
S2	C18	-x, -y+2, -z+1	0.013	0.14	0.13	0.02	-0.01	6.90
C9	H22B	x, y, z-1	0.013	0.13	0.11	0.04	-0.02	1.88
C15	C21	x, y+1, z	0.010	0.11	0.07	0.05	-0.01	0.55
S1	C4	-x+1, -y+1, -z+1	0.010	0.11	0.05	0.03	0.02	-0.62
C18	C4	x-1, y+1, z	0.010	0.11	0.05	0.03	0.02	-0.62
C9	C19	x+1, y-1, z	0.006	0.07	0.04	0.02	0.01	-0.76

Chapter 4

Copper(II) 3,5-dichlorobenzoate trihydrate

4.1 Introduction

Halogen atoms, when forming a covalent bond, feature a characteristic surface potential distribution where the atomic surface opposite to bound atom becomes electron poor. This phenomenon is caused primarily by electrostatic forces, which cause the neighbouring bound nucleus to attract non binding electrons towards itself, with the effect most prominent along the bond axis [48]. The resulting areas of more positive electrostatic potential on atomic surface are called σ-holes. These have, naturally, a very significant effect on atom's supramolecular properties. The halogen atom surface acquires anisotropic characteristics, with a positive charged spot placed across the covalent bond – a location that is inherently the least sterically hindered. The resulting radially symmetric dipole is strong enough to facilitate electrostatic interactions that parallel hydrogen bonds in a wide range of aspects, with σ-hole acting similarly to the hydrogen atom, but different in steric hindrance and extent of agreement with Lewis' acid–base theory [49]. Strong, highly directional halogen bonds are now one of key tools in crystal engineering [50–57]. Halogen$\cdots$halogen bonds are classically categorised, basing on angle of contact, into type I and type II halogen bonds: type I having two similar R—X$\cdots$X angles θ_X, often close to 180°, and type II having an orthogonal relationship, with one θ_X close to 180° and one close to 90° [49]. It has been argumented that only type II, where a clear electrostatic

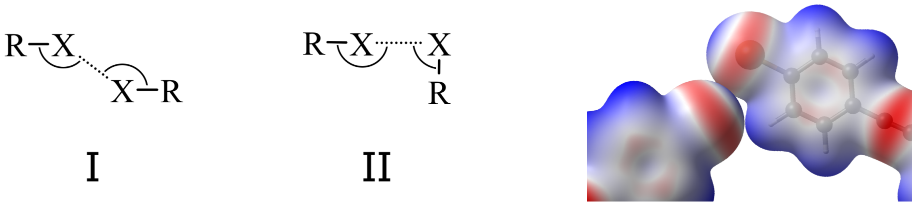

(a) Basic types of halogen bonds (b) Type II Br· · ·Br bond

Fig. 4.1 Halogen· · ·halogen bond taxonomy and an exemplary type II halogen bond depicted on basis of 1,2-bis(4-bromophenyl)ethyne crystal structure, with σ-holes visible in blue at molecules' termini.

attraction is present between differently charged areas of atomic surface, should be called a halogen bond [58, 59]. While it is true that the high directionality of a halogen bond is neatly explained by σ-holes concept, the charge-transfer, dispersion, electrostatic, polarization and repulsive components of interhalogen interaction may not be exhaustively represented with this model [60–62].

4.2 Structure

The crystal structure of Copper(II) 3,5-dichlorobenzoate trihydrate (**2**) has been previously reported at 295 K [63], 150 K [64] and at 120 K [65]. Research reported so far did not conduct charge density refinement analysis and studies. Constitutional symmetry of the compound does not translate to crystal organisation: molecules are not intersected by an internal mirror plane. The copper complex forms a supramolecular dimer in crystal, two copper atoms surrounding an inversion point, bound together through a compact tight system of hydrogen bonds involving carboxylate groups and hydrate water molecules. Oldest studies of **2** performed by Wołodkiewicz et al. suggested a hexacoordinate copper double bound to one of benzoate ligands, however this proposition did not withstand verification during structure revisits; the copper complex is pentacoordinate, in a geometry of tetragonal pyramid, bound to one of each carboxyl groups oxygen atoms in opposite pyramid base corners plus to three water molecules: two in plane, third in apical position. The pyramid base deviates from idealised form, with O1W-Cu-O2W angle measuring 168.2° and O3-Cu-O3W angle having value of 82.9°. Based on their topology, ligand – copper bonds are all to be classified as intermediate between shared and closed shell interactions:

they are characterized by lower $\rho(\mathbf{r})$, positive $\nabla^2\rho(\mathbf{r})$, and $|\mathrm{V_{CP}}|/\mathrm{G_{CP}}$ ratio near unity. They can be further divided in three subgroups: the O3 atom, which has a Cu—O bond shorter by approx. 0.05 Å than the second group, comprising the remaining coplanar oxygen atoms; finally, the apical O3W oxygen. There are two main characteristics that differ between the three: Cu—O3 becomes shorter in structures measured at higher temperatures like covalent bonds do, the second group has Cu—O bond lengths unaffected, while Cu—O3W distance becomes even greater. The second notable difference is bond ellipticity: Cu—O3 possesses ε value of over 0.1, a value that might have been interpreted as partial double bond character in other context. The heightened ellipticity is caused primarily by a smaller interatomic distance – in reality, the modelled multipoles population relating to carboxylate π bonds is actually marginally lower on the O3 side. The rest of coplanar ligands interface through unambiguously circular bonds. Being decidedly more distant than others, with interatomic distance of 2.293 Å, O3W oxygen atom's bond ellipticity is sourced mostly in lone electron pairs smearing caused by molecule's rotational wobble. Distance, positioning, topological characteristics more reminiscent of closed shell interactions than in case of other ligands all make O3W water appear different. Nevertheless, the coordination number of copper is here certain. Tetracoordinate copper complexes are predominantly formed by Cu(I), which is not the oxidation state found in studied compound. Moreover, the Cu—O3W bond is slightly weaker, but within expectations for an apex of tetragonal pyramid. Ligand O3W is also the only one not involved in

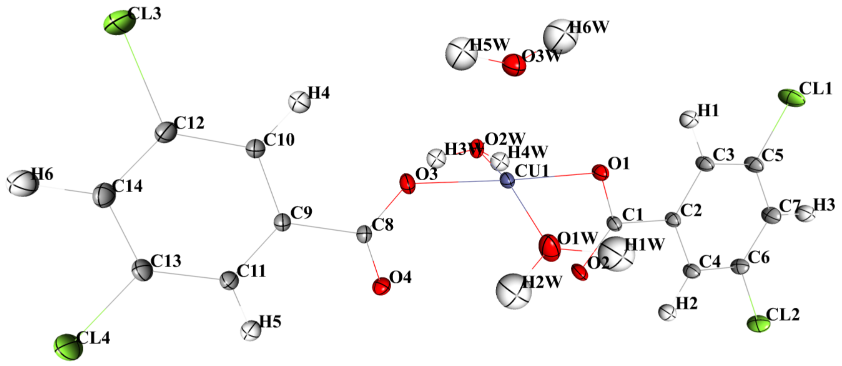

Fig. 4.2 Atom positions and thermal displacement ellipsoids of **2**. Ellipsoids are drawn at 50% probability level.

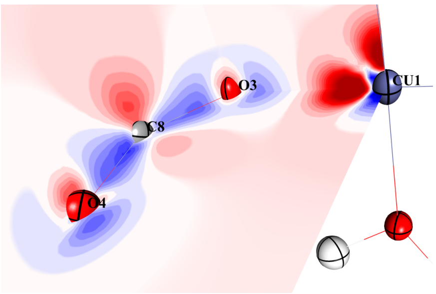

Fig. 4.3 Deformation density of C8 carboxyl group. Blue: higher negative charge, red: positive. Isovalues every 0.1 eÅ^{-3}.

the formation of a supramolecular dimer around an inversion point, but instead forms a different hydrogen bond which will be described in detail later on.

Chlorine atoms differ slightly in bond length measurements, ranging from 1.728 to 1.735 Å. This may safely be interpreted as differences in bond strength, given the corresponding differences in BCP charge density, as well as the intermolecular context: Cl2 and Cl3 remain in no contact with water molecules, whereas Cl1 and Cl4 do. In effect, Cl2 and Cl3 are positioned near lattice's electrostatic potential minima, with no attractants other than the covalent bound aryl ring. The carboxyl groups are slightly out of plane defined by relevant phenyl rings, with dihedral angles measuring 11.2° for C3-C2-C1-O1 and 9.4° for C10-C9-C8-O3, respectively. Oxygen atoms O2 and O4, which are not engaged in direct contact with copper, form shorter bonds than atoms O1 and O3. The consequent variations in bond critical point electron density and its second derivative are within expected range. Interestingly, carbon-oxygen bond ellipticity is higher for copper binding oxygen atoms than it is for for those in contact with water molecules only. The quantitative difference that is fully characterized in Table 5.4 can be also noticed in qualitative graphical assessment, as presented in **??** 2. Static deformation density maps let interpret the difference in ellipticity as higher π orbital expansion around oxygen atoms that coordinate to copper. Bond angles for carboxyl group carbon atoms deviate from 120° in extent typical for carboxylates in general, as well as for copper carboxylates specifically [66–68], although for closely bound O3 the deviation is near the higher boundary of reported values with O3-C8-O4 angle of 125.4° and O3-C8-C9 angle of 114.7°.

A set of several measurements, each performed at a different temperature, raises an opportunity for analyzing cell geometry changes and their implications. Of course,

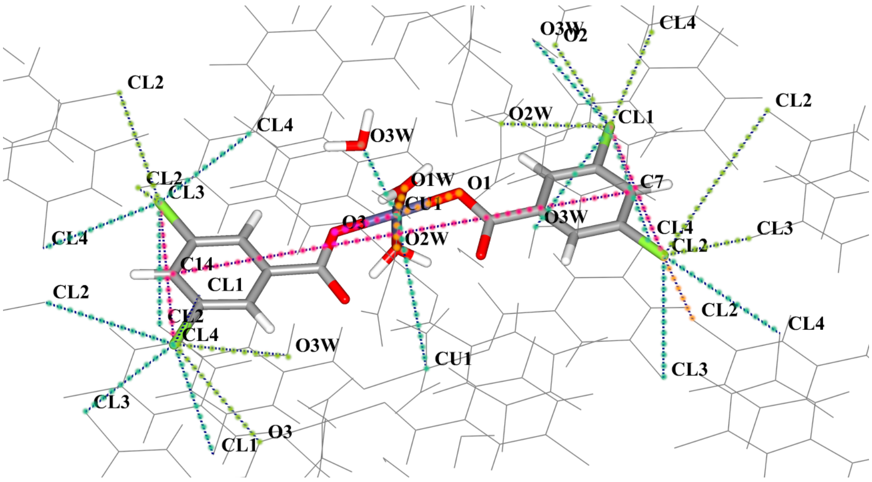

Fig. 4.4 Interatomic distances with estimated temperature dependence. Orange: temperature independent, magenta: inversely correlated, teal: directly correlated with growth rate value between that of unit cell dimensions growth rate, green: directly correlated and higher than any of unit cell dimensions growth rate.

the differences in final achieved resolution stemming from not only the measured crystal itself, but also from diffractometers, CCD matrices in particular, data reduction software used and seven structure resolution software itself – after all, the timespan between the oldest and newest measurement has reached a double-digit number of years – affect comparison accuracy even before accounting for the inherent differences between IAM and MM models. For this reason, the comparisons below are based on positions of atoms deemed most reliable: copper and chlorine, while positions of hydrogen atoms were excluded from all comparisons. The unit cell of **2** increases its dimensions with rising measurement temperature, without any detected solid phase change; dimensions b and c grow linearly, while a changes in manner which is bound to concurrent changes in β angle value. The angle β changes value by approx. 0.5° across the measurements temperature range, with direct proportionality between the angle and the temperature. The molecules are organized in flat layers of phenyl rings, with interactions in c direction relying primarily on stacking interactions that may allow for some degree of slide but will not change interlayer distance except for what's caused by thermal vibrations. Direction b, of course, is orthonormal to β and cannot account for its variations directly. The plane (1,0,0) between adjacent layers of molecules is crossed exclusively by weak intermolecular contacts basing on $\mathrm{Cl}\cdots\mathrm{H}$—C and $\mathrm{Cl}\cdots\mathrm{Cl}$ interactions, polarized or exclusively dispersive. All of those

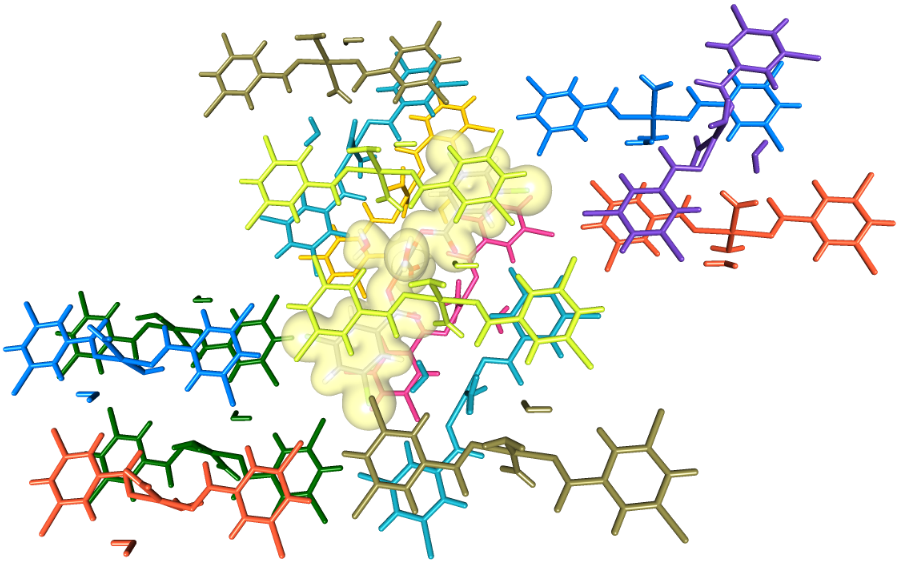

Fig. 4.5 Symmetry mates of **2** that form intermolecular bond paths

present in the studied system will allow for variations in contact geometry, including some variation of interatomic distance; even more so given that the phenyl rings neighbouring across (1,0,0) plane are staggered in relation to each other. Comparing selected dimensions across the system reveals the following: the supramolecular dimer behaves essentially as a single molecule, with the shape of the dimer tightly locked; the O3W water molecule is bound to copper but perturbed by contacting molecules enough to change its position as if it was an independent entity in the crystal; adjacent molecules related by a 2-fold screw axis that form stacking interactions (*ii* in Table 4.1) rotate slightly, taking advantage of stacking interactions' low positional rigidness; the rotation does not affect staggered layer configuration, but does change the contacts angle across the (1,0,0) plane; finally, due to nature of said contacts the rotation happens without changing the contact length outside the normal temperature related effects.

4.3 Intermolecular contacts

In crystal lattice, a molecule is surrounded with a total of 16 neighbours, of which 10 are engaged in symmetrically independent interactions, but makes meaningful

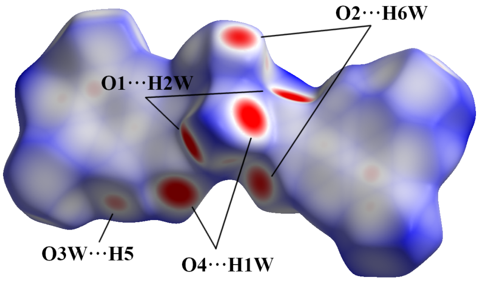

Fig. 4.6 Hirshfeld surface of **2**

contact with only 9 of them. The symmetry equivalent -x+2, -y, -z+1 does create a common zero flux surface, however either of the measuring 3.64 Å interatomic Cl – H distances are nearly 30% larger than the sum of relevant van der Waals radii [69]. For this reason, the contact is omitted in Fig. 4.5 and the most of further analyses. A relatively flat structure of **2** favours stacking, which indeed does dominate over all other weak interactions. delocalised π orbitals, which often act as very weak Lewis bases interfacing with positively charged hydrogen atoms or σ-holes, are here rendered completely inaccessible to anything but π orbitals of other dichlorobenzoate groups. This effects in the majority of Hirshfeld surface (Fig. 4.6) mapped with normalized interatomic distances to be virtually featureless. The only significant d_{norm} drops are related to strong hydrogen bonds formed by / with bound water molecules, in the center of the molecule. These are, of course, visually prominent – but most importantly, they are engaged in forming a very strong dimeric system. Outside this system, however, only a handful hydrogen bonds are found: three strong between water and carboxyl oxygen atoms (one per atom, with O3 again proving to be different in character from the rest), and one weak hydrogen bond formed between atoms O3W and H5. Chlorine atoms are generally not involved in any interactions that would result in significant breach of their van der Waals radii, with stacked rings staggered to accommodate chlorine's larger atomic radius. Interestingly, the shortest distance between atoms from different involved symmetry equivalents is not reflected in intermolecular bond strength; once again underlining the added value of sub molecular electron density studies.

Symmetry equivalent *i* involved in creating the supramolecular dimer is bound primarily by a set of four strong hydrogen bonds which are made between both carbonyl

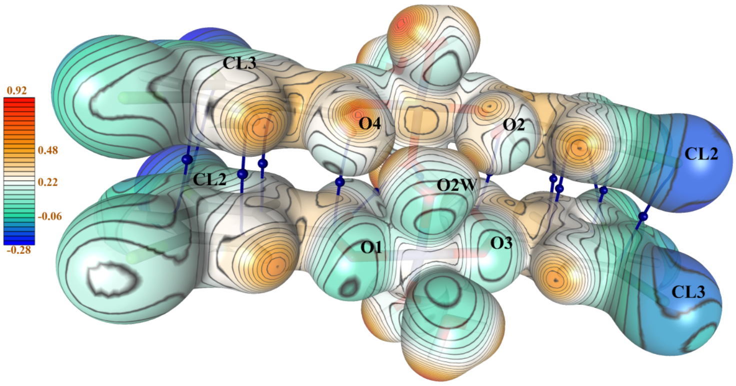

Fig. 4.7 (3,-1) critical points and bond paths formed with *i*. Electrostatic potential (eÅ^{-1}) mapped over the ED isosurface of 0.1 eÅ^{-3}. Redundant atom labels omitted for clarity.

oxygen atoms and water ligand bound to second molecule's copper atom. This strong bind is further increased by chlorobenzoate moieties stacking with significant ring overlap. A set of chlorine atoms involving interactions is also present, with mixed energetic effect.

The copper-carboxylate-water cage found in the dimer core involves numerous hydrogen bonds. The X-ray diffraction measurement taken did not allow for releasing distance constraints for involved hydrogen atoms, limiting the depth in which the

	interacting symmetry	number of involved (3,-1) critical points	E, kJ/mol
i	-x+1,-y+1,-z+1	17[a]	-196.76
ii	-x+1,y+½,-z+½	10[b]	-132.26
iii	-x+1,-y,-z+1	6	-14.23
iv	-x,y+½,-z+½	1	-6.17
v	x,y+1,z	6	-2.03
vi	x+2,-y+1,-z+1	1	6.33
vii	-x+2,-y,-z+1	2	4.58
viii	x+1,-y+½,z+½	2	2.51
ix	-x+1,-y+³⁄₂,z+½	1	2.16
x	-x+1,y+³⁄₂,-z+½	1	1.16

Table 4.1 Total electrostatic interaction energy values for symmetrically independent pairs of **2** as calculated from multipolar model.

---

[a] This contact involves stacking interactions of two benzoate moieties, which makes the count of CPs involved less meaningful even as a qualitative metric.

[b] See above, with one phenyl ring per contact.

strength of hydrogen bond can be assessed. Nevertheless, the oxygen atom positions, as well as hydrogen atoms spatial orientation, allow for qualifying cage forming hydrogen bonds as strong. This is indicated by O–O distances of 2.779 Å for O2W–O4^{i} and 2.669 Å for O2W – O^{i}, respectively. Both O-H-O angles measure around 170°, with exact values being the result of the dihedral angle present between the carboxyl groups as well as a slight rotation of the water molecule – the dihedral angles O1-Cu1-O2W-H4W and O3-Cu1-O2W-H3W measure 35° and 44°, respectively – caused by its orientation of the second lone pair towards H1^{iii}. Overall, the contact distance as well as exact bond angles are influenced by molecule's geometry as well as packing effects: hydrogen bond lengths might have been shorter if not for water molecule's lone electron pair coordinating to copper atom, the bond angles might have been closer to 180° if not for the other lone pair forming a weak hydrogen bond with adjacent phenyl ring. Even with these factors in play, this system remains the defining feature in crystal cell organisation. Due to aforementioned distance constraints, charge density values of approx. 0.19 eÅ^{-3} for H4W$\cdots$O4 and 0.15 eÅ^{-3} for H3W$\cdots$O2 should be treated as underestimated: charge density values at BCP are heavily dependent on interatomic distance especially for hydrogen bonds. One should expect O—H covalent bond lengthening of up to 0.05 Å in the analyzed cases [70, 71] and consequential shortening of intermolecular distances by an equal amount, which is enough to increase charge density parameters at BCP by up to 10%. The BCP related to O2W$\cdots$O2Wi bond path is placed directly on point symmetry, and is certainly involved in a repulsive interaction: it forms between two negatively charged species, the bond path is plotted through where one would expect to find antibonding orbitals, the BCP is characterized by high ellipticity and is surrounded by (3, +1) critical points in its direct vicinity.

The three–dimensional network is completed by a pair of symmetrically equivalent stacking interactions with a very strong electrostatic component, C1$\cdots$O4^{i}. Both C1 and O4 atoms possess a rather significant atomic charge: carbonyl oxygen atom is strongly negative, while carboxyl carbon is equally positive (-0.9 to -0.5 for O4, +0.4 to +0.8 for C1 depending on calculation method). Given the varying, very often mildly repulsive nature of stacking interactions, this geometry should be considered primarily a result of opposite partial charges attracting each other. The mutual positioning of these atoms promotes π orbital overlap, which is not directly reflected in BCP

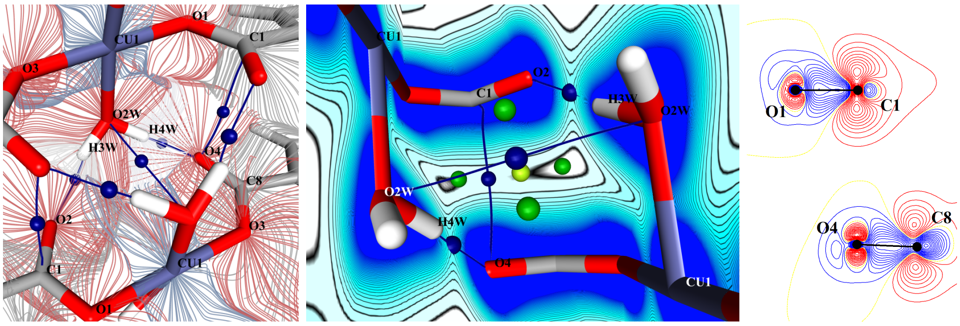

(a) (b) (c)

Fig. 4.8 Charge density around dimeric water – carboxylate – copper complex. Some atoms not relevant to interaction were hidden from figures for the sake of clarity. Fig. 4.8a: Atomic basins contours unveiled through trajectories of electron density gradient originating from selected atoms, coloured according to atom type. Atomic positions without plotted trajectory lines are not labelled. Fig. 4.8b: Total static electron density. Blue dots represent (3,-1) saddle points, green: (3,+1), lime: (3,+3); black contoursmark electron density isovalues, plotted every 0.03 eÅ^{-3}. Fig. 4.8c: Static deformation density map around C1···O4^i π orbitals overlap. Isovalues drawn every 0.05 eÅ^{-3}, blue: positive, red: negative.

numerical values: despite its short distance, $\rho(\mathbf{r})$ is found to have value of 0.040 eÅ^{-3}. Such a value, closely comparable to the rest of system's stacking BCPs, might be partly explained by carbon atom's strong positive charge combined with smaller atomic radius of oxygen, when compared to carbon or especially chlorine atoms present elsewhere. The overlap itself can be observed and visualised (Fig. 4.9a). Despite the large differences in atomic charge present, the bond critical point is found halfway between the two nuclei. The interatomic distance of 3.168 Å is the shortest of all stacking related interatomic distances measured in the crystal cell and quite short for such an interaction in general. Even if examples of tighter stacking are not unheard of in published structures (e.g. [72–87]), even more so regarding reciprocal carbon···oxygen contacts in the carboxyl moiety (e.g. [88–103]), a majority of them does not overlap over such a large area and/or has at least one of carboxyl groups rotated out of aryl ring plane. Those which do overlap are heavily substituted with electron-withdrawing groups; even more so than in case of **2**. The dichlorophenyl rings are stacked in a parallel displaced configuration, their phenyl ring planes deviating approx. 4° laterally and 5° longitudinally from perfect parallel orientation. This longitudinal incline can be attributed to steric hindrance related to chlorine atoms, while lateral roll is caused by packing effects outside of supramolecular dimer. Charge

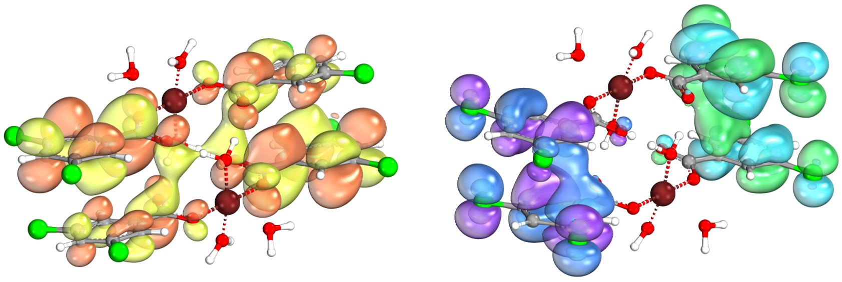

(a) LUMO + 5 (b) HOMO - 2, HOMO - 3

Fig. 4.9 Exemplary MOs overlap in $\mathbf{2}\cdots\mathbf{2}^i$ stacking.

density at found (3,-1) saddle points varies between 0.35 eÅ^{-3} up to 0.45 eÅ^{-3}, with $|\lambda_1| < |\lambda_2| \ll \lambda_3$. Thanks to the rings stagger, all four chlorine atoms are positioned between the ring terminal atoms of the other layer. This minimizes van der Waals repulsion, as well as allows for interesting interactions between the halogen atoms that will be described in detail later on.

The organisation of the supramolecular dimer $\mathbf{2}\cdots\mathbf{2}^i$, with strong mutually reinforcing hydrogen bonds causing the most polarised part of substrates to become largely inaccessible to polar solvents, as well as allowing the benzoate moieties to organize themselves with a very favourable distance and stagger [104–106], which serendipitously also allows for the chlorine atoms to minimize steric hindrance, largely explains the compound's poor solubility in water [63].

Strong hydrogen bonds are formed with only one other symmetry mate, namely with (marked on Fig. 4.5 using yellow-green colour) symmetry equivalents *ii*. These engage O1W and O3W water molecules in a set of contacts ranging from strong, short and well aligned to weaker, more distant and happening at an odd geometry. The bond $\mathrm{O1}^{ii}\cdots\mathrm{H2W}$ is the strongest of all formed in the molecular crystal of **2**, even though it is not formed with the shortest O–O distance. The difference — 1.733 Å compared to 1.719 Å for $\mathrm{O4}\cdots\mathrm{H4W}^i$ — is rather minor, and yet the electron density at bond critical point measuring 0.196 eÅ^{-3} compared to 0.191 eÅ^{-3} means that, if one follows the expected inverse exponential distance – density relationship [107], charge density value at BCP should be approx. 3% smaller for $\mathrm{O1}^{ii}\cdots\mathrm{H2W}$. However, it is actually 3% larger than one found for $\mathrm{O4}\cdots\mathrm{H4W}^i$. The discrepancy, if minor, is not insignificant. As with C—O bond ellipticity, the bond formed between oxygen atom and cooper coordination centre has a measurable effect on oxygen atom's noncovalent interactions.

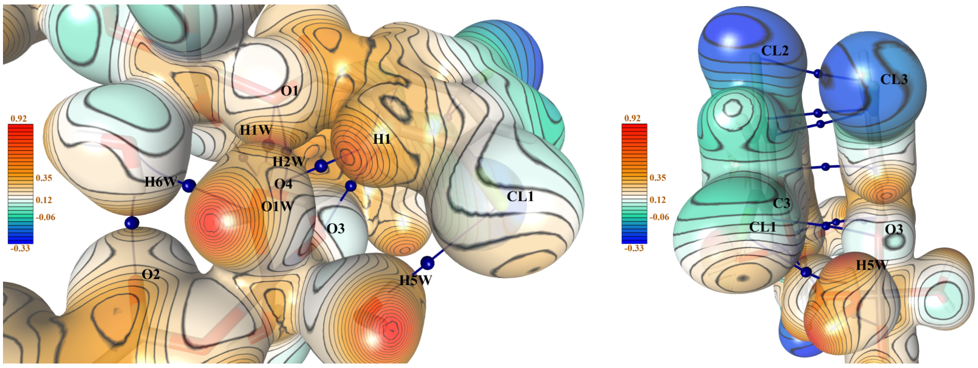

(a) (b)

Fig. 4.10 (3,-1) critical points formed with symmetry mate *ii*. Fig. 4.10a: hydrogen bonds side; Fig. 4.10a: weak forces side. Electrostatic potential (eÅ^{-1}) mapped over the ED isosurface of 0.1 eÅ^{-3}.

In this case, it manifests itself as difference in expansion/contraction coefficients between O1 and O4 atoms, causing the apparent distance – density relationship inversion. The relationship is not perturbed for O4$^{ii}\cdots$H1W hydrogen bond: here, the O–H distance of 1.758 Å is reflected in BCP electron density of 0.176 eÅ^{-3} and adequate lowering of λ_3. The water molecule O1W^{ii} forms two more bond paths with same symmetry mate, O1W$^{ii}\cdots$H6W and O1W$^{ii}\cdots$H1, their interatomic distances measuring 2.61 Å and 2.622 Å respectively. Similar interatomic distances are not, however, met with equally similar charge densities at BCPs: $\rho(\mathbf{r})$ takes value of 0.063 eÅ^{-3} for the former, and 0.049 eÅ^{-3} for the latter. Both contacts are characterized by unfavourable somewhat geometry, the X—H$\cdots$O1W^{ii} contact angles measuring 100.1° for the former and 140.0° for the latter. In either case, the interaction – even though clearly binding – is secondary to another, orientation–defining, in its vicinity. The two possess BCPs with similar eigenvalues and, in consequence, similar value of the Laplacian, despite differing angles and chemical character of hydrogen atom taking part in interaction. In this case, the convergence of topological characteristics is not an outcome of chemical similarity but rather similar distance and contact surface shape. For O3W water molecule, the orientation–defining contact would be that formed with O2^{ii}: the O3W-H6W-O2^{ii} angle measures 166°, the O3W-O2^{ii} distance has value of 2.98 Å. This is the only strong hydrogen bond formed by apical water ligand, and yet the deviation from perfect 180° geometry is significant; weak hydrogen bonds H5W$\cdots$Cl1^{ii} and H5W$\cdots$Cl4^{v} cause this, forming an almost perfect isosceles triangle

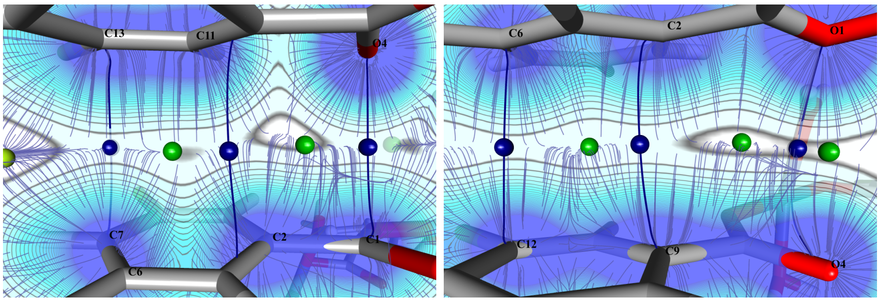

(a) Stacking with *i* (b) Stacking with *ii*

Fig. 4.11 Static total electron density and gradient trajectory plots for stacking interactions of **2**. Blue dots represent (3,-1) saddle, green (3,+1) ring, lime (3,+3) cage critical points; black contours mark electron density isovalues, plotted every 0.03 eÅ^{-3}.

with mean base angle of 49.75°. Positive charged hydrogen atom makes contact with both chlorine atoms' ring shaped negative charge concentration, stabilising the system with only little expense to the carbonyl atom angle. The contact distance – 3.62 Å – is equal to within a hundredth of an angstrom. Naturally, this translates to nearly identical charge density topology at the bond critical points, as listed in Table 4.2. The O3W atom also creates an isosceles triangle with chlorine atoms, indicating that their influence on water molecule's spatial orientation is significant and systemic, independent of hydrogen atoms modelling accuracy. This attracting interaction helps stabilize the suboptimal interaction Cl1$^{ii}\cdots$Cl4^{v}, described in detail later on.

Stacked dichlorobenzoate rings are staggered and rotated with relation to each other in such a manner, which allows for chlorine atoms to avoid causing van der Waals repulsion. In this case, carboxylate moieties are engaged in a repulsive interaction: the negatively charged oxygen atoms are in direct contact. While the contact C1$\cdots$O4^{i} is 0.05 Å shorter than the sum of relevant van der Waals radii [69], O1$\cdots$O4^{ii} is 0.13 Å longer. Notably, the carboxylate group of *ii* is rotated around C8—C9 bond, creating a 10.5° dihedral angle with the phenyl ring in such a way which increases the distance between two contacting oxygen atoms whilst decreasing it between *ii* and its own -x+1,-y+1,-z+1 symmetry mate. The rotation also causes minor lenghtening of H1W$\cdots$O4^{ii} hydrogen bond. Comparing topological characteristics of attractive and repulsive contacts further confirms this interpretation: (3,+1) ring critical point is not only positioned close to bond critical point, it lies on the shortest path between the two atoms. The bond path is significantly curved towards the aromatic ring (see Fig. 4.11b),

	interacting symmetry	distance, Å	$\rho(\mathbf{r})$, eÅ^{-3}	$\nabla^2\rho(\mathbf{r})$, eÅ^{-5}
Cl1···H2	x, y-1, z	2.746	0.035	0.635
Cl1···H3W	-x+1, -y, -z+1	3.231	0.025	0.337
Cl1···H5W	-x+1,y-½, -z+½	2.901	0.033	0.480
Cl3···H6	-x,y-½, -z+½	2.849	0.056	0.647
Cl3···H3	x1, -y+½, -z-½	2.860	0.049	0.605
Cl4···H4	x, y+1, z	2.961	0.026	0.397
Cl4···H5W	x, y+1, z	2.910	0.032	0.472
O1···H2W	-x+1, y-½, -z+½	1.733	0.196	4.710
O2···H6W	-x, y+½, -z+½	2.010	0.078	2.220
O2···H3W	-x+1, -y+1, -z+1	1.809	0.147	3.721
O4···H1W	-x+1, y+½, -z+½	1.758	0.175	4.148
O4···H4W	-x+1, -y+1, -z+1	1.719	0.191	4.768
O1W···H1	-x+1, y+½, -z+½	2,622	0,049	0,736
O1W···H6W	-x+1, y+½, -z+½	2.610	0.064	0.973
O2W···H1	-x+1, -y, -z+1	3.107	0.012	0.186
O3W···H5	x, y+1, z	2.350	0.065	1.070

Table 4.2 List of strong and weak hydrogen bonds

supporting the conclusion that the two oxygen atoms are spatially organized in a way that maximizes the distance between them. Bond critical point of this interaction has very similar Laplacian value to that of adjacent ring critical point: 0.37 eÅ^{-5} and 0.39 eÅ^{-5}, respectively. Unlike in the case of stacking in *i*, neither occupied nor unoccupied calculated molecular orbitals of an isolated symmetry pair exhibit significant simultaneous presence across both contacting aryl rings.

Halogen bonds

The crystal lattice of **2** comprises only a few other hydrogen bonds, almost all of them concentrated around the copper complex. The strongly polarized intermolecular contacts remain in contact with symmetrically equivalent molecules along the *b* and *c* axes, forming a (100) plane of strong interactions containing unit cell's inversion points. By rules of symmetry, unit cell in space group $P2_1/c$ contains a second set of inversion points position on another (100) plane distanced $a/2$ away from the first. Here, no strong hydrogen bonds are found: only chlorine and hydrogen atoms of dichlorobenzoate groups are exposed to this surface, creating an opportunity of studying less common halogen-halogen contact geometries. The predominant interactions

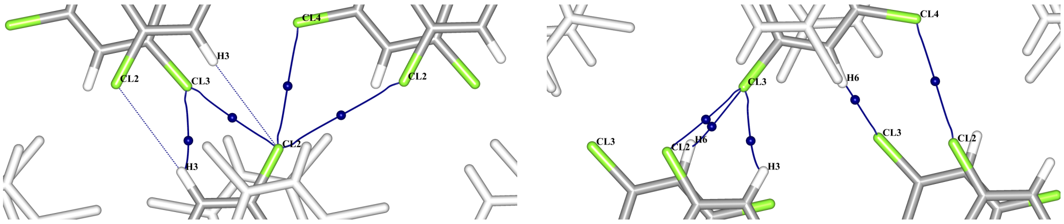

Fig. 4.12 Contacts across (100) plane. Symmetry mates involved coloured by chemical species, remaining symmetry equivalents surrounding **2** coloured white. Attractive electrostatic interactions that do not form bond paths marked with dotted lines.

found are type II halogen···halogen bonds, supplemented by weak hydrogen bonds taking place at unfavourable angles (Cl3···H3, Cl3···H6) or distance (Cl2···H3). In consequence, interaction energies evaluation from Table 4.1 indicates positive interaction energy for all symmetry mates. Of course, were these estimates accurate and exhaustive the crystal could not form. Binding energies estimated using a function of electrostatic potential distribution in atoms' vicinity, as done by VMoPro [108, 46], is sufficient for most applications. However, it omits London forces and weak attraction stemming from localized variations in charge distribution on molecular surface. Weak, odd-angled hydrogen bonds, electrostatic attraction of subatomic scale features and dispersion forces prove to be in this case enough for the crystal lattice to remain stable up to 500 K [63]. Relevant for contacts across (100) plane hydrogen bonds Cl3···H6 and Cl3···H3 are detailed in Table 4.2; halogen bonds Cl2···Cl3, Cl2···Cl4 and halogen contact Cl2···Cl2 in Table 4.3.

A list of all unique Cl···Cl contacts is presented in Table 4.3. It is discussed that from halogen-halogen contacts only type II interactions fulfil the definition of a halogen bond. Of those identified, only some seem to be true halogen bonds in the sense of IUPAC definition recommendation [59]. According to Metrangolo and Resnati [109], type I halogen-halogen interfacing is merely a result of minimizing repulsion in circumstances of forced proximity. The discussed dichlorobenzoate complex presents itself as interesting case study: all chlorine atoms are positions at the very fringes of the molecule. It is, therefore, worth investigating whether type I halogen contact geometries are an effect of repulsion minimization also in this specific case. Moreover, some of contacts found do not fit the classic definition of type I halogen contact (marked with a question mark in Table 4.3). When analyzing weak electrostatic interactions, it is often be useful to treat static deformation maps as a proxy for variations in electrostatic potential at atomic surface. Such parallels proved to correctly reproduce the reciprocal chalcogen$\cdots$chalcogen bond of **1**, and provide valuable insight into halogen$\cdots$halogen interactions of **2**, where the changes in chlorine atoms' electrostatic potential at atomic surface are drowned out by influence of water ligands. The electrostatic attraction of localized surface charges, even if a very weak interaction, is still important for packing found in crystal. It can be observed both on static deformation maps as well as through intermolecular bond path features near atomic centres, and to some extent on electrostatic potential maps of atomic surface.

The molecules of **2** are staggered in relation to (100) plane intersecting the halogen rich plane of intermolecular contacts, with a 2_1 rotation axis found in the vicinity of $\mathrm{Ar}_{\mathrm{CL3,Cl4}}$ moieties and inversion points closer to $\mathrm{Ar}_{\mathrm{CL1,Cl2}}$ rings. This pattern enforces the existence of contacts with a symmetry equivalent of a chemically identical atom. The ring stagger excludes the existence of unambiguously repulsive $\theta_1 \approx \theta_2 \approx 180°$ type I contacts, whilst enabling a larger number of different chlorobenzoate groups to interact with each other, stabilizing the lattice. The other source of halogen$\cdots$halogen contacts is related to chlorine atoms belonging to adjacent rings engaged in stacking briefly mentioned before. The only instance of a Cl$\cdots$Cl bond outside of these two groups is Cl3$\cdots$Cl4^{v}, which is a "classic" type II bond with θ_1 and θ_2 measuring 161.6° and 101.2°, respectively. Atom Cl4 is engaged in an already mentioned H5W$\cdots$Cl4^{v} halogen bond forming an isosceles triangle, with angle C13-Cl4-H5W measuring 95.4°. The other hydrogen$\cdots$halogen contact, H4$\cdots$Cl4, is placed at a disadvantageous C13-Cl4-H4 angle of 149.0°, which has the visible effect of bond path forming a curve away of shortest distance path and towards the (3,+1) ring CP, further indicating that the interaction may be repulsive.

A selection of Cl$\cdots$Cl interactions was analysed in detail. Related topological values are presented in Table 4.3, together with interaction types as proposed by Desiraju and Parthasarathy [49]. To help visualising the fine details of electrostatic interactions between atoms, deformation density maps were used (Fig. 4.13).

Apart from those with clearly definable contact types, contacts Cl1$\cdots$Cl4^{i} (ClB_{i}) and Cl1$\cdots$Cl4^{ix} (ClB_{ix}) were found. Both exhibit, to a different extent, signs of reciprocal weak electrostatic interaction. In general, one could argue that most type

	interacting symmetry	distance, Å	$\rho(\mathbf{r})$, eÅ^{-3}	$\nabla^2\rho(\mathbf{r})$, eÅ^{-5}	type
Cl2···Cl3	x+1, -y+½, z+½	3.476	0.055	0.64	II
Cl1···Cl4	-x+1, -y+1, -z+1	3.700	0.038	0.44	?
Cl3···Cl4	x, y-1, z	3.689	0.036	0.41	II
Cl4···Cl1	-x+1, y+³⁄₂, -z+½	3.754	0.031	0.38	I
Cl2···Cl4	x+1, -y+½, z+½	4.059	0.017	0.21	?
Cl2···Cl2	-x+2, -y+1, -z+1	4.315	0.010	0.13	I

Table 4.3 Halogen···halogen intermolecular contacts characterisation

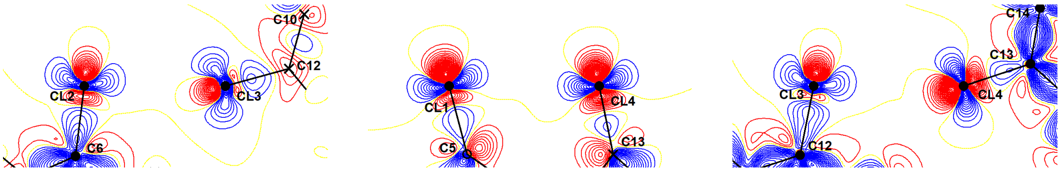

(a) Contact Cl2···Cl3^{viii} (across (100) plane) (b) Contact Cl1···Cl4^{i} (c) Contact Cl3···Cl4^{v}

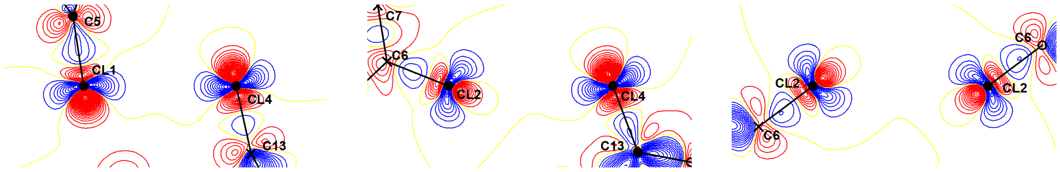

(d) Contact Cl1···Cl4^{x} (e) Contact Cl2···Cl4^{ix} (across (100) plane) (f) Contact Cl2···Cl2^{vi} (across (100) plane)

Fig. 4.13 Static deformation density in the plane of selected Cl···Cl contacts. Blue: positive, red: negative. Isovalues at 0.05e^{-1}.

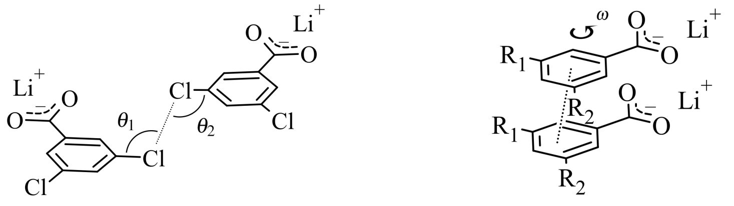

(a) Cl1$\cdots$Cl4^{ix} (b) Contact Cl1$\cdots$Cl4^{i}

Fig. 4.14 Simplified analogs of **2** used in DFT studies and their corresponding contacts. Fig. 4.14a, R$_1$=R$_2$=Cl: **4**; R$_1$=F, R$_2$=Cl: **5**; R$_1$=Cl, R$_2$=F: **6**; R$_1$=R$_2$=F: **7**.

I contacts with θ_X below 135° do; however, in this case the atoms have a varying degree of access to the covalent bond side of halogen atom, which clasically is not the case. Moreover, type I contacts are by definition approaching an antiparallel configuration; contact Cl1$\cdots$Cl4^{i} is closely approaching parallel geometry. Contacts ClB$_i$ and ClB$_{ix}$ found in crystal lattice are comparable in distance, measuring 3.700 and 3.754, respectively. Eigenvalues and $\nabla^2\rho(\mathbf{r})$, eÅ^{-5} differ in value more than expected judging by distance alone, however this is reliably explained through positional context: The parallel ClB$_i$ is placed at the covalent bond side of Cl1 atom, with neighbouring C5 atom engaged in delocalised phenyl ring bonds further increasing charge density in contact direction. Meanwhile, the antiparallel ClB$_{ix}$ is placed between two molecules with no points of contact other than ClB$_{ix}$, making the area devoid of electron density sources other than the chlorine atoms in question. The context difference is visible in Hessian matrix eigenvalues. Values of λ_1, primarily a result of distances from chlorine atoms, are relatively similar for both contacts: 0.55 eÅ^{-5} for ClB$_i$ and eÅ^{-5} 0.51 for ClB$_{ix}$. Values of λ_2, which can be interpreted as second order charge density change in direction along the C—Cl covalent bonds, vary noticeably: -0.03 for eÅ^{-5} for ClB$_i$ and eÅ^{-5} -0.07 for ClB$_{ix}$. The C5—Cl1 covalent bond adds, if slightly, to the rate of charge density drop happening when moving away from bond path; no such effect is possible for ClB$_{ix}$. Values of λ_3 are very similar – 0.08 eÅ^{-5} for ClB$_i$ and eÅ^{-5} 0.07 for ClB$_{ix}$ – since no neighbouring atomic centers are able to interfere with this direction of charge density drop. In end effect, this translates to $\rho(\mathbf{r})$ of 0.038 eÅ^{-3} for ClB$_i$ and 0.031 eÅ^{-3} for ClB$_{ix}$.

In order to computationally assess Cl$\cdots$Cl^{ix} interaction characteristic, an analog lithium chlorobenzoate (**3**) was used instead of **2**. Next, a series of single point

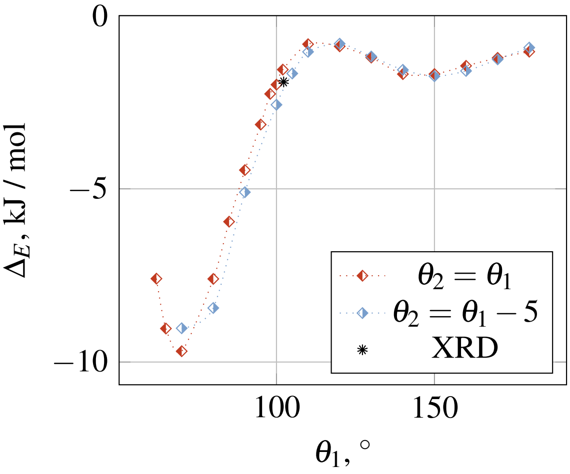

Fig. 4.15 Energetic effect of changing θ_1, θ_2 for **4**

energy calculations was performed for different θ_1, θ_2 values. The energetic effect of such constant-distance, antiparallel orientation changes is very subtle, but the trend observed is in agreement with expected behaviour. Like in the case of **1**, a reciprocal electrostatic bonding appears when geometric conditions are met; in the case of **4**, such occur for $\theta_{1,2}$ values in the range of 140° to 160°. For $\theta_{1,2}$ between 110° and 130° the negatively charged, ring shaped regions perpendicular to Cl—C covalent bond come in contact, resulting in electrostatic repulsion balancing out dispersion forces. Same is true for $\theta_{1,2}$ above 170°, where the repulsive component comes from positively charged σ holes. The rise in binding energy for $\theta_{1,2}$ below 90° is caused by chlorine atoms interacting with phenyl rings, both through London forces as well electrostatic interactions between the aryl ring and charge distribution features on chlorine atoms.

To better understand the character of interactions present in Cl1$\cdots$Cl4^i system without changes in stacking effects drowning out any interactions between chlorine substituents, a different approach was chosen: One of chlorobenzoate moieties was rotated around the geometric centre of its phenyl ring, without changing the distance nor inclination to the second molecule. Such approach allowed for qualitatively assessing the energetic effect of chlorine atoms' mutual orientation. For correct assessment of observed effects, a series of compound analogs was modeled: additionally to **4**, the energetic effect of varying ω was assessed also for **5**, **6**, and **7** (Fig. 4.14). Results strongly indicate that the orientation found in crystal is sub optimal for the chlorobenzoate group: the initial ring orientation is energetically favourable only if in compounds, in which chlorine

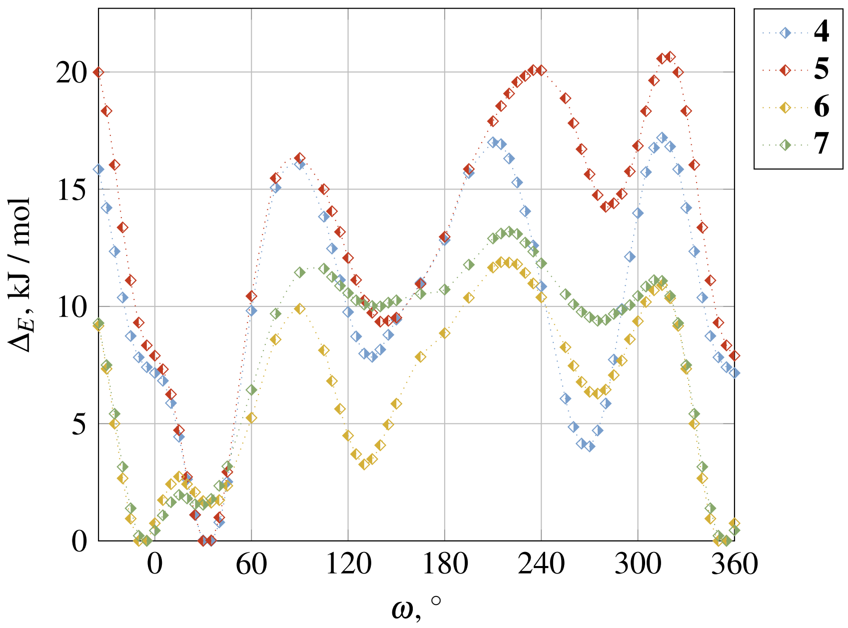

Fig. 4.16 Energetic effect of changing ω for **2** analogs **4**,**5**,**6**, and **7**

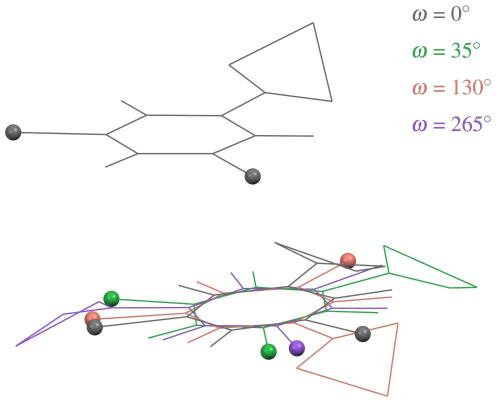

Fig. 4.17 Compounds **4** at ω values of particular interest. Spheres denote chlorine atoms positions, structures are colour coded according ω angle.

atoms of interest were subsituted with small, non-interacting fluorine atoms. Notably, the rate of interaction energy change drops significantly in the ω range close to 0°. It needs to be kept in mind that the energetic effect in this study is relative to the lowest spatial configuration, it may well be that in relation to single molecules even the least stable orientations found near ω=220° are preferred. In fact, such were the indications of draft interaction energy screening calculations conducted for **4**. Atoms orientation at ω values of 0°,35°,130°, and 265° were further analysed. For each of observed local interaction energy minima, at least one pair of chlorine atoms came in close contact. This, together with interaction patterns displayed by **7**, allow stating a (cautious) conclusion that interactions of chlorine atoms oriented parallel to each other are attractive. Such interaction might be explained by electrostatic attraction of fine features on chlorine atom surface, which become even more meaningful in close range. The topic deserves further investigation, with preliminary research in progress.

4.4 Summary

Intermolecular interactions found in crystal structure of **2**, ranging from strong hydrogen bonds to weak halogen bonds and halogen$\cdots$halogen contacts, were analysed and described in detail. The compound features a highly polarized centre and termini engaged in weakly polarized bonding interactions involving chlorine atoms. This setup allows for forming of very interesting cases of Cl$\cdots$Cl bonds, some of which escape the classic categories. These cases were investigated in further detail, including conducting series of DFT studies for hypothetical alternative molecule positioning. The results indicate that halogen atoms may form bonds not only when oriented in type II configuration, though further studies are necessary.

4.5 Experimental section

Altered geometry calculations

All interaction energies and geometry optimizations were perfomed using Orca 5.0.4 [110, 111]. I gratefully acknowledge Polish high-performance computing infrastructure PLGrid (HPC Centers: CI TASK, ACC Cyfronet AGH, WCSS) for providing computer facilities and support within computational grant no. PLG/2024/017342.

Coordinates of **4**, **6**, **5**, and **7** were created by abstracting stacked chlorobenzoate moieties from either **2** and $\mathbf{2}^{i}$ for ω related studies, or from **2** and $\mathbf{2}_{ix}$ for $\theta_{1,2}$ related investigations. Systems **6**, **5**, and **7** were then created by substituting selected chlorine atoms with fluorine, and optimizing their geometries (B97M-V/def2-TZVPD with nonlocal correction) against coordinate constrained source. To prevent anion repulsion from drowning out other noncovalent interaction forces, a pair of lithium atoms was placed near carboxyl groups in all cases. The lithium atoms geometry was optimised (B97M-V/def2-TZVPD with nonlocal correction) in a separate step set up to promote positions away from contact plane, in order to minimize their interaction with studied halogen atoms. A rotation centre was established in the middle of C2-C5-C6 triangle, with the three atoms used to define the rotation plane. New atom coordinates were then calculated using axis–angle representation, with their relative interaction energies calculated as a set of single point energies using ωB97M-V+D3BJ/def2-TZVPD in the final run. Since the intent was always to only compare these systems against other rotation angle values, counterpoise correction was omitted as BSSE would be nearly identical for all analyzed positions and thus not changed the calculated Δ_E values. For $\theta_{1,2}$ interaction analysis, counterpoise correction was calculated and applied. New atom coordinates for $\theta_{1,2}$ calculation series were obtained by first rotating a molecule around the contacting chlorine atom using axis–angle representation, with rotation vector normal to C-Cl-Cl^{ix} plane, then rotating the second molecule analogously around its chlorine atom, following θ_1 rotation angle for the first molecule and θ_2 for the second. In these repositioning of molecules to new hypothetical positions, geometry optimisation was not performed.

Refinement

Data quality obtained from SHELXL2014 proved sufficient for immediate charge density refinement in MoPro software [46, 47]. Scale factors were left at scalar level. Multipolar refinement was conducted in several steps, with each consecutive steps having fewer constraints and restraints applied. Non-hydrogen atoms underwent a separate high-order positional parameters refinement cycle, later followed by refinement of

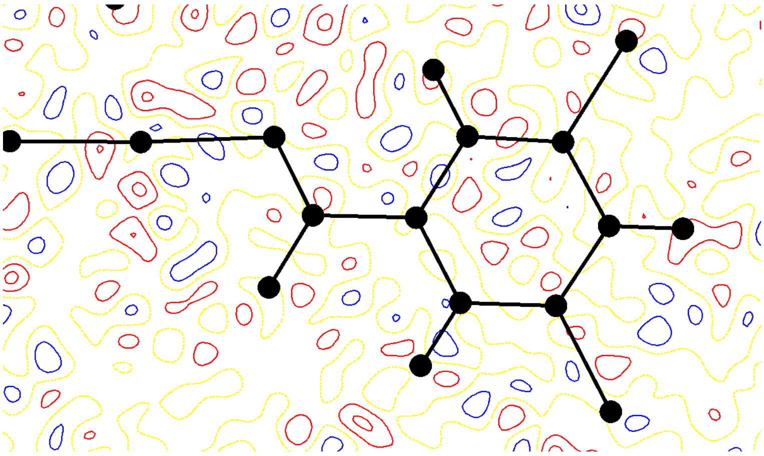

Fig. 4.18 Residual density map of **2**. Isocontours every 0.01 eÅ^{-3}, blue: positive, red: negative. Resolution cutoff: 0.85 eÅ^{-1}.

hydrogen atoms against the full reflection set. For final refinement cycle, anharmonic motion parameters were refined for chlorine atoms. The final set of constraints and restraints are attached in Section A.2 Final residuals for this step: I > 3.0σ(I) RI = 1.91%, wR2I = 2.47%, S = 1.0. Max/min $\Delta\rho$ values in the final ΔF map 0.35/-0.31 eÅ^{-3}, with residual density featureless and randomly distributed throughout the cell (Fig. 6.7b).

4.6 Supporting information

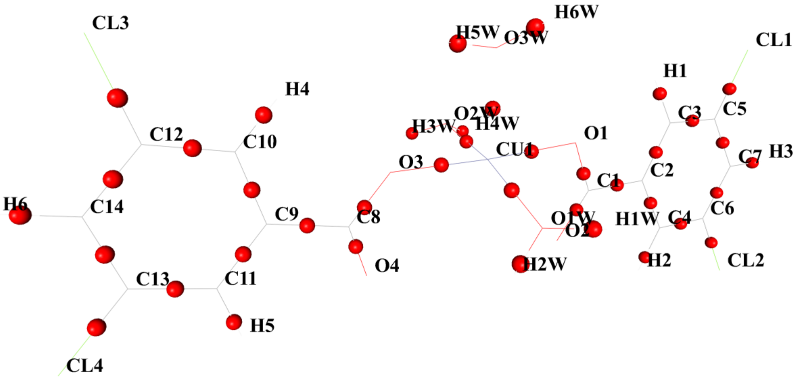

Fig. 4.19 Covalent bond (3,-1) critical points

Table 4.4 List of (3,-1) intramolecular critical points in **2**

	Atom1	Atom2	distance, Å	$\rho(\mathbf{r})$, eÅ^{-3}	$\nabla^2\rho(\mathbf{r})$, eÅ^{-5}		λ_1 ,eÅ^{-5}	λ_2 ,eÅ^{-5}	λ_3 ,eÅ^{-5}	Gcp	Vcp	ε
1	O2	C1	1.245	2.728	-30.50	-26.88	-24.57	20.95	0.424	-1.164	0.094	
2	O4	C8	1.254	2.709	-30.31	-26.63	-24.16	20.48	0.418	-1.150	0.102	
3	O3	C8	1.270	2.492	-26.36	-24.23	-21.83	19.71	0.363	-1.000	0.110	
4	O1	C1	1.287	2.462	-26.60	-23.56	-21.21	18.18	0.351	-0.978	0.111	
5	C3	C5	1.390	2.216	-20.64	-17.66	-14.48	11.50	0.306	-0.826	0.219	
6	C5	C7	1.391	2.185	-19.96	-17.51	-14.19	11.74	0.300	-0.808	0.234	
7	C10	C12	1.387	2.171	-20.11	-16.94	-14.19	11.02	0.295	-0.798	0.194	
8	C4	C6	1.389	2.161	-19.79	-17.08	-13.70	10.99	0.293	-0.792	0.247	
9	C11	C13	1.392	2.148	-19.77	-17.00	-13.94	11.17	0.289	-0.784	0.220	
10	C13	C14	1.391	2.142	-19.64	-17.05	-14.03	11.45	0.288	-0.780	0.215	
11	C6	C7	1.394	2.130	-19.55	-17.22	-13.66	11.33	0.285	-0.773	0.261	
12	C12	C14	1.391	2.124	-19.28	-17.25	-13.22	11.19	0.285	-0.770	0.305	
13	C9	C10	1.396	2.104	-19.06	-15.86	-13.21	10.01	0.280	-0.757	0.200	
14	C2	C3	1.396	2.103	-19.23	-16.01	-13.13	9.90	0.278	-0.756	0.219	
15	C4	C2	1.396	2.085	-18.67	-15.80	-12.77	9.90	0.276	-0.746	0.237	
16	C11	C9	1.394	2.082	-18.82	-15.96	-12.65	9.79	0.274	-0.744	0.261	
17	C3	H1	1.086	1.767	-18.37	-18.06	-16.83	16.52	0.181	-0.552	0.073	
18	C11	H5	1.085	1.760	-18.26	-17.74	-16.94	16.42	0.179	-0.548	0.048	

continued on next page

continued from previous page

	Atom1	Atom2	distance, Å	$\rho(\mathbf{r})$, eÅ^{-3}	$\nabla^2\rho(\mathbf{r})$, eÅ^{-5}	λ_1 ,eÅ^{-5}	λ_2 ,eÅ^{-5}	λ_3 ,eÅ^{-5}	Gcp	Vcp	ε
19	C4	H2	1.080	1.755	-18.01	-17.74	-16.67	16.40	0.180	-0.546	0.064
20	C7	H3	1.073	1.744	-19.01	-17.65	-16.56	15.20	0.170	-0.536	0.066
21	C1	C2	1.498	1.742	-11.19	-13.13	-11.59	13.53	0.223	-0.562	0.133
22	C8	C9	1.501	1.736	-11.06	-13.05	-11.55	13.54	0.222	-0.559	0.129
23	C10	H4	1.084	1.735	-17.44	-17.35	-16.41	16.32	0.178	-0.537	0.057
24	C14	H6	1.084	1.719	-18.31	-17.27	-16.18	15.14	0.167	-0.524	0.067
25	CL3	C12	1.728	1.381	-1.48	-8.14	-7.46	14.12	0.194	-0.403	0.090
26	CL2	C6	1.733	1.378	-1.42	-7.99	-7.38	13.95	0.194	-0.402	0.082
27	CL1	C5	1.733	1.320	-1.60	-7.70	-7.13	13.24	0.178	-0.373	0.080
28	CL4	C13	1.735	1.292	-1.62	-7.40	-6.85	12.63	0.171	-0.360	0.080
29	Cu	O3	1.913	0.625	12.05	-3.23	-2.91	18.18	0.138	-0.150	0.112
30	Cu	O2W	1.973	0.595	10.23	-3.06	-2.93	16.22	0.121	-0.136	0.041
31	Cu	O1W	1.972	0.584	9.91	-2.91	-2.90	15.72	0.117	-0.132	0.001
32	Cu	O1	1.946	0.583	11.00	-2.92	-2.66	16.58	0.125	-0.135	0.100
33	Cu	O3W	2.293	0.259	4.04	-1.06	-1.00	6.10	0.040	-0.039	0.061

Table 4.5 List of bound water molecules (3,-1) O—H critical points

	Atom1	Atom2	distance, Å	$\rho(\mathbf{r})$, eÅ^{-3}	$\nabla^2\rho(\mathbf{r})$, eÅ^{-5}		λ_1 ,eÅ^{-5}	λ_2 ,eÅ^{-5}	λ_3 ,eÅ^{-5}	Gcp	Vcp
1	O1W	H1W	0.983	2.122	-34.73	-33.73	-32.82	31.83	0.177	-0.715	0.028
2	O1W	H2W	0.983	2.095	-33.05	-32.94	-31.83	31.72	0.180	-0.703	0.035
3	O2W	H3W	0.983	2.081	-32.30	-32.21	-31.90	31.82	0.181	-0.697	0.010
4	O2W	H4W	0.983	2.103	-33.34	-32.75	-32.48	31.89	0.181	-0.707	0.008
5	O3W	H5W	0.983	2.100	-33.44	-32.84	-32.53	31.93	0.179	-0.705	0.009
6	O3W	H6W	0.983	2.056	-30.80	-31.77	-31.04	32.01	0.183	-0.686	0.024

Table 4.6 List of (3,-1) intermolecular critical points in **2**

Atom1	Atom2	symmetry mate	$\rho(\mathbf{r})$, eÅ^{-3}	$\nabla^2\rho(\mathbf{r})$, eÅ^{-5}	λ_1 ,eÅ^{-5}	λ_2 ,eÅ^{-5}	λ_3 ,eÅ^{-5}
O1	H2W	-x+1, y+½, -z+½	0.1965	4.71	-1.015	-0.999	6.723
O4	H4W	-x+1, -y+1, -z+1	0.1911	4.768	-0.955	-0.955	6.677
O4	H1W	-x+1, y+½, -z+½	0.1756	4.148	-0.872	-0.855	5.875
O2	H3W	-x+1, -y, -z	0.1468	3.722	-0.687	-0.676	5.085
O2	H6W	-x+1, y+½, -z+½	0.0784	2.22	-0.316	-0.303	2.839
O3W	H5	x, y+1, z	0.0657	1.07	-0.227	-0.203	1.5
O3W	O1W	-x+1, y+½, -z+½	0.0636	0.973	-0.164	-0.148	1.285
CL3	H6	-x, y+½, -z+½	0.0565	0.647	-0.151	-0.147	0.946
CL2	CL3	x+1, -y+½, z+½	0.0552	0.635	-0.122	-0.118	0.876
CL2	C14	-x+1, y+½, -z+½	0.0512	0.571	-0.108	-0.037	0.716
C6	C12	-x+1, y+½, -z+½	0.0505	0.528	-0.058	-0.027	0.613
CL3	H3	x+1, -y+½, z+½	0.0491	0.605	-0.128	-0.126	0.858
O1W	H1	-x+1, y+½, -z+½	0.0488	0.736	-0.168	-0.12	1.024
C7	C13	-x+1, -y+1, -z+1	0.045	0.473	-0.058	-0.021	0.551
C4	C9	-x+1, -y+1, -z+1	0.0399	0.419	-0.044	-0.039	0.501
C12	CL2	-x+1, -y+1, -z+1	0.0398	0.445	-0.062	-0.035	0.541
O4	C1	-x+1, -y+1, -z+1	0.0397	0.53	-0.065	-0.043	0.638
O2	CL1	x, y+1, z	0.0393	0.559	-0.102	-0.098	0.759

continued on next page

continued from previous page

Atom1	Atom2	symmetry mate	$\rho(\mathbf{r})$, eÅ^{-3}	$\nabla^2\rho(\mathbf{r})$, eÅ^{-5}	λ_1 ,eÅ^{-5}	λ_2 ,eÅ^{-5}	λ_3 ,eÅ^{-5}
C2	C9	-x+1, y+½, -z+½	0.0386	0.418	-0.041	-0.036	0.495
CL1	CL4	-x+1, -y+1, -z+1	0.0377	0.445	-0.077	-0.035	0.557
CL3	CL4	x, y+1, z	0.0355	0.414	-0.075	-0.073	0.563
CL1	H2	x, y+1, z	0.0354	0.635	-0.092	-0.086	0.812
C3	C11	-x+1, -y+1, -z+1	0.0348	0.384	-0.043	-0.016	0.443
C4	C13	-x+1, y+½, -z+½	0.0348	0.386	-0.043	-0.02	0.449
O3W	CL1	-x+1, y+½, -z+½	0.0333	0.48	-0.091	-0.082	0.653
O3W	CL4	x, y+1, z	0.0324	0.472	-0.089	-0.075	0.637
CL1	CL4	-x+1, y+³⁄₂, -z+½	0.0313	0.378	-0.068	-0.066	0.512
O2W	O2W	-x+1, -y+1, -z+1	0.0295	0.373	-0.034	-0.016	0.422
O1	O4	-x+1, y+½, -z+½	0.0271	0.376	-0.041	-0.015	0.431
CL4	H4	x, y+1, z	0.0258	0.397	-0.06	-0.059	0.516
O2W	CL1	-x+1, -y, -z+1	0.0251	0.337	-0.061	-0.05	0.449
O3	C3	-x+1, y+½, -z+½	0.022	0.279	-0.04	-0.011	0.33
CL2	CL4	x+1, -y+³⁄₂, z+½	0.017	0.207	-0.031	-0.03	0.268
CL1	H4	-x+1, -y, -z+1	0.0137	0.171	-0.028	-0.027	0.227
O2W	H1	-x+1, -y, -z+1	0.012	0.186	-0.029	-0.006	0.221
CL2	CL2	-x+2, -y+1, -z+1	0.0101	0.126	-0.019	-0.018	0.162

	this work	120 K [65]	150 K[64]	295 K [63]	growth rate	R-factor
a	16.799	16.814	16.828	16.854	15.07	91.2%
b	8.285	8.295	8.293	8.330	26.86	96.7%
c	13.436	13.468	13.470	13.655	83.33	98.1%
Cl1 – Cl2	5.396	5.397	5.392	5.381	-15.17	97.2%
Cl3 – Cl4	5.376	5.379	5.372	5.357	-20.06	95.0%
C7 – C14	13.706	13.703	13.687	13.650	-21.11	98.5%
Cu—O1	1.946	1.946	1.944	1.945	-2.12	14.4%
Cu—O3	1.913	1.912	1.911	1.905	-21.28	99.9%
Cu—O1W	1.972	1.971	1.968	1.971	-0.38	0.1%
Cu—O2W	1.973	1.969	1.966	1.968	-7.48	19.5%
Cu—O3W	2.293	2.292	2.291	2.310	42.32	89.8%
Cu – Cu^{i}	4.730	4.736	4.731	4.756	27.63	90.5%
Cl1 – Cl4^{x}	3.754	3.762	3.766	3.818	87.49	99.2%
Cl1 – Cl4^{i}	3.700	3.707	3.705	3.744	60.83	96.5%
Cl1 – O2^{v}	3.323	3.334	3.343	3.409	131.85	99.8%
Cl1 – O2W^{iii}	3.693	3.701	3.716	3.767	101.78	99.6%
Cl1 – O3W^{v}	3.281	3.293	3.298	3.325	63.04	96.4%
Cl1 – O3W^{ii}	3.610	3.623	3.620	3.652	55.05	94.4%
Cl2 – Cl2^{vi}	4.315	4.315	4.301	4.315	2.26	96.2%
Cl2 – Cl2^{vi}	5.363	5.379	5.397	5.484	113.99	99.9%
Cl2 – Cl3^{i}	3.925	3.932	3.927	3.956	39.63	92.0%
Cl2 – Cl3^{viii}	3.476	3.486	3.491	3.546	102.26	99.4%
Cl2 – Cl4^{viii}	4.059	4.066	4.064	4.089	36.45	95.9%
Cl3 – Cl2^{ii}	3.873	3.885	3.896	3.977	137.68	99.7%
Cl3 – Cl4^{v}	3.689	3.694	3.693	3.720	42.86	97.0%
Cl3 – Cl4^{iv}	3.916	3.923	3.930	3.956	50.25	98.9%
Cl4 – Cl1^{x}	3.754	3.762	3.766	3.818	87.49	99.2%
Cl4 – O3^{v}	4.491	4.503	4.513	4.563	79.63	99.5%
Cl4 – O3W^{v}	3.623	3.631	3.631	3.645	27.55	92.7%

Table 4.7 Temperature variation of selected distances, measured in Å. Growth rate defined as coefficient a of linear regression defined as $y = ax + b$, where measurement temperatures are represented as independents x and measured distances normalized against this work's measured value as dependants y, multiplied by 10^6 for enhanced readability. R-factor provided served as basis for classifying a dimension as temperature-independent.

Chapter 5

4-methylsulphanyl-2’,5’-dimethoxy-E-stilbene

5.1 Introduction

5.2 Structure

4-methylsulphanyl-2’,5’-dimethoxy-E-stilbene (**8**) is a stilbene derivative with three methylated chalcogene substituents. The compound crystallized in space group *Pna*2_1.

Despite being a stilbene derivative, a compound with planar geometry owed to its conjugated phenyl rings, stacking did not play decisive role in molecule’s spatial

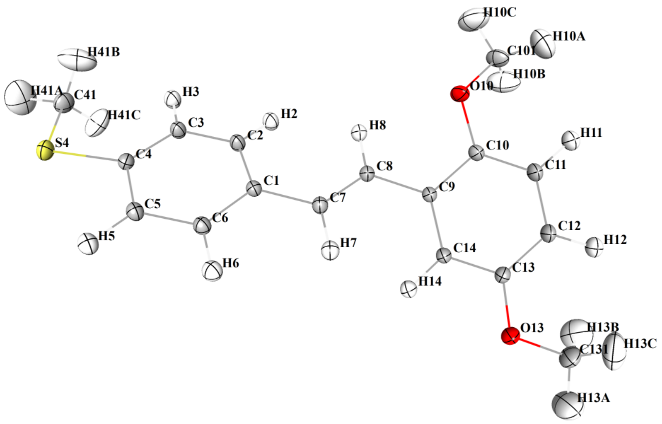

Fig. 5.1 Atom positions and thermal displacement ellipsoids of **8**.

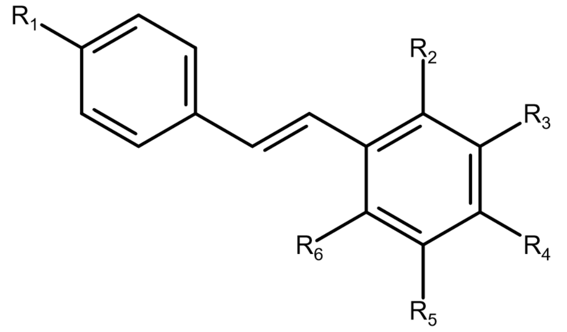

Fig. 5.2 Stilbene derivatives analog to **8**
9: R_1=H, R_2=OMe, R_3=OMe, R_4=OMe, R_5=H, R_6=H;
10: R_1=SMe, R_2=OMe, R_3=OMe, R_4=OMe, R_5=H, R_6=H;
11: R_1=SMe, R_2=OMe, R_3=H, R_4=H, R_5=H, R_6=H;
12: R_1=SMe, R_2=H, R_3=OMe, R_4=H, R_5=H, R_6=H;
??: R_1=SMe, R_2=OMe, R_3=OMe, R_4=H, R_5=H, R_6=H;
8: R_1=SMe, R_2=OMe, R_3=H, R_4=H, R_5=OMe, R_6=H;
13: R_1=SMe, R_2=H, R_3=OMe, R_4=H, R_5=OMe, R_6=H;
14: R_1=SMe, R_2=OMe, R_3=H, R_4=OMe, R_5=H, R_6=H;
15: R_1=SMe, R_2=OMe, R_3=H, R_4=OMe, R_5=OMe, R_6=H;
16: R_1=SMe, R_2=H, R_3=OMe, R_4=OMe, R_5=OMe, R_6=H;
17: R_1=SMe, R_2=OMe, R_3=H, R_4=OMe, R_5=H, R_6=OMe;

Table 5.1 Ar–Ar’ dihedral angle values

Compound	dihedral, °
9	16.0(7)
10	6.3(2)
11	10.2(2)
12	2.1(2)
?? (MM)	12.12(2)
?? (lit.)	12.44(7)
8 (MM)	37.15(5)
8 (lit.)	37.13(5)
13	26.42(11), 27.17(12)
14	9.4(2)
15	6.1(3)
16	26.84(5), 24.49(6)
17	4.24(9)

arrangement within crystal lattice. In fact, molecules are organized in such a way that phenyl rings of neighbouring molecules interface exclusively at high angles, that is between 40 and 90 degrees. This is in agreement with packing patterns of **??** and a majority of compounds from Table 5.1. The phenyl rings are not coplanar: the torsion angle between them measures approx. 37.1°. Intuitively one could attempt explaining this by steric hindrance coming from methoxy substituent on C10 carbon atom, however **??** remains planar in regard to its conjugated phenyl rings (as described in **??**), as well as almost all other members of same stilbene derivatives described in literature [112–115]. In fact, **8** measures the highest dihedral angle of the whole compound group (Table 5.1). The conformation of the compound is clearly strongly influenced by packing effects. Despite the angle, the energetic cost of this seems to be negligible, as indicated by torsion energy values presented in Table 5.2 This is supported by quantum mechanical models indicating that despite the significant torsion angle, packing geometry does not come at a cost of losing aromatic conjugation with one of phenyl rings.

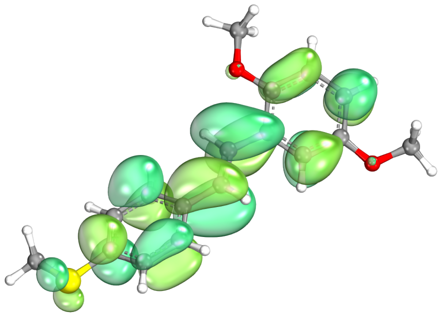

Fig. 5.3 LUMO of **8** for geometry found in lattice (M06-2X / 6-311G(d,p))

Table 5.2 Energy gained by system after torsion angle optimization

Functional, basis set	Δ_E, kJ/mol
B97M-V def2-TZVPD	-1.71
M06-2X 6-311++G(d,p)	-0.80

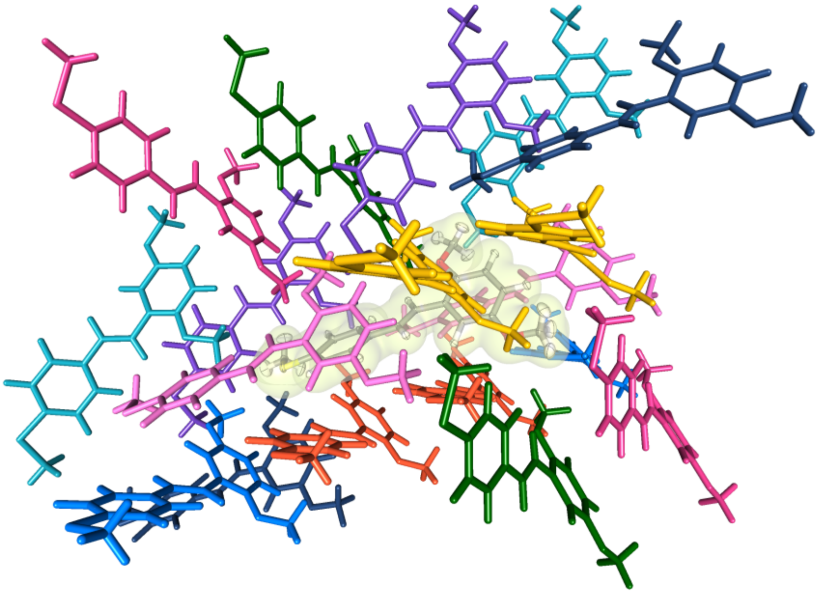

Fig. 5.4 Contacting symmetry mates of **8**

5.3 Intermolecular contacts

There is a total of 18 symmetry related molecules surrounding **8** (Fig. 5.4), all of them forming (3,-1) intermolecular bonds. Of these symmetry mates, half is symmetrically independent. Identified contacts are dominated by instances of hydrogen - π bond interactions, followed by C—H$\cdots$chalcogene bonds. A small number of low charge density contacts that may either add to or subtract from crystal stability has also been identified. The contact energy was calculated for each molecule pair and averaged between those which are symmetrically equivalent. Obtained values are collected in Table 5.3.

Fig. 5.5 Hirshfeld surfaces of **8**

interacting symmetry	number of involved (3,-1) critical points	E, kJ/mol	
		MM	DFT
-x+1,-y+1,z-½	5	-35.78	-33.09
x,y,1+z	4	-25.37	-34.41
-x+1,-y+2,z-½	4	-19.64	-29.94
³⁄₂-x,y-½,z-½	4	-13.08	-15.23
x-½,-y+³⁄₂,z+1	2	-1.48	-5.85
-x+½,y+½,z+½	1	-6.20	-4.29
x+½,-y+½,z	1	-3.48	-2.95
x,y-1,z-1	2	1.42	-1.65
-x+1,-y+1,z+³⁄₂	1	1.85	-1.70

Table 5.3 Total interaction energy values of contacting symmetrically independent pairs of **8**. Functional and basis set used: for DFT based calculations: ωB97M-V def2-TZVPD

As expected, C—H···chalcogene bonds are involved in energetically strongest interactions. In terms of largest charge density at critical point, C—H···π are more pronounced than weak hydrogen bonds present between molecules. Same is true for d_{norm} of Hirshfeld surfaces (**??**). Notably, around half of identified contacts are not meaningfully binding: they measure binding energies within several kJ/mol below zero, or – as calculated by VMoPro – may even be marginally repulsive (Table 5.3).

Symmetry mate -x+1,-y+1,z-½ (^{i}) and its equivalent -x+1,-y+1,z+½ are by far the most significant of all contacts analyzed in this system. They form individually and collectively strong bonds, which are immediately visible on Hirshfeld surface as strongly negative d_{norm} regions. In fact, all but one of named contacts on (**??**) belong to this set of five interactions. The S1 sulphur atom is positioned in such a way that one of its lone electron pairs are accessible to H7 atom of neighbouring symmetry mate (Figs. 5.6 and 5.7a). This C—H···S^i weak hydrogen bond is however limited by packing effects, resulting in a bond measuring 3.138 Å that is above the sum of van der Waals radii, and 0.036 eÅ^{-3} electron density at critical point. The adjacent methyl group is involved in a C—H^i···O weak hydrogen bond. With suboptimal C13-O13-H41C^i angle measuring 117.7°, contact almost perfectly in aromatic ring plane and O···H distance shorter than the sum of van der Waals radii, that is 2.53 Å, the charge density registers as one of medium strength at 0.038 eÅ^{-3}. It is, however, very

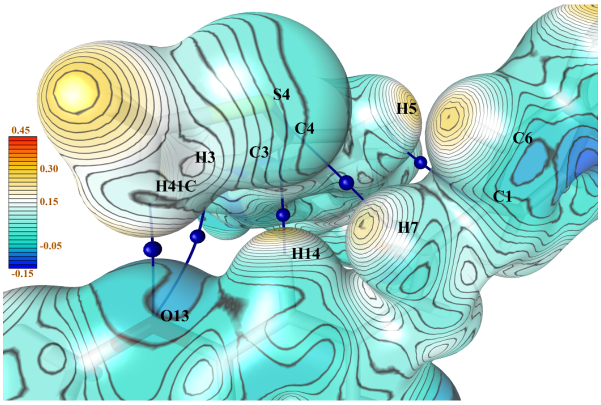

Fig. 5.6 (3,-1) critical points on contacts with -x+1,-y+1,z-½ symmetry equivalent. Electrostatic potential (eÅ^{-1}) mapped over the ED isosurface of 0.1 eÅ^{-3}.

well localized: the Laplacian value reaches 0.70 eÅ^{-5}. Same oxygen atom is involved in one more close contact, namely with H3 atom of same symmetry mate. Here, the hydrogen atom is positioned almost perfectly above a lone electron pair: angle C13-O13-H3^{i} measures 110.5°, the dihedral C14-C13-O13-H3^{i} 38.9°. The contact takes place almost sideways (Fig. 5.7b), with C3^{i}-H3^{i}-O13 angle equal to 109.2°. This, together with large O13-H3^{i} distance of 3.23 Å, causes the nominally weak hydrogen bond to be also substantially weak, with charge density at saddle point determined as 0.017 eÅ^{-5}. A fairly strong H$\cdots\pi$ bond was found between π(C1—C7) and H5^{i}. Negative d$_{\mathrm{norm}}$ value region on the Hirshfeld surface is accompanied by electron density value of 0.046 eÅ^{-3}. It is less localized than previously described contacts, with Laplacian value at critical point of 0.52 eÅ^{-5}. The existence and character of this contact, together C1—C7 saddle point ellipticity values at the lower end of those characteristic for delocalised aromatic bonds (Table 5.4), confirm that the high Ar-Ar' torsion angle does not compromise aromatic system conjugation. Geometrically between all of described above, a striking intermolecular bond is located. Distanced only 2.65 Å from each other, C14—H14$\cdots$C4^{i} make contact. The angle of contact is 149.2°, enough to directly expose hydrogen atom's positive region to the electron-rich, negatively charged delocalised π orbitals of carbon. The attraction between the two leads to a strong intermolecular contact, with 0.049 eÅ^{-3} measured electron density at critical point. As expected, it is somewhat spread, with λ_1 and λ_2 around -0.1 eÅ^{-5}. Effects of strong bonding are noticeable in critical point shifting towards hydrogen atom, from typical C$_{\mathrm{Ar}}$-CP$_{\mathrm{C_{Ar}-HAr}}$ distance of 0.749(2) Å to measured value of 0.757

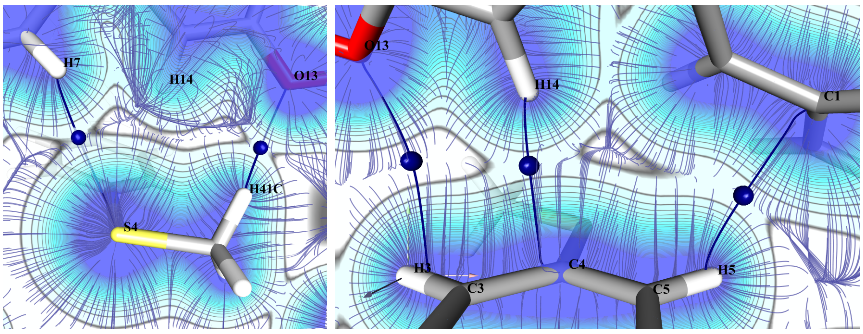

(a) Electron density gradient lines around S4 and O13 (b) Electron density gradient lines around H14 and phenyl ring

Fig. 5.7 Interaction details with -x+1,-y+1,z-½

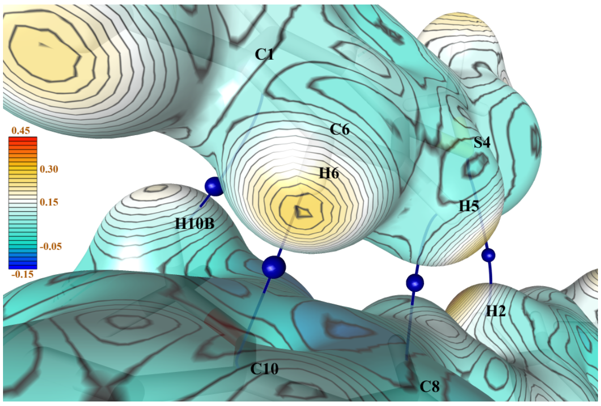

Fig. 5.8 (3,-1) critical points on contacts with x,y,z+1 symmetry mate.

Å. This bond is probably largely responsible for molecule's spatial configuration in crystal.

Symmetry mate x,y,z-1 (^{ii}) and its equivalent x,y,z+1 are engaged mostly in C—H$\cdots\pi$(C—C) interactions (Fig. 5.8). They are supplemented by a weak, distant and fairly unremarkable S4$\cdots$H2^{ii}—C2^{ii} hydrogen bond. Ar-Ar^{ii} planes are oriented at a compound angle, with the angle between their normals measuring around 39°. Positive regions of C—H are not directly in contact with the delocalised π electrons of the system, nevertheless the electrostatic interactions between symmetry mates are strong since the Ar' ring is double substituted with electron donating methoxy moieties, resulting in a region of negative electrostatic potential near contact points. The attractive molecular force present in C6—H6$\cdots$(Ar'^{ii}) contact (Fig. 5.9) is a particularly interesting case: the C6-H6-CP$_{Ar'^{ii}}$ angle value is, at 125.6° suboptimal. The angle to C10^{ii} atom, which the intermolecular bond path leads to, measures 97.6°. Based on

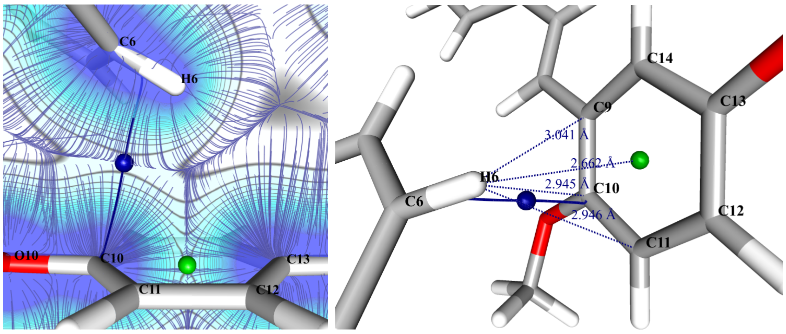

(a) Electron density gradient lines around H6$\cdots$Ar'^{ii}

(b) Distances between ring CP, selected ring members and H6

Fig. 5.9 CH $\cdots\pi$ interactions between H6 and delocalised π orbitals of x,y,z-1. Phenyl (3,+1) ring critical point marked in green.

a superficial analysis of geometrical features alone, one could come to an inaccurate conclusion: that this contact is a combination of dispersion forces and packing effects at play. In fact, while dispersion forces are of course important, this interaction is a case soft base – soft acid bonding. Despite the somewhat disadvantaging geometry, C6—H6$\cdots$Ar'^{ii} is a case of C—H$\cdots\pi$(Ar) hydrogen bond. This is supported by the prominent dip in d_{norm} visible in **??**, relatively short interatomic distances, high electron density value of 0.056 eÅ^{-3}, and small (in context of ρ value found) values of λ_1 and λ_2 in the range of negative hundredths of eÅ^{-5}. Moreover, geometrical analysis finds that H6 atom is positioned substantially closer to (3,+1) ring saddle point of Ar'^{ii} than to C10^{ii} atom, the origin of bond path depicted on Fig. 5.9b. The adjacent H5$\cdots\pi$(C7^{ii}-C8^{ii}) might have taken similar characteristics, leading to a similar, strong (for its type) hydrogen bond — were it not almost entirely prohibited by bonds geometry being even more unfavourable than in the former instance. With moieties meeting at an angle of only 8.5°, the positively charged part of hydrogen atom does not come in direct contact with C7^{ii}—C8^{ii} π bond. Thus, despite apparently similar numerical properties and contact distance much below van der Waals radii, this instance should be treated as dispersive. The C101^{ii} methoxy group reciprocates with C—H$^{ii}\cdots\pi$(C1) hydrogen bond. Here, the favourable C101^{ii}-H101^{ii}-C1 angle of 152.0° degrees is met with barely adequate H101^{ii}-C1 interatomic distance of 2.96 Å, slightly above mean values for such type of contact found in literature [116]. The resulting weak hydrogen bond characterizes with ρ of only 0.028 eÅ^{-3}, and has lateral eigenvalues in the range of low in the range of negative hundredths of eÅ^{-5}. This is expected for

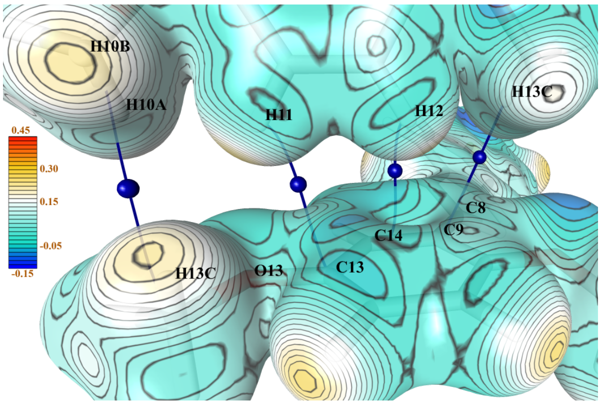

Fig. 5.10 (3,-1) critical points on contacts with -x+1,-y+2,z-½ symmetry mate

such contact. In its case, the hydrogen atom does not bind to all ring atoms, but is positioned unambiguously near C1. The factor driving both λ_1 and λ_2 towards a fuzzy quality is found not in the ring system, but in the adjacent conjugated π(C1-C7) bond.

Similarly to the described above, the symmetry equivalent -x+1,-y+2,z-½ (^{iii}) is engaged primarily in C—H$\cdots\pi$ binding. With arene rings oriented at nearly right angle, electron-rich phenyl ring, and a handful of hydrogen atoms oriented in just the right way for their positive end regions to make contact, this symmetry mate is a prime example of weak C—H$\cdots\pi$ bonding. The central of the three, H12$^{iii}\cdots$Ar’ (Fig. 5.10), has the highest charge density at saddle points of all intermolecular bonds in the described system. As in the previous example, the hydrogen atom lies closer to (3,+1) critical point than to any of carbon atoms constituting the phenyl ring (Fig. 5.12b). Values of second derivatives vary with direction, λ_1 taking value of -0.15 eÅ^{-5} due to the contact being slightly off phenyl ring centre and no adjacent atoms of same molecule outside of Ar’^{iii} plane. On the other hand, λ_2 indicates a less well localized bond in perpendicular direction with its value -0.08 eÅ^{-5}. This is caused primarily by H12^{iii} atom being equally close to C10 and C13 atoms, as well as - to much smaler extent - by the directly adjacent H11 atom. Last eigenvalue, λ_3 is again one of highest of all intermolecular contacts present in the system described. Overall, this is an interesting case of a part electrostatic, part dispersive C—H$\cdots\pi$ intermolecular bond, a class of interactions that has only recently garnered increased attention. The second C—H$\cdots\pi$ bond present is also well oriented, with C13^{iii}-H13^{iii}-CP$_{C8-C9}$ angle measuring 147.7°. This favourable orientation is, however, not followed by equally favourable separation. With H13^{iii}-CP$_{C8-C9}$ distance value of 2.916 Å, the

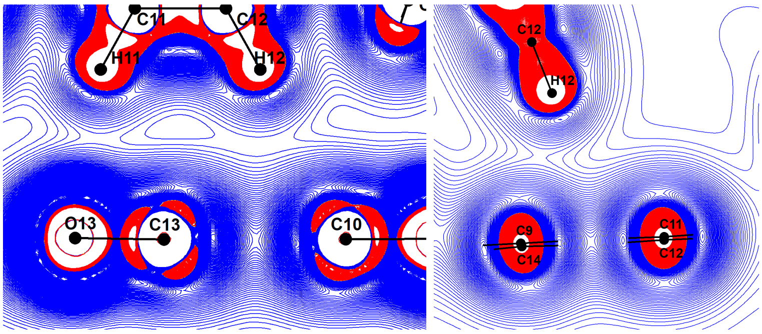

(a) H12$^{iii}\cdots\pi$(Ar') and H11$^{iii}\cdots$O13 bonds, in Ar'^{iii} plane (b) H12$\cdots\pi$(Ar') bond, across Ar'^{iii} plane

Fig. 5.11 Laplacian maps of H12$^{iii}\cdots\pi$(Ar') and H11$\cdots$O13 bonds. Isovalues every 0.1 eÅ^{-5}, blue: positive, red: negative.

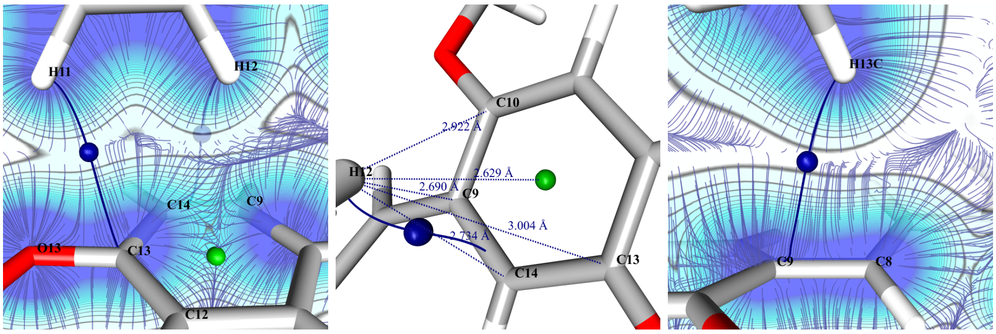

(a) Electron density gradient lines around CP 3 and CP 11 (b) Distances between ring CP, selected ring atoms and H12 (c) Electron density gradient lines around CP 18

Fig. 5.12 CH$\cdots\pi$ bonds between H11^{iii}, H12^{iii}, H13C^{iii} and delocalised π bonds of **8**.

electrostatic compound probably takes precedence over dispersion forces. A classic weak C—H$\cdots$O hydrogen bond is found between H11^{iii} and O13 atoms. As it happens, this contact is not explicitly listed in automated topological analysis results. Despite the clear attractive electrostatic interaction between oxygen atom's exposed negatively charged surface and hydrogen atom's positive region (angle of 158.1°) present, as well as bond-indicating interatomic distance of 2.63 Å, the bond is nowhere to be found in charge density distribution analysis output. This is caused by the neighbouring C9 atom, which is part of molecule's delocalised system, having more diffuse electron cloud across the contact plane (Fig. 5.12a). The effect can be directly attributed to π orbitals of C9. While there certainly do exist some dispersion effects between C9 and H11^{iii}, yielding them precedence over electrostatic effects of immediately adjacent O13 atom would be a mistake. Such cases serve as a gentle reminder that topological

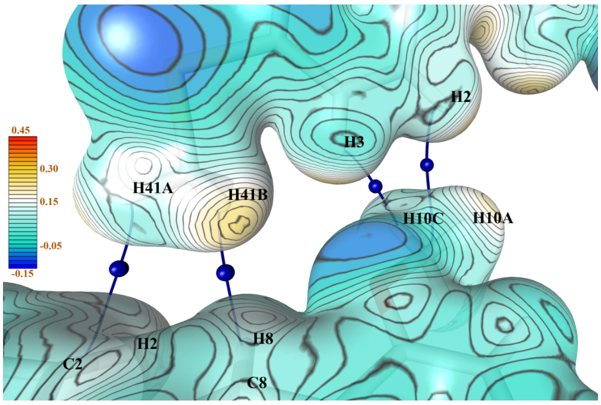

Fig. 5.13 (3,-1) critical points on contacts with -x+$^3/_2$,y+½,z+½ symmetry mate

features represent only a portion of the overall picture. Researchers must use their judgment to determine the significance of this portion within the research process.

Similar topology is found for weak hydrogen bond O1$\cdots$H3^{iv}, (^{iv} meaning -x+$^3/_2$,y+½,z+½, Fig. 5.13). In this case, however, the competing topological feature is much closer to the H3^{iv} hydrogen atom (Fig. 5.14a). The distance O1-H3^{iv} measures 2.62 /Å, which in itself would be enough to classify the interaction as weak electrostatic. In itself, this would yield electron density at CP of around 0.02 eÅ^{-3}. The nearby H10C atom forms a H10C$\cdots$H3^{iv} binding contact through dispersion forces, with $\rho(\mathbf{r})$ at CP of 0.048 eÅ^{-3} and $\nabla^2\rho(\mathbf{r})$ of 0.71 eÅ^{-5}. This obscures expected electrostatic forces based binding with oxygen atom (Fig. 5.14a). Two additional close H$\cdots$H contacts were found, namely H2$\cdots$H41A^{iv} and H8$\cdots$H41B^{iv}. The former was found to have charge density of 0.036 eÅ^{-3} at critical point, the latter 0.041 eÅ^{-3}. While H8$\cdots$H41B^{iv} falls within expected range of values for its length of 2.434 Å, bond H2$\cdots$H41A^{iv} exceeds found value expectations in context of its rather large separation measuring 2.734 Å. These results were confirmed with wavefunction based (ωB97M-V def2-TZVPD) topological analysis, where H2$\cdots$H41A^{iv} has also proven to possess comparatively large electron density value at critical point. Further analysis concluded that the most probable cause for such quality is sharp C2-H2-H41A^{iv} angle of 88.2°, partly exposing the methyl hydrogen to carbon atom electron cloud.

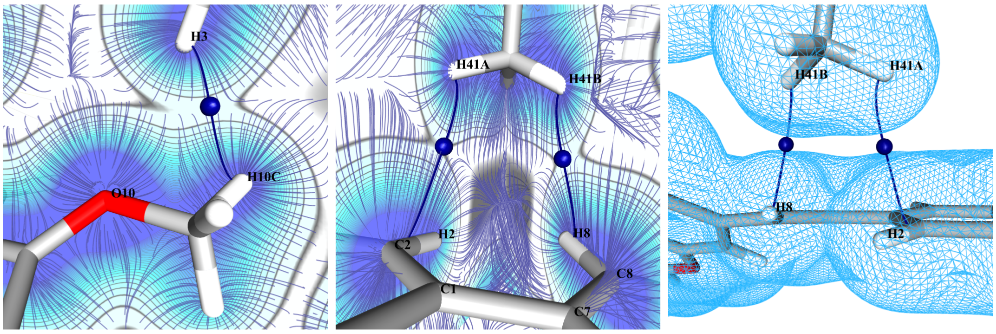

(a) Electron density gradient lines around H3...O10 hydrogen bond

(b) Electron density gradient lines around thiomethyl group and neighbouring conjugated aromatic system

(c) Electron density gradient isocontour mesh at 0.05 eÅ^{-3} near contact points

Fig. 5.14 Contact details of selected $-x+\frac{3}{2},y+\frac{1}{2},z+\frac{1}{2}$ hydrogen atoms.

5.4 Summary

A variety of intermolecular contacts was analyzed and described. With no strong hydrogen bond donors, only weak interactions could be formed in molecular crystal. Of these, CH$\cdots\pi$ weak hydrogen bonds were found a prominent feature of the analyzed system. Many of intermolecular bonds found possessed slightly higher electron density at saddle points than expected. This can be partly attributed to the presence of ring activating groups in the studied compound. A novel approach to multipolar model refinement was successfully employed, allowing to obtain physically meaningful, precise model from imperfect data set.

5.5 Experimental data

Data collection

A colorless crystal with dimensions 0.3 × 0.25 × 0.2 mm was used for data collection at 100 K on an Rigaku OD XCalibur EOS four circle κ-cradle diffractometer, equipped with the Sapphire CCD detector and the graphite-monochromated MoKα radiation (λ = 0.71073 Å). Temperature was controlled using an Oxford Instruments Cryosystem cooling device. Integration of the reflection intensities and data reduction were carried out with CrysAlis PRO. Data sorting and merging was performed with

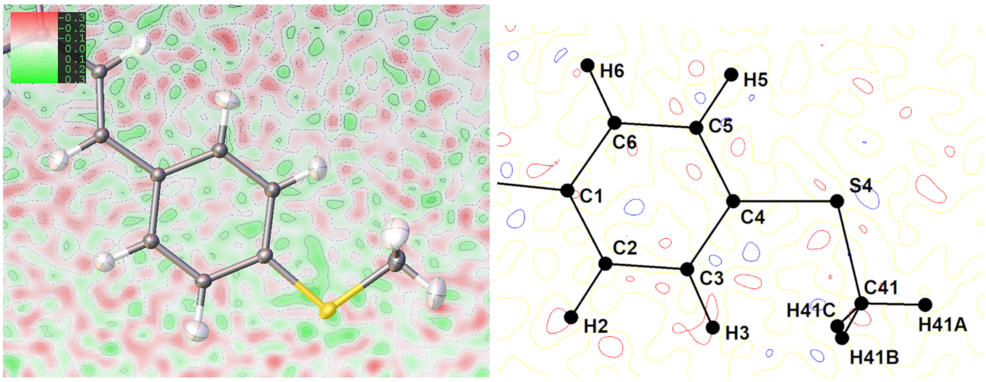

(a) After HAR procedure. Green: positive values, red: negative. Isovalues at 0.1eÅ^{-3}.

(b) After MM refinement in MoPro. Blue: positive values, red: negative. Isovalues at 0.05eÅ^{-3}.

Fig. 5.15 Residual density of **8** around Ar—SMe moiety at different steps of non spherical refinement

WinGX suite (v 1.80.05) [37] sortmerge tool. Hirshfeld surface analysis was performed with Crystal Explorer.

Crystal data: $C_{20}H_{16}N_2OS_2$, M_r = 364.47, triclinic $P\bar{1}$, a = 9.2605(8)Å, b = 10.5797(12)Å, c = 10.7704(15)Å, α = 60.921(10)°, β = 85.569(12)°, γ = 65.892(9)°, V = 831.98(18)Å^3 , Z = 2, F(000) = 380, d_x = 1.46 g/cm, (MoKα) = 0.33 mm^{-1}. A total of 82911 reflections collected up to $2\theta = 135°$ ($\sin(\theta/\lambda) = 1.31$Å^{-1}), of which 28749 were symmetry-independent (R_{int} = 2.30%), 18907 with $I > 2\sigma(I)$. Overall completeness 93.8%, mean redundancy 2.9.

Refinement

The crystal structure was initially solved using SHELXT2014 and standard Independent Atom Model (IAM) refinement was performed using SHELXL2014. Non-H atoms were refined anisotropically; H atoms positions were found in the difference Fourier maps and isotropically refined. Final residuals for for this step: for I > 2σ(I) R = 2.2%, wR2 = 6.0%, S = 1.05. Max/min $\Delta\rho$ values in the final ΔF map 0.33/-0.29 eÅ^{-3}, located on the covalent bonds. Data quality proved insufficient for immediate charge density refinement in MoPro software.

To improve the multipolar refinement starting point, the model obtained from SHELXL2014 was imported into Olex2 software [117]. Atomic positions and thermal parameters were subsequently refined with no restraints applied, using Hirshfeld atom refinement procedure [118, 119], with no restraints defined: The molecular wavefunction was calculated using Orca 5.0.4[110, 111], with R^2SCAN [120] functional and def2-TZVP basis set [121, 121]. Atomic non-spherical form factors were extracted by Hirshfeld partitioning using NoSpherA2 [122, 123]. Obtained non-spherical form factors were then used by Olex2 for next least-squares refinement cycle. During Hirshfeld atom refinement, hydrogen atoms' thermal parameters were refined anisotropically. Final residuals for for this step: for all reflections R = 5.2%, wR2 = 3.8%, for $I > 2\sigma(I)$ R = 2.92%, wR2 = 3.39%, S = 1.01. Max/min $\Delta\rho$ values in the final ΔF map 0.292/-0.273 $e\text{Å}^{-3}$, with residual density featureless and randomly distributed throughout the cell.

Obtained structure was imported into MoPro software[46, 47]. Scale factors were refined at different polynomial levels, determining the quadratic scale factor function to be optimal. The model was then refined incrementally, with each consecutive stage following the same general procedure of consecutive looped least squares refinements against the following parameters:

- scale factors
- valence population
- multipolar population
- expansion/contraction coefficients
- anharmonic motion coefficients of S4[1]

Each of stages, as the model improved, had generally fewer constraints and restraints applied. The final set of constraints and restraints are attached in Section A.3 Final residuals for for this step: Max/min $\Delta\rho$ values in the final ΔF map 0.481/-0.363 $e\text{Å}^{-3}$, with residual density featureless and randomly distributed throughout the cell.

In silico studies

Torsion angle energy calculation was performed by dividing **8** into three sections, as depicted on Fig. 5.16. Coordinates of each section were internally constrained.

---

[1] anharmonic parameters refinement was only included at later stages, when almost-featureless residual density maps indicated such necessity

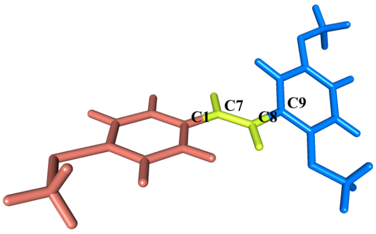

Fig. 5.16 Constrained sections of **8** for torsion angle energy cost assessments

Distances C1-C7 and C8-C9 were constrained to initial values, so that the possible minute changes in bond length do not drown out conformation change energies. Density functional theory (DFT) calculations were carried out using ORCA v.5.0.4 [110, 111, 124] with resources provided by the Wrocław Centre for Networking and Supercomputing (BEM2). We gratefully acknowledge Polish high-performance computing infrastructure PLGrid (HPC Centers: WCSS) for providing computer facilities and support within computational grant no. PLG/2024/017342. Contact energies calculated for Table 5.3 were carried out with counterpoise correction applied according to procedure described in section 8.1.6 of ORCA manual. Topological analysis of obtained wavefunction was carried out using MultiWfn software [125, 126].

5.6 Supplementary information

LUMO orbitals were rendered in IboView software [127]. Hirshfeld surface presented in **??** were calculated using CrystalExplorer v.21.5 with its bundled Tonto software [44, 128]. Calculations for electrostatic potential surface mapping was performed using B3LYP functional and cc-pVTZ basis set.

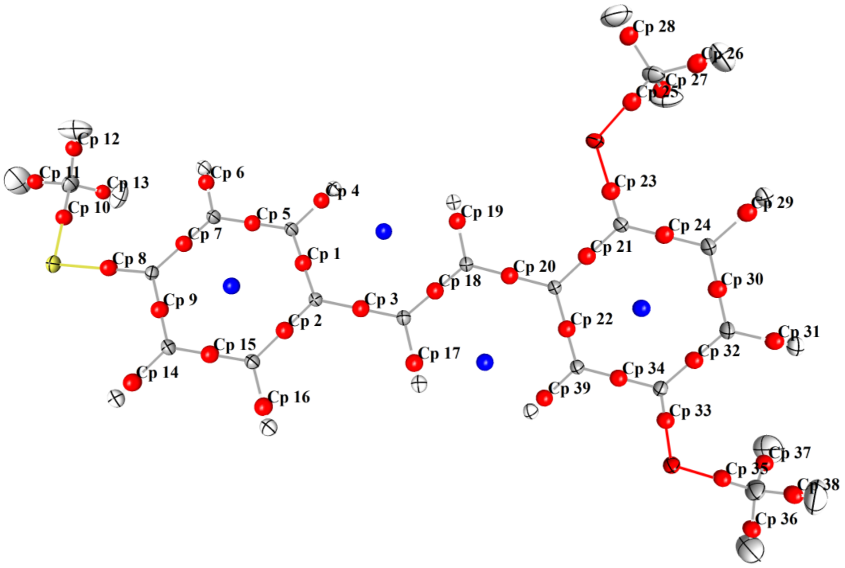

Fig. 5.17 Visualisation of (3,-1) bond critical points (red) and intramolecular (3,+1) ring critical points (blue) of **8**. Thermal ellipsoids reduced to 25% probability for visual clarity

Table 5.4 List of (3,-1) intramolecular critical points in **8**

	Atom1	Atom2	distance, Å	$\rho(\mathbf{r})$, eÅ^{-3}	$\nabla^2\rho(\mathbf{r})$, eÅ^{-5}	λ_1	λ_2	λ_3	Gcp	Vcp	ε
1	C1	C2	1.402	2.103	-16.75	-16.79	-13.84	13.88	0.295	-0.765	0.21
2	C1	C6	1.403	2.092	-16.50	-16.55	-13.76	13.82	0.294	-0.758	0.20
3	C1	C7	1.463	1.818	-13.31	-13.24	-11.74	11.68	0.231	-0.599	0.13
4	C2	H2	1.082	1.724	-16.80	-16.61	-15.90	15.71	0.179	-0.533	0.05
5	C2	C3	1.390	2.141	-19.34	-15.97	-13.39	10.03	0.290	-0.781	0.19
6	C3	H3	1.083	1.752	-18.25	-16.55	-15.69	13.99	0.177	-0.544	0.06
7	C3	C4	1.397	2.122	-18.85	-16.04	-13.20	10.39	0.287	-0.770	0.22
8	S4	C4	1.760	1.391	-4.52	-8.88	-8.01	12.36	0.175	-0.397	0.11
9	C4	C5	1.398	2.122	-18.44	-15.98	-12.98	10.52	0.290	-0.771	0.23
10	S4	C41	1.798	1.286	-4.27	-7.41	-7.27	10.41	0.152	-0.348	0.02
11	C41	H41A	1.082	1.747	-14.37	-16.24	-15.93	17.80	0.203	-0.554	0.02
12	C41	H41B	1.086	1.734	-14.07	-16.16	-15.78	17.87	0.201	-0.548	0.02
13	C41	H41C	1.074	1.774	-15.49	-16.63	-16.36	17.50	0.203	-0.566	0.02
14	C5	H5	1.082	1.756	-18.36	-16.60	-15.73	13.98	0.178	-0.546	0.06
15	C6	C5	1.387	2.149	-19.58	-16.06	-13.47	9.95	0.291	-0.785	0.19
16	C6	H6	1.083	1.725	-16.83	-16.63	-15.90	15.70	0.179	-0.533	0.05
17	C7	H7	1.083	1.715	-17.37	-15.63	-14.91	13.17	0.173	-0.525	0.05
18	C8	C7	1.345	2.284	-22.73	-17.31	-13.26	7.84	0.315	-0.865	0.31

continued on next page

continued from previous page

	Atom1	Atom2	distance, Å	$\rho(\mathbf{r})$, eÅ^{-3}	$\nabla^2\rho(\mathbf{r})$, eÅ^{-5}	λ_1 ,eÅ^{-5}	λ_2 ,eÅ^{-5}	λ_3 ,eÅ^{-5}	Gcp	Vcp	ε
19	C8	H8	1.082	1.719	-17.42	-15.68	-14.98	13.23	0.173	-0.528	0.05
20	C9	C8	1.463	1.845	-14.29	-13.08	-11.82	10.62	0.232	-0.612	0.11
21	C9	C10	1.410	2.094	-16.80	-16.23	-13.46	12.89	0.292	-0.759	0.21
22	C9	C14	1.394	2.181	-19.40	-16.80	-13.80	11.21	0.303	-0.807	0.22
23	O10	C10	1.369	1.961	-11.40	-14.93	-14.02	17.55	0.287	-0.693	0.07
24	C10	C11	1.389	2.156	-18.89	-16.59	-13.31	11.01	0.298	-0.792	0.25
25	C101	O10	1.419	1.667	-8.89	-10.86	-10.74	12.71	0.218	-0.528	0.01
26	C101	H10A	1.068	1.803	-13.92	-17.04	-16.32	19.43	0.222	-0.588	0.04
27	C101	H10B	1.076	1.807	-13.69	-17.30	-16.26	19.87	0.225	-0.591	0.06
28	C101	H10C	1.075	1.840	-14.55	-17.89	-16.87	20.21	0.229	-0.608	0.06
29	C11	H11	1.082	1.748	-17.81	-16.28	-15.71	14.18	0.179	-0.543	0.04
30	C11	C12	1.400	2.139	-20.05	-15.68	-13.62	9.25	0.284	-0.777	0.15
31	C12	H12	1.082	1.748	-17.80	-16.47	-15.50	14.18	0.179	-0.543	0.06
32	C12	C13	1.391	2.191	-19.53	-16.90	-13.66	11.04	0.305	-0.813	0.24
33	C13	O13	1.370	2.026	-12.98	-16.00	-15.09	18.12	0.297	-0.728	0.06
34	C13	C14	1.394	2.158	-18.77	-16.49	-13.79	11.51	0.300	-0.794	0.20
35	O13	C131	1.415	1.677	-9.28	-10.98	-10.75	12.45	0.218	-0.532	0.02
36	C131	H13A	1.071	1.854	-14.89	-18.11	-17.02	20.23	0.230	-0.615	0.06
37	H13B	C131	1.057	1.839	-14.81	-17.34	-16.89	19.42	0.226	-0.607	0.03

continued on next page

continued from previous page

	Atom1	Atom2	distance, Å	$\rho(\mathbf{r})$, eÅ^{-3}	$\nabla^2\rho(\mathbf{r})$, eÅ^{-5}	λ_1 ,eÅ^{-5}	λ_2 ,eÅ^{-5}	λ_3 ,eÅ^{-5}	Gcp	Vcp	ε
38	H13C	C131	1.100	1.731	-11.93	-16.10	-15.58	19.75	0.215	-0.553	0.03
39	C14	H14	1.083	1.752	-18.06	-16.55	-16.29	14.78	0.178	-0.544	0.02

Atom1	Atom2	symmetry mate	$\rho(\mathbf{r})$, eÅ^{-3}	$\nabla^2\rho(\mathbf{r})$, eÅ^{-5}	λ_1 ,eÅ^{-5}	λ_2 ,eÅ^{-5}	λ_3 ,eÅ^{-5}
H7	H14	x,y,z	0.083	1.04	-0.221	-0.191	1.457
H2	H18	x,y,z	0.077	0.96	-0.233	-0.232	1.426
π(C9…C14 ring)	H12	-x+1,-y+2,z-½	0.058	0.69	-0.156	-0.078	0.927
π(C9…C14 ring)	H6	x,y,1+z	0.056	0.59	-0.097	-0.055	0.746
π(C3—C4)	H14	-x+1,-y+1,z-½	0.049	0.64	-0.114	-0.070	0.820
H10C	H3	3/2⁄-x,y-½,z-½	0.048	0.71	-0.152	-0.111	0.974
S4	H10C	-x+½,y+½,z+½	0.048	0.53	-0.092	-0.091	0.715
π(C1…C7)	H5	-x+1,-y+1,z+½	0.046	0.52	-0.105	-0.064	0.688
C8	H5	x,y,1+z	0.043	0.51	-0.115	-0.073	0.699
H8	H41B	-x+3⁄2,y+½,z+½	0.041	0.51	-0.123	-0.121	0.751
O13 (C9)	H11	-x+1,-y+2,z-½	0.040	0.54	-0.079	-0.029	0.643
O13	H41C	-x+1,-y+1,z+½	0.038	0.70	-0.127	-0.118	0.946
S4	H7	-x+1,-y+1,z-½	0.036	0.40	-0.074	-0.065	0.537
H2	H41A	-x+½,y+½,z+½	0.036	0.43	-0.083	-0.079	0.594
π(C3—C4)	H13A	x+½,-y+3⁄2,z-1	0.031	0.42	-0.067	-0.018	0.501
H2	H10A	-x+3/2⁄,y-½,z-½	0.029	0.39	-0.063	-0.025	0.479
π(C1)	H10B	x,y,z-1	0.028	0.38	-0.063	-0.023	0.462
π(C8—C9)	H13C	-x+1,-y+2,z-½	0.026	0.35	-0.054	-0.019	0.419
H13B	H41A	-x+1,-y+1,z+3⁄2	0.024	0.38	-0.071	-0.045	0.497
H13C	H41B	x-½,3/2⁄-y,z+1	0.024	0.36	-0.068	-0.028	0.458
H10C	H13A	x+½,-y+½,z	0.018	0.27	-0.034	-0.021	0.324
O13	H3	-x+1,-y+1,z+½	0.017	0.23	-0.021	-0.003	0.249
S4	H2	x,y,z-1	0.015	0.20	-0.036	-0.026	0.266
C41-H41C	H10A	x,y-1,z-1	0.012	0.19	-0.030	-0.017	0.237
C101	C131	-x+1,-y+2,z+½	0.011	0.15	-0.015	-0.007	0.174
H11	H41C	x,y+1,z+1	0.008	0.11	-0.014	-0.007	0.133

Table 5.5 Symmetrically independent (3,-1) non covalent critical points found in molecular crystal of **8**

Chapter 6

1,4-diazabicyclo[2.2.2]octane

6.1 Introduction

Compound 1,4-diazabicyclo[2.2.2]octane (**18**), usually referred to as DABCO, is a bicyclic highly symmetric organic compound with practical use as a nucleophilic catalyst. It is used on industrial scale in polyurethane formation, as well as other reactions with carbon electrophile as one of substrates: Baylis–Hillman reaction [129, 130], azirines substitution [129, 131], Knoevenagel Condensation [130, 132], functional groups protection and deprotection [133, 134], and many others [129, 133–136]. In these reactions, DABCO serves the role of an efficient nucleophilic catalyst: the $\mathrm{p}K_a$ of conjugate acid $[\mathrm{HDABCO}]^+$ is comparable to acyclic tertiary amines, however the compound's specific constitution limits negative effects of steric hindrance on reactivity. In effect, the compound is more effective as a nucleophilic base than most tertiary amines. The reactions catalysed by **18** reach excellent yields and high selectivity, with some successful tries in catalyst reusability. Recently, DABCO has received interest as base for ionic liquids, including chiral substituted compounds for stereoselective synthesis [132, 137–140]. As a low-cost, easy to synthesize, environmentally friendly catalyst DABCO fully deserves its ongoing popularity.

The resulting synthetic popularity has an effect of DABCO's crystallographic structure being determined hundreds of times in temperatures ranging from 343 K down to 80 K [141, 142], very often through inadvertent catalyst cocrystallisation.

Despite compound's nigh ubiquity, direct studies of molecule's supramolecular features – either directly or as part of mechanistic investigations – are scarce.

6.2 Structure

Compound **18** crystallized in a highly symmetrical space group $P6_3/m$. The implied threefold axis, resulting from a sixfold inversion axis of this space group, corresponds perfectly to molecule's own threefold symmetry of three structurally equal, two-carbon alkyl fragments. The nitrogen atoms are positioned directly on the $\overline{6}$ rotation axis, with mirror plane intersecting carbon-carbon bonds. The inherent symmetry of studied organic compound is thus reflected in high crystal symmetry, with rotoinversion centre placed in the middle of structure and asymmetric unit consisting of only ⅙th of whole molecule. Of course, space group $P6_3/m$ implies twelve symmetric operations – whilst **18** contains only 6 carbon atoms. Unit cell of analyzed crystal contains two molecules, satisfying the mathematical constraints on the system. High internal symmetry, nitrogen atom positioning directly on an infrequently occurring symmetry element, the resulting odd multiplicity and asymmetric unit binding with itself in multiple locations had all put a strain on used tools, adding to the usual pitfalls of multipolar refinement.

Found bond lengths and angles are in agreement with previously determined for this structure [143–147]. The highly nucleophilic nitrogen atoms, which granted the substance its wide popularity among syntheticists, create prominent features on the molecule's electrostatic potential map. The most defining quality of **18** – chemical constitution facilitating access to nitrogen atoms – is quantifiable as share of intra-surface nitrogen atoms share in total Hirshfeld surface area. The value is exceptionally high for **18** when compared to other tertiary amines with no constitutional constraints on amine conformation (see Table 6.1). For other chemically similar compounds, conformational preference towards *anti* conformation causes hydrogen atoms of second nearest carbon atom orient along the same axis as the nucleophilic lone pair and restrict the nitrogen atom's lone pair exposition. Structural restrictions present in five membered rings of **19** limit this effect, making its nitrogen atoms significantly more exposed than those present in six membered rings of **21**.

compound	structure	share of nitrogen compound mass	 Hirshfeld surface
18	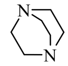	25.0%	6.8%
19 [148]	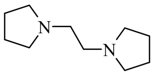	16.6%	2.9%
20 [149]	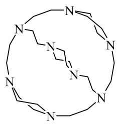	25.0%	2.3%
21 [150]	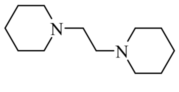	14.3%	1.9%
22 [151]	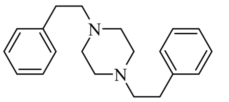	9.5%	1.5%
23 [152]	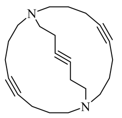	8.6%	1.3%
24 [153]	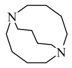	14.3%	0.0%
25 [154]	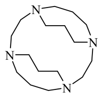	20.0%	0.0%

Table 6.1 Comparison of nitrogen atom exposure in selected crystal structures. Share in Hirshfeld surface defined as S_{d_i}/S_{tot}, where d_i is the distance from the surface to the nearest nucleus internal to the surface.

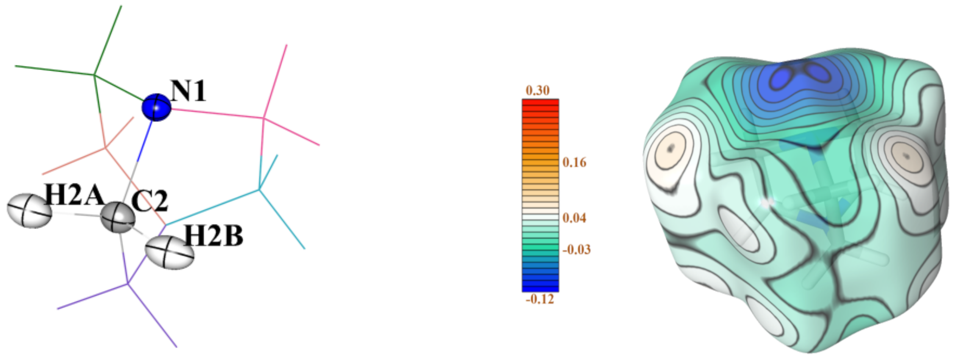

(a) (b)

Fig. 6.1 Molecular structure of **18**.
Fig. 6.1a: Measured structure. Thermal ellipsoids drawn for 50% probability, with relevant symmetry mate coloured by chemical species. Each other symmetry equivalent marked with distinct colour.
Fig. 6.1b: Electrostatic potential values mapped on MM-based Hirshfeld surface

Due to high internal symmetry, a complete list of symmetrically independent (3,-1) bond critical points of **18** contains only four entries. Measuring 1.556 Å, the carbon—carbon bond is slightly elongated when compared to C_α—C_β bond lengths from compounds listed in Table 6.1. This value falls in the middle of the range of distances found in previously published diffraction data. Of course, in case of molecule studied no β carbon atom is present; the measured value corresponds to a case of a $C2_\alpha$—$C2_\alpha{}^m$ bond. It is tempting to explain the increased distance with the repulsive effect of positive partial charges on C_α atoms; however, such charges interaction is present also in the structures of **19**, **20** (which also possesses exclusively C_α atoms), **21**, and **22**. Most of the above do not experience bond elongation; in fact, only a fraction of those found in **20** do. Despite different inherent partial charge distribution, C—C bond elongation is found in **24**. The common characteristic found between the elongated bonds of **18**, **20**, and **24** relates to spatial orientation: all are oriented in *anti* orientation in relation to nitrogen atom's lone pair. Similar lengths found in analogous compounds, as well as C—C bond length measuring 1.562 Å in gas phase [69], conclusively exclude the possibility of systemic error present in compound's structures deposited in CSD.

	distance, Å	$\rho(\mathbf{r})$, eÅ^{-3}	$\nabla^2\rho(\mathbf{r})$, eÅ^{-5}
N1—C2	1.4715	1.751	-13.95
C2—H2A	1.0687	1.687	-14.73
C2—H2B	1.0703	1.705	-15.61
C2—C2^m	1.5559	1.622	-10.82

Table 6.2 Unique intramolecular bond critical points in **18**. Superscript *m* denotes symmetry equivalent x, y, -z+½ (generated by internal mirror plane)

6.3 Intermolecular contacts

Fitting the symmetry patterns, **18** is surrounded by a total of 12 symmetry mates in its crystal lattice. Packing pattern closely resembles hexagonal close-packing. The studied compound is, of course, not perfectly spherical; the effects of molecule's shape on packing lower the symmetry from $P6_3/mmc$ to $P6_3/m$. The relatively usual number of neighbouring molecules translates to formed bond paths count. However, they are almost all symmetrically equivalent. Ultimately, the list of unique intermolecular (3,-1) bond critical points (Table 6.3) comprises a total of three entries: one weak hydrogen bond and two hydrogen$\cdots$hydrogen contacts.

The weak hydrogen bond N1$\cdots$H2B^i measures 2.709 Å in length, with three instances found per each nitrogen atom (symmetry equivalent *i*: -x+2, -y+1, -z). A near perfect tetrahedron is formed by these polar interactions, with N1 atom at the triangular pyramid tip and three H2B atoms at pyramid base corners. The deviation from platonic solid's geometry is minimal: H2B^i-N1-H2B^i*ii* angles measure 60.5°, while the base angle N1-H2B^i-H2B^i*ii* measures 59.7° (*iii*: y, -x+y+1, -z). Pyramid base lengths are longer than the hydrogen bond, measuring 2.730 Å. This is to be expected, as two hydrogen atoms are by all means equal and can only attract each other through London forces, over an order of magnitude weaker than even a weak hydrogen bond. Tetrahedral spatial configuration of intermolecular contacts positions the nitrogen lone electron pair along the pyramid axis. The three hydrogen atoms are bound by attractive forces competing with each other, and balanced by van der Waals repulsion between the attracted molecules (as well as the fourth one positioned at apical vertex). In effect, all form a bond at suboptimal geometry, with C2^i-H2B^i-N1 and C2-N1-H2B^i angles measuring 146.4° and 145.8°, respectively. This geometry

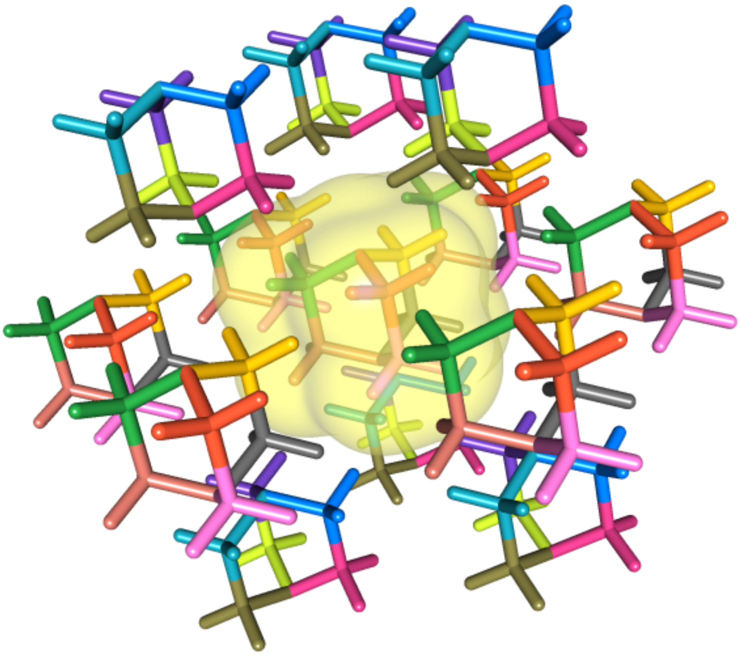

Fig. 6.2 Symmetry mates of **18**. Each symmetry equivalent marked with unique colour.

causes the BCP electron density having value of 0.045 eÅ^{-3}, which is relatively low for this kind of interaction.

The contact H2B$\cdots$H2B^{i}, despite having almost as high value of $\rho(\mathbf{r})$ as the weak hydrogen bond, should be regarded as repulsive. The (3,-1) bond critical point is positioned between two (3,+1) CPs, with inter-CP distance measuring 0.25 Å. Moreover, charge density at these ring critical points is merely 1% lower than the 0.042 eÅ^{-3} found at bond critical points. Hessian matrix eigenvalues are also very similar, with both λ_3 and λ_1 differing by 1%. The values of λ_2 differ, of course, in sign, however either has $|\lambda_2|$ value lower than 0.02 eÅ^{-5}. As one might expect, the ellipticity value of this BCP is very high. This is a typical characteristic of hydrogen atoms contacting sideways at close range. Indeed, the C2-H2B-H2B^{i} angle of these atoms contacting across a point of symmetry measures 106.6°.

In the described crystal lattice, only a single type of bond path is found between molecules positioned along same (0,0,1) plane. Fittingly to the space group, the molecule forms a total of 12 instances of such interactions with neighbours. The contact in question, H2A$\cdots$H2A^{ii} (*ii*: -x+y+1,-x+2,z) is formed between these two

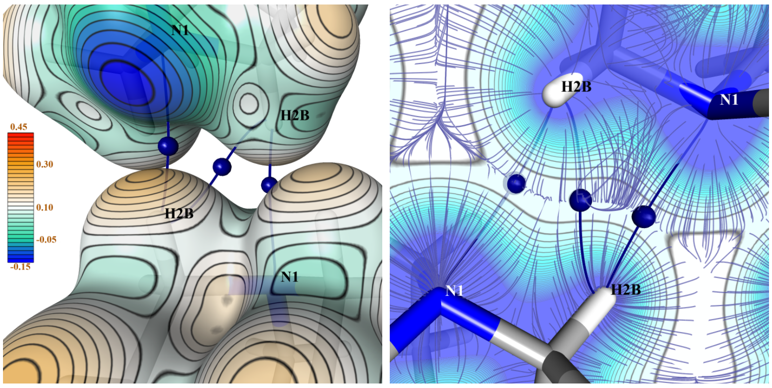

(a) Electrostatic potential (eÅ^{-1}) mapped over the ED isosurface of 0.1 eÅ^{-3}

(b) Electron density gradient lines on contact plane

Fig. 6.3 BCPs found for contacts with -x+2, -y+1, -z symmetry mate.

	distance, Å	$\rho(\mathbf{r})$, eÅ^{-3}	$\nabla^2\rho(\mathbf{r})$, eÅ^{-5}
N1···H2B^{i}	2.709	0.045	0.61
H2B···H2B^{i}	2.568	0.042	0.50
H2A···H2A^{ii}	2.537	0.034	0.43
N1···$_{IAM}$H2B^{i}	2.709	0.058	0.64
H2B···$_{IAM}$H2B^{i}	2.568	0.055	0.54
H2A···$_{IAM}$H2A^{ii}	2.537	0.051	0.47
H2B···$_{IAM}$H2B^{ii}	2.537	0.030	0.28

Table 6.3 Unique intermolecular bond critical points in **18**

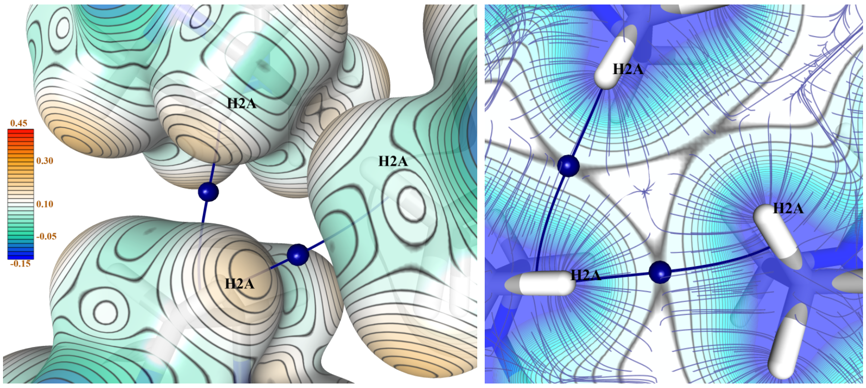

(a) Electrostatic potential (eÅ^{-1}) mapped over the ED isosurface of 0.1 eÅ^{-3}

(b) Electron density gradient lines on contact plane in the area of H2A$\cdots$H2A^{ii} contact

Fig. 6.4 Details of H2A$\cdots$H2A^{ii} contact

atoms mostly *de nomo*: in practice, the C2—H2A bond lies on almost exactly the same plane parallel to *c* axis as N1^{ii}—C2^{ii} bond does. The small deviation from perfect alignment makes the H2A-H2A^{ii} distance slightly shorter than H2A-H2B^{ii}, namely 2.537 Å for the former compared to 2.726 Å for the latter. While atoms H2B and H2B^{ii} could qualify as a contact judging by the interatomic distance of 2.730 Å alone, the charge density does not form saddle points between them. In fact, the area is almost entirely depleted of electrons. Such stark difference partly stems in hydrogen pseudoatoms having their dipoles along z axis take values directing electron density towards the bound atom. Of course, also in IAM the charge density values fall faster at the extension of C—H bond axis comparing to lateral change. In the case of studied system, the difference between IAM and MM is enough to create a "phantom" BCP between H2B and H2B^{ii} with $\rho(\mathbf{r})$ measuring 0.030 eÅ^{-3}. This seems comparable to 0.034 eÅ^{-3} density at BCP of H2A$\cdots$H2A^{ii} contact in MM model, however this would be a fundamentally flawed comparison. IAM does not account for orbital contraction nor change transfer in any way other than C—H bond length shortening, which of course will not be present in an IAM based off MM coordinates.

A series of single point energy calculations for dimolecular systems basing on crystallographically determined atomic coordinates of **18** was performed. The data obtained *in silico* is in good agreement with these determined using multipolar model. An interesting correlation is found when analysing the intermolecular BCPs: for dispersive interactions, the level of agreement between crystallographic and computed

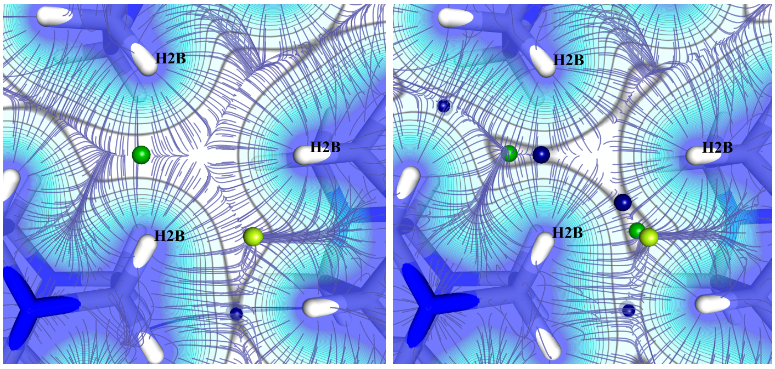

(a) Multipolar model. The (3,+1) CP is positioned 0.2 Å above contour plane; the (3,+3) CP 0.4 Å above contour plane.

(b) Independent atom model. The (3,+1) CP is positioned in contour plane; the (3,+3) CP 0.4 Å above contour plane.

Fig. 6.5 Electron density gradient lines in the electron poor area between H2B atoms as present in MM and IAM. (3,+1) CPs marked in green, (3,+3) CPs marked in lime. The blue (3,-1) BCP visible near the image edges are the H2A$\cdots$H2A^{ii} contacts depicted in detail on Fig. 6.4

values is primarily functional dependent; however, for the weak hydrogen bond the level of agreement is basis set dependent. The expected correlation puts functional as key source of differences in both topological analysis as well as calculated interaction energy. Of course, one must keep in mind that – as it historically were with London forces interaction energy corrections, on multiple occasions – a model might be "accidentally correct", that is correctly approximate a system by a serendipitous cancellation of calculation errors. Such is the case with H2A$\cdots$H2A^{ii} contacts where 6-31G(d,p), a somewhat simple basis set with no dedicated dispersion functions, performs marginally better than its dispersion-capable 6-31++G(d,p) counterpart. The effect is very subtle in intermolecular context and would have been considered an outlier, if not for interaction energies which follow the same trend with a much more pronounced difference. Here, the interaction energies are primarily functional dependent for *ii*-related contacts involving H2A and H2B atoms, and mixed – functional depenedent with the exception of 6-31++G(d,p) basis set, which certainly overestimates binding energy – for *i*-related contacts involving N1 and H2B atoms. In the specific case of **18**, functionals B3LYP, BP86, and PWPB95 have proved inadequate in modelling noncovalent interactions. These three yielded positive interaction energies for symmetry mates not involved in weak hydrogen bonding, and in case of BP86 and B3LYP also for the nitrogen

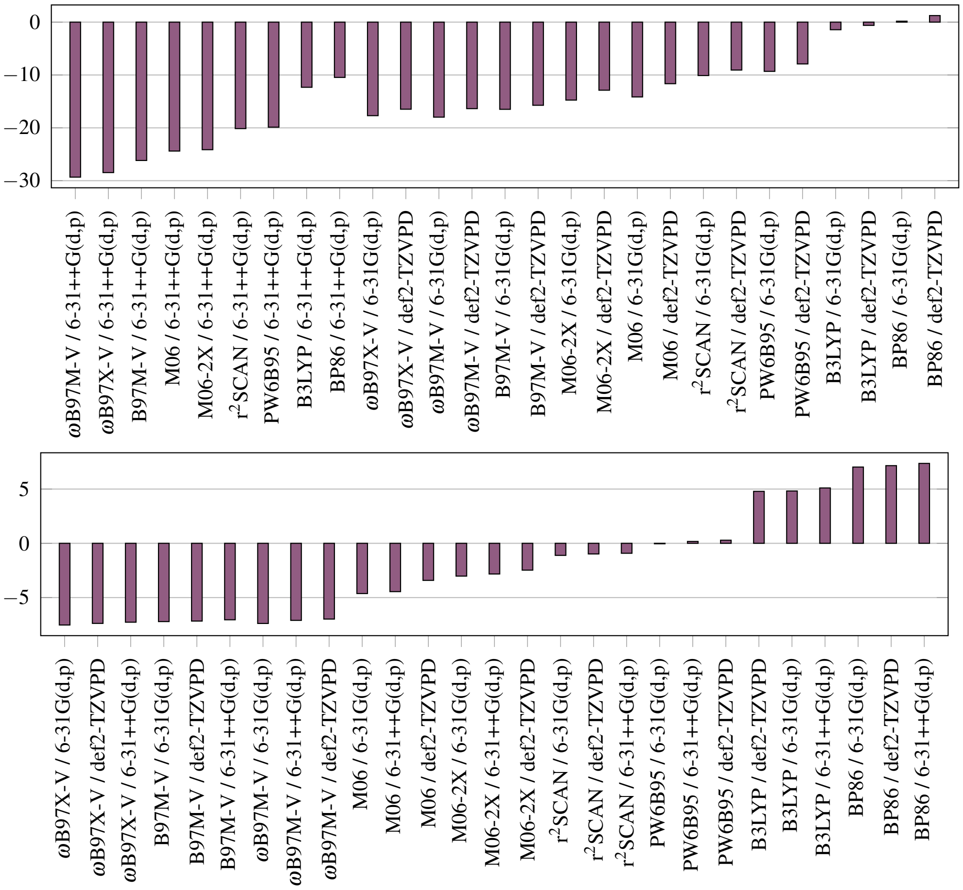

Fig. 6.6 Noncovalent interaction energies (kJ/mol) for either type of symmetry mates. Top: *i*-related, bottom: *ii*-related molecules.

involving interaction. This is, of course, not possible: were these interaction energies positive, the crystal would not form. The inadequacy of B3LYP and BP86 is not surprising: both are relatively simple and won their popularity decades ago, largely due to the cost/effect ratio offered. While GGA functional BP86 is nowadays much less common, hybrid B3LYP remains to be exceptionally popular. However, the result for double-hybrid functional PWPB95 was unexpected as it is regarded an adequate level of theory for all kinds of calculations, including noncovalent interactions [155, 156].

6.4 Summary

Structural characteristics of Chapter impacting its performance as a catalyst were analyzed and compared to analogous published structures. Excellent access to nucleophilic centre of **18**, a known feature of this versatile compound, was assessed quantitatively through these studies. Weak intermolecular interactions were described in detail, compared with results for independent atom model and with results of *in silico* studies. The performance of popular functionals and basis sets was compared against each other and against crystallographic data, with results for weakest of interactions going against the usual pattern. The highly symmetric nature of crystal lattice led to identifying several shortcomings in used computer programs, which thanks to active contact with software suite developers will allow for improving them for all users.

6.5 Experimental data

Refinement

The crystal structure was initially solved using SHELXT2014 and standard Independent Atom Model (IAM) refinement was performed using SHELXL2018/3 [157]. Non-H atoms were refined anisotropically; H atoms positions were found in the difference Fourier maps and isotropically refined. Final residuals for for this step: for all data wR2 = 10.1%, S = 1.1, R = 5.12%; for $F > 4\sigma(F)$ R = 3.3%. Max/min $\Delta\rho$ values in the final ΔF map 0.48/-0.21 $e\text{Å}^{-3}$, located on the covalent bonds. Data quality proved insufficient for immediate charge density refinement in MoPro software.

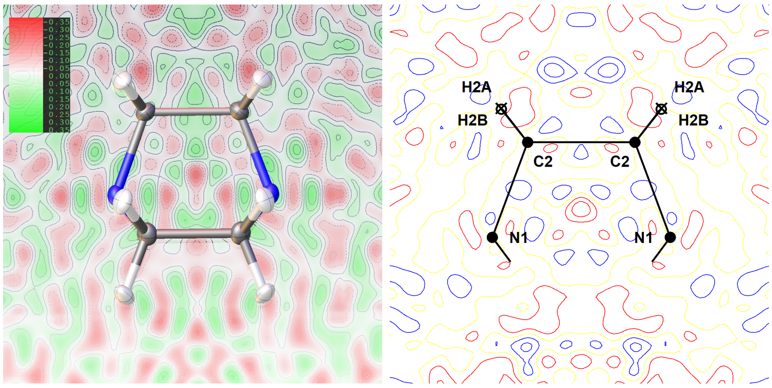

(a) Residual density of **18** as calculated by olex2 + NoSpherA2 Blue: positive values, red: negative. Isovalues at 0.05e^{-1}.

(b) Residual density of **18** after refinement by MoPro Blue: positive values, red: negative. Isovalues at 0.05e^{-1}. Resolution range: 0.00 → 1.05Å^{-1}

To improve the multipolar refinement starting point, the model obtained from SHELXL2018 was imported into Olex2 software [117]. Atomic positions and thermal parameters were subsequently refined with no restraints applied, using Hirshfeld atom refinement procedure [118, 119], with no restraints defined: The molecular wavefunction was calculated using Orca 5.0.4[110, 111], with ωB97X [158] functional and def2-TZVP basis set [121, 121]. Atomic non-spherical form factors were extracted by Hirshfeld partitioning using NoSpherA2 [122, 123]. Obtained non-spherical form factors were then used by Olex2 for next least-squares refinement cycle. During Hirshfeld atom refinement, hydrogen atoms' thermal parameters were refined anisotropically. Final residuals for for this step: for all reflections R = 3.8%, wR2 = 3.9%, for F > 4σ(F) R = 1.91%. Max/min $\Delta\rho$ values in the final ΔF map 0.242/-0.284 eÅ^{-3}, with residual density featureless and randomly distributed throughout the cell (Fig. 6.7a). Obtained structure was imported into MoPro software[46, 47]. Scale factor was left at the scalar level. The model was refined incrementally, with each consecutive stage following the same general procedure of consecutive looped least squares refinements against the following parameters: • scale factor • high-order refinement of positions and thermal coefficients for non-hydrogen atoms • full dataset refinement of hydrogen positions and anisotropic thermal coefficients of hydrogen atoms • valence populations • multipole populations • expansion/contraction coefficients . Each of stages, as the model improved, had generally fewer constraints and restraints applied. The final set of constraints and restraints are attached in Section A.4 Final residuals for this step: I $> 3.5\sigma$(I) RI = 2.76%, wR2I = 1.93%, S = 1.07. Max/min $\Delta\rho$ values in the final ΔF map 0.163/-0.167 $e\text{Å}^{-3}$, with residual density featureless and randomly distributed throughout the cell (Fig. 6.7b).

In silico studies

Density functional theory (DFT) calculations were carried out using ORCA v.5.0.4 [110, 111, 124] with resources provided by the Wrocław Centre for Networking and Supercomputing (BEM2) and Academic Computer Centre Cyfronet AGH (Ares). We gratefully acknowledge Polish high-performance computing infrastructure PLGrid (HPC Centers: ACC Cyfronet AGH, WCSS) for providing computer facilities and support within computational grant no. PLG/2024/017342. Contact energies calculated for Tables 6.6 and 6.8 were carried out with counterpoise correction applied according to procedure described in section 8.1.6 of ORCA manual. Topological analysis of obtained wavefunction was carried out using MultiWfn software [125, 126].

6.6 Supplementary information

	Atom1	Atom2	distance, Å	$\rho(\mathbf{r})$, eÅ^{-3}	$\nabla^2\rho(\mathbf{r})$, eÅ^{-5}	λ_1 ,eÅ^{-5}	λ_2 ,eÅ^{-5}	λ_3 ,eÅ^{-5}	Gcp	Vcp	ε
1	N1	C2	1.4714	1.751	-13.95	-11.75	-11.35	9.156	0.207	-0.558	0.035
2	C2	C2^i	1.5558	1.622	-10.82	-10.61	-9.94	9.743	0.192	-0.496	0.067
3	C2	H2A	1.0686	1.687	-14.73	-14.95	-14.25	14.470	0.183	-0.519	0.050
4	C2	H2B	1.0703	1.705	-15.61	-15.50	-14.78	14.680	0.182	-0.526	0.049

Table 6.4 List of unique (3,-1) covalent bond critical points in **18**

Atom1	Atom2	symmetry mate	$\rho(\mathbf{r})$, eÅ^{-3}	$\nabla^2\rho(\mathbf{r})$, eÅ^{-5}	λ_1 ,eÅ^{-5}	λ_2 ,eÅ^{-5}	λ_3 ,eÅ^{-5}	ε
N1	H2B	x-y, x-1, -z y, -x+y+1, -z -x+2, -y+1, -z	0.045	0.607	-0.093	-0.075	0.775	4.15
H2A	H2A	-x+y+1, -x+2, z -y+2, x-y+1, z	0.042	0.433	-0.091	-0.053	0.578	3.65
H2B	H2B	-x+2, -y+1, -z	0.034	0.502	-0.103	-0.011	0.616	3.97

Table 6.5 Asymmetric unit bound (3,-1) intermolecular critical points found in molecular crystal of **18**

level of theory	Δ_E, kJ/mol
ωB97M-V / 6-31++G(d,p)	-29.33
ωB97X-V / 6-31++G(d,p)	-28.47
B97M-V / 6-31++G(d,p)	-26.18
M06 / 6-31++G(d,p)	-24.40
M06-2X / 6-31++G(d,p)	-24.14
r^2SCAN / 6-31++G(d,p)	-20.14
PW6B95 / 6-31++G(d,p)	-19.88
B3LYP / 6-31++G(d,p)	-12.33
BP86 / 6-31++G(d,p)	-10.46
ωB97X-V / 6-31G(d,p)	-17.70
ωB97X-V / def2-TZVPD	-16.48
ωB97M-V / 6-31G(d,p)	-17.98
ωB97M-V / def2-TZVPD	-16.37
B97M-V / 6-31G(d,p)	-16.50
B97M-V / def2-TZVPD	-15.73
M06-2X / 6-31G(d,p)	-14.75
M06-2X / def2-TZVPD	-12.88
M06 / 6-31G(d,p)	-14.15
M06 / def2-TZVPD	-11.65
r^2SCAN / 6-31G(d,p)	-10.10
r^2SCAN / def2-TZVPD	-9.07
PW6B95 / 6-31G(d,p)	-9.32
PW6B95 / def2-TZVPD	-7.91
B3LYP / 6-31G(d,p)	-1.43
B3LYP / def2-TZVPD	-0.61
BP86 / 6-31G(d,p)	0.18
BP86 / def2-TZVPD	1.24

Table 6.6 Noncovalent interaction energies used for top graph in Fig. 7.12

level of theory	$\rho(\mathbf{r})$, eÅ^{-3}	$\nabla^2\rho(\mathbf{r})$, eÅ^{-5}	$\Delta_{\rho(\mathbf{r})}$	$\Delta_{\nabla^2\rho(\mathbf{r})}$
MM (XRD)	0.0451	0.607	—-	—-
B3LYP / 6-31G(d,p)	0.0508	0.469	0.0057	-0.138
B97M-V / 6-31G(d,p)	0.0497	0.470	0.0046	-0.137
BP86 / 6-31G(d,p)	0.0515	0.464	0.0064	-0.143
M06 / 6-31G(d,p)	0.0508	0.474	0.0057	-0.133
M06-2X / 6-31G(d,p)	0.0506	0.483	0.0055	-0.124
PW6B95 / 6-31G(d,p)	0.0496	0.472	0.0045	-0.135
r^{2}SCAN / 6-31G(d,p)	0.0504	0.471	0.0053	-0.136
ωB97X-V / 6-31G(d,p)	0.0502	0.478	0.0051	-0.129
B3LYP / 6-31++G(d,p)	0.0494	0.478	0.0043	-0.129
B97M-V / 6-31++G(d,p)	0.0486	0.477	0.0035	-0.130
BP86 / 6-31++G(d,p)	0.0502	0.473	0.0051	-0.134
M06 / 6-31++G(d,p)	0.0499	0.479	0.0048	-0.128
M06-2X / 6-31++G(d,p)	0.0496	0.489	0.0045	-0.118
PW6B95 / 6-31++G(d,p)	0.0482	0.481	0.0031	-0.126
r^{2}SCAN / 6-31++G(d,p)	0.0490	0.480	0.0039	-0.127
ωB97X-V / 6-31++G(d,p)	0.0489	0.486	0.0038	-0.121
B3LYP / def2-TZVPD	0.0479	0.511	0.0028	-0.096
B97M-V / def2-TZVPD	0.0467	0.514	0.0016	-0.093
BP86 / def2-TZVPD	0.0488	0.503	0.0037	-0.104
M06 / def2-TZVPD	0.0496	0.501	0.0045	-0.106
M06-2X / def2-TZVPD	0.0484	0.520	0.0033	-0.087
PW6B95 / def2-TZVPD	0.0465	0.515	0.0014	-0.092
r^{2}SCAN / def2-TZVPD	0.0474	0.516	0.0023	-0.091
ωB97X-V / def2-TZVPD	0.0471	0.517	0.0020	-0.090

Table 6.7 Topological parameters of N1$\cdots$H2B^i BCPs. Δ_{value} are calculated as a difference between values obtained *in silico* and those from multipolar model.

level of theory	Δ_E, kJ/mol
ωB97X-V / 6-31G(d,p)	-7.53
ωB97X-V / def2-TZVPD	-7.38
ωB97X-V / 6-31++G(d,p)	-7.27
B97M-V / 6-31G(d,p)	-7.21
B97M-V / def2-TZVPD	-7.17
B97M-V / 6-31++G(d,p)	-7.05
ωB97M-V / 6-31G(d,p)	-7.39
ωB97M-V / 6-31++G(d,p)	-7.10
ωB97M-V / def2-TZVPD	-6.98
M06 / 6-31G(d,p)	-4.63
M06 / 6-31++G(d,p)	-4.45
M06 / def2-TZVPD	-3.42
M06-2X / 6-31G(d,p)	-3.02
M06-2X / 6-31++G(d,p)	-2.83
M06-2X / def2-TZVPD	-2.47
r^2SCAN / 6-31G(d,p)	-1.11
r^2SCAN / def2-TZVPD	-0.98
r^2SCAN / 6-31++G(d,p)	-0.92
PW6B95 / 6-31G(d,p)	-0.04
PW6B95 / 6-31++G(d,p)	0.17
PW6B95 / def2-TZVPD	0.29
B3LYP / def2-TZVPD	4.79
B3LYP / 6-31G(d,p)	4.82
B3LYP / 6-31++G(d,p)	5.10
BP86 / 6-31G(d,p)	7.03
BP86 / def2-TZVPD	7.16
BP86 / 6-31++G(d,p)	7.37

Table 6.8 Noncovalent interaction energies used for bottom graph in Fig. 7.12

level of theory	$\rho(\mathbf{r})$, eÅ^{-3}	$\nabla^2\rho(\mathbf{r})$, eÅ^{-5}	$\Delta_{\rho(\mathbf{r})}$	$\Delta_{\nabla^2\rho(\mathbf{r})}$
MM (XRD)	0.0340	0.433	—-	—-
B3LYP / 6-31G(d,p)	0.0300	0.339	0.0040	-0.094
B3LYP / 6-31++G(d,p)	0.0299	0.339	0.0041	-0.094
B3LYP / def2-TZVPD	0.0301	0.350	0.0039	-0.083
B97M-V / 6-31G(d,p)	0.0297	0.342	0.0043	-0.091
B97M-V / 6-31++G(d,p)	0.0296	0.342	0.0044	-0.091
B97M-V / def2-TZVPD	0.0298	0.350	0.0042	-0.083
BP86 / 6-31G(d,p)	0.0304	0.338	0.0036	-0.095
BP86 / 6-31++G(d,p)	0.0303	0.338	0.0037	-0.095
BP86 / def2-TZVPD	0.0305	0.348	0.0035	-0.085
M06 / 6-31G(d,p)	0.0304	0.345	0.0036	-0.088
M06 / 6-31++G(d,p)	0.0304	0.346	0.0036	-0.087
M06 / def2-TZVPD	0.0310	0.359	0.0030	-0.074
M06-2X / 6-31G(d,p)	0.0302	0.340	0.0038	-0.093
M06-2X / 6-31++G(d,p)	0.0301	0.341	0.0039	-0.092
M06-2X / def2-TZVPD	0.0303	0.352	0.0037	-0.081
PW6B95 / 6-31G(d,p)	0.0294	0.338	0.0046	-0.095
PW6B95 / 6-31++G(d,p)	0.0292	0.339	0.0048	-0.094
PW6B95 / def2-TZVPD	0.0293	0.350	0.0047	-0.083
r^{2}SCAN / 6-31G(d,p)	0.0297	0.344	0.0043	-0.089
r^{2}SCAN / 6-31++G(d,p)	0.0295	0.344	0.0045	-0.089
r^{2}SCAN / def2-TZVPD	0.0297	0.357	0.0043	-0.076
ωB97X-V / 6-31G(d,p)	0.0295	0.342	0.0045	-0.091
ωB97X-V / 6-31++G(d,p)	0.0294	0.343	0.0046	-0.090
ωB97X-V / def2-TZVPD	0.0295	0.353	0.0045	-0.080

Table 6.9 Topological parameters of H2A$\cdots$H2A^{ii} BCPs. Δ_{value} are calculated as a difference between values obtained *in silico* and those from multipolar model.

Chapter 7

2-[(2,4-Dimethoxyphenyl)amino]-1,3-thiazolidin-4-one

7.1 Introduction

Thiazolidin-4-ones feature a heterocyclic ring known for its significant biological activities. This group of compounds is an important scaffold of several classes of natural and synthetic pharmaceuticals. These display antimicrobial [159–170], antifungal [160, 166, 171], antiviral [171–173], antiparasitic [174, 175], anticancer [167, 164, 176–182], antioxidant [171, 182, 183], anti-inflammatory [183–188], analgesic [171, 183, 187, 189], anticonvulsant [171, 190–192], and antidiabetic [193–196] activities. The functionalized derivatives of thiazolidin-4-one are approachable to synthesize, given the heterocyclic ring is obtainable through one-pot cyclocondensation of desired substituent possessing substrates in lab-friendly conditions [162–164, 180–182, 184, 191, 192, 197–201]. The combined effect of great medical potency and synthetic viability has made this class of chemicals extensively studied. In consequence, thiazolidin-4-ones' supramolecular characteristics are of prime interest.

7.2 Structure

The compound 2-[(2,4-Dimethoxyphenyl)amino]-1,3-thiazolidin-4-one (**26**) has been previously reported [202]. High resolution charge density research was not performed. Hydrogen atom is nearly unambiguously positioned near N1 nitrogen

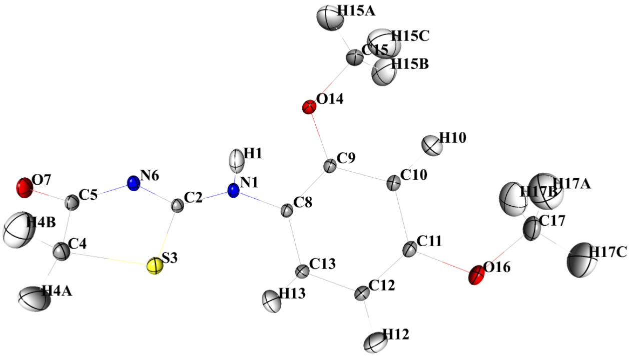

Fig. 7.1 Atom positions and thermal displacement ellipsoids (50% probability) of **26**.

in density maps. Found interatomic distances and geometry are in agreement with previously reported (selected values colected in Table 7.1 in section below), with the exception of differences in hydrogen atoms bond lengths which are to be expected and caused by systematic differences between models.

Imine-amine tautomerism

The structure may exist in one of 8 isomeric forms, depicted on Fig. 7.2 It is known that hydrogen bonds can lead to proton transfer tautomerism, also intermolecularly. Such behaviour has been described through theoretical and experimental work [203–205]. Series of DFT based studies of imine-amine tautomerism, which could theoretically take place inside crystal structure, were carried out. With atomic coordinates constrained to X-ray values for all atoms except the acidic hydrogen, the energy delta between two isomers is higher than for a free molecule. Constrained bond geometries make this result very much expected, since variations in bond order are reflected in interatomic distance – constraining interatomic distance has pronounced effect on what bond population is energetically favourable. This poses a challenge of how does one meaningfully model a sterically constrained system like crystal lattice, without modelling the whole lattice - to which the following reasoning was applied: since the compound forms a closely bound dimer, changes in geometry between the two almost perfectly planar thiazolidinone rings should not meaningfully affect contacts with the rest of symmetry mates. Therefore, it is possible to simulate the proton transfer and its

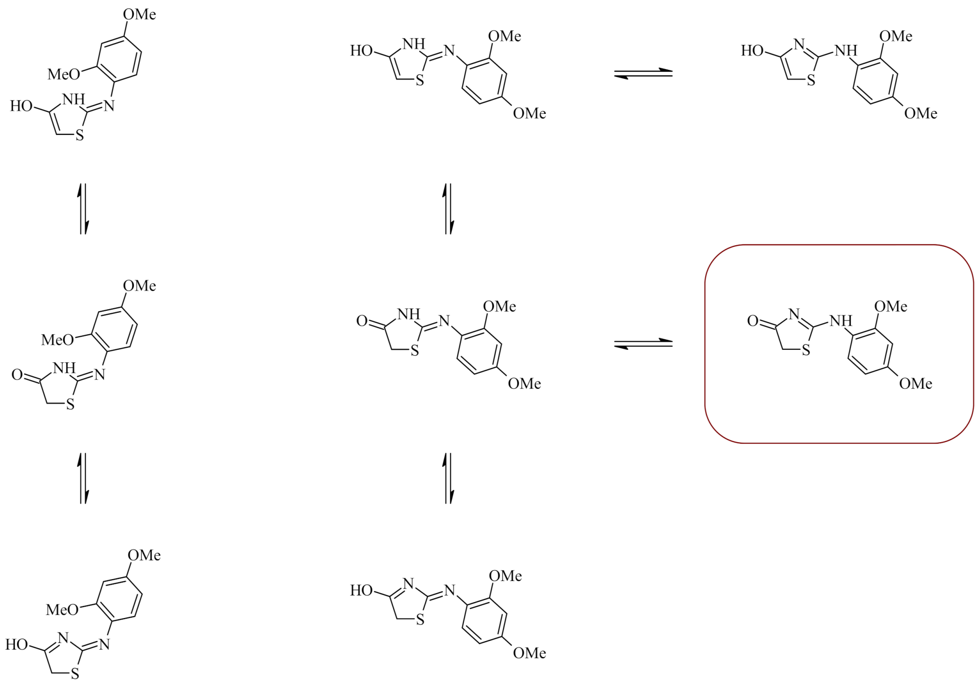

Fig. 7.2 Isomeric forms of **26**. Form found in crystal marked in red.

effect on nitrogen atoms bonds without losing the crystallographic context as long as changes in geometry do not extend too far outside the area of interest.

Single molecule optimization did not align perfectly with previous studies of this compound. However, while Nowaczyk et al. assessed **26** to be energetically favourable by 2 kcal/mol [202], in the course of current research iso-**26** was determined to be favourable by 0.5 kcal/mol for free molecule. Such difference is not outside acceptable margin of error, and has been determined to have primary cause in chosen density functional. Preliminary studies conducted for this system also used B3LYP density functional, giving similar results as found in original paper – which were then subverted by more advanced DFs that are less prone to introducing systematic errors. A quantitatively small disparity leads here to qualitatively opposite result; an outcome that researchers should bear in mind when performing superficial preliminary analysis, but also when using popular tools which fail to deliver adequate quality solutions with frustrating consistency.

Geometry optimization done for dimer pair led to results which are transferable to crystal structure (Fig. 7.3). Differences in molecular bond lengths do not transfer meaningfully to intermolecular contacts formed by the tautomerism affected moiety.

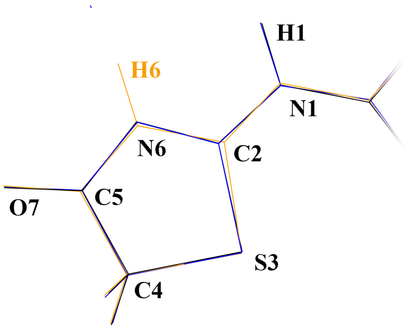

Fig. 7.3 Structures overlay of **26**$_{\mathrm{XRD}}$ (black), **26**$_{\mathrm{DFT}}$ (blue), and *iso*-**26**$_{\mathrm{DFT}}$ (orange).

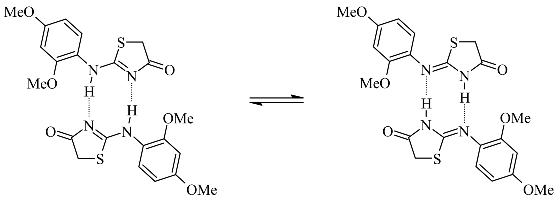

Fig. 7.4 Tautomerism of low energetic barrier isomers. Left: **26** dimer, right: *iso*-**26**

Analysis of isomers leads to a surprising observation: even though both possess a sp^2 C2 carbon atom bound to an amine and an imine, **26** has two equal C2–nitrogen bond lengths both in XRD and DFT studies; meanwhile, the two bond lengths in *iso*-**26** measure 1.267 and 1.380 Å. Expected bond length values are 1.279 Å for $Csp^2{=}N$ and 1.339 Å for $Csp^2{-}N$, respectively [69]. Intermediate bond length values of N1-amine form are a sign of intermediate bond order. Intuitively, this could be explained by effects of two tautomers averaging out their position in structure factors. This is not the case: N1-amine isomer has C2—N1 and C2—N6 bond lengths of almost equal lengths also in results obtained from *in silico* studies, but N1-imine has not. Partially double bond order is indeed found in MM and DFT based bond order assessments of **26**, the *iso*-**26** does not feature such characteristics: in this case, C2—N1(imine) bond is shorter and more populous than C2—N6(amine). This difference does not translate to atomic charges and other bonds, including the transferred hydrogen atom. The tautomerism is observable in charge density map, if ever so slightly: there is a small but noticeable density peak above lone electron pair of N6, as well as minimal amounts of charge density along $N\cdots H$ hydrogen bond that do not exceed 2σ level. The thiazolidinone ring features more noise on residual density map than the phenyl

Bond	length, Å			$\rho(\mathbf{r})$, eÅ^{-3}			$\nabla^2\rho(\mathbf{r})$, eÅ^{-5}		
	X	D	*i*D	X	D	*i*D	X	D	*i*D
N1—C2	1.326	1.324	1.267	2.503	2.428	2.594	-30.54	-26.98	-22.89
N1—C8	1.419	1.416	1.410	1.879	2.294	1.914	-14.38	-22.24	-18.65
N6—C2	1.326	1.315	1.380	2.400	2.075	2.071	-24.52	-20.37	-21.47
N6—C5	1.376	1.372	1.367	2.287	2.145	2.107	-22.10	-23.02	-20.53
O7—C5	1.222	1.209	1.206	2.820	2.759	2.785	-21.24	-0.19	-0.90
S3—C2	1.762	1.777	1.788	1.381	1.299	1.275	-5.24	-7.83	-7.43
S3—C4	1.800	1.809	1.817	1.230	1.223	1.205	-2.61	-6.77	-6.52
C4—C5	1.530	1.541	1.524	1.690	1.619	1.678	-11.07	-12.73	-13.95

Table 7.1 Selected XRD / DFT determined characteristics of **26**$_{\text{XRD}}$ (X), **26**$_{\text{DFT}}$ (D), and *iso*-**26**$_{\text{DFT}}$ (*i*D) bonds. Functional and basis set used: M06-2X / 6-311++G(d,p). DFT calculation carried out for dimeric compound.

ring, with some of concentrated along N1–C2–N6 bonds. The sub 2σ traces of disorder could not be modelled in any scientifically meaningful way.

The two tautomers differ only minimally in intermolecular contact strength. Optimized hydrogen bond distance is in agreement with crystallographically determined value for both forms. *Iso*-**26** creates a slightly more stable contact: both in the sense of being more energetically beneficial, and in the sense fo remaining stable over a wider range of intermolecular distance values. Given that the difference in tautomer stability is within margin of error for an isolated molecule, it is understandable – even if not expected – that minor packing effects could lead to pronounced effects in molecular constitution.

7.3 Intermolecular contacts

Sixteen symmetry related molecules surround **26** (Fig. 7.6), all of them involved in at least one (3, -1) intermolecular saddle point. Of these symmetry mates, ten are symmetrically independent. The single reciprocal pair of strong hydrogen bonds creates a nearly flat dimeric system around a symmetry center with symmetry mate -x,-y,-z (^{i}), including thiazolidinone rings in the flat structure. With a third of compound's non hydrogen atoms being heteroatoms, weak C—H$\cdots$X hydrogen bonds are plentiful. The aromatic ring is not engaged in stacking interactions, but are engaged in weak C—H$\cdots\pi$ bonds instead. On the d$_{\text{norm}}$ mapping of Hirshfeld surface (Fig. 7.7), a handful

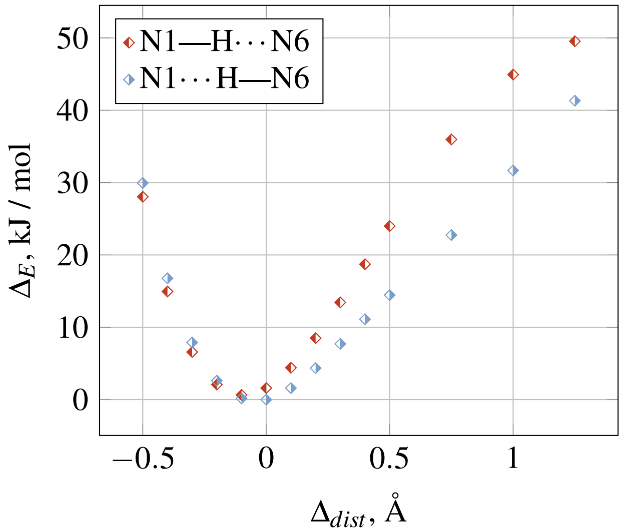

Fig. 7.5 Energetic effect of changing **26**···**26**^{i} separation for two most stable tautomers

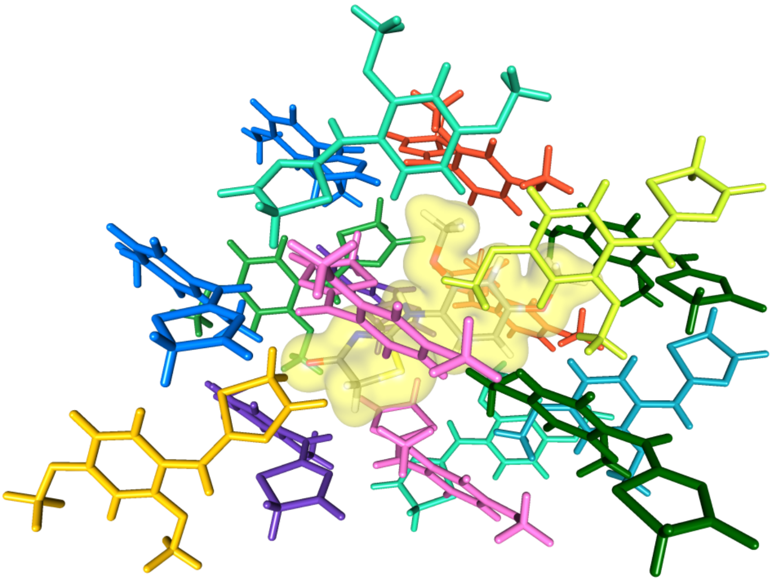

Fig. 7.6 Symmetry mates surrounding **26**

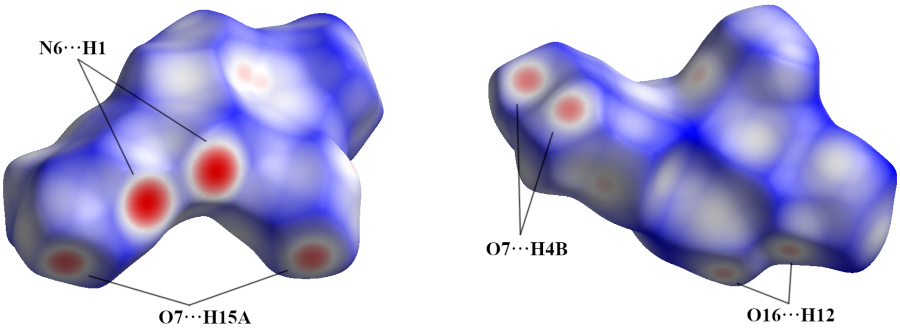

Fig. 7.7 Hirshfeld surfaces of **26**

of contacts is found to be significantly shorter than the sum of van der Waals radii. All of the shortest ones are caused by hydrogen bonds, with double N1—H1···N6 being the most prominent feature of the d_{norm} map.

Results of contact energy calculations are presented in table Table 7.2. There are noticeable differences between contact energies calculated using standard tools. Clearly, binding energies estimated using a function of electrostatic potential distribution in atoms' vicinity, as done by VMoPro [108, 46], are in this case leading to overestimating highly polarized contacts and underestimating those which are mostly based on dispersion forces. Unlike in the case of **8** and **??**, there is much weaker correlation between the number of bond paths found and symmetry equivalent's interaction energy, especially for electrostatic potential based calculation method. Such a result is to be expected when molecule's sources of charged interactions are strong and unevenly distributed.

Dimer involved symmetry mate -x,-y,-z forms, if taken at face value, two strong hydrogen bonds with electron density of 0.142 $e\text{Å}^{-3}$ at saddle point. The chemistry of studied molecule, as discussed in **??** 26, makes the hydrogen bond pair slightly less reliable than other parts of the model. Following the relation between Gibbs free energy and chemical equilibrium, at measurement temperature the dimer pair from Fig. 7.4 is estimated to exist in approx. 5:1 ratio in favour of the amine form. The lone electron pair of sp^2 nitrogen and the σ_{N---H} bond exist interchangeably in the same space, with the standard "lone pair size" being around 0.6–0.7 Å [206, 207], a third shorter than the standard N—H bond length of 1.015 Å [208, text]. The two would be very difficult to reliably differentiate even with very good quality, high

interacting symmetry	number of involved (3,-1) critical points	E, kJ/mol	
		MM	DFT
-x,-y,-z	4	-116.21	-99.04
-x+1,-y,-z	4	-68.97	-29.69
-x,-y+1,-z	3	-16.36	-26.44
-x,y+½,-z+½	4	-8.71	-23.26
-x,-y+½,z+½	4	5.77	-21.40
-x,y+½,-z-½	1	-30.76	-19.79
-x,-y-½,z+½	3	-12.24	-16.63
-x+1,-y,-z+1	2	-14.30	-10.79
-x+1,y+½,-z+½	2	-23.67	-10.34
+x,+y,+z-1	1	7.15	0.55

Table 7.2 Total interaction energy values of symmetrically independent contacting pairs of **26**. Functional and basis set used for DFT based calculations: ωB97M-V def2-TZVPD

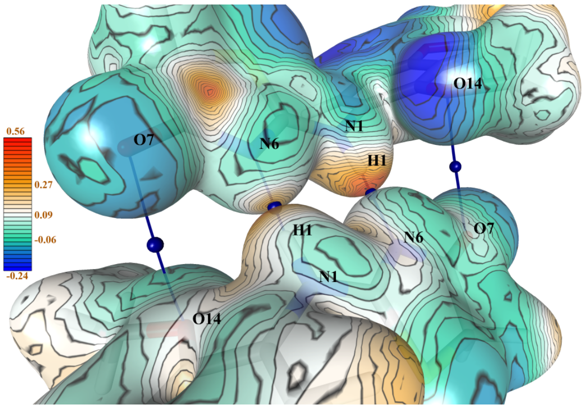

Fig. 7.8 (3,-1) critical points on contacts with -x,-y,-z symmetry equivalent. Electrostatic potential (eÅ^{-1}) mapped over the ED isosurface of 0.1 eÅ^{-3}.

resolution measurement. It is nonetheless worth noting, that these discarded imine-amine disorder model obtained with Hirshfeld atom refinement procedure came to occupancy ratios in agreement with estimated tautomer ratio. The other pair of saddle points is found between contacts O14$\cdots$O7^{i} and its inverted counterpart. Nominally they are a case of weak, distant O$\cdots$O contact with lone electron pairs of O7^{i} oriented towards neighbouring oxygen atom's area of lower electrostatic potential. Like in many other analogous cases, the true attracting force is probably present away from found bond path, namely between hydrogen atoms of C15 methyl group and negatively

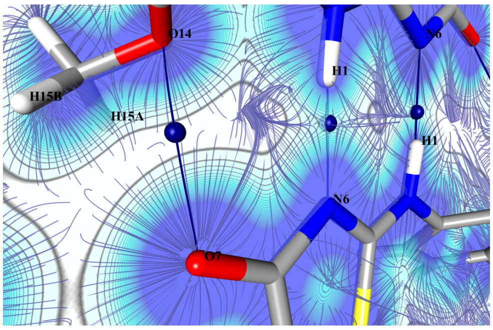

Fig. 7.9 Electron density gradient lines around N1—H1$\cdots$H6^i and O7$\cdots$O14^i

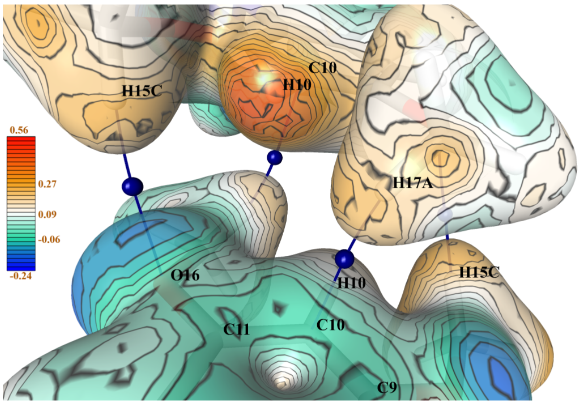

Fig. 7.10 (3,-1) critical points on contacts with *ii* symmetry equivalent. Electrostatic potential (eÅ^{-1}) mapped over the ED isosurface of 0.1 eÅ^{-3}.

charged O7$^{\mathrm{i}}$ atom. At 3.23 Å, the distance H15B - O7$^{\mathrm{i}}$ is also smaller than 3.46 Å long separation O14 - O7$^{\mathrm{i}}$.

There is a strong electrostatic component to binding with symmetry mate *ii*, which interfaces with a combination of weak C—H$\cdots$O and C—H$\cdots\pi$ hydrogen bonds (Fig. 7.10). Each of four oxygen atoms involved possesses significant negative charge (Fig. 7.12), while methyl groups are moderately positive. The two present types of contacts are engaged in an interesting play of characterizing factors: comparable interatomic distances turn out to differ in electron density at critical point by 50% in favour of contact that does not breach van der Waals atomic radii. The C—H$\cdots$O bond, despite its generally favourable geometry – distance of 2.885 Å and angles facilitating contact with one of lone electron pairs – is much less electron rich than C—H$\cdots\pi$ bond formed nearby (Table 7.3). The difference is noticeably pronounced, but consistent with other systems analyzed in this work. Diffuse, far-reaching delocalised π orbitals of aryl rings yet again prove to bind well to weakly charged hydrogen atoms.

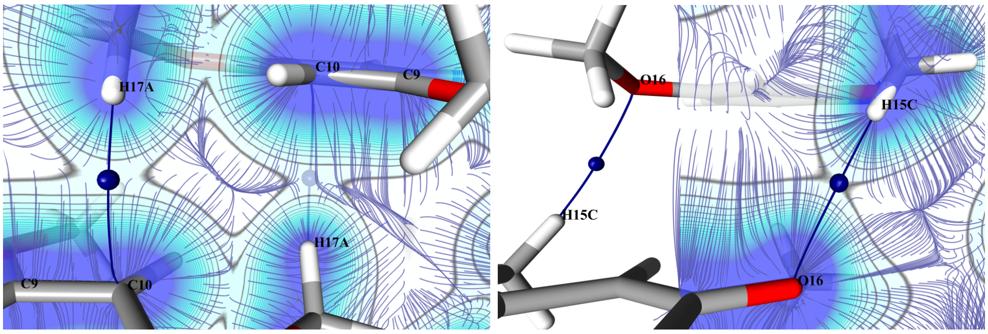

(a) H17A$\cdots\pi$(C9-C10^{ii}) (b) O16$\cdots$H15C^{ii}

Fig. 7.11 Electron density gradient lines around symmetry mate -x+1,-y,-z contacts

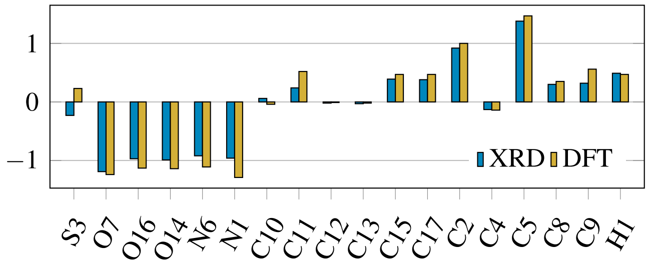

Fig. 7.12 Selected atomic charges in **26** evaluated by atomic basin charge density integration. XRD: multipolar model, DFT: ωB97M-V/def2-TZVPD

Contact	distance	$\Delta_{\text{dist.VdW}}$	source	$\rho(\mathbf{r})$, eÅ^{-3}	$\nabla^2\rho(\mathbf{r})$, eÅ^{-5}	ε
O16$\cdots$H15C	2.885	-0.2647	XRD	0.031	0.29	0.018
			DFT	0.026	0.31	0.070
C10$\cdots$H17A	2.779	0.0206	XRD	0.045	0.38	0.121
			DFT	0.047	0.43	0.231

Table 7.3 Critical points topological characteristics for -x+1,-y,-z symmetry mate contacts. XRD: multipolar model, DFT: ωB97M-V/def2-TZVPD

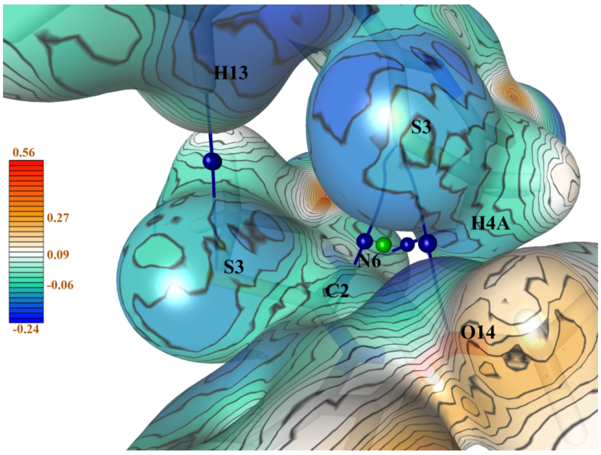

Fig. 7.13 Intermolecular contacts formed with x,-y+½,z+½ symmetry mate

At opposite surface of phenyl ring, tom H15B forms a weak C—H$\cdots\pi$(Ar) hydrogen bond with x,-y-½,z+½ symmetry equivalent. All phenyl ring carbon atoms are within contact distance: measurements vary from 2.676 Å up to 3.004 Å, with distance to (3,+1) aryl ring CP measuring 2.56 Å. Intermolecular bond path leads to the nearest one, with electron density at saddle point measuring 0.079 eÅ^{-3}, Laplacian of 0.58 eÅ^{-5} and (expectedly) high ellipticity of 0.96. Molecules form two more contacts through H17B hydrogen from ring's *p*-methoxy group, distant, with charge density measuring below 0.2 eÅ^{-3} each and Laplacian values of approx. 0.2 eÅ^{-5}. Their effect on interaction energy of two molecules is clearly minimal.

Sulfur atom S3 makes contact with only few molecules, forming a hydrogen bond with H17A hydrogen from methoxy moiety of -x+1,y+½,-z+½ symmetry mate. With a distance of 2.99 Å and electron density at CP of 0.045 eÅ^{-3}, the weak hydrogen bond is typical for its kind. All other contacts are symmetrically equivalent to those formed with x,-y+½,z+½ and presented on Fig. 7.13. The contact with O14 oxygen atom bears traits of a weak chalcogen$\cdots$chalcogen bond: sulphur's *sigma*-hole, not too well pronounced and perturbed in its location, aligns with one of oxygen's lone electron pairs. The resulting contact has charge density of 0.061 eÅ^{-3} at a distance of 3.22 Å, its CP eigenvalues in agreement with a weak contact formed by a third row element.

It could be expected that H4A and H4B, bound to an aliphatic sp^3 carbon forming covalent bonds with two chalcogen atoms, will form close contacts with strongly negative heteroatoms in their vicinity. This is true for O7$\cdots$H4B interaction, where the

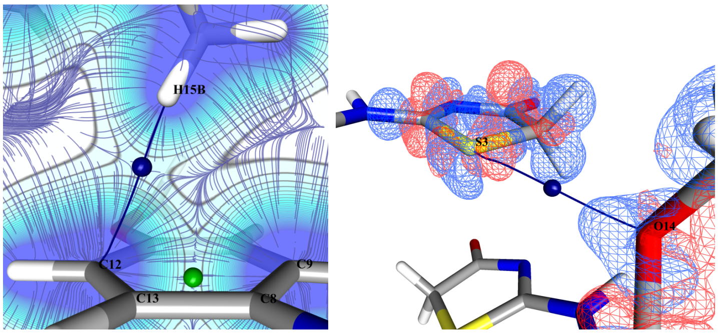

(a) (b)

Fig. 7.14 Fig. 7.14a: Electron density gradient lines near C—H$\cdots\pi$(Ar) contact
Fig. 7.14b: Deformation density around S3$\cdots$O13 contact

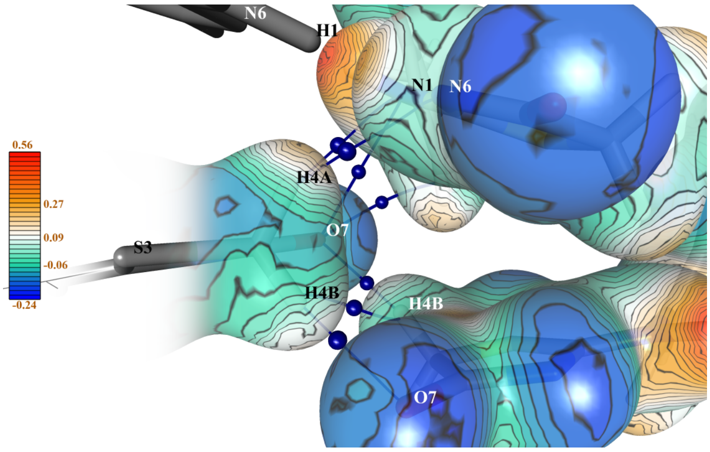

Fig. 7.15 (3,-1) critical points on contacts with -x,-y+1,-z (top-right) and -x, y+½, -z+½ (bottom-right) symmetry mates. Electrostatic potential (eÅ^{-1}) mapped over the ED isosurface of 0.1 eÅ^{-3}.

interatomic distance measuring 2.29 Å is short. The bind between the symmetry mates is further cemented by a nearby inversion point, creating a second instance of same interaction. This results in 0.084 eÅ^{-3} charge density at saddle point, and Laplacian values intermediate between those typical for weak and strong hydrogen bonds: $\nabla^2\rho(\mathbf{r})$ is found to have value of over 1.1 eÅ^{-5}, with λ_3 exceeding 1.8 eÅ^{-5}. Interestingly, interaction energy estimates of multipolar model based on electrostatic forces are lower than those determined by *in silico*. Given that DFT values are (by practical necessity) determined for only pairs of molecules, the simulation might have in this case overoptimized molecular orbitals towards the only neighbour, potentially skewing the result. Atom H4A, despite its contacts with both highly negative nitrogen atoms, does not form a strong bond with either. As a matter of fact, it is uncertain if the contacts

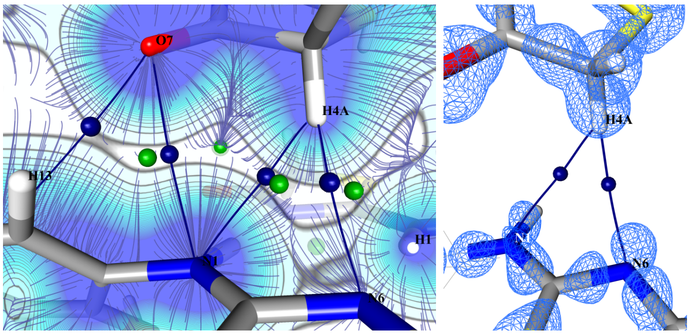

(a) (b)

Fig. 7.16 Electron density gradient lines and deformation density in the contact area with -x,-y+1,-z symmetry mate. Deformation density isosurface drawn at +0.1 eÅ^{-3}.

formed are bonding at all. This conclusion is supported by two observations. One, the contact geometry: distances of 2.86 Å for N1$\cdots$H4A and 2.71 Å for N6$\cdots$H4A both exceed the sum of van der Waals radii for these chemical species; additionally, the C—N$\cdots$H angle value of approx. 130° means that the positive region of hydrogen atom surface has poor orientation towards any of negatively charged nitrogen atom regions (**??**). Two, the topology: critical point on H4A$\cdots$N1 bond lies very close to a (3,+1) ring saddle point, and has the absolute values of λ_1 and λ_2 over 12 times smaller than λ_3. Overall, the packing context of this symmetry mate does agree with repulsion stated in Table 7.2: H4A is adjacent to dimer forming nitrogen pairs, but so is the O7 oxygen atom. The O7-N1 distance measures 3.369 Å, only 0.29 Å above the sum of their van der Waals radii. Naturally, the two create a repulsive force between them: the found bond path has very low electron density at critical point, measuring only 0.025 eÅ^{-3} despite the short contact distance. Furthermore, λ_1 and λ_2 are approx. an order of magnitude smaller than λ_3, indicating a non bonding contact (see Table 7.6). Another common sign of possibly non binding interaction is close proximity of (3,-1) and (3,+1) critical points. In this case, they are 0.33 Å apart. The numerical topological characteristics of saddle point and are also very close to each other: $\rho(\mathbf{r})$ and $\nabla^2\rho(\mathbf{r})$ values both differ by less than 1%. Another possibly repulsive contact in the area is the H4B$\cdots$H4B bond path positioned on point symmetry between them: the two hydrogen atoms are almost forced into contact by packing effects and, of course, strong attraction found in H4B$\cdots$O7. The resulting BCP is characterized by unassuming $\rho(\mathbf{r})$ and $\nabla^2\rho(\mathbf{r})$ values, however a detailed insight reveals lowest λ_2/λ_3 ratio of all bond critical points identified, and a bewildering ellipticity of 39.9. Of course, the high ellipticity comes from two C—H bonds longitudinally interfusing through somewhat forced interaction. To quote Bader: Bond paths are not chemical bonds [209].

7.4 Summary

A multipolar model was created for 2-[(2,4-Dimethoxyphenyl)amino]-1,3-thiazolidin-4-one on basis of medium-high order diffraction data. A novel approach to multipolar model refinement was successfully employed, allowing to obtain physically meaningful, precise model from imperfect data set with hidden low ratio disorder. Key intermolecular contacts were analyzed and described on basis of crystallographic measurements, as well as *in silico* studies. Where the thiazolidinone ring is involved in antimicrobial activity [171], understanding how tautomers interconvert in vivo is essential for effective drug design. Possible in-crystal tautomerism has been investigated through DFT structural and topological analysis, concluding that while N1-imine form might be energetically favourable, it is so by a minimal margin; enough for the packing effects to shift the equilibrium the N1-amine form exists in studied crystal almost exclusively.

7.5 Experimental section

Data collection

MoKα radiation (λ = 0.71073 Å) X-ray diffraction measurements were carried out on an Agilent Xcalibur A diffractometer. The structure of **26** was initially solved by direct methods using the SHELXS-97 program, then further refined by the full-matrix least-squares method on F$^2 susingtheSHELXL-97program$[210, 211].

Crystal data: $C_{11}H_{12}N_2O_3S$, M_r = 252.28, monoclinic $P2_1/c$, a = 14.1176(1)Å, b = 10.0122(1)Å, c = 8.1092(1)Å, α = 90°, β = 96.806(1)°, γ = 90°, V = 1138.14(2) Å^3 , Z = 4, F(000) = 528, d_x = 1.473 g/cm, (MoKα) = 0.33 mm^{-1}. A total of 70963 reflections collected up to $2\theta = 53.91^\circ$ ($\sin(\theta/\lambda) = 1.14\text{Å}^{-1}$), of which 13901 were symmetry-independent, 12307 with $I > 2\sigma(I)$.

Refinement

Data quality proved insufficient for immediate charge density refinement in MoPro software. To improve the multipolar refinement starting point, the model obtained from SHELXL2014 was imported into Olex2 software [117]. Atomic positions and thermal parameters were subsequently refined with no restraints applied, using Hirshfeld atom refinement procedure [118, 119], with no restraints defined: The molecular wavefunction was calculated using Orca 5.0.4[110, 111], with R^{2}SCAN [120] functional and def2-TZVP basis set. Atomic non-spherical form factors were extracted by Hirshfeld partitioning using NoSpherA2 [122, 123]. Obtained non-spherical form factors were then used by Olex2 for next least-squares refinement cycle. During Hirshfeld atom refinement, hydrogen atoms' thermal parameters were refined anisotropically. Final residuals for for this step: for all reflections R = 3.02%, wR2 = 3.8%, for $I > 2\sigma(I)$ R = 2.22%, wR2 = 3.33%, S = 1.13. Max/min $\Delta\rho$ value in the final ΔF map 0.206/-0.243 eÅ^{-3}, with residual density featureless and randomly distributed throughout the cell.

Obtained structure was then imported into MoPro software[46, 47]. Scale factors were refined at different polynomial levels, determining the linear scale factor function to be optimal. Direct incremental refinement, analogous to procedure described in Section 5.5, brought unsatisfactory results. Positional and thermal parameters calculated by Olex2 HAR procedure were used as basis for transfer from mulipolar pseudo-atom library [212]. Initial multipolar model obtained in this fashion was then iteratively refined in two consecutive stages, as described:

- Multiple iterations of following steps:
  - scale factors
  - multipolar population
  - expansion/contraction coefficients
- Multiple iterations of following steps:
  - scale factors
  - valence population
  - additional iterations of above for sulphur only

- multipolar population
- additional iterations of above for sulphur only
- expansion/contraction coefficients
- additional iterations of above for sulphur only
- positional, thermal and anharmonic motion parameters of chalcogen atoms

Each of stages, as the model improved, had fewer constraints and restraints applied. The final set of constraints and restraints are attached in Section A.5 Final residuals for for this step: for all reflections R_{free} = 3.025%, $wR2_{free}$ = 4.131%, for $I > 2\sigma(I)$ R = 2.380%, wR2 = 1.962%, S = 1.09.

In silico studies

Density functional theory (DFT) calculations were carried out using ORCA v.5.0.4 [110, 111, 124] with resources provided by the Wrocław Centre for Networking and Supercomputing (BEM2) and Academic Computer Centre Cyfronet AGH (Ares). Ie gratefully acknowledge Polish high-performance computing infrastructure PLGrid (HPC Centers: ACC Cyfronet AGH, WCSS) for providing computer facilities and support within computational grant no. PLG/2024/017342. Contact energies calculated for Table 5.3 were carried out with counterpoise correction applied according to procedure described in section 8.1.6 of ORCA manual. Topological analysis of obtained wavefunction was carried out using MultiWfn software [125, 126].

7.6 Supplementary information

Table 7.4 List of (3,-1) covalent bond critical points in **26**

	Atom1	Atom2	distance, Å	$\rho(\mathbf{r})$, eÅ^{-3}	$\nabla^2\rho(\mathbf{r})$, eÅ^{-5}	λ_1	λ_2	λ_3	Gcp	Vcp	ε
1	S3	C2	1.762	1.381	-5.24	-8.67	-6.53	9.96	0.168	-0.390	0.33
2	S3	C4	1.800	1.230	-2.61	-7.42	-6.27	11.08	0.150	-0.327	0.18
3	C4	C5	1.530	1.690	-11.07	-11.60	-10.28	10.81	0.209	-0.533	0.13
4	O7	C5	1.222	2.820	-21.24	-27.45	-24.12	30.33	0.524	-1.268	0.14
5	N6	C5	1.376	2.287	-22.10	-18.09	-16.51	12.51	0.320	-0.870	0.10
6	N6	C2	1.326	2.400	-24.52	-19.25	-17.08	11.82	0.343	-0.940	0.13
7	N1	C2	1.326	2.503	-30.54	-21.81	-17.47	8.74	0.339	-0.994	0.25
8	N1	C8	1.419	1.879	-14.38	-14.17	-12.02	11.81	0.241	-0.632	0.18
9	C8	C9	1.403	2.169	-21.64	-17.35	-13.40	9.11	0.283	-0.791	0.30
10	C10	C9	1.400	2.062	-18.66	-15.46	-12.18	8.98	0.269	-0.731	0.27
11	C11	C10	1.399	2.159	-19.30	-16.20	-12.30	9.20	0.296	-0.793	0.32
12	C12	C11	1.397	2.136	-19.76	-16.45	-12.73	9.42	0.285	-0.776	0.29
13	C12	C13	1.391	2.035	-17.76	-15.52	-11.33	9.09	0.267	-0.717	0.37
14	C8	C13	1.393	2.220	-21.86	-17.19	-13.22	8.56	0.299	-0.825	0.30
15	O14	C9	1.353	2.143	-20.43	-17.17	-14.79	11.53	0.283	-0.778	0.16
16	O14	C15	1.428	1.583	-4.58	-9.62	-9.26	14.30	0.225	-0.497	0.04
17	O16	C11	1.366	1.955	-17.55	-14.78	-13.87	11.10	0.243	-0.668	0.07
18	O16	C17	1.424	1.674	-6.88	-11.21	-10.25	14.57	0.234	-0.539	0.10

continued on next page

continued from previous page

	Atom1	Atom2	distance, Å	$\rho(\mathbf{r})$, eÅ^{-3}	$\nabla^2\rho(\mathbf{r})$, eÅ^{-5}	λ_1 ,eÅ^{-5}	λ_2 ,eÅ^{-5}	λ_3 ,eÅ^{-5}	Gcp	Vcp	ε
19	N1	H1	1.012	2.124	-26.86	-27.95	-26.02	27.11	0.232	-0.743	0.07
20	C4	H4A	1.081	1.878	-18.78	-16.90	-16.37	14.49	0.211	-0.616	0.03
21	C4	H4B	1.091	1.809	-18.42	-16.22	-15.36	13.16	0.193	-0.576	0.06
22	C10	H10	1.075	1.766	-17.96	-16.51	-15.41	13.96	0.183	-0.553	0.07
23	C12	H12	1.069	1.974	-21.43	-18.46	-18.36	15.39	0.222	-0.666	0.01
24	C13	H13	1.068	1.847	-19.57	-17.47	-16.43	14.33	0.196	-0.595	0.06
25	C15	H15A	1.062	1.958	-21.94	-17.79	-17.21	13.06	0.213	-0.654	0.03
26	C15	H15B	1.077	2.022	-23.21	-18.71	-18.57	14.07	0.225	-0.690	0.01
27	C15	H15C	1.074	1.881	-20.34	-16.91	-16.08	12.65	0.201	-0.613	0.05
28	C17	H17A	1.092	1.849	-19.44	-16.43	-15.94	12.94	0.197	-0.597	0.03
29	C17	H17B	1.097	1.907	-20.57	-17.20	-16.78	13.42	0.207	-0.628	0.03
30	C17	H17C	1.082	1.927	-20.99	-17.57	-16.80	13.38	0.210	-0.638	0.05

Atom1	Atom2	symmetry mate	$\rho(\mathbf{r})$, eÅ^{-3}	$\nabla^2\rho(\mathbf{r})$, eÅ^{-5}	λ_1 ,eÅ^{-5}	λ_2 ,eÅ^{-5}	λ_3 ,eÅ^{-5}
N6	H1	-x,-y,-z	0.142	2.62	-0.747	-0.705	4.068
O7	H15A	-x,y+½,-z-½	0.108	1.03	-0.498	-0.492	2.021
O7	H4B	-x,-y+1,-z	0.084	1.12	-0.357	-0.346	1.826
C12	H15B	-x,-y-½,z+½	0.079	0.56	-0.265	-0.138	0.959
O14	S3	-x,-y+½,z+½	0.061	0.76	-0.166	-0.130	1.058
O16	H12	-x+1,-y,-z+1	0.058	0.85	-0.242	-0.198	1.290
S3	H17C	-x+1,y+½,-z+½	0.045	0.35	-0.132	-0.131	0.613
C10	H17A	-x+1,-y,-z	0.044	0.38	-0.121	-0.107	0.610
N6	H4A	-x,-y+½,z+½	0.041	0.66	-0.082	-0.078	0.822
C13	O7	-x,y+½,-z+½	0.037	0.56	-0.104	-0.067	0.735
N6	H4A	-x,y+½,-z+½	0.035	0.51	-0.105	-0.097	0.710
C2	S3	-x,-y+½,z+½	0.033	0.39	-0.030	-0.020	0.437
H4B	H4B	-x,-y+1,-z	0.033	0.61	-0.104	-0.003	0.718
C17	C12	-x+1,y+½,-z+½	0.033	0.50	-0.078	-0.031	0.615
O16	H15C	-x+1,-y,-z	0.031	0.29	-0.104	-0.102	0.499
H12	H15C	+x,+y,+z-1	0.028	0.37	-0.106	-0.052	0.524
N1	H4A	-x,y+½,-z+½	0.026	0.45	-0.046	-0.039	0.537
O7	N1	-x,y+½,-z+½	0.025	0.39	-0.057	-0.034	0.482
S3	H13	-x,-y+½,z+½	0.020	0.21	-0.049	-0.046	0.308
H12	H17B	-x,-y-½,z+½	0.017	0.17	-0.048	-0.032	0.251
O7	O14	-x,-y,-z	0.015	0.26	-0.036	-0.029	0.327
O16	H17B	-x,-y-½,z+½	0.014	0.24	-0.037	-0.015	0.293

Table 7.5 Symmetrically independent (3,-1) intermolecular critical points found in molecular crystal of **26**

Atom	P_{val}	Bader charges				Mulliken charges		
		XRD	DFT_1	DFT_2	DFT_3	DFT_1	DFT_2	DFT_3
S3	6.22	-0.23	0.23	0.22	0.28	-0.11	0.27	0.07
O7	6.14	-1.19	-1.24	-1.19	-1.23	-0.60	-0.84	-0.32
O14	6.26	-0.99	-1.14	-1.12	-1.17	-0.47	-0.84	-0.09
O16	6.25	-0.97	-1.13	-1.12	-1.16	-0.45	-0.75	-0.10
N1	4.96	-0.96	-1.29	-1.26	-1.35	-0.19	-0.61	0.08
N6	4.99	-0.92	-1.11	-1.12	-1.14	-0.75	-0.79	-0.09
C2	4.11	0.92	1.00	0.98	1.08	0.65	0.75	-0.32
C4	3.81	-0.13	-0.14	-0.15	-0.04	-0.29	-0.75	-0.42
C5	4.19	1.38	1.47	1.45	1.59	0.37	0.84	0.19
C8	4.03	0.30	0.35	0.34	0.42	-0.31	0.46	-1.21
C9	4.04	0.32	0.56	0.55	0.61	0.37	1.46	0.05
C10	4.05	0.06	-0.04	-0.04	0.04	-0.34	-1.25	1.28
C11	4.12	0.24	0.52	0.51	0.58	0.38	1.26	-1.32
C12	4.12	-0.02	-0.01	-0.01	0.09	-0.99	-0.77	-0.16
C13	4.02	-0.03	-0.02	-0.01	0.05	0.14	-0.57	0.49
C15	3.64	0.39	0.47	0.47	0.62	-0.94	-0.71	-0.31
C17	3.68	0.38	0.47	0.47	0.62	-0.79	-0.67	-0.38
H1	0.72	0.49	0.47	0.47	0.50	0.29	0.07	0.36
H4A	1.03	0.11	0.09	0.08	0.06	0.30	0.25	0.23
H4B	1.03	0.07	0.08	0.09	0.05	0.28	0.28	0.25
H10	0.81	0.20	0.05	0.05	0.02	0.47	0.41	0.16
H12	0.89	0.09	0.08	0.07	0.02	0.45	0.27	0.26
H13	0.84	0.14	0.07	0.06	0.04	0.62	0.29	0.21
H15A	1.00	0.07	0.06	0.05	0.02	0.26	0.36	0.22
H15B	1.00	0.05	0.03	0.02	0.00	0.40	0.31	0.16
H15C	1.00	0.06	0.02	0.03	0.00	0.35	0.31	0.16
H17A	1.00	0.06	0.03	0.01	0.00	0.30	0.24	0.16
H17B	1.00	0.05	0.01	0.03	0.00	0.35	0.26	0.16
H17C	1.00	0.06	0.06	0.06	0.03	0.24	0.47	0.22

Table 7.6 Detailed atomic charge values of **26**, calculated using a selection of methods. P_{val}: Atomic electron valence populations obtained directly from multipolar model; XRD: multipolar model; DFT_1: ωB97M-V/def2-TZVPD; DFT_2: M06-2X/6-311++G(d,p); DFT_3: PWPB95/aug-cc-pVQZ+aug-cc-pVQZ/C.

References

[1] P. Coppens, T. N. Guru Row, P. Leung, E. D. Stevens, P. J. Becker, and Y. W. Yang, “Net atomic charges and molecular dipole moments from spherical-atom x-ray refinements, and the relation between atomic charge and shape,” *Acta Crystallographica Section A*, vol. 35, no. 1, pp. 63–72, 1979. DOI:10.1107/S0567739479000127

[2] N. K. Hansen and P. Coppens, “Testing aspherical atom refinements on small-molecule data sets,” *Acta Crystallographica Section A*, vol. 34, no. 6, pp. 909–921, Nov 1978. DOI:10.1107/S0567739478001886

[3] R. F. Stewart, “Electron population analysis with rigid pseudoatoms,” *Acta Crystallographica Section A*, vol. 32, no. 4, pp. 565–574, Jul 1976. DOI:10.1107/S056773947600123X

[4] F. J. Anscombe, “Graphs in statistical analysis,” *The American Statistician*, vol. 27, no. 1, pp. 17–21, Feb. 1973. DOI:10.1080/00031305.1973.10478966

[5] P. Hohenberg and W. Kohn, “Inhomogeneous electron gas,” *Phys. Rev.*, vol. 136, pp. B864–B871, Nov 1964. DOI:10.1103/PhysRev.136.B864

[6] S. Kumar, S. Bawa, and H. Gupta, “Biological activities of quinoline derivatives,” *Mini-Reviews in Medicinal Chemistry*, vol. 9, no. 14, pp. 1648–1654, Dec. 2009. DOI:10.2174/138955709791012247

[7] I.-S. Chen, S.-J. Wu, I.-L. Tsai, T.-S. Wu, J. M. Pezzuto, M. C. Lu, H. Chai, N. Suh, and C.-M. Teng, “Chemical and bioactive constituents from zanthoxylum simulans,” *Journal of Natural Products*, vol. 57, no. 9, pp. 1206–1211, Sep. 1994. DOI:10.1021/np50111a003

[8] B. S. Matada, R. Pattanashettar, and N. G. Yernale, “A comprehensive review on the biological interest of quinoline and its derivatives,” *Bioorganic amp; Medicinal Chemistry*, vol. 32, p. 115973, Feb. 2021. DOI:10.1016/j.bmc.2020.115973

[9] I. A. Bala, O. F. Al Sharif, A. M. Asiri, and R. M. El-Shishtawy, “Quinoline: A versatile bioactive scaffold and its molecular hybridization,” *Results in Chemistry*, vol. 7, p. 101529, Jan. 2024. DOI:10.1016/j.rechem.2024.101529

[10] A. Fournet, M. E. Ferreira, A. Rojas De Arias, S. Torres De Ortiz, S. Fuentes, H. Nakayama, A. Schinini, and R. Hocquemiller, “In vivo efficacy of oral and intralesional administration of 2-substituted quinolines in experimental treatment of new world cutaneous leishmaniasis caused by leishmania amazonensis,” *Antimicrobial Agents and Chemotherapy*, vol. 40, no. 11, pp. 2447–2451, Nov. 1996. DOI:10.1128/aac.40.11.2447

[11] M. C. Mandewale, U. C. Patil, S. V. Shedge, U. R. Dappadwad, and R. S. Yamgar, “A review on quinoline hydrazone derivatives as a new class of potent antitubercular and anticancer agents,” *Beni-Suef University Journal of Basic and Applied Sciences*, vol. 6, no. 4, pp. 354–361, Dec. 2017. DOI:10.1016/j.bjbas.2017.07.005

[12] O. H. Rizk, M. G. Bekhit, A. A. B. Hazzaa, E.-S. M. El-Khawass, and I. A. Abdelwahab, “Synthesis, antibacterial evaluation, and dna gyrase inhibition profile of some new quinoline hybrids,” *Archiv der Pharmazie*, vol. 352, no. 10, Aug. 2019. DOI:10.1002/ardp.201900086

[13] S. I. Eissa, A. M. Farrag, S. Y. Abbas, M. F. El Shehry, A. Ragab, E. A. Fayed, and Y. A. Ammar, “Novel structural hybrids of quinoline and thiazole moieties: Synthesis and evaluation of antibacterial and antifungal activities with molecular modeling studies,” *Bioorganic Chemistry*, vol. 110, p. 104803, May 2021. DOI:10.1016/j.bioorg.2021.104803

[14] D. Zeleke, R. Eswaramoorthy, Z. Belay, and Y. Melaku, “Synthesis and antibacterial, antioxidant, and molecular docking analysis of some novel quinoline derivatives,” *Journal of Chemistry*, vol. 2020, pp. 1–16, Jul. 2020. DOI:10.1155/2020/1324096

[15] N. Nayak, J. Ramprasad, and U. Dalimba, “Synthesis and antitubercular and antibacterial activity of some active fluorine containing quinoline–pyrazole hybrid derivatives,” *Journal of Fluorine Chemistry*, vol. 183, pp. 59–68, Mar. 2016. DOI:10.1016/j.jfluchem.2016.01.011

[16] M. Wang, G. Zhang, J. Zhao, N. Cheng, Y. Wang, Y. Fu, Y. Zheng, J. Wang, M. Zhu, S. Cen, J. He, and Y. Wang, “Synthesis and antiviral activity of a series of novel quinoline derivatives as anti-rsv or anti-iav agents,” *European Journal of Medicinal Chemistry*, vol. 214, p. 113208, Mar. 2021. DOI:10.1016/j.ejmech.2021.113208

[17] I. A. Seliem, S. S. Panda, A. S. Girgis, Y. Moatasim, A. Kandeil, A. Mostafa, M. A. Ali, E. S. Nossier, F. Rasslan, A. M. Srour, R. Sakhuja, T. S. Ibrahim, Z. K. Abdel-samii, and A. M. Al-Mahmoudy, “New quinoline-triazole conjugates: Synthesis, and antiviral properties against sars-cov-2,” *Bioorganic Chemistry*, vol. 114, p. 105117, Sep. 2021. DOI:10.1016/j.bioorg.2021.105117

[18] D. Verbanac, R. Malik, M. Chand, K. Kushwaha, M. Vashist, M. Matijašić, V. Stepanić, M. Perić, H. Paljetak, L. Saso, and S. C. Jain, “Synthesis and evaluation of antibacterial and antioxidant activity of novel 2-phenyl-quinoline analogs derivatized at position 4 with aromatically substituted 4h-1, 2, 4-triazoles,” *Journal of Enzyme Inhibition and Medicinal Chemistry*, vol. 31, no. sup2, pp. 104–110, Jun. 2016. DOI:10.1080/14756366.2016.1190714

[19] K. Krafts, E. Hempelmann, and A. Skórska-Stania, “From methylene blue to chloroquine: a brief review of the development of an antimalarial therapy,” *Parasitology Research*, vol. 111, no. 1, pp. 1–6, Mar. 2012. DOI:10.1007/s00436-012-2886-x

[20] F. Zongo, C. Ribuot, A. Boumendjel, and I. Guissou, “Botany, traditional uses, phytochemistry and pharmacology of waltheria indica l. (syn. waltheria

americana): A review," *Journal of Ethnopharmacology*, vol. 148, no. 1, pp. 14–26, Jun. 2013. DOI:10.1016/j.jep.2013.03.080

[21] S. I. Eissa, A. M. Farrag, S. Y. Abbas, M. F. El Shehry, A. Ragab, E. A. Fayed, and Y. A. Ammar, "Novel structural hybrids of quinoline and thiazole moieties: Synthesis and evaluation of antibacterial and antifungal activities with molecular modeling studies," *Bioorganic Chemistry*, vol. 110, p. 104803, May 2021. DOI:10.1016/j.bioorg.2021.104803

[22] M. Akhter, R. Saha, O. Tanwar, M. Mumtaz Alam, and M. S. Zaman, "Synthesis and antimalarial activity of quinoline-substituted furanone derivatives and their identification as selective falcipain-2 inhibitors," *Medicinal Chemistry Research*, vol. 24, no. 2, pp. 879–890, Jul. 2014. DOI:10.1007/s00044-014-1139-1

[23] N. Suresh, H. N. Nagesh, K. V. G. Chandra Sekhar, A. Kumar, A. N. Shirazi, and K. Parang, "Synthesis of novel ciprofloxacin analogues and evaluation of their anti-proliferative effect on human cancer cell lines," *Bioorganic amp; Medicinal Chemistry Letters*, vol. 23, no. 23, pp. 6292–6295, Dec. 2013. DOI:10.1016/j.bmcl.2013.09.077

[24] A. Mrozek-Wilczkiewicz, M. Kuczak, K. Malarz, W. Cieślik, E. Spaczyńska, and R. Musiol, "The synthesis and anticancer activity of 2-styrylquinoline derivatives. a p53 independent mechanism of action," *European Journal of Medicinal Chemistry*, vol. 177, pp. 338–349, Sep. 2019. DOI:10.1016/j.ejmech.2019.05.061

[25] R. Z. Batran, S. M. El-Daly, W. A. El-Kashak, and E. Y. Ahmed, "Design, synthesis, and molecular modeling of quinoline–based derivatives as anti–breast cancer agents targeting egfr/akt signaling pathway," *Chemical Biology amp; Drug Design*, vol. 99, no. 3, pp. 470–482, Jan. 2022. DOI:10.1111/cbdd.14012

[26] S. Jain, V. Chandra, P. Kumar Jain, K. Pathak, D. Pathak, and A. Vaidya, "Comprehensive review on current developments of quinoline-based anticancer agents," *Arabian Journal of Chemistry*, vol. 12, no. 8, pp. 4920–4946, Dec. 2019. DOI:10.1016/j.arabjc.2016.10.009

[27] Baji, A. Gyovai, J. Wölfling, R. Minorics, I. Ocsovszki, I. Zupkó, and Frank, "Microwave-assisted one-pot synthesis of steroid–quinoline hybrids and an evaluation of their antiproliferative activities on gynecological cancer cell lines," *RSC Advances*, vol. 6, no. 33, pp. 27 501–27 516, 2016. DOI:10.1039/c6ra03910c

[28] R. F. George, E. M. Samir, M. N. Abdelhamed, H. A. Abdel-Aziz, and S. E.-S. Abbas, "Synthesis and anti-proliferative activity of some new quinoline based 4, 5-dihydropyrazoles and their thiazole hybrids as egfr inhibitors," *Bioorganic Chemistry*, vol. 83, pp. 186–197, Mar. 2019. DOI:10.1016/j.bioorg.2018.10.038

[29] K. H. Narasimhamurthy, D. K. M. Guruswamy, Chandra, N. Kallesha, Basappa, and K. S. Rangappa, "Synthesis of bioactive quinoline acting as anticancer agents and their mode of action using in silico analysis towards aurora kinase a inhibitors," *Chemical Data Collections*, vol. 35, p. 100768, Oct. 2021. DOI:10.1016/j.cdc.2021.100768

[30] K. Murugan, C. Panneerselvam, J. Subramaniam, M. Paulpandi, R. Rajaganesh, M. Vasanthakumaran, J. Madhavan, S. S. Shafi, M. Roni, J. S. Portilla-Pulido, S. C. Mendez, J. E. Duque, L. Wang, A. T. Aziz, B. Chandramohan, D. Dinesh, S. Piramanayagam, and J.-S. Hwang, "Synthesis of new series of quinoline derivatives with insecticidal effects on larval vectors of malaria and dengue diseases," *Scientific Reports*, vol. 12, no. 1, Mar. 2022. DOI:10.1038/s41598-022-08397-5

[31] S. Kumar Gupta and A. Mishra, "Synthesis, characterization amp; screening for anti-inflammatory amp; analgesic activity of quinoline derivatives bearing azetidinones scaffolds," *Anti-Inflammatory amp; Anti-Allergy Agents in Medicinal Chemistry*, vol. 15, no. 1, pp. 31–43, Sep. 2016. DOI:10.2174/1871523015666160210124545

[32] S. Mukherjee and M. Pal, "Medicinal chemistry of quinolines as emerging anti-inflammatory agents: An overview," *Current Medicinal Chemistry*, vol. 20, no. 35, pp. 4386–4410, Oct. 2013. DOI:10.2174/09298673113209990170

[33] K. Ilina and M. Henary, "Cyanine dyes containing quinoline moieties: History, synthesis, optical properties, and applications," *Chemistry – A European Journal*, vol. 27, no. 13, pp. 4230–4248, Dec. 2020. DOI:10.1002/chem.202003697

[34] I. Pyszka and B. Jędrzejewska, "Design of dyes based on the quinoline or quinoxaline skeleton towards visible light photoinitiators," *International Journal of Molecular Sciences*, vol. 25, no. 8, p. 4289, Apr. 2024. DOI:10.3390/ijms25084289

[35] D. Utreja, R. Salotra, G. Kaur, S. Sharma, and S. Kaushal, "Chemistry of quinolines and their agrochemical potential," *Current Organic Chemistry*, vol. 26, no. 20, pp. 1895–1913, Oct. 2023. DOI:10.2174/1385272827666221219101902

[36] S. Boryczka, A. Maślankiewicz, M. Wyszomirski, T. Borowiak, and M. Kubicki, "Structure assignment of some 3,4'-diquinolinyl sulfides studied by nuclear overhauser effects, x-ray analysis and reactions with sodium methoxide," *Recueil des Travaux Chimiques des Pays-Bas*, vol. 109, no. 10, pp. 509–514, 1990. DOI:10.1002/recl.19901091004

[37] L. J. Farrugia, "*WinGX* and *ORTEP for Windows*: an update," *Journal of Applied Crystallography*, vol. 45, no. 4, pp. 849–854, Aug 2012. DOI:10.1107/S0021889812029111

[38] A. D. Becke, "Density-functional thermochemistry. iii. the role of exact exchange," *The Journal of Chemical Physics*, vol. 98, no. 7, pp. 5648–5652, Apr. 1993. DOI:10.1063/1.464913

[39] C. Lee, W. Yang, and R. G. Parr, "Development of the colle-salvetti correlation-energy formula into a functional of the electron density," *Physical Review B*, vol. 37, no. 2, pp. 785–789, Jan. 1988. DOI:10.1103/physrevb.37.785

[40] J. T. H. Dunning and P. J. Hay, "Gaussian basis sets for molecular calculations," in *Modern Theoretical Chemistry*, H. F. S. III, Ed. New York: Plenum, 1977, vol. 3.

[41] D. Andrae, U. Huermann, M. Dolg, H. Stoll, and H. Preu, “Energy-adjustedab initio pseudopotentials for the second and third row transition elements,” *Theoretica Chimica Acta*, vol. 77, no. 2, pp. 123–141, 1990. DOI:10.1007/bf01114537

[42] A. Bergner, M. Dolg, W. Küchle, H. Stoll, and H. Preuß, “Ab initio energy-adjusted pseudopotentials for elements of groups 13–17,” *Molecular Physics*, vol. 80, no. 6, pp. 1431–1441, Dec. 1993. DOI:10.1080/00268979300103121

[43] M. J. Frisch, G. W. Trucks, H. B. Schlegel, G. E. Scuseria, M. A. Robb, J. R. Cheeseman, G. Scalmani, V. Barone, B. Mennucci, G. A. Petersson, H. Nakatsuji, M. Caricato, X. Li, H. P. Hratchian, A. F. Izmaylov, J. Bloino, G. Zheng, J. L. Sonnenberg, M. Hada, M. Ehara, K. Toyota, R. Fukuda, J. Hasegawa, M. Ishida, T. Nakajima, Y. Honda, O. Kitao, H. Nakai, T. Vreven, J. A. M. Jr., J. E. Peralta, F. Ogliaro, M. Bearpark, J. J. Heyd, E. Brothers, K. N. Kudin, V. N. Staroverov, R. Kobayashi, J. Normand, K. Raghavachari, A. Rendell, J. C. Burant, S. S. Iyengar, J. Tomasi, M. Cossi, N. Rega, J. M. Millam, M. Klene, J. E. Knox, J. B. Cross, V. Bakken, C. Adamo, J. Jaramillo, R. Gomperts, R. E. Stratmann, O. Yazyev, A. J. Austin, R. Cammi, C. Pomelli, J. W. Ochterski, R. L. Martin, K. Morokuma, V. G. Zakrzewski, G. A. Voth, P. Salvador, J. J. Dannenberg, S. Dapprich, A. D. Daniels, O. Farkas, J. B. Foresman, J. V. Ortiz, J. Cioslowski, and D. J. Fox, *Gaussian 09, Revision D.01*, Gaussian, Inc., Wallingford, CT, 2009.

[44] P. R. Spackman, M. J. Turner, J. J. McKinnon, S. K. Wolff, D. J. Grimwood, D. Jayatilaka, and M. A. Spackman, “*CrystalExplorer*: a program for Hirshfeld surface analysis, visualization and quantitative analysis of molecular crystals,” *Journal of Applied Crystallography*, vol. 54, no. 3, Jun 2021. DOI:10.1107/S1600576721002910

[45] G. M. Sheldrick *et al.*, “Shelxl-97, program for the refinement of crystal structures,” ” 1997.

[46] C. Jelsch, B. Guillot, A. Lagoutte, and C. Lecomte, “Advances in protein and small-molecule charge-density refinement methods using *MoPro*,” *Journal of Applied Crystallography*, vol. 38, no. 1, pp. 38–54, Feb 2005. DOI:10.1107/S0021889804025518

[47] B. Guillot, L. Viry, R. Guillot, C. Lecomte, C. Jelsch, B. Centre, C. Hermite, and B. Ãtiment, “Refinement of proteins at subatomic resolution with mopro,” *Journal of Applied Crystallography*, vol. 34, pp. 214–223, 04 2001. DOI:10.1107/S0021889801001753

[48] P. Politzer, J. S. Murray, and T. Clark, “Halogen bonding and other σ-hole interactions: a perspective,” *Physical Chemistry Chemical Physics*, vol. 15, no. 27, p. 11178, 2013. DOI:10.1039/c3cp00054k

[49] G. R. Desiraju and R. Parthasarathy, “The nature of halogen$\cdots$halogen interactions: are short halogen contacts due to specific attractive forces or due to close packing of nonspherical atoms?” *Journal of the American Chemical Society*, vol. 111, no. 23, pp. 8725–8726, Nov. 1989. DOI:10.1021/ja00205a027

[50] Y. Le Gal, A. Colas, F. Barrière, V. Dorcet, T. Roisnel, and D. Lorcy, “Halogen and chalcogen-bonding interactions in sulphur-rich -electron acceptors,” *CrystEngComm*, vol. 21, no. 12, pp. 1934–1939, 2019. DOI:10.1039/c8ce02046a

[51] A. Mukherjee, S. Tothadi, and G. R. Desiraju, “Halogen bonds in crystal engineering: Like hydrogen bonds yet different,” *Accounts of Chemical Research*, vol. 47, no. 8, pp. 2514–2524, 2014. DOI:10.1021/ar5001555

[52] V. Nemec, T. Vitasović, and D. Cinčić, “Halogen-bonded cocrystals of donepezil with perfluorinated diiodobenzenes,” *CrystEngComm*, vol. 22, no. 34, pp. 5573–5577, 2020. DOI:10.1039/d0ce01065k

[53] S. R. Kennedy, M. U. Main, C. R. Pulham, I. Ling, and S. J. Dalgarno, “A self-assembled nanotube supported by halogen bonding interactions,” *CrystEngComm*, vol. 21, no. 5, pp. 786–790, 2019. DOI:10.1039/c8ce01824c

[54] A. Pizzi, N. Demitri, G. Terraneo, and P. Metrangolo, “Halogen bonding at the wet interfaces of an amyloid peptide structure,” *CrystEngComm*, vol. 20, no. 36, pp. 5321–5326, 2018. DOI:10.1039/c8ce01205a

[55] L. González, S. Graus, R. M. Tejedor, A. Chanthapally, J. L. Serrano, and S. Uriel, “The combination of halogen and hydrogen bonding: a versatile tool in coordination chemistry,” *CrystEngComm*, vol. 22, no. 36, pp. 6010–6018, 2020. Available online: http://dx.doi.org/10.1039/D0CE00832J. DOI:10.1039/d0ce00832j

[56] M. Foyle and N. G. White, “Anion templated crystal engineering of halogen bonding tripodal tris(halopyridinium) compounds,” *CrystEngComm*, vol. 22, no. 14, pp. 2526–2536, 2020. DOI:10.1039/d0ce00241k

[57] E. Bosch, S. J. Kruse, E. W. Reinheimer, N. P. Rath, and R. H. Groeneman, “Regioselective [2 + 2] cycloaddition reaction within a pair of polymorphic co-crystals based upon halogen bonding interactions,” *CrystEngComm*, vol. 21, no. 43, pp. 6671–6675, 2019. DOI:10.1039/c9ce01379b

[58] G. Cavallo, P. Metrangolo, R. Milani, T. Pilati, A. Priimagi, G. Resnati, and G. Terraneo, “The halogen bond,” *Chemical reviews*, vol. 116, no. 4, pp. 2478–2601, Aug 2016. DOI:10.1021/acs.chemrev.5b00484

[59] G. R. Desiraju, P. S. Ho, L. Kloo, A. C. Legon, R. Marquardt, P. Metrangolo, P. Politzer, G. Resnati, and K. Rissanen, “Definition of the halogen bond (IUPAC Recommendations 2013),” *Pure and Applied Chemistry*, vol. 85, no. 8, pp. 1711–1713, Aug 2013. DOI:10.1351/PAC-REC-12-05-10

[60] L. P. Wolters, P. Schyman, M. J. Pavan, W. L. Jorgensen, F. M. Bickelhaupt, and S. Kozuch, “The many faces of halogen bonding: a review of theoretical models and methods,” *WIREs Computational Molecular Science*, vol. 4, no. 6, pp. 523–540, Jun. 2014. DOI:10.1002/wcms.1189

[61] K. E. Riley and P. Hobza, “Investigations into the nature of halogen bonding including symmetry adapted perturbation theory analyses,” *Journal of Chemical Theory and Computation*, vol. 4, no. 2, pp. 232–242, Jan. 2008. DOI:10.1021/ct700216w

[62] O. A. Syzgantseva, V. Tognetti, and L. Joubert, “On the physical nature of halogen bonds: A qtaim study,” *The Journal of Physical Chemistry A*, vol. 117, no. 36, pp. 8969–8980, Sep. 2013. DOI:10.1021/jp4059774

[63] W. Wołodkiewicz, W. Brzyska, and T. Głowiak, “Preparation, structure, and thermal decomposition of Cu (II) 3, 5-dichlorobenzoate trihydrate,” *Monatshefte für Chemie*, vol. 129, pp. 111–119, 1998. DOI:10.1007/PL00010147

[64] J. Medvecká, J. Halaška, K. Jomova, and J. Moncol, “Structures of copper(ii) 2-chlorobenzoate monohydrate and copper(ii) 3,5-dichlorobenzoate trihydrate,” *Acta Chimica Slovaca*, vol. 5, no. 1, pp. 15–20, 2012. DOI:10.2478/v10188-012-0003-5

[65] M. Korabik and M. Holynska, “CCDC 722664: Experimental crystal structure determination,” 2009. DOI:10.5517/CCS7ZRQ

[66] B.-L. Lee, M. D. Kärkäs, E. V. Johnston, A. K. Inge, L.-H. Tran, Y. Xu, O. Hansson, X. Zou, and B. Åkermark, “Synthesis and characterization of oligonuclear ru, co and cu oxidation catalysts,” *European Journal of Inorganic Chemistry*, vol. 2010, no. 34, pp. 5462–5470, Oct. 2010. DOI:10.1002/ejic.201000758

[67] L. Mei, J. Li, L. S. Tai, L. S. Song, L. Q. Rong, and Z. S. Ming, “Synthesis and catalytic activity of novel zn–n and cu–n complexes,” *Inorganic Chemistry Communications*, vol. 13, no. 9, pp. 1009–1013, Sep. 2010. DOI:10.1016/j.inoche.2010.05.017

[68] M. J. Andrews, A. Carpentier, A. M. Z. Slawin, D. B. Cordes, S. A. Macgregor, and A. J. B. Watson, “Mechanism of cu-catalyzed iododeboronation: A description of ligand-enabled transmetalation, disproportionation, and turnover in cu-mediated oxidative coupling reactions,” *ACS Catalysis*, vol. 13, no. 16, pp. 11 117–11 126, Aug. 2023. DOI:10.1021/acscatal.3c02839

[69] W. M. Haynes, *CRC Handbook of Chemistry and Physics*. CRC Press, Jun. 2016. DOI:10.1201/9781315380476

[70] G. Desiraju and T. Steiner, *The Weak Hydrogen Bond: In Structural Chemistry and Biology*. Oxford University Press, 05 2001. DOI:10.1093/acprof:oso/9780198509707.001.0001

[71] J. MacLeod and F. Rosei, “3.02 - directed assembly of nanostructures,” in *Comprehensive Nanoscience and Technology*, D. L. Andrews, G. D. Scholes, and G. P. Wiederrecht, Eds. Amsterdam: Academic Press, 2011, pp. 13–68. DOI:10.1016/B978-0-12-374396-1.00098-2

[72] P. A. Wood, R. S. Forgan, A. R. Lennie, S. Parsons, E. Pidcock, P. A. Tasker, and J. E. Warren, “The effect of pressure and substituents on the size of pseudo-macrocyclic cavities in salicylaldoxime ligands,” *CrystEngComm*, vol. 10, no. 2, pp. 239–251, 2008. DOI:10.1039/b712397c

[73] C. Zhu, K. Shoyama, and F. Würthner, “Conformation and aromaticity switching in a curved non–alternant sp2 carbon scaffold,” *Angewandte Chemie International Edition*, vol. 59, no. 48, pp. 21 505–21 509, Sep. 2020. DOI:10.1002/anie.202010077

[74] V. M. Abbinante, M. Zambra, G. García-Espejo, C. Pipitone, F. Giannici, S. Milita, A. Guagliardi, and N. Masciocchi, "Molecular design and crystal chemistry of polyfluorinated naphthalene-bis-phenylhydrazimides with superior thermal and polymorphic stability and high solution processability," *Chemistry – A European Journal*, vol. 29, no. 14, Feb. 2023. DOI:10.1002/chem.202203441

[75] F. B. de Almeida, M. da Silva Cunha, W. P. Barros, H. A. De Abreu, and R. Diniz, "Structure, electronic, magnetic, and gas adsorption properties of zinc(ii) and cobalt(ii) coordination polymers assembled from isonicotinylhydrazine and trimesic acid," *The Journal of Physical Chemistry C*, vol. 124, no. 38, pp. 21 103–21 112, Aug. 2020. DOI:10.1021/acs.jpcc.0c06479

[76] R. Chadha, J. Dureja, and M. Karan, "Tempering trans-resveratrol from the molecule to crystal level: A contemporary approach toward polymorphic pursuits and morphological insights," *Crystal Growth amp; Design*, vol. 16, no. 2, pp. 605–616, Dec. 2015. DOI:10.1021/acs.cgd.5b01004

[77] O. A. Myshkina, S. S. Kharitonova, S. Y. Balandina, R. R. Makhmudov, and N. Y. Lisovenko, "Synthesis, antimicrobial, and antinociceptive activity of 4-substituted 5-hydroxy-5-(tricholoromethyl)dihydrofuran-2, 3-diones," *Russian Journal of Organic Chemistry*, vol. 59, no. 5, pp. 743–755, May 2023. DOI:10.1134/s1070428023050019

[78] S. Khatua, S. Goswami, S. Biswas, K. Tomar, H. S. Jena, and S. Konar, "Stable multiresponsive luminescent mof for colorimetric detection of small molecules in selective and reversible manner," *Chemistry of Materials*, vol. 27, no. 15, pp. 5349–5360, Jul. 2015. DOI:10.1021/acs.chemmater.5b01773

[79] A. Ziółkowska, N. Szynkiewicz, J. Pikies, and Ponikiewski, "Synthesis of compounds with c=p-p and c=p-p bond systems based on the phospha-wittig reaction," *Dalton Transactions*, vol. 49, no. 39, pp. 13 635–13 646, 2020. DOI:10.1039/d0dt02728f

[80] C. Dou, W. Kosaka, and H. Miyasaka, "Gate-open-type sorption in a zigzag paddlewheel ru dimer chain compound with a phenylenediamine linker instructed by a preliminary structural change of desolvation," *Chemistry Letters*, vol. 46, no. 9, pp. 1288–1291, Sep. 2017. DOI:10.1246/cl.170509

[81] A. Valverde-González, M. C. Borrallo-Aniceto, U. Díaz, E. M. Maya, F. Gándara, F. Sánchez, and M. Iglesias, "Nitrogen-rich cobalt (ii) mofs as efficient bifunctional catalysts for single or tandem oxidation and co2 conversion reactions," *Journal of CO2 Utilization*, vol. 67, p. 102298, Jan. 2023. DOI:10.1016/j.jcou.2022.102298

[82] T. Soya, K. Naoda, and A. Osuka, "Niii metalations of [40]– and [42]nonaphyrins(1.1.1.1.1.1.1.1.1): The largest doubly twisted hückel antiaromatic molecule," *Chemistry – An Asian Journal*, vol. 10, no. 1, pp. 231–238, Sep. 2014. DOI:10.1002/asia.201402933

[83] Q. Wang, Y. Li, Z. Qi, F. Xie, Y. Lan, and X. Li, "Rhodium(iii)-catalyzed annulation between n-sulfinyl ketoimines and activated olefins: C–h activation assisted by an oxidizing n–s bond," *ACS Catalysis*, vol. 6, no. 3, pp. 1971–1980, Feb. 2016. DOI:10.1021/acscatal.5b02297

[84] T. Balić, B. Marković, J. Jaźwiński, and D. Matković-Čalogović, “Synthesis and structural characterization of new n2o2-donor schiff base macrocycles and their silver(i) coordination polymers,” *Inorganica Chimica Acta*, vol. 435, pp. 283–291, Aug. 2015. DOI:10.1016/j.ica.2015.07.016

[85] A. Friedrich, I. E. Collings, K. F. Dziubek, S. Fanetti, K. Radacki, J. Ruiz-Fuertes, J. Pellicer-Porres, M. Hanfland, D. Sieh, R. Bini, S. J. Clark, and T. B. Marder, “Pressure-induced polymerization of polycyclic arene–perfluoroarene cocrystals: Single crystal x-ray diffraction studies, reaction kinetics, and design of columnar hydrofluorocarbons,” *Journal of the American Chemical Society*, vol. 142, no. 44, pp. 18 907–18 923, Oct. 2020. DOI:10.1021/jacs.0c09021

[86] S. Takamizawa, E.-i. Nakata, and T. Akatsuka, “Magnetic behavior of a 1d molecular–oxygen system included within a transformable single–crystal adsorbent,” *Angewandte Chemie International Edition*, vol. 45, no. 14, pp. 2216–2221, Mar. 2006. DOI:10.1002/anie.200501639

[87] I. Nemec, P. Zoufalý, R. Herchel, and Z. Trávníček, “Cobalt(iii) schiff-base cyanido complex usable as a ligand in preparation of heterobimetallic co(iii)–fe(iii) building blocks,” *Inorganic Chemistry Communications*, vol. 35, pp. 50–53, Sep. 2013. DOI:10.1016/j.inoche.2013.05.026

[88] S. Tothadi, K. Koner, K. Dey, M. Addicoat, and R. Banerjee, “Morphological evolution of two-dimensional porous hexagonal trimesic acid framework,” *ACS Applied Materials amp; Interfaces*, vol. 12, no. 13, pp. 15 588–15 594, Mar. 2020. DOI:10.1021/acsami.0c01398

[89] S. Panja, S. Maity, B. Majhi, and B. C. Ranu, “Palladium-catalyzed olefination of 4h-benzo[d][1, 3]oxazin-4-one derivatives with activated alkenes via preferential cyclic imine-n-directed aryl c-h activation,” *European Journal of Organic Chemistry*, vol. 2019, no. 33, pp. 5777–5786, Aug. 2019. DOI:10.1002/ejoc.201900935

[90] P. Fischer, P. Zolliker, B. Meier, R. Ernst, A. Hewat, J. Jorgensen, and F. Rotella, “Structure and dynamics of terephthalic acid from 2 to 300 k,” *Journal of Solid State Chemistry*, vol. 61, no. 1, pp. 109–125, Jan. 1986. DOI:10.1016/0022-4596(86)90012-5

[91] M. K. Węcławski, M. Jakešová, M. Charyton, N. Demitri, B. Koszarna, K. Oppelt, S. Sariciftci, D. T. Gryko, and E. D. Głowacki, “Biscoumarin-containing acenes as stable organic semiconductors for photocatalytic oxygen reduction to hydrogen peroxide,” *J. Mater. Chem. A*, vol. 5, no. 39, pp. 20 780–20 788, 2017. DOI:10.1039/c7ta05882a

[92] A. SAKON and H. UEKUSA, “Supramolecular structure of 5-hydroxyisophthalic acid-ethanol 2:1 solvate,” *X-ray Structure Analysis Online*, vol. 28, no. 0, pp. 35–36, 2012. DOI:10.2116/xraystruct.28.35

[93] V. López-Mejías, J. W. Kampf, and A. J. Matzger, “Nonamorphism in flufenamic acid and a new record for a polymorphic compound with solved structures,” *Journal of the American Chemical Society*, vol. 134, no. 24, pp. 9872–9875, Jun. 2012. DOI:10.1021/ja302601f

[94] Y. Zhang, B. Ourri, P.-T. Skowron, E. Jeamet, T. Chetot, C. Duchamp, A. M. Belenguer, N. Vanthuyne, O. Cala, E. Dumont, P. K. Mandal, I. Huc, F. Perret, L. Vial, and J. Leclaire, "Self-assembly of achiral building blocks into chiral cyclophanes using non-directional interactions," *Chemical Science*, vol. 14, no. 26, pp. 7126–7135, 2023. DOI:10.1039/d3sc01235b

[95] Y. Zhang, B. Ourri, P.-T. Skowron, E. Jeamet, T. Chetot, C. Duchamp, A. M. Belenguer, N. Vanthuyne, O. Cala, E. Dumont, P. K. Mandal, I. Huc, F. Perret, L. Vial, and J. Leclaire, "Self-assembly of achiral building blocks into chiral cyclophanes using non-directional interactions," *Chemical Science*, vol. 14, no. 26, pp. 7126–7135, 2023. DOI:10.1039/d3sc01235b

[96] O. M. Yaghi, H. Li, and T. L. Groy, "Construction of porous solids from hydrogen-bonded metal complexes of 1, 3, 5-benzenetricarboxylic acid," *Journal of the American Chemical Society*, vol. 118, no. 38, pp. 9096–9101, Jan. 1996. DOI:10.1021/ja960746q

[97] L. Frentzel-Beyme, P. Kolodzeiski, K. Terlinden, and S. Henke, "Microporous, crystalline, and water-processable framework materials of organic amphiphile salts," *Advanced Functional Materials*, vol. 33, no. 36, May 2023. DOI:10.1002/adfm.202302033

[98] S. Pradhan, P. Gurung, A. Chettri, P. Chhetri, N. D. Sherpa, T. Dutta, and B. Sinha, "Synthesis of her-capable cobalt metal organic framework using a straightforward reflux method and a thorough spectroscopic and theoretical analysis," *Journal of the Indian Chemical Society*, vol. 101, no. 6, p. 101166, Jun. 2024. DOI:10.1016/j.jics.2024.101166

[99] H. Abourahma, B. Moulton, V. Kravtsov, and M. J. Zaworotko, "Supramolecular isomerism in coordination compounds: Nanoscale molecular hexagons and chains," *Journal of the American Chemical Society*, vol. 124, no. 34, pp. 9990–9991, Aug. 2002. DOI:10.1021/ja027371v

[100] L. Golič and I. Leban, "Structures of tert-butyl 3-nitroperbenzoate (i) and tert-butyl 4-nitroperbenzoate (ii), c11h13no5," *Acta Crystallographica Section C Crystal Structure Communications*, vol. 40, no. 3, pp. 447–450, Mar. 1984. DOI:10.1107/s0108270184004479

[101] M. V. Lucky, S. Sivakumar, M. L. P. Reddy, A. K. Paul, and S. Natarajan, "Lanthanide luminescent coordination polymer constructed from unsymmetrical dinuclear building blocks based on 4-((1h-benzo[d]imidazol-1-yl)methyl)benzoic acid," *Crystal Growth amp; Design*, vol. 11, no. 3, pp. 857–864, Jan. 2011. DOI:10.1021/cg101519b

[102] S. M. Cohen, Z. Zhang, and J. A. Boissonnault, "Toward "metallomofzymes": Metal–organic frameworks with single-site metal catalysts for small-molecule transformations," *Inorganic Chemistry*, vol. 55, no. 15, pp. 7281–7290, May 2016. DOI:10.1021/acs.inorgchem.6b00828

[103] T.-J. M. Luo and G. T. R. Palmore, "Engineering crystalline architecture with supramolecular tapes: studies on secondary donoracceptor interactions in cocrystals of the cyclic dipeptide of glycine," *Crystal Growth amp; Design*, vol. 2, no. 5, pp. 337–350, Aug. 2002. DOI:10.1021/cg025535d

[104] M. O. Sinnokrot and C. D. Sherrill, “High-accuracy quantum mechanical studies of $\pi\pi$ interactions in benzene dimers,” *The Journal of Physical Chemistry A*, vol. 110, no. 37, pp. 10 656–10 668, Aug. 2006. DOI:10.1021/jp0610416

[105] C. A. Hunter and J. K. M. Sanders, “The nature of π-π interactions,” *Journal of the American Chemical Society*, vol. 112, no. 14, pp. 5525–5534, Jul. 1990. DOI:10.1021/ja00170a016

[106] S. E. Wheeler, “Understanding substituent effects in noncovalent interactions involving aromatic rings,” *Accounts of Chemical Research*, vol. 46, no. 4, pp. 1029–1038, Jun. 2012. DOI:10.1021/ar300109n

[107] E. Espinosa, M. Souhassou, H. Lachekar, and C. Lecomte, “Topological analysis of the electron density in hydrogen bonds,” *Acta Crystallographica Section B Structural Science*, vol. 55, no. 4, pp. 563–572, Aug. 1999. DOI:10.1107/s0108768199002128

[108] E. Aubert, F. Porcher, M. Souhassou, and C. Lecomte, “Electrostatic potential and interaction energies of molecular entities occluded in the alpo4-15 molecular sieve: determination from x-ray charge density analysis,” *Journal of Physics and Chemistry of Solids*, vol. 65, no. 12, pp. 1943–1949, 2004. DOI:10.1016/j.jpcs.2004.08.005

[109] P. Metrangolo and G. Resnati, “Type II halogen···halogen contacts are halogen bonds,” *IUCrJ*, vol. 1, no. 1, pp. 5–7, Jan 2014. DOI:10.1107/S205225251303491X

[110] F. Neese, “The orca program system,” *WIREs Computational Molecular Science*, vol. 2, no. 1, pp. 73–78, 2012. DOI:10.1002/wcms.81

[111] F. Neese, “Software update: The orca program system—version 5.0,” *WIREs Computational Molecular Science*, vol. 12, no. 5, p. e1606, 2022. DOI:10.1002/wcms.1606

[112] A. M. Grześkiewicz, T. Stefański, Z. Dutkiewicz, and M. Kubicki, “Weak intermolecular interactions in a series of biologically active 4′-methylthio-*trans*-stilbenes,” *Acta Crystallographica Section C*, vol. 78, no. 2, pp. 107–115, Feb 2022. DOI:10.1107/S2053229622000420

[113] A. Gielara-Korzańska, T. Stefański, A. Korzański, and S. Sobiak, “(*E*)-1-[4-(Methylsulfanyl)phenyl]-2-(2,3,4-trimethoxyphenyl)ethene,” *Acta Crystallographica Section E*, vol. 68, no. 9, p. o2791, Sep 2012. DOI:10.1107/S1600536812036288

[114] J. P. Glusker, M. Lewis, and M. Rossi, *Crystal structure analysis for chemists and biologists*. John Wiley & Sons, 1996, vol. 16.

[115] J. Sopková-de Oliveira Santos, M.-A. Bazin, J.-F. Lohier, L. El Kihel, and S. Rault, “1,2,3-Trimethoxy-4-[(*E*)-2-phenylvinyl]benzene and (*E*,*E*)-1,4-bis-(2,3,4-trimethoxyphenyl)buta-1,3-diene,” *Acta Crystallographica Section C*, vol. 65, no. 7, pp. o311–o313, Jul 2009. DOI:10.1107/S0108270109019702

[116] M. Nishio, “The ch/π hydrogen bond: Implication in chemistry,” *Journal of Molecular Structure*, vol. 1018, pp. 2–7, 2012, a Collection of Papers from the XIXth International Conference "Horizons in Hydrogen Bond Research", Gottingen, Germany, 12-17 September 2011. DOI:10.1016/j.molstruc.2012.03.012

[117] O. V. Dolomanov, L. J. Bourhis, R. J. Gildea, J. A. K. Howard, and H. Puschmann, “*OLEX2*: a complete structure solution, refinement and analysis program,” *Journal of Applied Crystallography*, vol. 42, no. 2, pp. 339–341, Apr 2009. DOI:10.1107/S0021889808042726

[118] D. Jayatilaka and B. Dittrich, “X-ray structure refinement using aspherical atomic density functions obtained from quantum-mechanical calculations,” *Acta Crystallographica Section A*, vol. 64, no. 3, pp. 383–393, May 2008. DOI:10.1107/S0108767308005709

[119] S. C. Capelli, H.-B. Bürgi, B. Dittrich, S. Grabowsky, and D. Jayatilaka, “Hirshfeld atom refinement,” *IUCrJ*, vol. 1, no. 5, pp. 361–379, Sep 2014. DOI:10.1107/S2052252514014845

[120] J. W. Furness, A. D. Kaplan, J. Ning, J. P. Perdew, and J. Sun, “Accurate and numerically efficient r2scan meta-generalized gradient approximation,” *The Journal of Physical Chemistry Letters*, vol. 11, no. 19, pp. 8208–8215, 2020. DOI:10.1021/acs.jpclett.0c02405

[121] F. Weigend and R. Ahlrichs, “Balanced basis sets of split valence, triple zeta valence and quadruple zeta valence quality for h to rn: Design and assessment of accuracy,” *Physical Chemistry Chemical Physics*, vol. 7, no. 18, p. 3297, 2005. DOI:10.1039/b508541a

[122] F. Kleemiss, O. V. Dolomanov, M. Bodensteiner, N. Peyerimhoff, L. Midgley, L. J. Bourhis, A. Genoni, L. A. Malaspina, D. Jayatilaka, J. L. Spencer, F. White, B. Grundkötter-Stock, S. Steinhauer, D. Lentz, H. Puschmann, and S. Grabowsky, “Accurate crystal structures and chemical properties from nosphera2,” *Chem. Sci.*, vol. 12, pp. 1675–1692, 2021. DOI:10.1039/D0SC05526C

[123] L. Midgley, L. J. Bourhis, O. V. Dolomanov, S. Grabowsky, F. Kleemiss, H. Puschmann, and N. Peyerimhoff, “Vanishing of the atomic form factor derivatives in non-spherical structural refinement – a key approximation scrutinized in the case of Hirshfeld atom refinement,” *Acta Crystallographica Section A*, vol. 77, no. 6, pp. 519–533, Nov 2021. DOI:10.1107/S2053273321009086

[124] F. Neese, “The shark integral generation and digestion system,” *Journal of Computational Chemistry*, vol. 44, no. 3, pp. 381–396, 2023. DOI:10.1002/jcc.26942

[125] T. Lu and F. Chen, “Multiwfn: A multifunctional wavefunction analyzer,” *Journal of Computational Chemistry*, vol. 33, no. 5, pp. 580–592, 2012. DOI:10.1002/jcc.22885

[126] T. Lu, “A comprehensive electron wavefunction analysis toolbox for chemists, multiwfn,” *The Journal of Chemical Physics*, vol. 161, no. 8, Aug. 2024. DOI:10.1063/5.0216272

[127] G. Knizia and J. E. M. N. Klein, "Electron flow in reaction mechanisms—revealed from first principles," *Angewandte Chemie International Edition*, vol. 54, no. 18, pp. 5518–5522, 2015. DOI:10.1002/anie.201410637

[128] D. Jayatilaka and D. J. Grimwood, *Tonto: A Fortran Based Object-Oriented System for Quantum Chemistry and Crystallography*. Springer Berlin Heidelberg, 2003, pp. 142–151. DOI:10.1007/3-540-44864-0$_1$5

[129] D. K. Jangid, "Dabco as a base and an organocatalyst in organic synthesis: A review," *Current Green Chemistry*, vol. 7, no. 2, pp. 146–162, Sep. 2020. DOI:10.2174/2213346107666191227101538

[130] D. I. Bugaenko, A. V. Karchava, and M. A. Yurovskaya, "The versatility of dabco: synthetic applications of its basic, nucleophilic, and catalytic properties part 1. catalysis of morita–baylis–hillman and knoevenagel reactions," *Chemistry of Heterocyclic Compounds*, vol. 56, no. 2, pp. 128–144, Feb. 2020. DOI:10.1007/s10593-020-02636-1

[131] D. I. Bugaenko, A. V. Karchava, and M. A. Yurovskaya, "The versatility of dabco: synthetic applications of its basic, nucleophilic, and catalytic properties part 2*. catalysis of michael and biginelli reactions and nucleophilic addition at c=x and cx bonds," *Chemistry of Heterocyclic Compounds*, vol. 56, no. 2, pp. 145–160, Feb. 2020. DOI:10.1007/s10593-020-02637-0

[132] A. Ying, Y. Ni, S. Xu, S. Liu, J. Yang, and R. Li, "Novel dabco based ionic liquids: Green and efficient catalysts with dual catalytic roles for aqueous knoevenagel condensation," *Industrial amp; Engineering Chemistry Research*, vol. 53, no. 14, pp. 5678–5682, Mar. 2014. DOI:10.1021/ie500440w

[133] B. Bita, "1, 4-diazabicyclo[2.2.2]octane (dabco) as a useful catalyst in organic synthesis," *European Journal of Chemistry*, vol. 1, no. 1, pp. 54–60, Mar. 2010. DOI:10.5155/eurjchem.1.1.54-60.2

[134] N. Chakraborty and A. K. Mitra, "The versatility of dabco as a reagent in organic synthesis: a review," *Organic amp; Biomolecular Chemistry*, vol. 21, no. 34, pp. 6830–6880, 2023. DOI:10.1039/d3ob00921a

[135] L. Cecchi, F. De Sarlo, and F. Machetti, "1, 4-diazabicyclo[2.2.2]octane (dabco) as an efficient reagent for the synthesis of isoxazole derivatives from primary nitro compounds and dipolarophiles: The role of the base," *European Journal of Organic Chemistry*, vol. 2006, no. 21, pp. 4852–4860, Oct. 2006. DOI:10.1002/ejoc.200600475

[136] D. I. Bugaenko, A. V. Karchava, and M. A. Yurovskaya, "The versatility of dabco: synthetic applications of its basic, nucleophilic, and catalytic properties: Part 3. catalysis of substitution, cycloaddition, isomerization, and rearrangement reactions," *Chemistry of Heterocyclic Compounds*, vol. 56, no. 3, pp. 265–278, Mar. 2020. DOI:10.1007/s10593-020-02655-y

[137] M. J. Aalam, Deepa, P. Chaudhary, D. R. Meena, G. D. Yadav, and S. Singh, "Dabco-based chiral ionic liquids as recoverable and reusable organocatalyst for asymmetric diels–alder reaction," *Chirality*, vol. 34, no. 1, pp. 134–146, Nov. 2021. DOI:10.1002/chir.23385

[138] P. Pinate, A. A. A. Saifan, and S. Makone, “Study of dabco based acidic ionic liquids strategy for the synthesis of 1, 3-dithiolane and benzothiazolo-[2, 3-b]-quinazolin-1-one derivatives,” *Catalysis Letters*, vol. 154, no. 4, pp. 1462–1478, Jul. 2023. DOI:10.1007/s10562-023-04411-1

[139] N. Seyyedi, F. Shirini, and M. S. Nikoo Langarudi, “Dabco-based ionic liquids: green and recyclable catalysts for the synthesis of barbituric and thiobarbituric acid derivatives in aqueous media,” *RSC Advances*, vol. 6, no. 50, pp. 44 630–44 640, 2016. DOI:10.1039/c6ra05878g

[140] D. I. Bugaenko, A. V. Karchava, and M. A. Yurovskaya, “The versatility of dabco: synthetic applications of its basic, nucleophilic, and catalytic properties part 4*. ionic liquids and reagents (selectfluor, dabso) derived from dabco, dabco as piperazine source,” *Chemistry of Heterocyclic Compounds*, vol. 56, no. 3, pp. 279–298, Mar. 2020. DOI:10.1007/s10593-020-02656-x

[141] Z.-S. Yao, K. Yamamoto, H.-L. Cai, K. Takahashi, and O. Sato, “Above room temperature organic ferroelectrics: Diprotonated 1, 4-diazabicyclo[2.2.2]octane shifts between two 2-chlorobenzoates,” *Journal of the American Chemical Society*, vol. 138, no. 37, pp. 12 005–12 008, Sep. 2016, CCDC: 1463262. DOI:10.1021/jacs.6b03747

[142] S. Löffler, A. Wuttke, B. Zhang, J. J. Holstein, R. A. Mata, and G. H. Clever, “Influence of size, shape, heteroatom content and dispersive contributions on guest binding in a coordination cage,” *Chem. Commun.*, vol. 53, no. 87, pp. 11 933–11 936, 2017, CCDC: 1557039. DOI:10.1039/c7cc04855f

[143] T. Wada, E. Kishida, Y. Tomiie, H. Suga, S. Seki, and I. Nitta, “Crystal structure and thermodynamical investigations of triethylenediamine, c6h12n2,” *Bulletin of the Chemical Society of Japan*, vol. 33, no. 9, pp. 1317–1318, Sep. 1960. DOI:10.1246/bcsj.33.1317

[144] G. S. Weiss, A. S. Parkes, E. R. Nixon, and R. E. Hughes, “Vibrational spectra and the structure of crystalline triethylenediamine,” *The Journal of Chemical Physics*, vol. 41, no. 12, pp. 3759–3767, Dec. 1964. DOI:10.1063/1.1725809

[145] J. K. Nimmo and B. W. Lucas, “Solid-state phase transition in triethylenediamine, n(ch2ch2)3n. i. the crystal structure of phase ii at 298 k,” *Acta Crystallographica Section B Structural Crystallography and Crystal Chemistry*, vol. 32, no. 2, pp. 348–353, Feb. 1976. DOI:10.1107/s0567740876003038

[146] J. L. Sauvajol, “Molecular motions of triethylenediamine in its low-temperature phase,” *Journal of Physics C: Solid State Physics*, vol. 13, no. 32, pp. L927–L934, Nov. 1980. DOI:10.1088/0022-3719/13/32/002

[147] A. Churakov, “CCDC 1580071: Experimental crystal structure determination,” 2017. DOI:10.5517/CCDC.CSD.CC1Q1610

[148] A. Lennartson and M. Hakansson, “CCDC 840299: Experimental crystal structure determination,” 2011. DOI:10.5517/CCX6DFX

[149] M. Y. Redko, J. E. Jackson, R. H. Huang, and J. L. Dye, “Design and synthesis of a thermally stable organic electride,” *Journal of the American Chemical Society*, vol. 127, no. 35, pp. 12 416–12 422, Aug. 2005. DOI:10.1021/ja053216f

[150] A. Lennartson and M. Hakansson, "CCDC 840298: Experimental crystal structure determination," 2011. DOI:10.5517/CCX6DDW

[151] J. P. Safko and R. D. Pike, "Synthesis and crystal structures of n, n-disubstituted piperazines," *Journal of Chemical Crystallography*, vol. 42, no. 9, pp. 981–987, Jul. 2012. DOI:10.1007/s10870-012-0346-1

[152] T. von Hirschheydt, V. Wolfart, R. Gleiter, H. Irngartinger, T. Oeser, F. Rominger, and F. Eisenträger, "A short survey of bicyclic diamines–syntheses and properties of n, n-bridged-1, 10-diazabicyclooctadeca-5, 14-diynes," *Journal of the Chemical Society, Perkin Transactions 2*, no. 2, pp. 175–183, 2000. DOI:10.1039/a907609c

[153] R. W. Alder, A. G. Orpen, and R. B. Sessions, "The structure of 1, 6-diazabicyclo[4.4.4]tetradecane and of its inside protonated ion," *Journal of the Chemical Society, Chemical Communications*, no. 18, p. 999, 1983. DOI:10.1039/c39830000999

[154] R. T. Watson, C. Hu, D. G. VanDerveer, D. T. Musashe, and P. S. Wagenknecht, "Synthesis and characterization of a highly topologically constrained tetraazamacrocyclic ligand," *Inorganic Chemistry Communications*, vol. 9, no. 2, pp. 180–182, Feb. 2006. DOI:10.1016/j.inoche.2005.10.026

[155] M. Bursch, J.-M. Mewes, A. Hansen, and S. Grimme, "Best-practice dft protocols for basic molecular computational chemistry," *Angewandte Chemie International Edition*, vol. 61, no. 42, p. e202205735, 2022. DOI:10.1002/anie.202205735

[156] N. Mardirossian and M. Head-Gordon, "Thirty years of density functional theory in computational chemistry: an overview and extensive assessment of 200 density functionals," *Molecular Physics*, vol. 115, no. 19, pp. 2315–2372, Jun. 2017. DOI:10.1080/00268976.2017.1333644

[157] I. Usón and G. M. Sheldrick, "An introduction to experimental phasing of macromolecules illustrated by shelx; new autotracing features," *Acta Crystallographica Section D Structural Biology*, vol. 74, no. 2, pp. 106–116, Feb. 2018. DOI:10.1107/s2059798317015121

[158] J.-D. Chai and M. Head-Gordon, "Long-range corrected hybrid density functionals with damped atom–atom dispersion corrections," *Physical Chemistry Chemical Physics*, vol. 10, no. 44, p. 6615, 2008. DOI:10.1039/b810189b

[159] N. Trotsko, "Antitubercular properties of thiazolidin-4-ones – a review," *Eur. J. Med. Chem.*, vol. 215, no. 113266, p. 113266, Apr. 2021. DOI:10.1016/j.ejmech.2021.113266

[160] S. J. Gilani, K. Nagarajan, S. P. Dixit, M. Taleuzzaman, and S. A. Khan, "Benzothiazole incorporated thiazolidin-4-ones and azetidin-2-ones derivatives: Synthesis and in vitro antimicrobial evaluation," *Arabian Journal of Chemistry*, vol. 9, pp. S1523–S1531, Nov. 2016. DOI:10.1016/j.arabjc.2012.04.004

[161] C. Tratrat, A. Petrou, A. Geronikaki, M. Ivanov, M. Kostić, M. Soković, I. S. Vizirianakis, N. F. Theodoroula, and M. Haroun, "Thiazolidin-4-ones as potential antimicrobial agents: Experimental and in silico evaluation," *Molecules*, vol. 27, no. 6, p. 1930, Mar. 2022. DOI:10.3390/molecules27061930

[162] C. Sanjeeva Reddy, M. Vani Devi, M. Sunitha, and A. Nagaraj, “Synthesis and antimicrobial study of linked heterocyclics containing pyrazole-pyrimidine-thiazolidin-4-one,” *Chem. Pharm. Bull. (Tokyo)*, vol. 58, no. 12, pp. 1622–1626, Dec. 2010. DOI:10.1016/j.molstruc.2024.139431

[163] N. Trotsko, U. Kosikowska, A. Paneth, M. Wujec, and A. Malm, “Synthesis and antibacterial activity of new (2,4-dioxothiazolidin-5-yl/ylidene)acetic acid derivatives with thiazolidine-2,4-dione, rhodanine and 2-thiohydantoin moieties,” *Saudi Pharm. J.*, vol. 26, no. 4, pp. 568–577, May 2018. DOI:10.1016/j.jsps.2018.01.016

[164] N. Trotsko, A. Przekora, J. Zalewska, G. Ginalska, A. Paneth, and M. Wujec, “Synthesis and in vitro antiproliferative and antibacterial activity of new thiazolidine-2,4-dione derivatives,” *J. Enzyme Inhib. Med. Chem.*, vol. 33, no. 1, pp. 17–24, Jan. 2018. DOI:10.1080/14756366.2017.1387543

[165] N. Georgiou, A. Cheilari, D. Karta, E. Chontzopoulou, J. Plavec, D. Tzeli, S. Vassiliou, and T. Mavromoustakos, “Conformational properties and putative bioactive targets for novel thiosemicarbazone derivatives,” *Molecules*, vol. 27, no. 14, p. 4548, Jul. 2022. DOI:10.3390/molecules27144548

[166] D. K. Aneja, P. Lohan, S. Arora, C. Sharma, K. R. Aneja, and O. Prakash, “Synthesis of new pyrazolyl-2,4-thiazolidinediones as antibacterial and antifungal agents,” *Org. Med. Chem. Lett.*, vol. 1, no. 1, p. 15, Nov. 2011. DOI:10.1186/2191-2858-1-15

[167] H. Kumar, A. Deep, and R. K. Marwaha, “Design, synthesis, in silico studies and biological evaluation of 5-((E)-4-((E)-(substituted aryl/alkyl)methyl)benzylidene)thiazolidine-2,4-dione derivatives,” *BMC Chem.*, vol. 14, no. 1, p. 25, Dec. 2020. DOI:10.1186/s13065-020-00678-2

[168] N. Trotsko, “Thiazolidin-4-ones as a promising scaffold in the development of antibiofilm agents—a review,” *International Journal of Molecular Sciences*, vol. 25, no. 1, art. no. 325, 2024. DOI:10.3390/ijms25010325

[169] S. Y. Bhat, S. Bhandari, P. S. Thacker, M. Arifuddin, and I. A. Qureshi, “Development of quinoline-based hybrid as inhibitor of methionine aminopeptidase 1 from leishmania donovani,” *Chem. Biol. Drug Des.*, vol. 97, no. 2, pp. 315–324, Feb. 2021. DOI:10.1111/cbdd.13783

[170] A. E. Evren, L. Yurttaş, and H. K. Gencer, “Synthesis of new thiazole derivatives bearing thiazolidin-4(5h)-one structure and evaluation of their antimicrobial activity,” *Braz. J. Pharm. Sci.*, vol. 58, 2022. DOI:10.1590/s2175-97902022e19248

[171] D. Mech, A. Kurowska, and N. Trotsko, “The bioactivity of thiazolidin-4-ones: A short review of the most recent studies,” *Int. J. Mol. Sci.*, vol. 22, no. 21, p. 11533, Oct. 2021. DOI:10.3390/ijms222111533

[172] T. S. Chitre, S. M. Patil, A. G. Sujalegaonkar, and K. D. Asgaonkar, “Designing of thiazolidin-4-one pharmacophore using QSAR studies for anti-HIV activity,” *Ind. J. Pharm. Educ.*, vol. 55, no. 2, pp. 581–589, May 2021. DOI:10.5530/ijper.55.2.97

[173] A. Messore, P. Malune, E. Patacchini, V. N. Madia, D. Ialongo, M. Arpacioglu, A. Albano, G. Ruggieri, F. Saccoliti, L. Scipione, E. Tramontano, S. Canton, A. Corona, S. Scognamiglio, A. Paulis, M. Suleiman, H. M. Al-Maqtari, F. M. A. Abid, S. M. A. Kawsar, M. Sankaranarayanan, R. Di Santo, F. Esposito, and R. Costi, "New thiazolidine-4-one derivatives as sars-cov-2 main protease inhibitors," *Pharmaceuticals*, vol. 17, no. 5, p. 650, May 2024. DOI:10.3390/ph17050650

[174] A. Kryshchyshyn, D. Kaminskyy, O. Karpenko, A. Gzella, P. Grellier, and R. Lesyk, "Thiazolidinone/thiazole based hybrids - new class of antitrypanosomal agents," *Eur. J. Med. Chem.*, vol. 174, pp. 292–308, Jul. 2019. DOI:10.1016/j.ejmech.2019.04.052

[175] N. Trotsko, A. Bekier, A. Paneth, M. Wujec, and K. Dzitko, "Synthesis and in vitro anti-toxoplasma gondii activity of novel thiazolidin-4-one derivatives," *Molecules*, vol. 24, no. 17, p. 3029, Aug. 2019. DOI:10.3390/molecules24173029

[176] V. Asati and S. K. Bharti, "Design, synthesis and molecular modeling studies of novel thiazolidine-2,4-dione derivatives as potential anti-cancer agents," *J. Mol. Struct.*, vol. 1154, pp. 406–417, Feb. 2018. DOI:10.1016/j.molstruc.2017.10.077

[177] V. Asati, D. K. Mahapatra, and S. K. Bharti, "Thiazolidine-2,4-diones as multi-targeted scaffold in medicinal chemistry: Potential anticancer agents," *Eur. J. Med. Chem.*, vol. 87, pp. 814–833, Nov. 2014. DOI:10.1016/j.ejmech.2014.10.025

[178] P. Roszczenko, S. Holota, O. K. Szewczyk, R. Dudchak, K. Bielawski, A. Bielawska, and R. Lesyk, "4-thiazolidinone-bearing hybrid molecules in anticancer drug design," *Int. J. Mol. Sci.*, vol. 23, no. 21, p. 13135, Oct. 2022. DOI:10.3390/ijms232113135

[179] H. M. A. Abumelha and A. Saeed, "Synthesis of some 5-arylidene-2-(4-acetamidophenylimino)-thiazolidin-4-one derivatives and exploring their breast anticancer activity," *J. Heterocycl. Chem.*, vol. 57, no. 4, pp. 1816–1824, Apr. 2020. DOI:10.1002/jhet.3906

[180] S. Thakral, D. Saini, A. Kumar, N. Jain, and S. Jain, "A synthetic approach and molecular docking study of hybrids of quinazolin-4-ones and thiazolidin-4-ones as anticancer agents," *Med. Chem. Res.*, vol. 26, no. 8, pp. 1595–1604, Aug. 2017. DOI:10.1007/s00044-017-1857-2

[181] S. A. Hassan, J. B. Ziwar, D. M. Aziz, and M. N. Abdullah, "Sonochemical synthesis of new thiazolidin-4-one derivatives as potent anticancer and antimicrobial agents with docking design, and energy gap estimation," *J. Mol. Struct.*, vol. 1301, no. 137282, p. 137282, Apr. 2024. DOI:10.1016/j.molstruc.2023.137282

[182] A. M. Isloor, D. Sunil, P. Shetty, S. Malladi, K. S. R. Pai, and N. Maliyakkl, "Synthesis, characterization, anticancer, and antioxidant activity of some new thiazolidin-4-ones in MCF-7 cells," *Med. Chem. Res.*, vol. 22, no. 2, pp. 758–767, Feb. 2013. DOI:10.1007/s00044-012-0071-5

[183] A. Sharma, V. Kumar, S. Jain, and P. C. Sharma, "Thiazolidin-4-one and hydrazone derivatives of capric acid as possible anti-inflammatory, analgesic and hydrogen peroxide-scavenging agents," *Journal of Enzyme Inhibition and Medicinal Chemistry*, vol. 26, no. 4, pp. 546–552, 2011. DOI:10.3109/14756366.2010.535796

[184] A. M. Shawky, M. A. S. Abourehab, A. N. Abdalla, and A. M. Gouda, "Optimization of pyrrolizine-based schiff bases with 4-thiazolidinone motif: Design, synthesis and investigation of cytotoxicity and anti-inflammatory potency," *Eur. J. Med. Chem.*, vol. 185, no. 111780, p. 111780, Jan. 2020. Available online: 10.1016/j.ejmech.2019.111780

[185] C. D. Barros, A. A. Amato, T. B. de Oliveira, K. B. R. Iannini, A. L. d. Silva, T. G. d. Silva, E. S. Leite, M. Z. Hernandes, M. d. C. Alves de Lima, S. L. Galdino, F. d. A. R. Neves, and I. d. R. Pitta, "Synthesis and anti-inflammatory activity of new arylidene-thiazolidine-2,4-diones as PPARgamma ligands," *Bioorg. Med. Chem.*, vol. 18, no. 11, pp. 3805–3811, Jun. 2010. DOI:10.1016/j.bmc.2010.04.045

[186] M. Rezaei, H. Ghafoori, M. R. Aghamaali, and M. Shourian, "Thiazolidinedione derivative suppresses lps-induced cox-2 expression and no production in raw 264.7 macrophages," *Iranian Journal of Pharmaceutical Research*, vol. 18, no. 3, Jul. 2019. DOI:10.22037/ijpr.2019.1100730

[187] I.-M. Vasincu, M. Apotrosoaei, S. Constantin, M. Butnaru, L. Vereștiuc, C.-E. Lupușoru, F. Buron, S. Routier, D. Lupașcu, R.-G. Taușer, and L. Profire, "New ibuprofen derivatives with thiazolidine-4-one scaffold with improved pharmaco-toxicological profile," *BMC Pharmacology and Toxicology*, vol. 22, no. 1, Feb. 2021. DOI:10.1186/s40360-021-00475-0

[188] E. T. B. Mohr, T. L. Lubschinski, J. M. D. de Oliveira, P. G. F. de Oliveira, B. G. M. Borba, I. G. Demarchi, and E. M. Dalmarco, "Thiazolidines derivatives and their anti-inflammatory activity in lps-induced raw 264.7 macrophages: a systematic review and meta-analysis," *Natural Product Research*, vol. 0, no. 0, pp. 1–17, 2024. DOI:10.1080/14786419.2024.2394103

[189] I. Piątkowska-Chmiel, "The analgesic effect of 1, 3-thiazolidin-4-one derivatives as potential modulators of the serotoninergic system," *FARMACIA*, vol. 67, no. 2, pp. 258–266, Mar. 2019. DOI:10.31925/farmacia.2019.2.9

[190] Archana and S. Saini, "Synthesis and anticonvulsant studies of thiazolidinone and azetidinone derivatives from indole moiety," *Drug Res (Stuttg)*, vol. 69, no. 8, pp. 445–450, Dec. 2018. DOI:10.1055/a-0809-5098

[191] S. Saini and Archana, "Synthesis and anticonvulsant studies of thiazolidinone and azetidinone derivatives from indole moiety," *Drug Res. (Stuttg.)*, vol. 69, no. 08, pp. 445–450, Aug. 2019. DOI:10.1055/a-0809-5098

[192] A. P. Nikalje, A. Ansari, S. Bari, and V. Ugale, "Synthesis, biological activity, and docking study of novel isatin coupled thiazolidin-4-one derivatives as anticonvulsants," *Arch. Pharm. (Weinheim)*, vol. 348, no. 6, pp. 433–445, Jun. 2015. DOI:10.1002/ardp.201500020

[193] P. R. Devchand, T. Liu, R. B. Altman, G. A. FitzGerald, and E. E. Schadt, “The pioglitazone trek via human PPAR gamma: From discovery to a medicine at the FDA and beyond,” *Front. Pharmacol.*, vol. 9, p. 1093, Oct. 2018. DOI:10.3389/fphar.2018.01093

[194] S. Nazreen, M. S. Alam, H. Hamid, M. S. Yar, A. Dhulap, P. Alam, M. A. Q. Pasha, S. Bano, M. M. Alam, S. Haider, C. Kharbanda, Y. Ali, and K. K. Pillai, “Thiazolidine-2,4-diones derivatives as PPAR-γ agonists: synthesis, molecular docking, in vitro and in vivo antidiabetic activity with hepatotoxicity risk evaluation and effect on PPAR-γ gene expression,” *Bioorg. Med. Chem. Lett.*, vol. 24, no. 14, pp. 3034–3042, Jul. 2014. DOI:10.1016/j.bmcl.2014.05.034

[195] A. Kumar, A. Chawla, S. Jain, P. Kumar, and S. Kumar, “3-aryl-2-4-[4-(2,4-dioxothiazolidin-5-ylmethyl)phenoxy]-phenyl-acrylic acid alkyl ester: synthesis and antihyperglycemic evaluation,” *Med. Chem. Res.*, vol. 20, no. 6, pp. 678–686, Jul. 2011. DOI:10.1007/s00044-010-9369-3

[196] A. D. Patel, T. Y. Pasha, P. Lunagariya, U. Shah, T. Bhambharoliya, and R. K. P. Tripathi, “A library of thiazolidin-4-one derivatives as protein tyrosine phosphatase 1B (PTP1B) inhibitors: An attempt to discover novel antidiabetic agents,” *ChemMedChem*, vol. 15, no. 13, pp. 1229–1242, Jul. 2020. DOI:10.1002/cmdc.202000055

[197] S. Amini, A. Momeni Tikdari, and H. Khabazzadeh, “Reaction between thiocarbamidoalkyl naphthols and acetylenic esters: An interesting cyclocondensation reaction for the synthesis of new thiazolidin-4-one derivatives,” *J. Chem. Sci. (Bangalore)*, vol. 127, no. 10, pp. 1795–1800, Oct. 2015. DOI:10.1007/s12039-015-0944-5

[198] N. Foroughifar and S. Ebrahimi, “One-pot synthesis of 1,3-thiazolidin-4-one using bi(sch2cooh)3 as catalyst,” *Chinese Chemical Letters*, vol. 24, no. 5, pp. 389–391, 2013. DOI:10.1016/j.cclet.2013.03.019

[199] S. Kumar, H. R. Bhat, M. K. Kumawat, and U. P. Singh, “Design and one-pot synthesis of hybrid thiazolidin-4-one-1, 3, 5-triazines as potent antibacterial agents against human disease-causing pathogens,” *New Journal of Chemistry*, vol. 37, no. 3, p. 581, 2013. DOI:10.1039/c2nj41028a

[200] S. Ebrahimi, “One-pot synthesis of 1, 3-thiazolidin-4-one using ammonium persulfate as catalyst,” *Journal of Sulfur Chemistry*, vol. 37, no. 6, pp. 587–592, Aug. 2016. DOI:10.1080/17415993.2016.1223298

[201] J. Safaei-Ghomi, M. Navvab, and H. Shahbazi-Alavi, “One-pot sonochemical synthesis of 1, 3-thiazolidin-4-ones using nano-cdzr4(po4)6 as a robust heterogeneous catalyst,” *Ultrasonics Sonochemistry*, vol. 31, pp. 102–106, Jul. 2016. DOI:10.1016/j.ultsonch.2015.12.008

[202] A. Nowaczyk, M. Kowiel, A. Gzella, Fijałkowski, V. Horishny, and R. Lesyk, “Conformational space and vibrational spectra of 2-[(2,4-dimethoxyphenyl)amino]-1,3-thiazolidin-4-one,” *Journal of Molecular Modeling*, vol. 20, pp. 2366–2375, 2014. DOI:10.1007/s00894-014-2366-6

[203] L. Antonov, Ed., *Tautomerism: Methods and Theories*. Weinheim, Germany: Wiley-VCH Verlag, Dec. 2013. DOI:10.1002/9783527658824

[204] A. K. Ghosh, P. Chatterjee, and T. Chakraborty, "Keto-enol tautomerization and intermolecular proton transfer in photoionized cyclopentanone dimer in the gas phase," *The Journal of Chemical Physics*, vol. 141, no. 4, Jul. 2014. DOI:10.1063/1.4890501

[205] H.-H. Limbach, S. Baumgärtner, R. Franke, F. Männle, G. Scherer, and G. S. Denisov, "Double proton tautomerism via intra- or intermolecular pathways? the case of tetramethyl reductic acid studied by dynamic nmr: Hydrogen bond association, solvent and kinetic h/d isotope effects," *Molecules*, vol. 26, no. 14, p. 4373, Jul. 2021. DOI:10.3390/molecules26144373

[206] N. L. Allinger, J. A. Hirsch, and M. A. Miller, "The "size" of the lone pair on nitrogen," *Tetrahedron Letters*, vol. 8, no. 38, pp. 3729–3734, 1967. DOI:10.1016/S0040-4039(01)89782-3

[207] J. Galy, G. Couégnat, E. Vila, and S. F. Matar, "Stereochemistry of nitrogen E lone pair in NH3E, NOFE, N2O3E2, AgNO2E, and NCl3E," *Comptes Rendus Chimie*, vol. 20, no. 4, pp. 446–459, Aug. 2016. DOI:10.1016/S0040-4039(01)89782-3

[208] F. H. Allen and I. J. Bruno, "Bond lengths in organic and metal-organic compounds revisited: *X*—H bond lengths from neutron diffraction data," *Acta Crystallographica Section B*, vol. 66, no. 3, pp. 380–386, Jun 2010. DOI:10.1107/S0108768110012048

[209] R. F. W. Bader, "Bond paths are not chemical bonds," *The Journal of Physical Chemistry A*, vol. 113, no. 38, pp. 10 391–10 396, Sep. 2009. DOI:10.1021/jp906341r

[210] G. M. Sheldrick and T. R. Schneider, *[16] SHELXL: High-resolution refinement*. Elsevier, 1997, pp. 319–343. DOI:10.1016/s0076-6879(97)77018-6

[211] G. M. Sheldrick, "Crystal structure refinement with *SHELXL*," *Acta Crystallographica Section C*, vol. 71, no. 1, pp. 3–8, Jan 2015. DOI:10.1107/S2053229614024218

[212] B. Zarychta, V. Pichon-Pesme, B. Guillot, C. Lecomte, and C. Jelsch, "On the application of an experimental multipolar pseudo-atom library for accurate refinement of small-molecule and protein crystal structures," *Acta Crystallographica Section A*, vol. 63, no. 2, pp. 108–125, Mar 2007. DOI:10.1107/S0108767306053748

Appendix A

Refinement details

This section contains the setup details of final least squares refinement runs. Naturally, one should not expect to successfully obtain final multipolar model starting from just IAM and a reflections file; Refinement in general, and especially for data on the lower end of high resolution datasets, is an iterative process. Constraints and restraints definitions are attached for the sake of research integrity, as well as for extending model quality description further outside the realm of plain numerical values.

A.1 4-[[4-(Methoxy)-3-quinolinyl]thio]-3-thiomethylquinoline

Constraints

```
FIXUIJ    H7 1  0.030769  0.045423  0.037830 -0.021208  0.008047 -0.027988
FIXUIJ   H16 1  0.024177  0.032652  0.037153 -0.007421 -0.002179 -0.021258
FIXUIJ    H6 1  0.029924  0.038176  0.024007 -0.015339  0.008701 -0.020347
FIXUIJ    H8 1  0.030754  0.049211  0.040533 -0.025504  0.017423 -0.026955
FIXUIJ   H19 1  0.021828  0.030581  0.039229 -0.002402 -0.004248 -0.017411
FIXUIJ   H17 1  0.036804  0.031165  0.043016 -0.012275  0.004519 -0.026668
FIXUIJ    H9 1  0.037488  0.046065  0.027365 -0.021854  0.016015 -0.023716
FIXUIJ   H18 1  0.030134  0.023017  0.045731 -0.001340  0.003126 -0.020378
FIXUIJ  H22C 1  0.028743  0.040432  0.030244 -0.003400  0.007412 -0.019883
FIXUIJ    H2 1  0.039230  0.045953  0.031573 -0.024203  0.009509 -0.027589
```

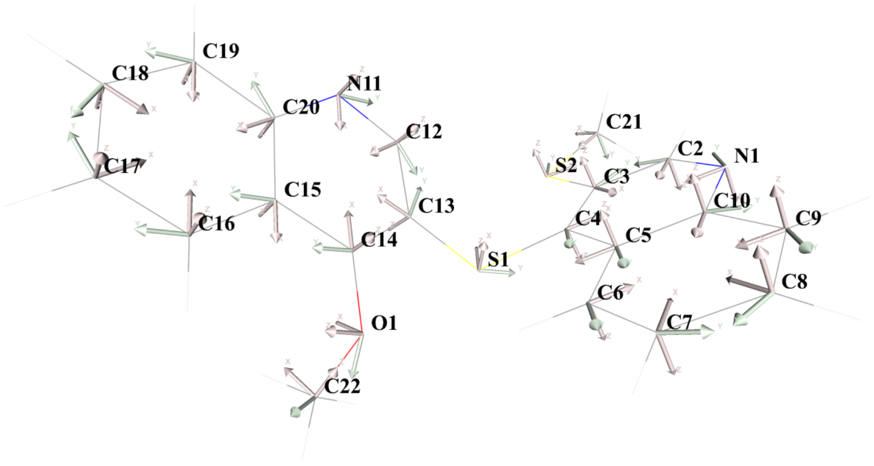

Fig. A.1 Local axes definitions of pseudoatoms for **1**. All multipoles freely refined. Hydrogen positions axes omitted for clarity.

```
FIXUIJ  H21B 1  0.039586  0.048710  0.053063 -0.013772  0.010895 -0.039431
FIXUIJ  H21C 1  0.056865  0.041881  0.033005 -0.023448  0.002846 -0.019681
FIXUIJ  H21A 1  0.048633  0.066812  0.053034 -0.042447  0.025592 -0.042257
FIXUIJ  H22B 1  0.035808  0.052505  0.032964 -0.021294 -0.000981 -0.022143
FIXUIJ  H22A 1  0.052970  0.023553  0.029401 -0.010614  0.002946 -0.014057
FIXUIJ   H12 1  0.028506  0.031409  0.034457 -0.011963  0.001347 -0.022032
```

Restraints

```
KAPPA1 CHEM  H    1.16  0.06
KAPPA2 CHEM  H    1.18  0.015
KAPPA1 H21C  1    1.16  0.01
KAPPA2 H21C  1    1.18  0.01
KAPPA1 H22B  1    1.16  0.01
KAPPA1 H19   1    1.16  0.01

VALRES H21C  1    1.00  0.1
VALRES H22C  1    1.00  0.01
VALRES H22C  1    1.00  0.1

SIMANG N11 1 C12 1 H12 1 C13 1 C12 1 H12 1 0.02
```

```
SIMANG C15 1 C16 1 H16 1 C17 1 C16 1 H16 1 0.02
SIMANG C5 1 C6 1 H6 1 C7 1 C6 1 H6 1 0.02
SIMANG C20 1 C19 1 H19 1 C18 1 C19 1 H19 1 0.02
SIMANG C16 1 C17 1 H17 1 C18 1 C17 1 H17 1 0.02
SIMANG C9 1 C8 1 H8 1 C7 1 C8 1 H8 1 0.02
SIMANG N1 1 C2 1 H2 1 C3 1 C2 1 H2 1 0.02
SIMANG C6 1 C7 1 H7 1 C8 1 C7 1 H7 1 0.02
SIMANG C10 1 C9 1 H9 1 C8 1 C9 1 H9 1 0.02
SIMANG H22A 1 C22 1 H22C 1 H22A 1 C22 1 H22B 1 H22C 1 C22 1 H22B 1 0.2
SIMANG C19 1 C18 1 H18 1 C17 1 C18 1 H18 1 0.02
SIMANG H21B 1 C21 1 H21C 1 H21B 1 C21 1 H21A 1 H21C 1 C21 1 H21A 1 0.2

DISTAN  C12 1  H12  1    1.083  0.002
DISTAN  C16 1  H16  1    1.083  0.002
DISTAN  C6  1  H6   1    1.083  0.05
DISTAN  C19 1  H19  1    1.083  0.002
DISTAN  C17 1  H17  1    1.083  0.001
DISTAN  C8  1  H8   1    1.083  0.002
DISTAN  C2  1  H2   1    1.083  0.002
DISTAN  C7  1  H7   1    1.083  0.002
DISTAN  C9  1  H9   1    1.083  0.002
DISTAN  C22 1  H22A 1    1.066  0.002
DISTAN  C22 1  H22C 1    1.066  0.002
DISTAN  C22 1  H22B 1    1.066  0.002
DISTAN  C18 1  H18  1    1.083  0.002
DISTAN  C21 1  H21B 1    1.066  0.002
DISTAN  C21 1  H21C 1    1.066  0.002
DISTAN  C21 1  H21A 1    1.066  0.001
```

A.2 Copper(II) 3,5-dichlorobenzoate trihydrate

Constraints

```
CONKAP O1W 1  O2W 1  O3W 1
CONKAP H1  1  H2  1  H4  1  H5  1
```

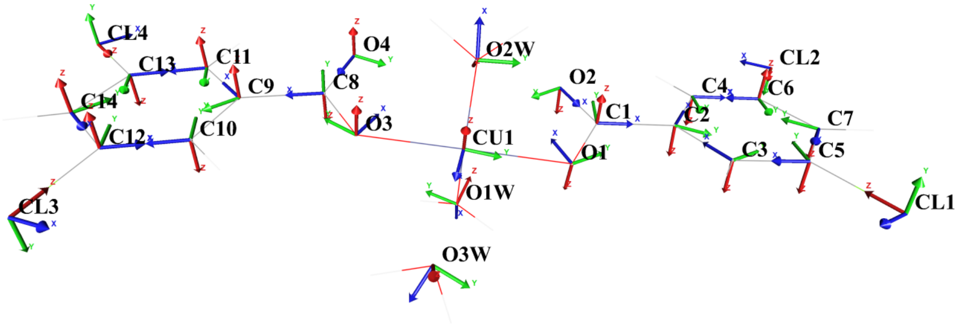

Fig. A.2 Local axes definitions of pseudoatoms of **2**. All non-hydrogen positions have geometrical restraints. Hydrogen positions dipoles refined freely, their axes omitted for clarity.

```
CONKAP H3  1  H6  1
CONKAP H1W 1  H2W 1  H3W 1  H4W 1  H5W 1  H6W 1

AVEVAL O1  1  O3  1
AVEVAL O2  1  O4  1
AVEVAL O1W 1  O2W 1  O3W 1

AVEPVM H1  1  H2  1  H4  1  H5  1
AVEPVM H3  1  H6  1
AVEPVM H1W 1  H2W 1  H3W 1  H4W 1  H5W 1  H6W 1

AVEPLM H1  1  H3  1

CONURA 1 O1W  H2W    1.5
CONURA 1 O1W  H1W    1.5
CONURA 1 O2W  H3W    1.5
CONURA 1 O2W  H4W    1.5
CONURA 1 O3W  H5W    1.5
CONURA 1 O3W  H6W    1.5

CONDIS O1W 1  H2W 1  0.983
CONDIS O1W 1  H1W 1  0.983
CONDIS O2W 1  H3W 1  0.983
```

```
CONDIS O2W 1  H4W 1  0.983
CONDIS O3W 1  H5W 1  0.983
CONDIS O3W 1  H6W 1  0.983
```

Restraints

```
RIGIDB ALL BON 0.005
RIGUIJ ALL BON 0.05
SIMK12 CHEM H  0.01

SIMKAP 1 CL1 CL3        0.01
SIMKAP 1 CL2 CL4        0.01
SIMKAP 1 O1 O3          0.01
SIMKAP 1 O2 O4          0.01
SIMKAP 1 C1 C8          0.01
SIMKAP 1 C2 C9          0.01
SIMKAP 1 C3 C4 C10 C11  0.01
SIMKAP 1 C5 C6 C12 C13  0.01
SIMKAP 1 C7 C14         0.01

KAPPA2 1 O1        0.9  0.005

SIMPVM 1  O2  O4        0.005
SIMPVM 1  C1  C8        0.005
SIMPVM 1  C2  C9        0.005
SIMPVM 1  C3  C11       0.005
SIMPVM 1  C5  C13       0.005
SIMPVM 1  C7  C14       0.005

RSYMUL 4m     CU1 1     0.004
RSYMUL cy     CL1 1     0.003
RSYMUL cy     CL2 1     0.001
RSYMUL cy     CL3 1     0.001
RSYMUL cy     CL4 1     0.003
RSYMUL 3m     O1  1     0.002
```

```
RSYMUL 3m     O2  1     0.006
RSYMUL mz     O2  1     0.004
RSYMUL 3m     O3  1     0.002
RSYMUL 3m     O4  1     0.006
RSYMUL mz     O4  1     0.004
RSYMUL mz     C1  1     0.01
RSYMUL my     C2  1     0.01
RSYMUL my     C3  1     0.01
RSYMUL my     C4  1     0.01
RSYMUL my     C5  1     0.01
RSYMUL my     C6  1     0.01
RSYMUL my     C7  1     0.01
RSYMUL mz     C8  1     0.01
RSYMUL my     C9  1     0.01
RSYMUL my     C10 1     0.01
RSYMUL my     C11 1     0.01
RSYMUL my     C12 1     0.01
RSYMUL my     C13 1     0.01
RSYMUL my     C14 1     0.01
RSYMUL my     O1W 1     0.03
RSYMUL mz     O1W 1     0.003
RSYMUL mymz   O2W 1     0.03
RSYMUL my     O3W 1     0.02
RSYMUL mz     O3W 1     0.003

URATIO 1 C3  H1         1.2  0.01
URATIO 1 C4  H2         1.2  0.01
URATIO 1 C7  H3         1.2  0.01
URATIO 1 C10 H4         1.2  0.01
URATIO 1 C11 H5         1.2  0.01
URATIO 1 C14 H6         1.2  0.01

SIMDIS 1 C5 H1 C2 H1        0.005
SIMDIS 1 C6 H2 C2 H2        0.005
SIMDIS 1 C5 H3 C6 H3        0.005
```

```
SIMDIS 1 C12 H4 C9 H4       0.005
SIMDIS 1 C13 H5 C9 H5       0.005
SIMDIS 1 C12 H6 C13 H6      0.005

DISTAN C3  1  H1  1   1.083 0.005
DISTAN C4  1  H2  1   1.083 0.005
DISTAN C7  1  H3  1   1.083 0.005
DISTAN C10 1  H4  1   1.083 0.005
DISTAN C11 1  H5  1   1.083 0.005
DISTAN C14 1  H6  1   1.083 0.005
```

A.3 4-methylsulphanyl-2’,5’-dimethoxy-E-stilbene

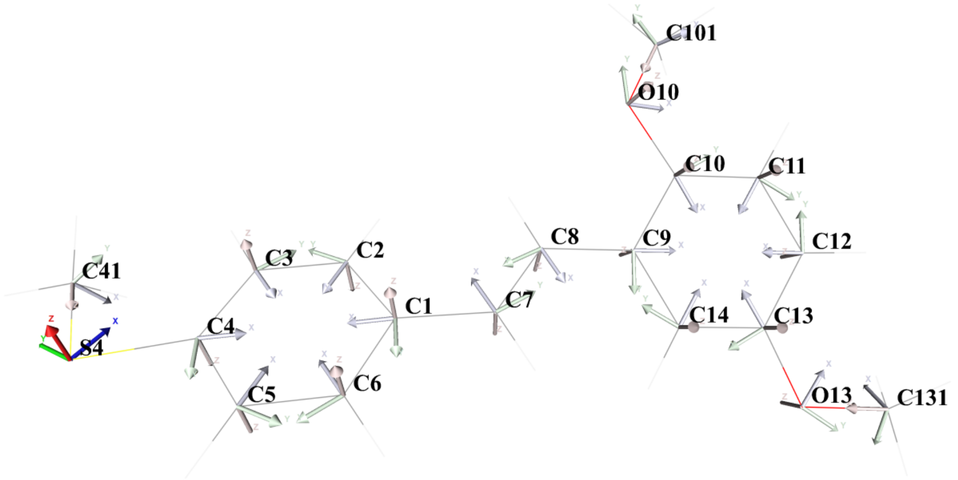

Fig. A.3 Local axes definitions of pseudoatoms of **8**. Vibrant arrows for multipoles with geometrical restraints, pale for freely refined. Hydrogen positions dipoles refined freely, their axes omitted for clarity.

Constraints

```
CONKAP C2    1  C6    1
CONKAP C3    1  C5    1
CONKAP C11   1  C12   1
CONKAP O10   1  O13   1
```

```
CONKAP C10   1  C13   1
CONKAP C101  1  C131  1
CONKAP C7    1  C8    1
CONKAP H2    1  H6    1
CONKAP H7    1  H8    1
CONKAP H3    1  H5    1
CONKAP H11   1  H12   1  H14    1
CONKAP H41A  1  H41B  1  H41C   1
CONKAP H10A  1  H10B  1  H10C   1  H13A   1  H13B   1  H13C   1

AVEPVM C2    1  C6    1
AVEPVM C3    1  C5    1
AVEPVM O10   1  O13   1
AVEPVM C101  1  C131  1
AVEPVM C11   1  C12   1
AVEPLM C7    1  C8    1
AVEPVM H2    1  H6    1  H7     1  H8     1
AVEPVM H3    1  H5    1
AVEPVM H41A  1  H41B  1  H41C   1
AVEPVM H10A  1  H10B  1  H10C   1  H13A   1  H13B   1  H13C   1
AVEPVM H11   1  H12   1  H14    1
AVEPLM H2    1  H3    1  H11    1
```

Restraints

```
RIGIDB ALL BON 0.001
RIGUIJ ALL BON 0.002
SIMK12 CHEM H  0.01

SIMPVM 1    C7    C8  0.01

RSYMUL my   S4   1    0.03
RSYMUL mz   S4   1    0.02
```

A.4 1,4-diazabicyclo[2.2.2]octane

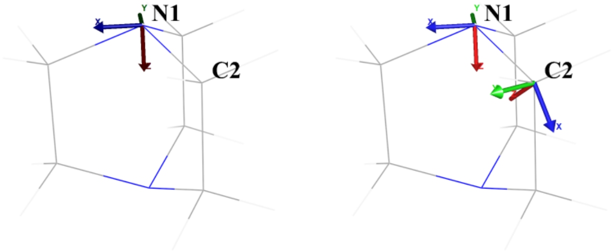

Fig. A.4 Local axes definitions of pseudoatoms of **18**. Dark arrows for constrained multipolar geometries, vibrant for restrained. Hydrogen positions dipoles refined freely, their axes omitted for clarity.

Constraints

```
POINTS X=0.666667 1 N1
POINTS Y=0.333333 1 N1

POINTS U11=U22 N1 1
POINTS U12=U11:2 N1 1
POINTS U13=0 N1 1
POINTS U23=0 N1 1

SYMPLM 3z N1 1
```

Restraints

```
RIGIDB ALL BON 0.002
RIGUIJ ALL BON 0.005
SIMK12 CHEM H  0.005

KAPPA2 N1 1 1.0 0.002
KAPPA2 C2 1 1.0 0.003

UIJRAT  1  C2  H2B   1.2   0.04
```

```
UIJRAT  1  C2  H2A   1.2   0.04
ISOTRO  CHEM  H            0.03

SIMVAL      1   H2A H2B 0.005
SIMPLM      1   H2A H2B 0.01
RSYMUL my 1 C2 0.005
RSYMUL -43m 1 C2 0.02
RSYMUL mz 1 N1 0.004

SIMANG 1 N1 1 C2 1 H2B 1 N1 1 C2 1 H2A 1 0.01
SIMDIS 1 C2 H2B   C2 H2A      0.005
SIMDIS 1 N1 H2B   N1 H2A      0.01
DISTAN C2  1  H2B 1    1.092  0.001
DISTAN C2  1  H2A 1    1.092  0.001
```

A.5 2-[(2,4-Dimethoxyphenyl)amino]-1,3-thiazolidin-4-one

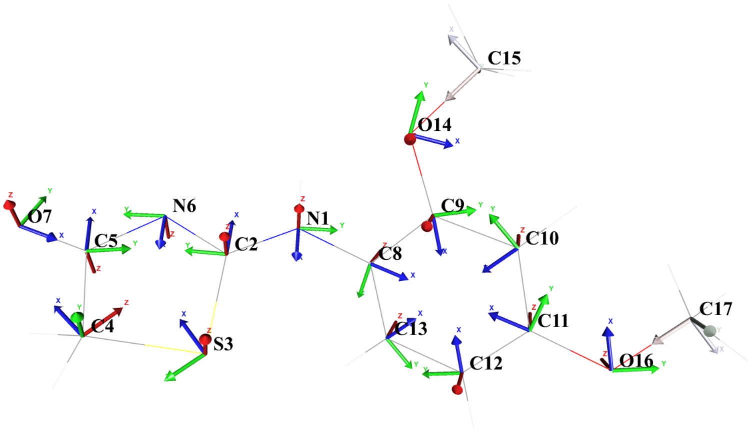

Fig. A.5 Local axes definitions of pseudoatoms of **26**. Vibrant arrows for restrained multipolar geometries, pale arrows for multipoles freely refined. Hydrogen positions dipoles refined freely, their axes omitted for clarity.

Constraints

```
CONKAP C15  1  C17   1

CONKAP H4A  1  H4B   1

CONKAP H15A 1  H15B  1  H15C 1  H17A 1  H17B 1  H17C 1


AVEPVM H4A  1  H4B   1

AVEPVM H15A 1  H15B  1  H15C 1  H17A 1  H17B 1  H17C 1

AVEPLM H10  1  H12   1  H13  1
```

Restraints

```
RIGIDB ALL BON 0.001

RIGUIJ ALL BON 0.002

SIMK12 CHEM H  0.01


KAPPA1 CHEM H  1.16  0.03

KAPPA2 CHEM H  1.18  0.02


RSYMUL mz   1  N1    0.003

RSYMUL mz   1  C2    0.003

RSYMUL mz   1  S3    0.01

RSYMUL my   1  S3    0.001

RSYMUL mz   1  C4    0.003

RSYMUL mz   1  C5    0.003

RSYMUL mz   1  N6    0.003

RSYMUL mymz 1  O7    0.003

RSYMUL mz   1  C8    0.003

RSYMUL mz   1  C9    0.003

RSYMUL mymz 1  C10   0.003

RSYMUL mz   1  C11   0.003

RSYMUL mz   1  C12   0.003

RSYMUL mz   1  C13   0.003

RSYMUL mymz 1  O14   0.003

RSYMUL mymz 1  O16   0.003
```

```
SIMPVM 1 C15  1 C17  0.03
SIMPVM 1 O14  1 O16  0.05
```

Appendix B

Scientific publications

Converging with dissertation

Experimental and Theoretical Charge Density Studies of Chalcogen Bonding and Other Intermolecular Contacts in 4-[[4-(Methoxy)-3-quinolinyl]thio]-3-thiomethylquinoline
DOI:10.1021/acs.cgd.5b00676

Intermolecular backbonding of halogen atoms: charge density studies of copper 3,5-dichlorobenzoate trihydrate
(In submission)

Charge Density Studies of 4-methylsulphanyl-E-stilbene derivatives with potential biological activity
(In preparation)

DABCO revisited: crystallographic and quantum chemical studies charge density distribution
(In preparation)

Other

Synthesis, crystal structures, spectroscopic studies and antibacterial properties of a series of mononuclear cobalt(III) Schiff base complexes
DOI:10.1007/s11243-014-9841-x

New Vinylgermanium Derivatives of Silsesquioxanes and Their Ruthenium Complexes – Synthesis, Structure, and Reactivity
DOI:10.1021/acs.organomet.5b00142

Selective Hydrosilylation of Alkynes with Octaspherosilicate $(HSiMe_2O)_8Si_8O_{12}$

DOI:10.1002/asia.201800726

Synthesis of G0 aminopolyol and aminosugar dendrimers, controlled by NMR and MALDI TOF mass spectrometry

DOI:10.1080/15685551.2016.1231048

Numbers with style: syntax highlighting for MoPro suite input files

(In preparation)

"The first gulp from the glass of natural sciences will turn you into an atheist,
but at the bottom of the glass God is waiting for you."

–Werner Heisenberg